



Natural Resources
Canada

Ressources naturelles
Canada

**GEOLOGICAL SURVEY OF CANADA
OPEN FILE 8976**

**ARA13C cruise report: 2022 Korea-Canada-USA Beaufort
Sea Research Program**

Edited by

J.K. Hong, V.I. Brake, Y. Choi, and C.K. Paull

2023

Canada 

**GEOLOGICAL SURVEY OF CANADA
OPEN FILE 8976**

**ARA13C cruise report: 2022 Korea-Canada-USA Beaufort
Sea Research Program**

Edited by

J.K. Hong¹, V.I. Brake², Y. Choi², and C.K. Paull³

¹Division of Polar Earth-System Sciences, Korea Polar Research Institute, KIOST, 26 Songdomirae-ro, Yeosu-gu, Incheon 21990, Korea

²Geological Survey of Canada, 490, rue de la Couronne, Québec, Quebec

³Monterey Bay Aquarium Research Institute, 7700 Sandholdt Road, Moss Landing, California 95039 U.S.A.

2023

© His Majesty the King in Right of Canada, as represented by the Minister of Natural Resources, 2023

Information contained in this publication or product may be reproduced, in part or in whole, and by any means, for personal or public non-commercial purposes, without charge or further permission, unless otherwise specified.

You are asked to:

- exercise due diligence in ensuring the accuracy of the materials reproduced;
- indicate the complete title of the materials reproduced, and the name of the author organization; and
- indicate that the reproduction is a copy of an official work that is published by Natural Resources Canada (NRCan) and that the reproduction has not been produced in affiliation with, or with the endorsement of, NRCan.

Commercial reproduction and distribution is prohibited except with written permission from NRCan. For more information, contact NRCan at copyright-droitdauteur@nrcan-rncan.gc.ca.

Permanent link: <https://doi.org/10.4095/331924>

This publication is available for free download through GEOSCAN (<https://geoscan.nrcan.gc.ca/>).

Recommended citation

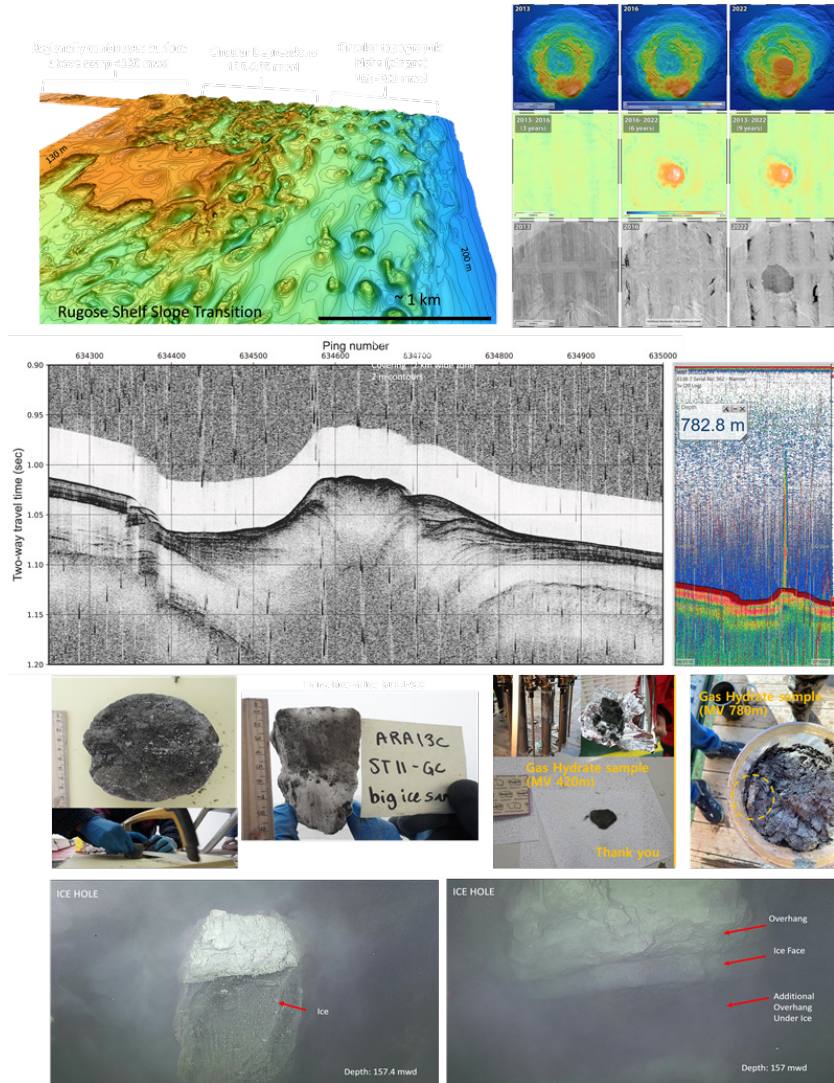
Hong, J.K., Brake, V.I., Choi, Y., and Paull, C.K. (ed.), 2023. ARA13C cruise report: 2022 Korea-Canada-USA Beaufort Sea Research Program; Geological Survey of Canada, Open File 8976, 293 p.
<https://doi.org/10.4095/331924>

Publications in this series have not been edited; they are released as submitted by the author.

ISSN 2816-7155
ISBN 978-0-660-48757-1
Catalogue No. M183-2/8976E-PDF

ARA13C Cruise Report

2022 Korea-Canada-USA Beaufort Sea Research Program



Utqiagvik, USA-Beaufort Sea-Nome, USA
 August 22 – September 19, 2022

J.K. Hong and Shipboard Scientific Party



Contact Information

Jong Kuk Hong

Division of Polar Earth-System Sciences

Korea Polar Research Institute, KIOST

26 Songdomirae-ro, Yeonsu-gu, Incheon 21990, Korea

Tel : +82 32-760-5404

Email : jkhong@kopri.re.kr

Citation

J.K. Hong and Shipboard Scientific Party, 2023. ARA13C Cruise Report: 2022 Korea-Canada-USA Beaufort Sea Research Program, Korea Polar Research Institute

ARA13C Cruise report

Contents

Summary	1
J.K. Hong, V.I. Brake, C.K. Paull, M.J. Duchesne, M.M. Côté and J.B. Obelcz	
Chapter 1. Introduction	5
V.I. Brake, M.J. Duchesne, J.K. Hong, C.K. Paull, M.M. Côté and J.B. Obelcz	
1.1. Context of Research Collaboration.....	5
1.2. Geologic Setting	5
1.3. Research Activity	6
1.4. Permits and Licensing.....	6
Chapter 2. Subbottom Profiling (Geophysical Survey)	9
S.-G. Kang, Y.J. Choi, H.J. Kim, Y. Choi and J.K. Hong	
2.1. Introduction	9
2.2. System Descriptions	10
2.3. Results/Highlights	13
2.3.1. Mud volcano located in 420 m depth, Beaufort Shelf area	14
2.3.2. Mud volcano located in 780 m depth, Beaufort Shelf area	15
2.3.3. Pingo-like Feature, Beaufort shelf area.....	17
2.3.4. Sub-bottom profiles for the shelf edge related to thawing subsea permafrost, Beaufort Shelf	18
Chapter 3. Seafloor Mapping Using Autonomous Underwater Vehicles	20
D.W. Caress, J.B. Paduan, C.K. Paull, R. Prickett, J. Caress, T.P. Poling, E. Martin and E. Lundsten	
3.1. Introduction	20
3.2. MBARI Mapping AUV Description, Operations, and Data Processing	21
3.2.1. Vehicle Description	21
3.2.2. MBARI AUV Team.....	23
3.2.3. AUV Launch and Recovery on the IBRV Araon.....	24
3.2.4. Mapping AUV Data Processing.....	26
3.3. High Resolution Seafloor Mapping Results	31
3.3.1. Introduction.....	31
3.3.2. Results From Each AUV Mission.....	33
3.3.2.1. Mission 20220830m1 – Shelf Edge Intact (1).....	33
3.3.2.2. Mission 20220901m1 – Shelf Edge Failed	38
3.3.2.3. Mission 20220902m1 – 420m Mud Volcano.....	43
3.3.2.4. Mission 20220906m1 – ARA05C Seismic Line 1; Shelf Edge Intact (2).....	47
3.3.2.5. Mission 20220906m2 –Shelf Edge Intact (3).....	52
3.3.2.6. Mission 20220907m1 –740 m Mud Volcano.....	57

3.3.3. Differencing of Bathymetry by Region.....	62
3.3.3.1. Shelf Edge Intact.....	63
3.3.3.2. Shelf Edge Failed.....	68
3.3.3.3. 420 m Mud Volcano.....	71
3.3.3.4. 740 m Mud Volcano.....	74
Chapter 4. MiniROV Diving.....	79
C. K. Paull, E. Lundsten, D. W. Caress, R. Gwiazda, D. Graves and F. Flores	
4.1. Introduction.....	79
4.2. MiniROV System.....	79
4.2.1. MiniROV Specifications.....	79
4.2.2. MiniROV operations off the IBRV Araon.....	80
4.2.3. ROV data types.....	83
4.3. Results / Highlights.....	84
4.3.1. Summary of MiniROV dive sites.....	84
4.3.2. ARA13C ROV-01.....	85
4.3.3. ARA13C ROV-02.....	93
4.3.4. ARA13C ROV-03.....	102
4.3.5. ARA13C ROV-04.....	106
4.3.6. ARA13C ROV-05.....	118
4.3.7. ARA13C ROV-06.....	124
4.3.8. ARA13C ROV-07.....	130
4.3.9. ARA13C ROV-08.....	142
4.3.10. ARA13C ROV-09.....	147
Chapter 5. Sediment coring.....	158
J.-H. Kim, Y. M. Lee, H.-S. Moon, Y. Ahn, J. Obelcz, S.-R. Seong, M. Walton, R. Gwiazda, H. T. H. Nguyen, S. Lee, J. Mok	
5.1. Introduction.....	158
5.1.1. Permafrost, shelf edge morphology, and freshening background.....	158
5.1.2. Microbial background.....	159
5.2. Methods.....	160
5.2.1. Sediment coring by multi-corer and gravity corer.....	160
5.2.2. ROV push coring.....	163
5.2.3. Pore water.....	166
5.2.4. Gas sampling.....	167
5.2.5. Dissociated ice water sampling.....	169
5.2.6. Sampling for microbial diversity and metagenome analysis.....	169
5.2.7. Biomarker.....	169
5.2.8. Mineralogy.....	171
5.2.9. Biological samples.....	173
5.3. Results.....	174
5.3.1. Sedimentology.....	174
5.3.2. Pore water chemistry.....	174
5.3.3. Oxygen measurement.....	179
5.4. Summary.....	180
Chapter 6. Heat flow measurements.....	182
Y.-G. Kim, H. Kim and Y. Baek	
6.1. Introduction.....	182

6.2. Methods	184
6.2.1. Temperature, pressure, and tilt.....	184
6.2.2. Experiment with descending the probe by a controlled distance during overpenetration	185
6.2.3. Bottom water temperature and pressure calibration.....	187
6.3. Results	188
6.3.1. Locations.....	188
6.3.2. Time series of probe sensors and winch readings	191
6.4. Future Work.....	198
6.4.1. Estimation of bulk density and thermal structure and their change with time	198
6.4.2. Estimation of other geotechnical properties.....	198
6.4.3. Geotechnical properties in relation to eruption activity	199
Chapter 7. Water Column Characterization.....	202
T.S. Rhee, M.-S. Kim, M. Kim and H. Park	
7.1. Introduction	202
7.2. Methods	204
7.2.1. In situ hydrographic measurements	204
7.2.2. Ocean current measurements	205
7.2.3. Supplementary measurements.....	206
7.2.4. Seawater sampling	206
7.2.5. Surface sediment sampling	206
7.2.6. Methane analysis.....	206
7.2.7. Dissolved inorganic carbon and total alkalinity	207
7.2.8. Nutrients.....	207
7.2.9. Underway pCO ₂ measurement.....	207
7.2.10. Dissolved oxygen.....	208
7.2.11. Dissolved organic carbon.....	208
7.2.12. Microbial oxidation experiments	208
7.3. Results	209
7.3.1. Physical properties of water masses.....	209
7.3.2. Methane in the surface waters and overlying air.....	210
7.3.3. Dissolved oxygen.....	212
7.3.4. Other parameters	213
7.4. Summary.....	213
Chapter 8. Mercury Study	214
S.W. Eom, J.H. Chae, H.K. Jeong, S.H. Lim and Y.G. Kim	
8.1. Introduction	214
8.2. Methods	215
8.2.1. Seawater sampling	215
8.2.2. Sediment sampling.....	218
8.2.3. DGM analysis	220
8.2.4. Photoreduction rate constant (k _r) of Hg(II)	221
8.2.5. Sampling procedure for stable Hg isotopes.....	222
8.3. Results	225
8.4. Summary.....	226
Appendix 1. Participants	229
Appendix 2. List of Stations and Line Survey.....	231
Appendix 3. Photos and Descriptions of Sediment Cores	241
3.1. Multi Cores	241
3.2. Gravity Cores.....	256

Appendix 4. Marine mammal observations report.....	271
Appendix 5. Group Photo	292

ARA13C Cruise report

Summary

J.K. Hong, V.I. Brake, C.K. Paull, M.J. Duchesne, M.M. Côté and J.B. Obelcz

Research experiments conducted and preliminary findings

Expedition ARA13C was an international research expedition undertaken jointly by the Korea Polar Research Institute (KOPRI), the Geological Survey of Canada (GSC), the Monterey Bay Aquarium Research Institute (MBARI) and the U.S. Naval Research Lab (NRL). The research took place over a period of 29 days from August 22 to September 19, 2022, onboard the Ice Breaking Research Vessel (IBRV) Araon operated by KOPRI. This is the fourth research mission for the IBRV Araon in the Canadian Beaufort Sea, and builds upon expeditions conducted in 2013, 2014 and 2017.

During the expedition, scientists from multiple disciplines applied their expertise to gain a comprehensive understanding of geological processes involved in subsea permafrost degradation and the impact it has on marine ecosystems, seafloor instability and methane concentration within the water column. Moreover, the dynamics of mud volcanoes, features that form on the seafloor when fluids from depth are venting, was studied.

The expedition targeted two main areas: the Mackenzie Trough and an area of known seabed and sub-surface change on the shelf-slope transition roughly in the center of the study area polygon (Figure S1).

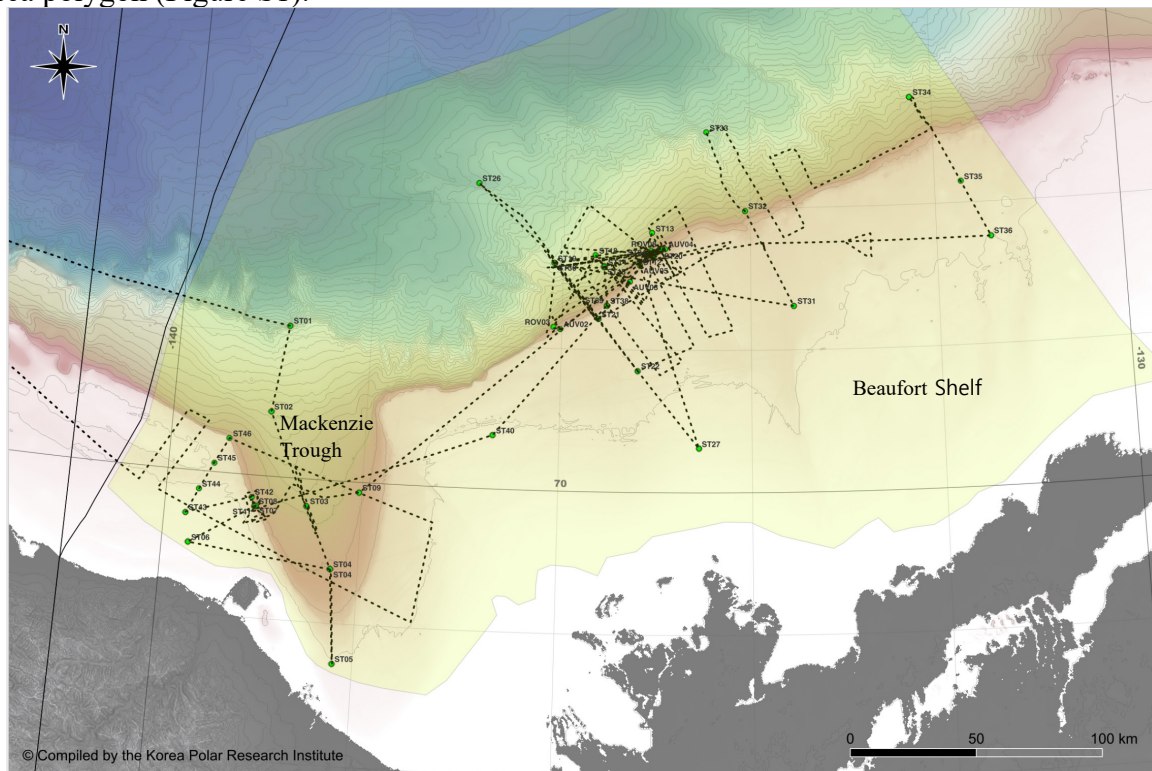


Figure S1. Study area map indicating ship track and stations during expedition ARA13C.

Continuous multibeam bathymetry and sub-bottom profile (SBP) data were collected along ship's track for a total line length of 3,300 and 3,395 line-kilometers respectively. Multibeam and SBP data provide an image of the seafloor and subsurface that assist in core site selection and contribute to the repertoire of surface and subsurface data. Where possible, an effort was made to fill in gaps in the existing multibeam and SBP coverage of the Beaufort Shelf and slope. The IBRV Araon was equipped with an echo sounder, or 'fish finder' capable of detecting acoustic anomalies in the water column indicative of rising plumes of methane gas bubbles. Such plumes were noted during the acquisition of new multibeam and SBPs over two known mud volcanoes at 420 and 780 mwd (metres water depth). Multichannel seismic data acquired by the Araon in 2014 demonstrated Bottom Simulating Reflectors (BSRs) interpreted to be related to gas hydrates. Coring activities at both the 420 and 780 mwd mud volcanoes sampled methane gas hydrates on these features.

Two MBARI mapping AUV's were used to obtain high resolution bathymetry and backscatter maps of the seafloor as well as chirp 1-6 kHz subbottom profiles. A total of 6 successful mapping expeditions generated a combined track length of roughly 480 line-km of 1-m scale data. AUV expeditions targeted the shelf edge east of the Mackenzie Trough as well as the 420 and 780 mwd mud volcanoes located on the slope. Five of the six AUV mapping targets aimed to re-survey areas covered by previous AUV surveys, while one was designed to coincide with multichannel seismic collected on the Araon in 2014. Comparisons with previous surveys that were conducted as long as 12 years apart and as short as 3 years apart, revealed sites of significant recent morphological changes. These data provide quantitative data on the rates of changes associated with permafrost degradation, mass wasting (the product of seafloor failure) and mud volcano activity. New and previous AUV data were then used as the basis for determining ROV targets as well as ship-based coring targets.

Detailed visual inspection of the seafloor was conducted on 9 dives of MBARI's MiniROV. In addition to continuous video footage, the MiniROV is capable of limited sampling via its manipulator arm, collection of up to 7 shallow push cores and deployment of a temperature probe. The 9 MiniROV dive sites were at locations surveyed by the AUV during this mission or since 2010, and with one site being located along ARA05C multi-channel seismic line 1. Visual inspection of the seafloor provides a way to ground truth calibrations with other data types and offers a glimpse of seafloor conditions. The objective of the MiniROV dives was to investigate areas that experienced large morphological changes as indicated by AUV mapping or re-visit features such as the 420 mwd mud volcano, to observe their continued evolution. The majority of the MiniROV missions were to investigate the morphological changes expressed as newly formed depressions or by the lateral retreat of scarps on the AUV data. Investigation by MiniROV provides observations concerning the timing and morphologic development of newly formed seafloor depressions. By observing multiple depressions in various stages of development we get a portrait of the evolution of such features. Unique to this mission was what we believe to be the first time that massive permafrost ice has been observed to be exposed on the seafloor along an underwater outcrop.

The coring program during ARA13C collected a total of 45 cores principally located on the shelf and upper continental slope in water depths less than 500 m. This total includes 20 multi-cores that were collected for sedimentological, geochemical and biological analyses as well as 15 gravity cores to determine sedimentary units and overall sedimentary history. Additionally, a number of shallow push cores were collected by the MiniROV in a variety of environments. Preliminary analyses and selection of samples for subsequent analysis were conducted onboard the vessel. Post-expedition analyses will be conducted by MBARI and KOPRI as well as by KOPRI's university collaborators in Korea. Further analysis will include studies related to

sedimentology, mineralogy, geochemistry, geochronology and microbiology. As mentioned, gas hydrates were observed in two of the cores recovered from mud volcanoes. Another notable discovery was the presence of ice within 3 gravity cores located in less than 200 mwd.

To study the thermal conditions of the previously mentioned 420 mwd mud volcano, a heat probe was deployed at 4 pre-determined stations corresponding to locations of heat flow measurements collected on the Araon in 2017. The gravity corer was used as a frame for the heat probe and sensors for pressure, temperature and tilt were attached. Three of the stations aimed to penetrate the thermal structure of MV 420 mwd while one station was located directly north of the mud volcano to provide an estimate of the gas hydrate stability zone. Due to past concerns of possible overpenetration, winch cable information (line out, tension) was collected. The newly acquired information, including details of the cable tension allow additional geotechnical properties of sediments to be derived.

In order to investigate the potential release of methane from melting permafrost, a number of water sampling and underway measurements were conducted. Continuous underway methane measurements along ship's track involved analyses of surface seawater from a depth of approximately 6 m pumped directly to the ship Chemistry laboratory. Hydrogeographic casting of the Conductivity-Temperature-Depth (CTD) sensors/water sampling Rosette, was conducted at 31 stations to measure the physical and chemical properties *in situ*. To support routine measurements an ARO-USB05 oxygen sensor was periodically installed on the AUV and on the frame of the CTD/Rosette. A Solo-T, RBR thermometer and ARO-USB oxygen sensor were also mounted on the multi-corer frame to log temperature and dissolved oxygen conditions near the seafloor. Information on the stratification and mixing of water masses was evaluated when planning AUV deployments. Preliminary methane measurements along ship's track indicate that surface seawater was mildly super-saturated with respect to atmospheric methane. Some higher concentrations were observed on the Yukon shelf.

Numerous studies of mercury, in its various forms, are underway, mainly as student projects, thanks to the data collected during the mission. In addition to continuous atmospheric measurements, seawater and sediment samples were collected and prepared onboard the vessel from multiple stations. Two stations in the Mackenzie Trough were chosen for Bongo net trawl to collect plankton and zooplankton from depths ranging from 35 to 190 m. Measurements of mercury concentration, mercury stable isotopes and, where possible, methylmercury concentrations will be conducted at GIST and POSTECH. Table S1 provides a summary of newly acquired data; analyses and interpretation are ongoing.

Table S1. Summary of datasets collected during expedition ARA13C

Type of data/instrument	Lines/Stations
Sub-bottom profiler	3, 395 km
Multibeam bathymetry	3, 300 km
CTD	31
Heat flow	4
Gravity core	15
Multi-core	20
Bongo net	2
AUV missions	6
MiniROV dives	9

Acknowledgments

The ARA13C marine research program was part of a research collaboration between Korea, Canada and the United States of America, which began in 2009. Lead organizations in the collaboration are the Korea Polar Research Institute, the Geological Survey of Canada and the

Monterey Bay Aquarium Research Institute. We thank the Planning Committee members of this collaboration for their vision and perseverance to bring this research program to reality during a global pandemic.

This marine geoscience research program takes place in the Inuvialuit Settlement Region. The research program was reviewed by Inuvialuit Environmental Impact Screening Committee (EISC Registry File: 01-22-08), the Government of Northwest Territories (Licence No. 16995), the Government of Yukon (License No. 22-11S&E), and the Department of Foreign Affairs, Trade and Development Canada (Permit – IGR-1283).

The efficiency of the captain and crew of Araon is graciously acknowledged and played a large factor in the productivity of the research program. Coordination of operations between the deck and the bridge were facilitated with the excellent interpretation and helping hands of Youngil Choi who at times acted simultaneously as a member of the crew and the science teams.

Funding for the research program was provided by the Ministry of Oceans and Fisheries (MOF), Korea. The Geological Survey of Canada conducted their studies as part of the Environmental Geoscience Program with the support from the Polar Continental Shelf Program (PCSP). The David and Lucile Packard Foundation provided the primary support for the AUV and ROV operations. Additional support for MBARI's costs were contributed by NRL.

Edward (Ned) King is acknowledged for acting as the critical reviewer of this contribution.

ARA13C Cruise report

Chapter 1. Introduction

V.I. Brake, M.J. Duchesne, J.K. Hong, C.K. Paull, M.M. Côté and J.B. Obelcz

1.1. Context of Research Collaboration

The Korea Polar Research Institute (KOPRI) is engaged in a collaborative study of the Arctic Ocean with the Geological Survey of Canada (GSC), the Monterey Bay Aquarium Research Institute (MBARI) and the U.S. Naval Research Laboratory (NRL). Our collaborative research program includes ship-based surveys, geologic surveys and sampling, and oceanographic and atmospheric measurements with the intent to acquire geoscience knowledge about the outer shelf and slope of the Beaufort Sea to address knowledge gaps related to thawing of subsea permafrost and seabed stability. The research collaboration onboard the Araon compliments our mutual ongoing research priorities and contributes to the state of knowledge of the Beaufort Sea and the Arctic ecosystem.

1.2. Geologic Setting

The continental shelf of Canadian Beaufort Sea (CBS) corresponds to the southern margin of the Canada Basin. Its development was initiated by an early Cretaceous rifting episode followed by a subsequent upper Cretaceous flooding and shale deposition into the Mackenzie Basin derived largely from sediment sources that lie further to the south (Grantz et al., 2011). The CBS is part of the Beaufort–Mackenzie Tectono-Sedimentary Element, a post-rift sequence of the Canada Basin formed by Late Cretaceous–Pleistocene sedimentary strata with a maximum thickness of over 12 km (Chen et al., 2021). From early to mid-Tertiary (beginning Eocene), further folding and thrusting lead to development of the Beaufort Foldbelt. This tectonic element hosts a series of unconformities and sequence-bounded mixed clastics associated with the Mackenzie River and Amundsen Gulf. Oligocene pull-apart resulted in the formation of a deep basin beneath the Beaufort Shelf and local broad folding. Within the shallow subsurface of the shelf under the CBS, a late Miocene unconformity is overlain by a thick, prograding sequence of Plio-Pleistocene muds including deltaic bodies, shelf-edge facies and abundant mass failures. The stratigraphic units as defined by Dixon et al. (1994) and Graves et al. (2010), include the Kugmallit Formation that is correlative to the most recent pull-apart episode, the thick Mackenzie Bay that overlies the Miocene unconformity, covered by the equally thick Akpak Formation, and a Pliocene shelf-top wedge with thick and multiple-failed slope equivalents termed the Iperk Formation.

The shallow subsurface geology of the CBS's shelf is underlain by continuous to discontinuous subsea permafrost that can be up to 700m thick. The permafrost formed during the Pleistocene when the shelf was subaerially exposed and subsequently inundated by relatively warm seawater as a consequence of post-glacial sea level rise(s). The permafrost body beneath the shelf extends far offshore yet pinches out at or before the shelf break at approximately 100 m water depth (Pullan et al., 1987; Taylor et al, 2013). Intrapermafrost gas

hydrates occur under the continental shelf and conventional gas hydrates on the continental slope where pressure and temperature favor their formation and preservation (Dallimore and Collett, 1995; Riedel et al., 2017).

Permafrost degradation and gas hydrate dissociation have the potential to modify the seafloor and the shallow subsurface of the CBS. Warming associated with climate changes results in some of the submarine permafrost and hydrate decomposing, which reduces the sediment strength, increasing the risk of seafloor failure, and potentially contribute to increase the rate of greenhouse gas emissions which provides a positive feedback effect. Recently, Paull et al. (2021) suggested that fluid venting and overpressure may have played a role in the development of the extensive slope failures seen along the continental slope of CBS. Gas venting has also been observed from conical ice extrusions on the shelf which are referred to as pingo-like features (Paull et al., 2007). Gwiazda et al. (2018) also revealed that regional groundwater flow related to subsea permafrost degradation exists beneath the CBS, discharging through seepages located near the shelf edge. Finally, Paull et al. (2022) used repeat high-resolution bathymetric surveys (2-9 yrs) to reveal rapid morphologic changes associated with submarine permafrost degradation that sculpt the seafloor of the CBS.

1.3. Research Activity

The 2022 marine research program sought to gain a comprehensive understanding of the marine geology of the Beaufort shelf and slope, including the stability and temporal changes of offshore permafrost. A primary objective of the mission was to re-survey a zone of known change on the shelf edge to gain an understanding of the frequency and rate of such changes. A focus of particular interest was the geologic processes and release of fluids and gas from thawing offshore permafrost. Our research contributes to the understanding of the geologic and glacial history of the Canadian Beaufort Sea while assessing ongoing changes and processes.

Principal activities included:

- Underway seafloor mapping using multibeam sonar
- Underway 3.5-kHz chirp (multifrequency) sub-bottom profiles for seismic visualization of shallow (10's of meters) sediments
- High-resolution seafloor mapping surveys using two AUVs (Autonomous Underwater Vehicles)
- Strategic collection of sediment using gravity, multi-core and push core equipment at sites identified on multibeam or sub-bottom profiles
- Deployment of water sampling and profiling equipment (Conductivity, Temperature Depth, CTD) to measure the physical and chemical properties of seawater
- Deployment of heat probes to measure geothermal heat flux at a mud volcano in 420 m water depth
- Ground-truthing of seafloor features using a mini Remotely Operated Vehicle (ROV)
- Deployment of Bongo nets to sample plankton for mercury content
- Underway measurement of methane, as well as visualization of methane bubble anomalies via fish finding equipment

1.4. Permits and Licensing

The scientific research permits and licenses required for the mission were obtained based on the rules and regulations of the study area and surrounding jurisdictions. The permits and licenses obtained in 2022 were based on similar submissions in 2013, 2014 and 2017.

Marine Scientific Research Permit – IGR-1283

The Department of Foreign Affairs, Trade and Development Canada (DFAIT) administers clearance for foreign vessels conducting research in Canadian waters. DFAIT approved diplomatic clearance for the Korean research vessel Araon on August 17, 2022. Obligations under the Marine Scientific Research Permit include: reporting to the nearest Canada Border Services Agency (CBSA) Marine Reporting office when entering Canadian waters, complying with the Licence to Fish for Scientific Purposes Licence # S-22/23-4002-IN from the Department of Fisheries and Oceans (DFO), and providing copies of all bathymetric data derived from the research expedition to DFO's Canadian Hydrographic Service (CHS).

Inuvialuit Environmental Impact Screening Committee (EISC)- EISC Registry File: [01-22-08]

The Environmental Impact Screening Committee (EISC) reviews applications for development or research purposes within the Inuvialuit settlement region. The EISC determined that the project did meet the definition of development as defined by the Inuvialuit Final Agreement but qualified for exemption from environmental impact screening given that the project would not have a significant impact on air, water, land or renewable resources, or negatively affect present or future wildlife harvesting. The post field report and scientific contributions will be provided to the EISC for their records.

Northwest Territories Scientific Research License – Scientific Research License # 16995

Northwest Territories Scientific Research Licence No. 16995 was issued by Aurora Research Institute on March 28, 2022. The post field report and scientific contributions will be provided to communities in the Inuvialuit Settlement Region (ISR) via their Hunter and Trapper Committee.

Yukon Scientists and Explorer Act License – Scientific Research License # 22-11S&E

In accordance with the Scientists and Explorers Act (1958) of the Yukon, a scientific research permit was issued on March 4, 2022. A final report of the research will be submitted within a year of the project's termination and scientific contributions will be provided to the Heritage Resources Unit as well as to First Nation(s).

References

- Chen, Z., Dietrich, J., Lane, L.S., Li, M and Dixon, J. 2021. Beaufort-Mackenzie Tectono-Sedimentary Element. In: Drachev, S.S., Brekke, H., Henriksen, E and Moore, T. (eds) Sedimentary Successions of the Arctic Region and their Hydrocarbon Prospectivity. *Geological Society*, London, Memoirs, 57.
- Dallimore, S.R. and Collett, T.S. 1995. Intrapermafrost gas hydrates from a deep corehole in the Mackenzie Delta. Northwest Territories, Canada. *Geology*, 23, 237–530,
- Dixon, J., Morrel, G.R. et al. 1994. Petroleum Resources of the Mackenzie Delta and Beaufort Sea. *Geological Survey of Canada Bulletin*, 474.
- Graves, J., Chen, Z., Dietrich, J.R. and Dixon J. 2010. Seismic interpretation and structural analysis of the Beaufort – Mackenzie Basin, Open File 6217, 22 p.
- Grantz, A., Scott, R.A., Drachev, S.S., Moore, T.E. and Valin, Z.C. 2011. Sedimentary successions of the Arctic Region (58–64° to 90°N) that may be prospective for hydrocarbons. *Geological Society*, London, Memoirs, 35, 17–37.
- Gwiazda, R., Paull, C.K., Dallimore, S.R., Melling, H., Jin, Y.K., Hong, J.K., Riedel, M., Lundsten, E., Anderson, K., Conway, K., 2018. Freshwater seepage into sediments of the shelf, shelf edge and continental slope of the Canadian Beaufort Sea. *Geol. Geochem. Geophys. Geosyst.* 19.
- Taylor, A.E., Dallimore, S.D., Hill, P.R., Issler, D.R., Blasco, S., and Wright, F. 2013. Numerical model of the geothermal regime on the Beaufort Shelf, arctic Canada since the Last Interglacial. *Journal of Geophysical Research: Earth Surface*, 118: 2365-2379.
- Paull, C.K., Ussler, W., Dallimore, S.D., Blasco, S.M., Lorenson, T.D., Melling, H., Medioli, B.E., Nixon F.M., and McLaughlin, F.A. 2007. Origin of pingo-like features on the Beaufort Sea Shelf and their possible relationship to decomposing methane gas hydrates. *Geophysical Research Letters*, 34: 1-5.
- Paull, C.K., Dallimore, S.R., Caress, D.W., Gwiazda, R., Lundsten, E., Anderson, K., Melling, H., Jin, Y.K., Duchesne, M.J., Kang, S-G., Kim, S., Riedel, M., King, E.L. and Lorenson, T. 2021. A 100-km wide slump along the upper slope of the Canadian Arctic was likely preconditioned for failure by brackish pore water flushing. *Marine Geology*, 435: 106453.
- Paull, C.K., Dallimore, S., Jin, Y.K., Caress, D.W., Lundsten, E., Gwiazda, R., Anderson, K., Hughes Clarke, J., Youngblut, S., and Melling H. 2022. Rapid seafloor changes associated with the degradation of Arctic submarine permafrost. *Proceeding of the National Academy of Sciences*, 119 (12) e2119105119.
- Pullan, S.E., MacAuley, H.A., Hunter, J.A.M., Good, R.L., Gagne, R.M., and Burns, R.A. 1987. Permafrost distribution determined from seismic refraction. In B. R. Pelletier (Ed.), Marine Science Atlas of the Beaufort Sea: Geology and Geophysics/Atlas Des Sciences Marines De La Mer De Beaufort: Géologie Et Géophysique. Geological Survey of Canada, Miscellaneous Report 40, p. 37.
- Riedel, M., Brent, T.A., Taylor, G., Taylor, A.E., Hong, J.-K., Jin, Y.-K., and Dallimore, S.R. 2017. Evidence for gas hydrate occurrences in the Canadian Arctic Beaufort Sea within the permafrost-associated shelf and deep-water marine environments, *Marine and Petroleum Geology*, v. 81, p. 66-78.

ARA13C Cruise report

Chapter 2. Subbottom Profiling (Geophysical Survey)

S.-G. Kang, Y.J. Choi, H.J. Kim, Y. Choi and J.K. Hong

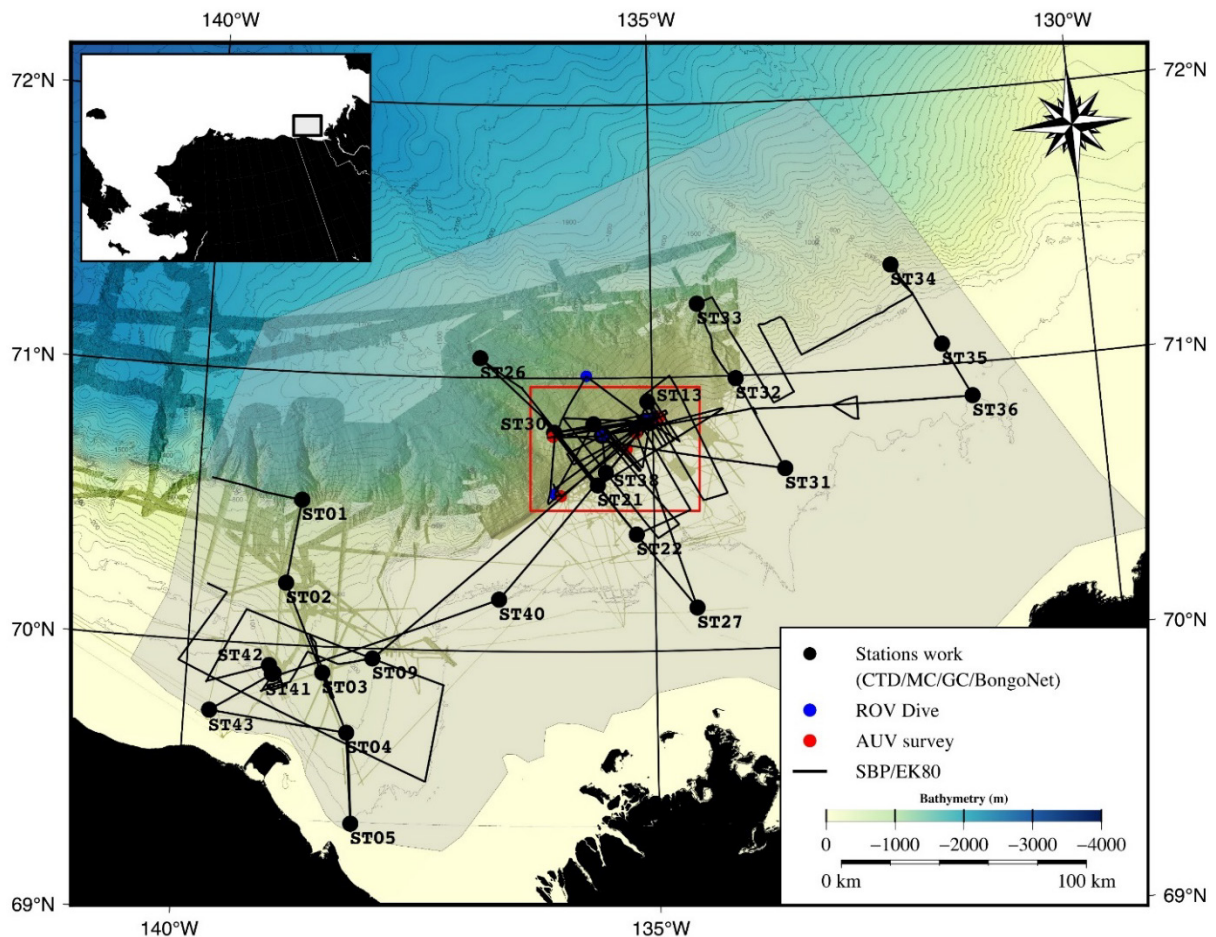


Figure 2.1. Track-chart of the SBP survey in the ARA13C research cruise.

2.1. Introduction

Continuous multibeam (MB) and sub-bottom profiler (SBP) data were acquired during the ARA13C cruise for a total line length of 3,330 and 3,395 km in the Canadian Beaufort Sea (Figure 2.1). The SBP and MB data were processed on board using CARIS HIPS&SIPS 9.0 version and Fledermaus, a specialized bathymetry processing software, during the survey and viewed immediately to assist in other research fieldwork and samplings. These datasets were used to choose autonomous underwater vehicle (AUV) survey sites, and remotely operated vehicle (ROV) dives. Acquired datasets identified elongated troughs and ridges, thawing permafrost, and Pingo-Like Features (PLFs) along the western shelf. Subsequent MB and SBP transects crossing the marked bank edge and into the Mackenzie Trough confirmed its continuity.

Multibeam bathymetry and sub-bottom profiler surveys were conducted using the Kongsberg EM122 and SBP27 that are installed on the IBRV Araon. The multibeam and SBP data were continuously recorded during the whole period of the ARA13C Expedition from August 26th to September 12th, 2022, in UTC. During the expedition, an effort was made to collect regional bathymetric and shallow subsurface data to fill spatial gaps in the existing data coverage on the Canadian Beaufort Sea continental shelf (Figure 2.2).

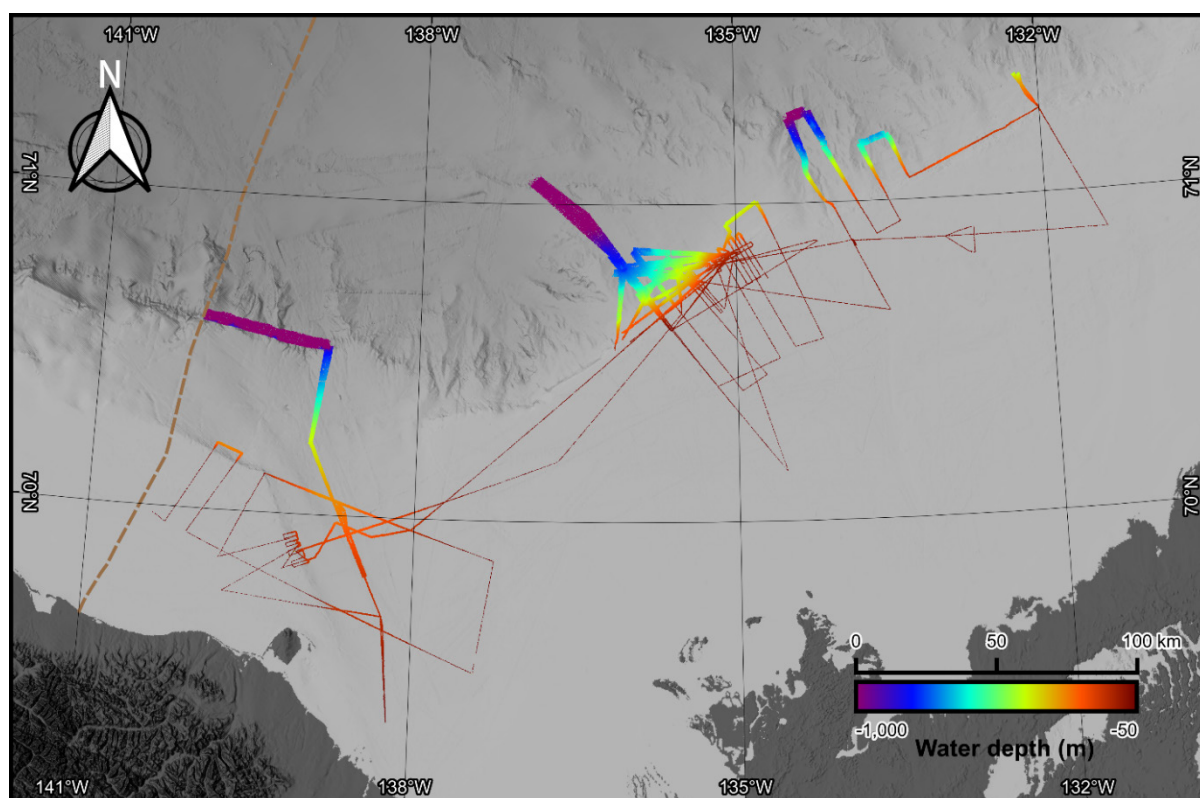


Figure 2.2. Track-chart of the Multibeam survey in the ARA13C research cruise.

2.2. System Descriptions

The multibeam echo sounder system (Kongsberg EM122) installed on the IBRV Araon consists of a hull-mounted transmit and receive transducer, transceiver unit, and operator station (Figure 2.3). EM122 has a wide beam angle (-65 to $+65$ degrees) and a capability of measuring into the deep ocean. The technical specifications and settings of EM122 and SBP27 are listed in Tables 2.1 and 2.2, respectively. The sub-bottom profiler (Kongsberg SBP27) is an optional extension to the EM122 multibeam echo sounder. The system diagram of SBP27 is shown in Figure 2.4. The receiving transducer hydrophone array used by the EM122 multibeam system is a broadband system; by adding a separate low-frequency transmitting transducer and electronic cabinets and operator stations, the EM122 can be extended to include the sub-bottom profiling capability, as provided by the SBP27. A system beam width is 12 degrees with 24 transducers, equivalent to a footprint of 20 m in 100 m water depth (or 20% of water depth). The ping rate is synchronized to that of the multibeam echo sounder transmitter if both are running simultaneously. SBP data show detailed sediment structures to shallow depths (10s of meters) below the seafloor with high resolution (10s of centimeters). The resolution of SBP is the highest among other reflection methods, such as sparker, boomer, and air-gun seismic instruments. Theoretically, SBP has a vertical resolution of up to 10 cm, depending on sound velocity in the subsurface sediments. In most cases, the vertical resolution is ~ 0.5 m or better.

About 3,000 line-km of multibeam and SBP data were acquired on the Canadian Beaufort Sea continental shelf during the ARA13C Araon Expedition of 2022. The multibeam and SBP data were recorded simultaneously during geophysical mapping survey (e.g., multi-channel seismic survey) and on transects related to transiting to geological and oceanographic sampling operations (e.g., sediment coring, heat flow measurement, dredge, and CTD casting). Data quality of the multibeam and SBP is largely affected by weather and sea ice conditions. In particular, sea ice breaking generated multibeam scattering and high amplitude noise in the SBP data. In order to calibrate multibeam bathymetry data, sound velocity profiles (SVPs) are updated frequently using the depth-velocity data obtained from CTD casting.

The data produced by SBP27 were logged in the Kongsberg proprietary Topas raw and SEG-Y formats. The SEG-Y format file of the SBP data has every even number of ping points of the Topas raw format. The SEG-Y format data allow post-processing by standard seismic processing software package Seismic Unix (SU). The SEG-Y files were directly processed after the end of recording for each individual survey line. The SEG-Y files of the same survey line were combined into bigger-size files in SU format to apply delay time shifting, sample rate change, signal enveloping, spherical divergence correction, and time-to-depth conversion. Navigation information of every ping point can be extracted from the SEG-Y file header. The processed SU format files were re-converted into SEG-Y files and will be imported to the seismic interpretation software OpendTect or SeisWare for seismic stratigraphic interpretation and mapping.

The EK80 is a wide band scientific echo sounder system that has a frequency range of 38 to 200 kHz to quantify and monitor underwater ecosystems. During the ARA13C expedition, the EK80 was used for detecting the gas bubbles (or flares) within the water columns.

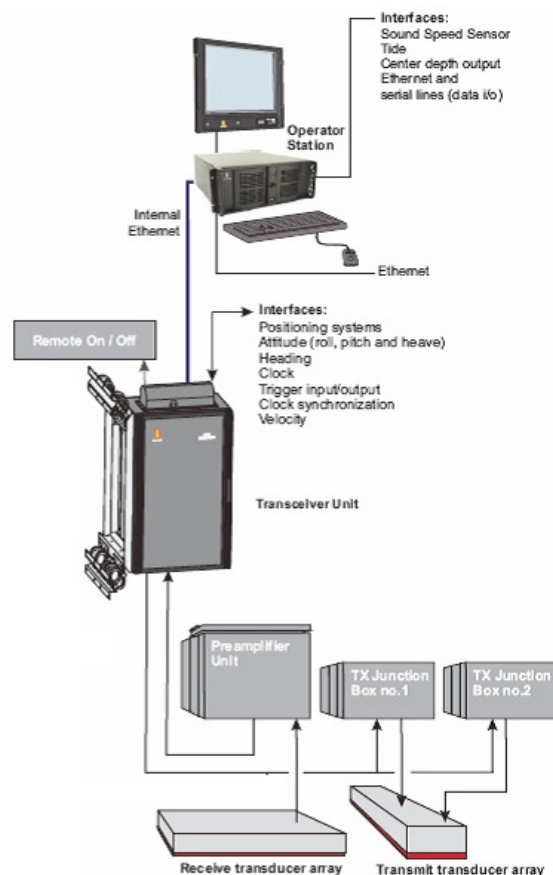


Figure 2.3. System diagram of EM122 multibeam system (Kongsberg, 2008).

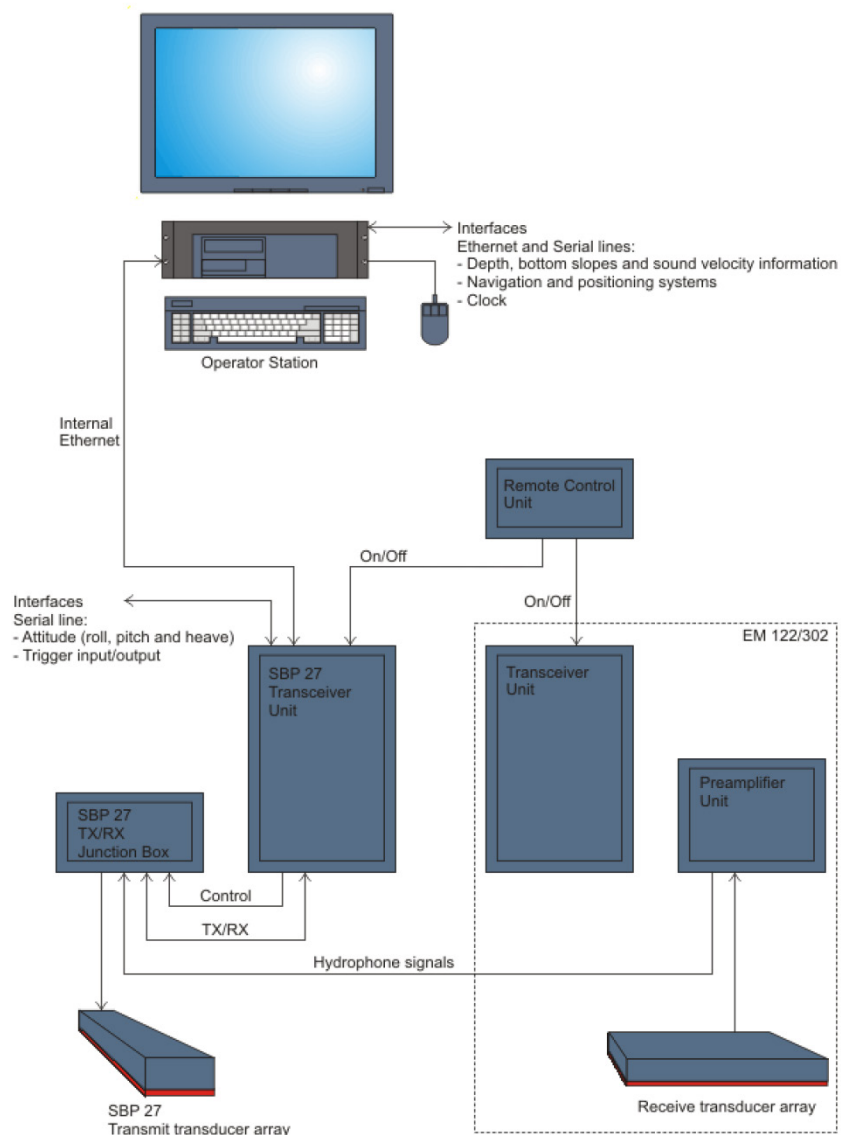


Figure 2.4. System diagram of SBP27 sub bottom profiler system (Kongsberg, 2019).

Table 2.1. Technical specifications of EM122

Operating frequency		12 kHz
Depth range		20 – 11000 m
Swath width		6 × Depth, to approx 30 km
Pulse forms		CW and FM chirp
No. of beams		288
Swath profiles per ping		1 or 2
Motion compensation	Yaw	± 10 degrees
	Pitch	± 10 degrees
	Roll	± 15 degrees
Sounding pattern		Equi-distant on bottom/equiangular
Depth resolution of soundings		1 cm
High resolution mode		High Density processing
Sidelobe suppression		-25 dB
Modular design, beamwidth		0.5 to 4 degrees

Table 2.2. Setting information of SBP27 during the ARA13C cruise

Used Settings	Value	Unit
Runtime Parameter		
Transmit mode	Normal	
Synchronization	Fixed ping rate	ms
Acquisition delay	Manual & automatic mode	ms
Acquisition window	400	ms
Pulse form	Linear chirp up	
Sweep low frequency	2500	Hz
Sweep high frequency	7000 – 9000	Hz
Pulse shape	80	%
Pulse length	30	ms
Source power	0	dB
Beam widths Tx	Normal	
Beam widths Rx	Normal	
Number of Rx beams	1	
Beam spacing	3	1 deg
Calculate delay from depth	X	
Delay hysteresis	30	%
Bottom screen position	50	%
Automatic slope corrections	On	
Gain	15 & 20 & 30	dB
Bottom tracker		
Window start	Manual & automatic mode	ms
Window length	20	ms
Threshold	80	%
Time Variable Gain		
TVG control	Tracking	

2.3. Results/Highlights

A geophysical survey consisting of sub-bottom profiling, echo-sounder, and multibeam was conducted to find abnormal geological structures of the subsurface related to climate change in the Arctic continental shelf area. Echo-sounder profiles confirmed the presence of gas flares for the 420 m and 780 m mud volcanos (MV) in the Beaufort continental shelf area. SBP data were also collected for detailed subsurface geological structures for both mud volcanos. A giant pingo-like feature was observed on the multibeam and SBP in shallow water depths under 40 meters on the western region of the central Beaufort shelf. We collected the SBP data on the shelf edge to compare with the surface morphologies (on the seafloor) related to subsea permafrost distribution in the Beaufort shelf region.

2.3.1. Mud volcano located in 420 m depth, Beaufort Shelf area

To image the subsurface geological structures of the 420 m MV, we collected SBP data, as shown in Figure 2.5. Detailed shape of 420 m MV and sediment around the MV structure. Acoustic blanking (masking) was also observed under the MV. According to the image of the echo-sounder presented in Figure 2.6, we can confirm the gas flare on the MV. In 2014, Araon collected multi-channel seismic data which showed BSR occur near the MV 420 m mud volcano. In 2022, gas hydrate samples were successfully recovered near the seafloor of the MV structure by the multi-core; the field photos are presented in Figure 2.7.

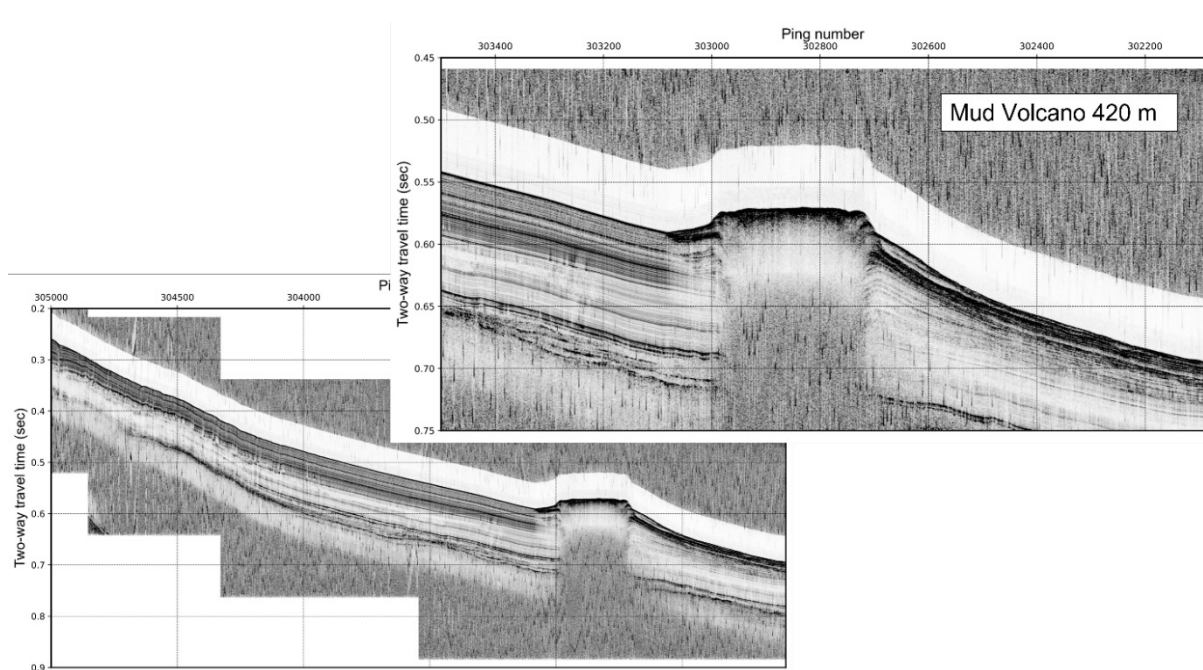


Figure 2.5. Sub-bottom profile image for the mud-volcano at 420 meters depth.

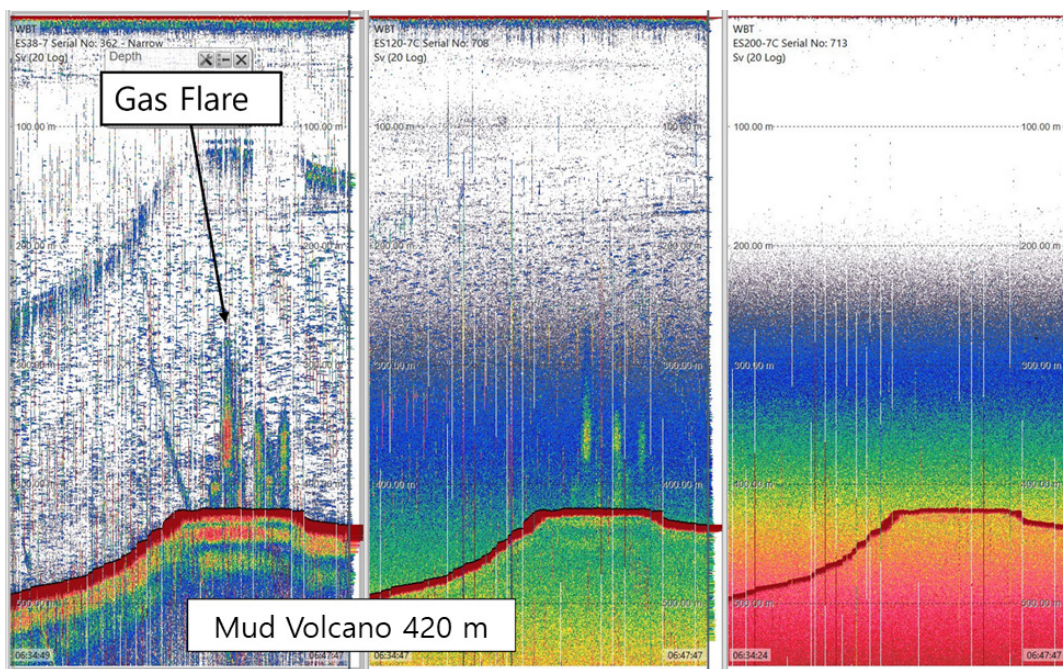


Figure 2.6. Gas flare on the mud volcano at 420 meters in echo-sounder data.



Figure 2.7. Gas hydrate samples, mud volcano 420 m. Photos courtesy of Korea Polar Research Institute.

2.3.2. Mud volcano located in 780 m depth, Beaufort shelf area

We also collected SBP data for imaging the subsurface geological structures of the 780 m MV, as shown in Figure 2.8. We can confirm the detailed shape of 780 MV and sediment around the MV structure. According to the image of the echo-sounder presented in Figure 2.9, we also confirmed gas flare on this structure. In 2014, we collected multi-channel seismic data in this area, and BSR structures were observed near the MV structure. It means that this MV is also a gas hydrate-related geological structure just as MV 420m. We also successfully recovered the gas hydrate samples located on the surface of the MV structure by the gravity-core; the field photos are presented in Figure 2.10.

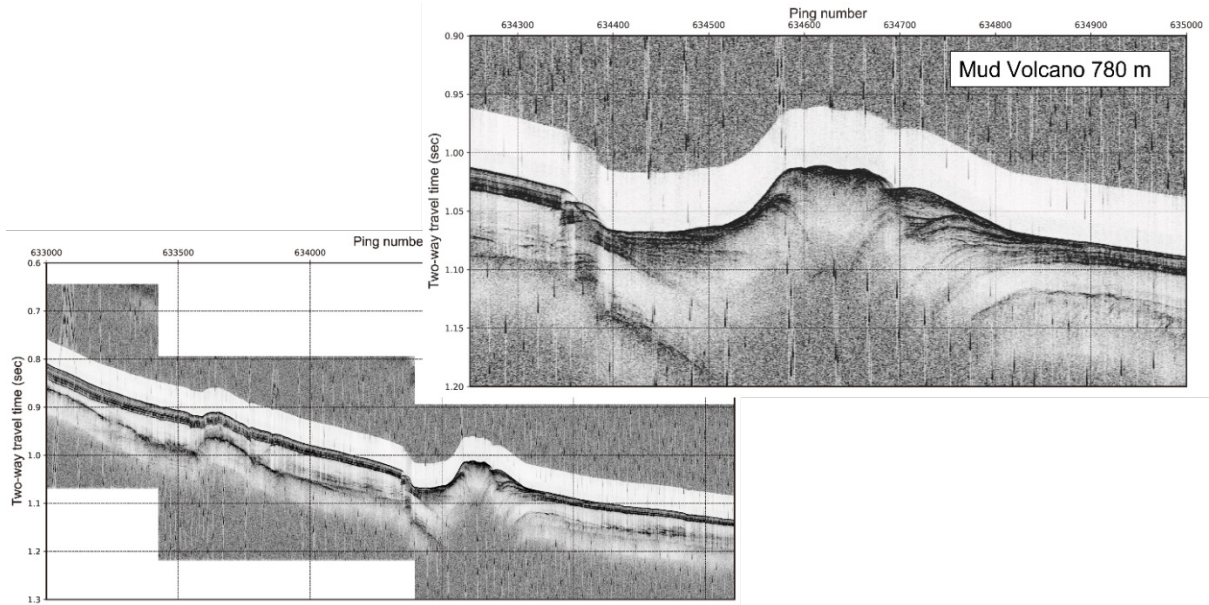


Figure 2.8. Sub-bottom profile image for the mud-volcano at 780 meters depth.

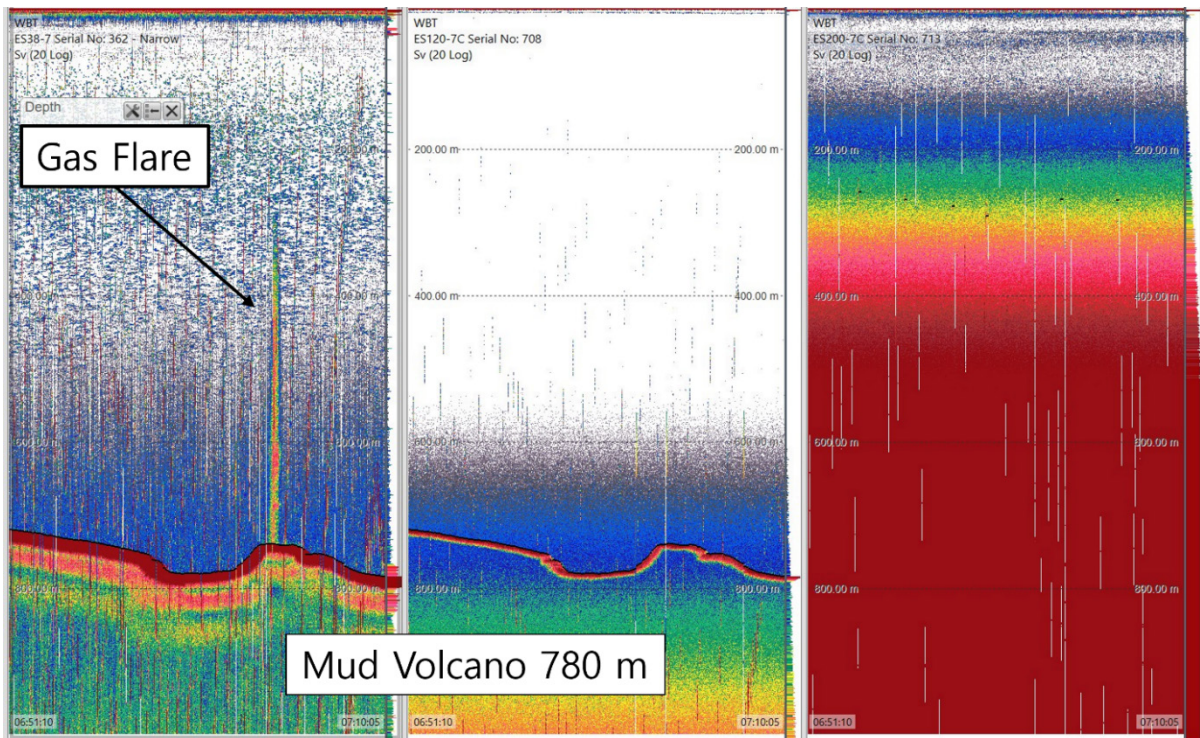


Figure 2.9. Gas flare extending nearly 400 m above the seabed on the mud volcano at 780 meters in echosounder data.



Figure 2.10. Gas hydrate samples, mud volcano 780 m. Orange circle indicates the gas hydrate sample in the gravity coring barrel. Photo courtesy of Korea Polar Research Institute.

2.3.3. Pingo-like Feature, Beaufort Shelf area

On the western continental shelf, a giant pingo-like feature was identified on multibeam and SBP data, as shown in Figure 2.11. The height is 30 meters, and the width is 500 m, respectively.

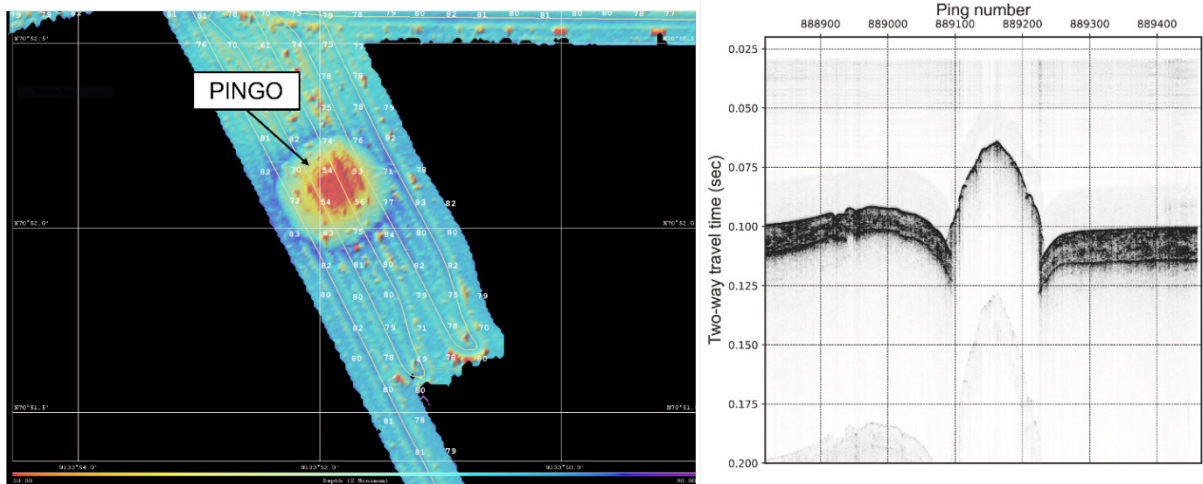


Figure 2.11. Pingo-like Feature, located in Beaufort shelf.

2.3.4. Sub-bottom profiles for the shelf edge related to thawing subsea permafrost, Beaufort Shelf

The primary aim of the SBP survey conducted on the continental shelf region was to explore the morphologic characteristics potentially related to the presence and/or thawing of subsea permafrost. Kang et al. (2021) investigated the occurrence of subsea permafrost on the Beaufort Shelf area by a seismic P-wave velocity model constructed by the full waveform inversion algorithm sleeve gun multichannel seismic lines surveyed in 2014 (Jin and Dallimore, 2016). The P-wave velocity models for indicated discontinuous permafrost may still extend to the shelf edge on some lines (e.g., ARA05C-L01') but not on other lines (e.g., ARA05C-L05). To investigate further, we intend to compare surface morphologies using the higher resolution SBP data in more detail. Figures 2.12 and 2.13 are the corresponding SBP images along the ARA05C-L01 and -L05 tracks, respectively.

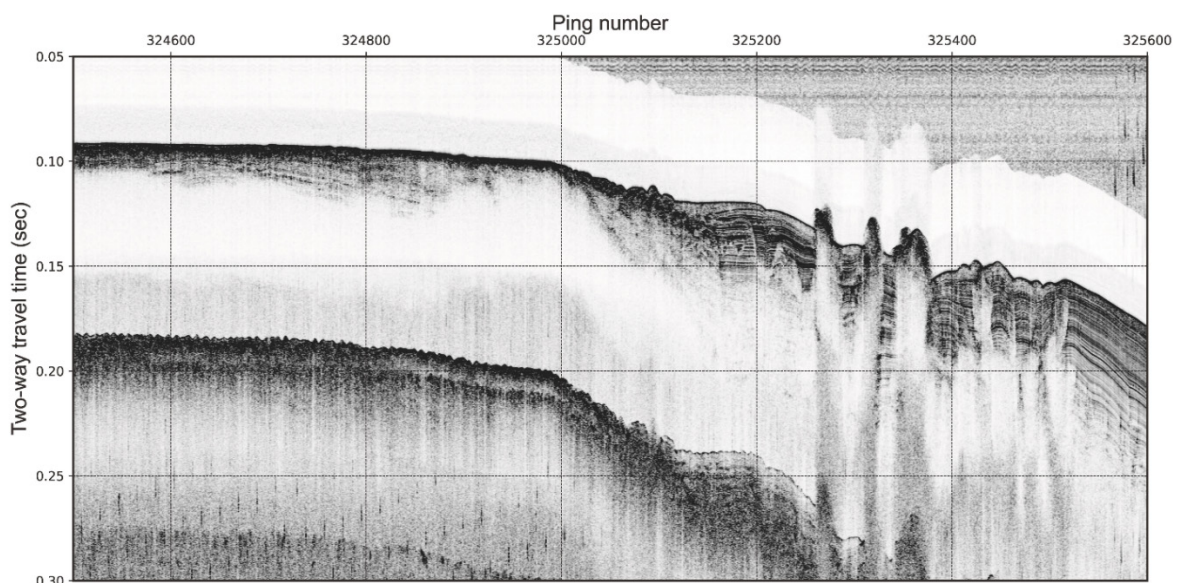


Figure 2.12. Sub-bottom profile image for the shelf edge (corresponding to the ARA05C-L01, MCS Track).

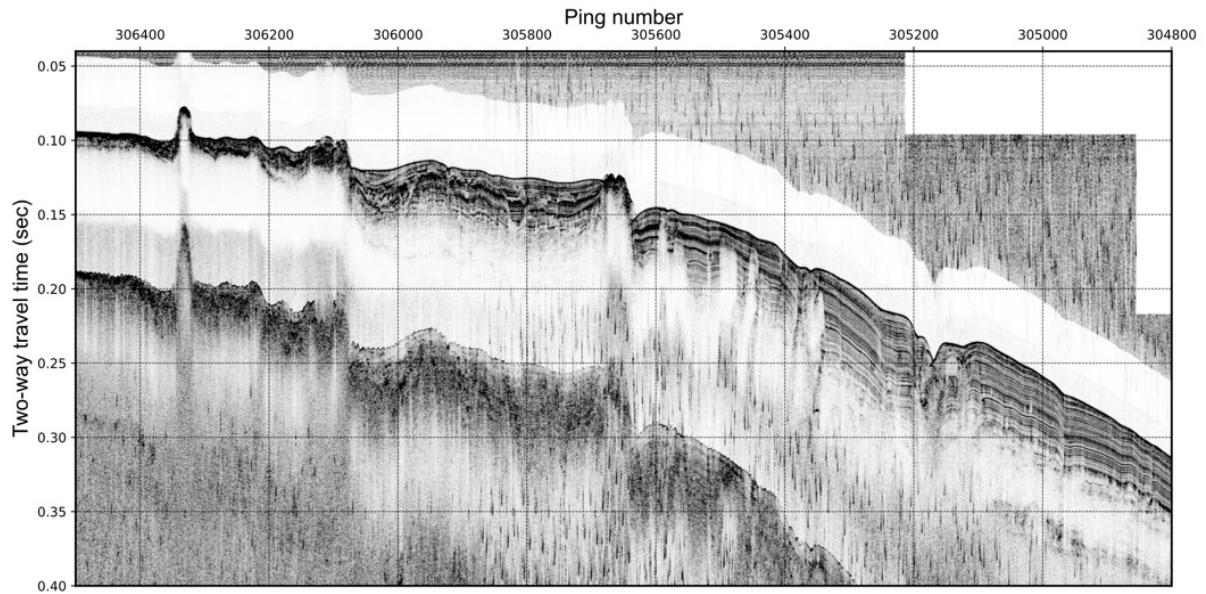


Figure 2.13. Sub-bottom profile image for the shelf edge (corresponding to the ARA05C-L05, MCS Track).

References

- Jin, Y.K. & Dallimore, S. R., 2016, ARA05C marine research expedition, Canada–Korea–USA Beaufort Sea Geoscience Research Program: summary of 2014 activities. Geological Survey of Canada, Open File 7999.
- Kang, S.-G., Jin, Y. K., Jang, U., Duchesne, M. J., Shin, C., Kim, S., Riedel, J., Dallimore, S. R., Paull, C. K., Choi, Y. and Hong, J. K. 2021. Imaging the P-Wave Velocity Structure of Arctic Subsea Permafrost Using Laplace-Domain Full-Waveform Inversion. *J. Geophys. Res.* 124.
- Kongsberg, 2008. Installation Manual: EM 122 Multibeam echo sounder. Horten, Norway, 12 pp.
- Kongsberg, 2019. Kongsberg SBP 27 Sub-bottom profiler Product Description. Horten, Norway, 9 pp.

ARA13C Cruise report

Chapter 3. Seafloor Mapping Using Autonomous Underwater Vehicles

D.W. Caress, J.B. Paduan, C.K. Paull, R. Prickett, J. Caress, T.P. Poling, E. Martin and E. Lundsten



Figure 3.1. Recovery of MBARI Mapping AUV 2 following a mission to survey a mud volcano at 740 m depth during ARA13C. Photo courtesy of Monterey Bay Aquarium Research Institute.

3.1. Introduction

Due to the importance of the seafloor as an interface and as the locus of many globally important geological, geochemical, and biological processes, seafloor mapping through acoustic remote sensing of topography, bottom character, and subsurface structure is one of the fundamental activities in Oceanography. In order to achieve high resolution seafloor mapping, the sonars must be operated close to the seafloor. The most efficient means currently available are autonomous robots called autonomous underwater vehicles (AUVs) equipped with both high frequency mapping sonars and high precision navigation systems. On this expedition we operated two Dorado class AUVs designed, built, and operated by MBARI (Figure 3.1) to obtain 1-m-scale bathymetry and backscatter seafloor maps along with chirp subbottom profiles.

During ARA13C, new and previously collected MBARI Mapping AUV data has provided basic observations of seafloor morphology, character, and structure along with providing context for ROV-based inspection and sampling and ship-based coring. A particular focus has been to utilize repeated AUV 1-m-scale bathymetric surveys to detect change on the seafloor, and to relate these changes (or the lack of change) to processes such as permafrost dissolution, mass wasting, and mud volcano activity.

3.2. MBARI Mapping AUV Description, Operations, and Data Processing

3.2.1. Vehicle Description

The MBARI mapping AUVs [Caress et al, 2008] are Dorado class autonomous underwater vehicles equipped with 400 kHz multibeam sonar, 110 and 410 kHz sidescan sonars, and a 1-6 kHz subbottom profiler (Figure 3.2). These robots provide 1-meter-scale bathymetry and backscatter and subsurface imaging penetrating as much as 80 m in stratified sediment. The Dorado AUVs are maintained and operated by the Autonomous Systems Group within MBARI's Division of Marine Operations. Since 2006, more than 700 successful survey missions have been conducted using the Mapping AUVs, including the six achieved during this expedition. MBARI Mapping AUVs have been operated on several non-MBARI vessels, include R/V Thomas Thompson, R/V Atlantis, CCGS Sir Wilfrid Laurier, Ocean Researcher 1, Ocean Researcher 5, R/V Falkor, and IBRV Araon.

The core vehicles are rated to 6,000 m depth, and all current sensors are rated to at least 4000 m depth. Using precise navigation and attitude data from a laser-ring-gyro-based inertial navigation system (INS) integrated with a Doppler velocity log (DVL) sonar, MBARI Mapping AUVs can image the deep-ocean seafloor and shallow subsurface structure with much greater resolution than is possible with sonars operated from surface vessels. Typical survey operations use a vehicle speed of 1.5 m per second (3 knots) and an altitude of 50 m to achieve about 1 m horizontal and 10 cm vertical resolution. Mission durations are up to 18 hours, allowing survey tracklines as long as 90 km that cover areas up to 13 km². Battery recharge and data download between missions requires about 5 hours. The Mapping AUVs are 0.53 m (21 inches) in diameter and 5.5 m (18 feet) long. Launch and recovery operations can be challenging, as the AUVs weigh about 680 kg (1500 lbs) dry and about twice that as they are initially lifted during recovery due to the water entrained within the hulls.

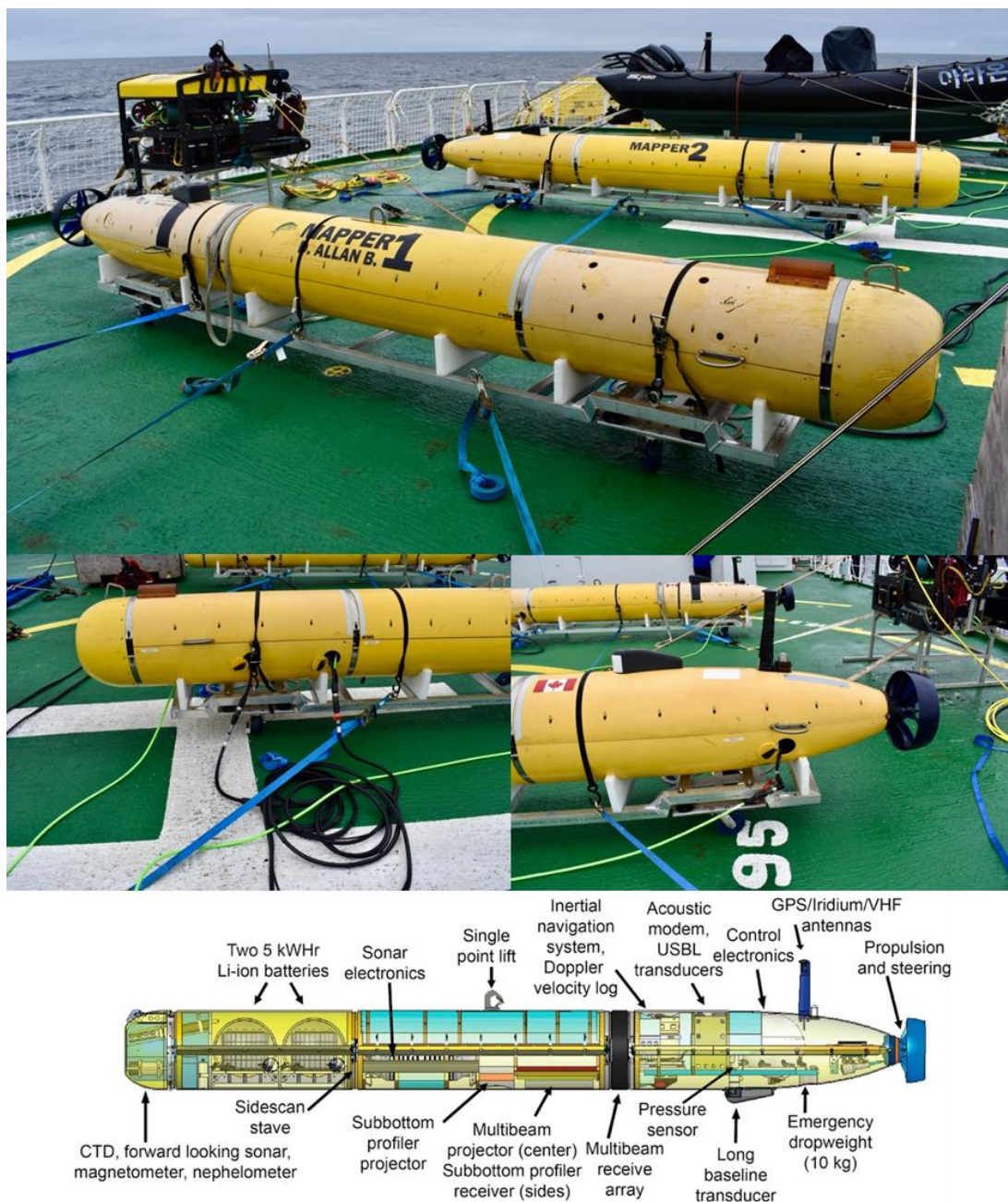


Figure 3.2. (Top) Both MBARI Mapping AUVs secured on the Araon helideck during ARA13C. The AUVs were charged, maintained, and launched from the helideck. (Middle-left) View of an AUV nose showing the network and charging cables attached to the robot. (Middle-right) AUV tail showing the single articulating propeller and the propeller duct, which is the sole control surface on this torpedo shaped robot. Also visible is the attached high speed data download cable. (Bottom) CAD drawing showing system level layout of the AUV internals. Photos courtesy of Monterey Bay Aquarium Research Institute.

Although the vehicles fielded during ARA13C have been in operation for over a decade, many key systems have been upgraded or replaced as the available mapping and navigation technology has improved. The mapping sonars and other sensors integrated with the Mapping AUV on this expedition include:

- Multibeam sonar: Teledyne Reson T50-S 400 kHz
- Sidescan sonar: Edgetech 2205 110 kHz chirp sidescan
- Subbottom sonar: Edgetech 2205 1-6 kHz subbottom profiler

- CTD: SeaBird Electronics SBE49 Fastcat CTD
- Doppler Velocity Log (DVL): 300 kHz Teledyne-RDI Workhorse Navigator DVL
- Inertial Navigation System (INS): Kearfott SeaDevil w/300 kHz DVL
- Pressure Sensor: Paroscientific 8CB4000 4000-m rated Intelligent Depth Sensor
- Ultra Short Baseline tracking beacon: Sonardyne AvTrak 6G
- Acoustic Modem: Teledyne-Benthos 3G LF Acoustic Modem, directional transducer
- Batteries: Two MBARI-design 5 kWhr battery spheres using lithium ion battery packs from Inspired Energy

A key requirement for AUV operations is a capability to track the subsea location of the AUV during missions. *IBRV Araon* has a Sonardyne Ranger I Ultra Short Baseline (USBL) sonar mounted on a retractable pole extending through the hull; this pole can be fully retracted into a pressurizable space so that the USBL head can be serviced or replaced without drydocking or diver operations.

3.2.2. MBARI AUV Team

The MBARI Mapping AUVs were operated by Randy Prickett, Jordan Caress, and Tanner Poling of the Autonomous Systems Group (MBARI Department of Marine Operations) assisted by Eric Martin of the Electrical Engineering Group (MBARI Research and Development). The AUV mission definition and data processing were done by David Caress and Jenny Paduan of the Seafloor Mapping Group; Caress and Paduan also participated in the vehicle check out procedures for every mission. The MBARI Co-Principal Investigator for expedition ARA13C, Charlie Paull, defined the mission targets and priorities.



Figure 3.3. The MBARI AUV team during ARA13C. From the left: Principal Engineer David Caress, Senior Research Specialist Jennifer Paduan, AUV Operations Engineer Tanner Poling, Electrical Engineer Eric Martin, AUV Operations Engineer Randy Prickett, AUV Operations Engineer Jordan Caress. Photo courtesy of Monterey Bay Aquarium Research Institute.

3.2.3. AUV Launch and Recovery on the IBRV Araon

The approach used for launch and recovery of Dorado AUVs varies between ships according to the available deck space, crane configuration, and for large ships with high freeboard, the crew comfort level for small boat operations. Following a detailed review of previous MBARI AUV launch and recovery scenarios, for ARA13C the MBARI AUV team and the Araon crew jointly chose to locate the AUVs on the heliport between operations, to launch and recover the AUV over the starboard side using the large starboard crane located on the fantail, and to use the ship's small boat to capture and side-tow the AUV to the Araon where it could be hooked into the crane. There were two significant differences between the AUV operations during ARA08C in 2017 and this expedition. First, deployments were made in a single pick from the heliport to the water instead of having an intermediate stage on the starboard main deck where tag lines were switched from clipped to slip lines. Second, the small boat recoveries included side towing the AUVs on the boat's starboard side, followed by snugging the boat's port side against the ship's starboard quarter so that the boat was between the ship and the AUV, the small boat was secured by passing its bow and stern lines to the ship, and then clipping in a tag line to the AUV's nose and hooking the towing/lifting line into the crane. For this expedition the AUVs were configured with lateral tag line bales on both sides fore and aft, another tag line bale on top of the nose section, and with a closed main lifting bale (on MBARI ships the lifting bale is open with a spring-loaded gate) on top of the AUV midbody. The specifics of the launch and recovery procedures are illustrated in Figure 3.4 and Figure 3.5, respectively.

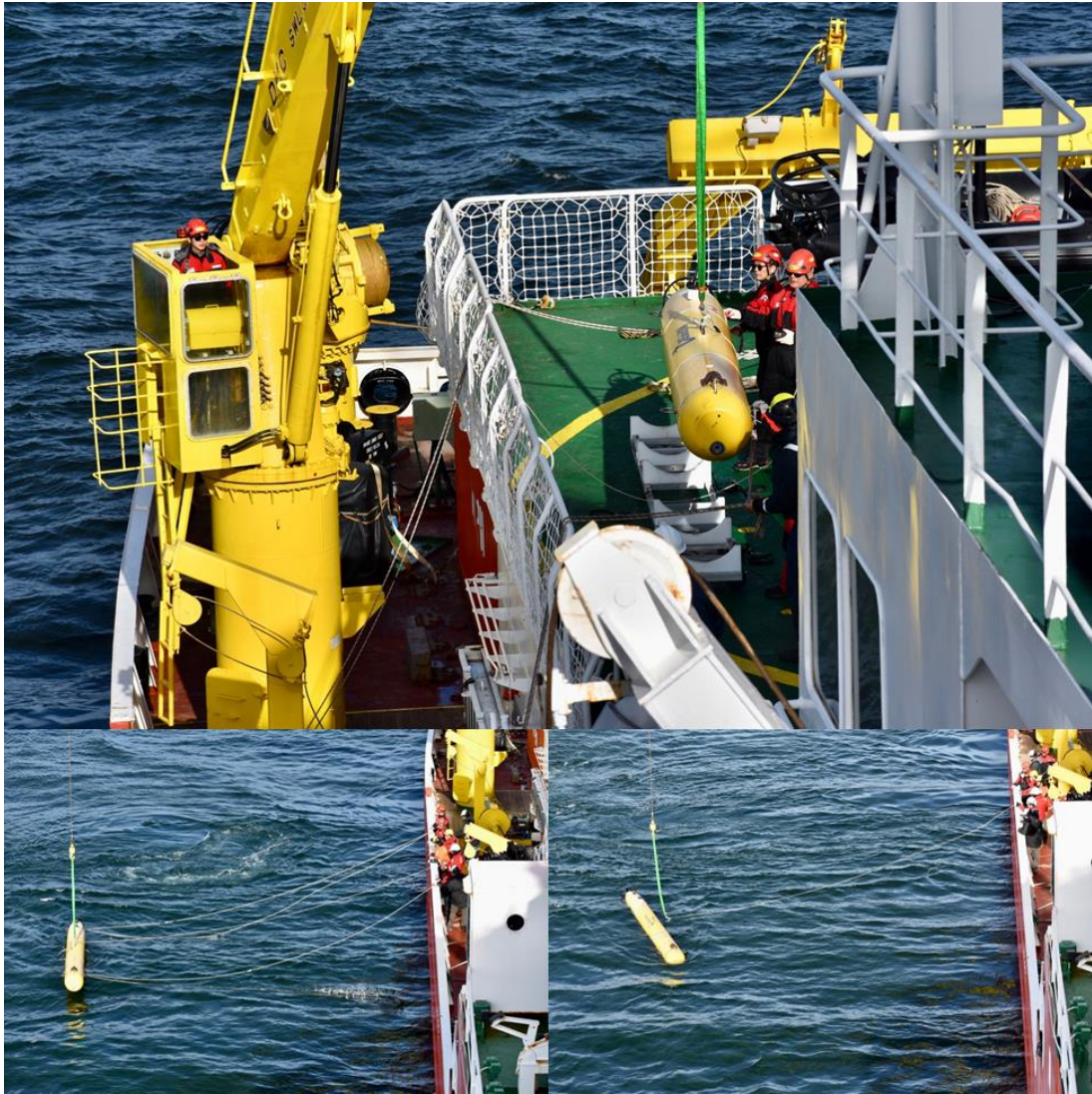


Figure 3.4. AUV launch sequence. (Top) The AUV was lifted off its cradle on the helideck with two slip tag lines attached and handled from the starboard main deck. The main lifting line had an open hook with a separate tag line. (Bottom left) After the crane slewed to take the AUV outboard, the AUV was lowered almost to the water, and then the tag lines were slipped. (Bottom right) When the AUV was lowered into the water, the lifting line went slack and the hook was pulled out using its tag line, leaving the AUV floating free about 20 m from the ship. Photos courtesy of Monterey Bay Aquarium Research Institute.



Figure 3.5. AUV recovery sequence. (Top left) After positioning the ship so that the AUV was floating less than 200 m off the starboard side, the small boat was launched with three Araon crew and two MBARI AUV engineers. **(Top right)** The AUV was secured to the starboard side of the small boat with a line from the top nose bale to the boat's forward cleat, and the towing/recovery line, utilizing a stainless-steel hook, from the main lifting bale, to the boat's aft starboard cleat. It was important to secure the lines to the boat as the AUV's drag was too great for the lines to be held directly. The AUV was then side towed back to the ship. **(Middle left)** The boat approached the starboard side of the ship and was secured using the boat's fore and aft mooring lines, with the AUV still secured outboard from the ship. Once the boat was stably secure to the ship, the crane head was lowered over the AUV with a double tag line clipped on. The tag line was unclipped from the crane head and clipped onto the AUV top nose bale, and then the towing/lifting strap was attached from the AUV's lifting bale to the crane head hook. **(Middle right)** After the boat's mooring lines were released, the boat backed away from the ship and the AUV was lifted out of the water. **(Bottom)** A second tag line was attached to the AUV's tail before it was brought aboard directly to the helideck. Photos courtesy of Monterey Bay Aquarium Research Institute.

3.2.4. Mapping AUV Data Processing

The Mapping AUV multibeam, sidescan, and subbottom profiler data have been processed using the open source software package MB-System [*Caress and Chayes, 1996; Caress et al., 2022*]. The workflow largely proceeded as follows:

- Data download from AUV (approximately 40 minutes), typically 150 GB raw data.
 - Multibeam data are logged in the Reson s7k format, with file suffixes *.s7k.
 - Sidescan and subbottom profiler data are logged together in files in the Edgetech jstar format, with file suffixes *.jsf.

- AUV INS navigation and attitude data, CTD data, and other AUV data streams are logged in MBARI Dorado MVC log files, with file suffixes *.log. These files are in a format particular to MBARI, but all data can be extracted using the MB-System program mbauvloglist.
- Multibeam data
 - Preprocessing using program mbpreprocess
 - Apply platform offsets and time latencies
 - Recalculate bathymetry using improved sound speed values
 - Apply autofiltering of soundings based on sonar data metrics
 - Interactive editing of soundings using program mbeditviz (Figure 3.6)
 - Navigation adjustment using program mbnadjust (Figure 3.7), which identifies overlapping and crossing swathes, picks relative navigation offsets required for bathymetric features to match in overlapping data, and solves for an optimal navigation model.
 - Calculate empirical multibeam backscatter correction function using program mbackangle. Mbackangle uses the multibeam bathymetry to determine bottom grazing angles for each backscatter value, allowing the calculation of an average backscatter versus grazing angle model (Figure 3.8).
 - Apply all edits and corrections, merge the adjusted navigation, and produce a set of processed swath files using the program mbprocess. The processed multibeam data are in the same data format as the original logged data, which is the Reson s7k format. Since s7k files are supported by MB-System as format 88, the processed files all have the suffix *.mb89 according to MB-System file naming conventions.
- Edgetech Sidescan and Subbottom data
 - Sidescan data are in the form of match filtered envelope time series, not yet associated with position on the seafloor
 - Subbottom data are in the form of the raw match filtered, complex correlate time series.
 - Preprocessing using program mbpreprocess
 - Merge optimal navigation model from multibeam processing
 - Apply platform offsets
 - Output still in Edgetech jstar format, though with MB-System file suffix *.mb132
- Sidescan data
 - Extract sidescan using program mbsslayout
 - Lays out raw time series sidescan onto a 1-m bathymetry model derived from the multibeam data.
 - Organizes sidescan data into sequential lines organized according to the waypoints of the AUV mission.
 - Output is sidescan in the form of pixels on the seafloor, stored in MB-System generic format 71, with file suffixes *.mb71
 - Calculate empirical sidescan backscatter correction function using program mbackangle. Mbackangle uses a bathymetric model from the multibeam data to determine bottom grazing angles for each sidescan sample, allowing the calculation of an average backscatter versus grazing angle model.
 - Apply the backscatter correction using program mbprocess. The processed sidescan files have the suffix *.mb71.
 - Apply a spatial smoothing filter to the sidescan using program mbfilter.

- Subbottom profiler data
 - Extract subbottom using program mbextractsegy
 - Calculate envelope times series
 - Output SEGY format files (SIOSEIS variant with deep water delay field in trace header).
 - Generate subbottom section plots (Figure 3.9)
- Visualization
 - Mbgrdviz (Figure 3.10) is a general purpose 2D/3D visualization tool for viewing gridded/mosaiced seafloor mapping data overlain with navigation, site, and waypoint data.

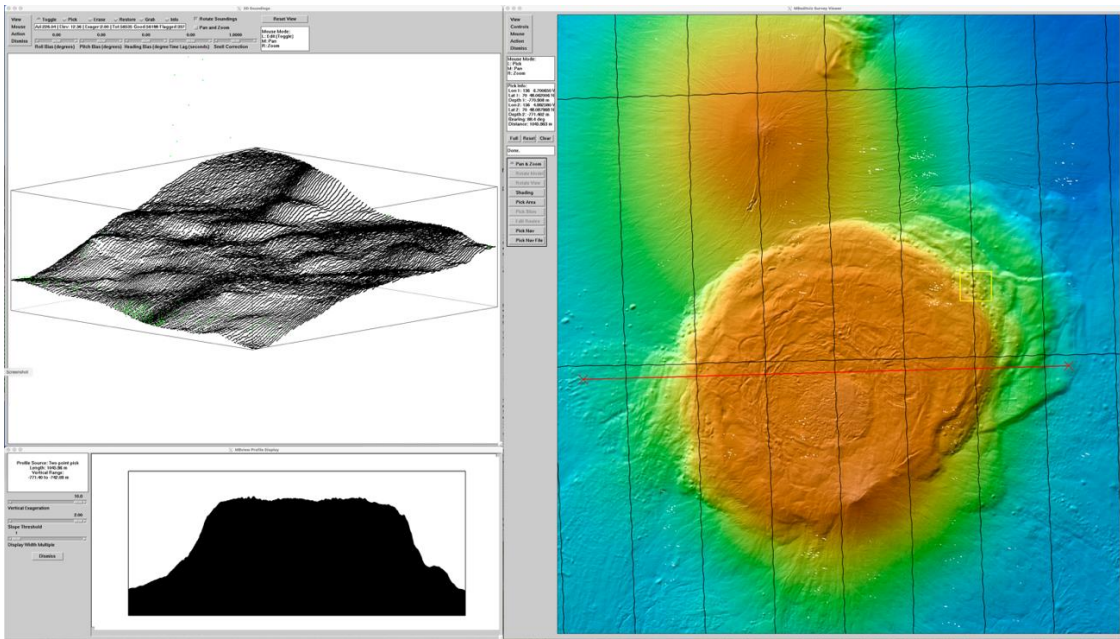


Figure 3.6. MB-System program mbeditviz used to edit the Mapping AUV multibeam bathymetry from mission 20220907m1.

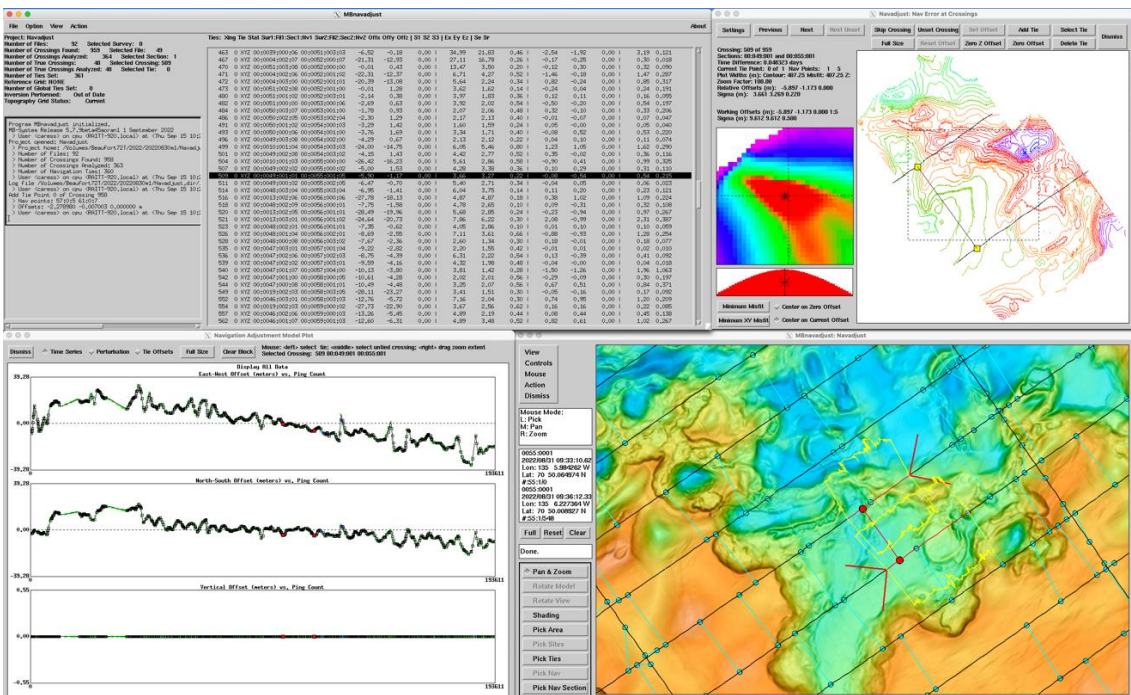


Figure 3.7. MB-System program mbnavadjust is used to create an adjusted navigation model that matches features in overlapping swath bathymetry data. The program finds sections of data that overlap, determines the relative navigation offsets required to make features match through both automated and interactive analysis, and then solves for an optimal navigation model that aligns features while minimizing perturbations to the original navigation.

Correction of 400 kHz Multibeam Backscatter

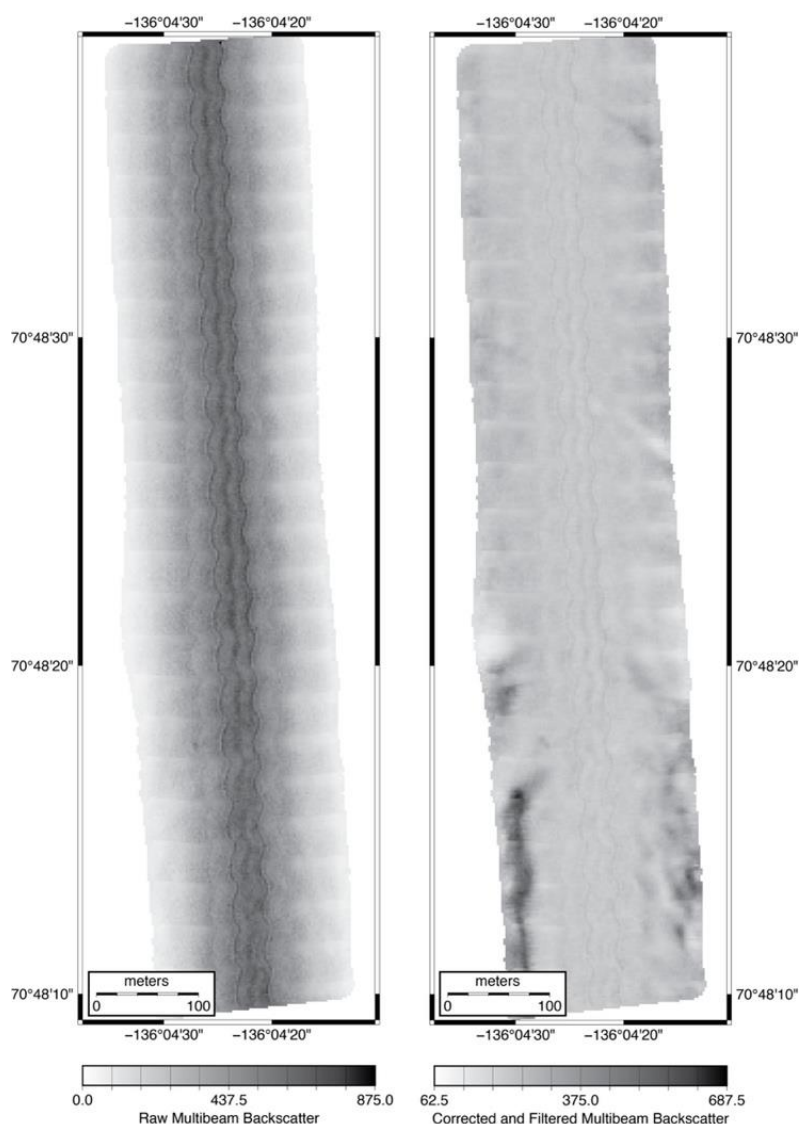


Figure 3.8. Example of beam pattern correction of the 400 kHz multibeam backscatter collected by the Mapping AUVs. MB-System program `mbackangle` was used to estimate the correction function applied by `mbprocess`.

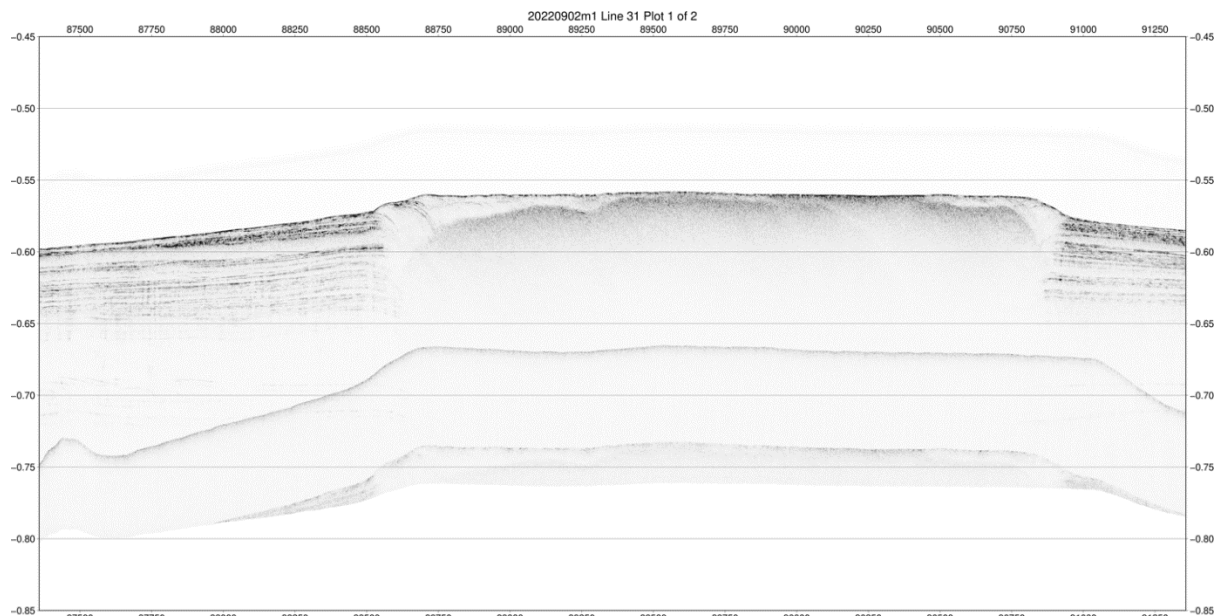


Figure 3.9. The MB-System program `mbextractseg` produces SEGY format subbottom profile files for each survey line and a series of section plots for each line. This is an example subbottom profiler section plot from mission 20220902m1 imaging part of a crossing of the 420 m mud volcano. Vertical scale is in seconds below sea level, two-way travel time.

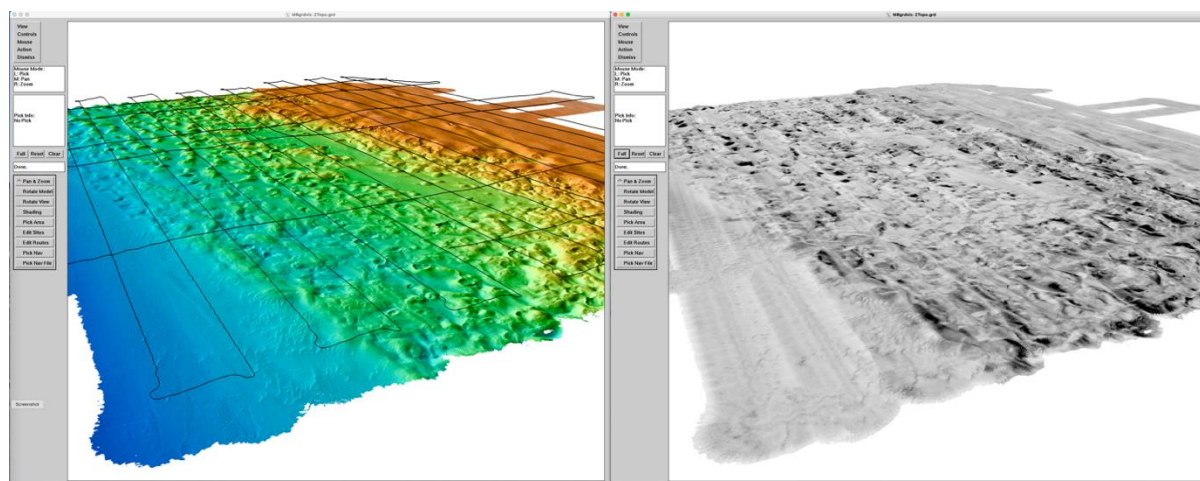


Figure 3.10. MB-System program `mbgrdviz` used to visualize Mapping AUV multibeam data from mission 20220906m2, showing both bathymetry in color shaded by illumination and bathymetry draped with multibeam backscatter (high amplitudes dark).

3.3. High Resolution Seafloor Mapping Results

3.3.1. Introduction

Six successful AUV missions were conducted during the expedition: two at mud volcanoes and four on the shelf edge east of the MacKenzie Trough (Table 3.1). Five were with the AUV “Mapper2”, and one was with the AUV “Mapper1”, abbreviated respectively as MAUV2 and MAUV1. Summaries of each of the missions will follow in Section 3.3.2. Five were deployed in shallow enough water (<130 m depth) to enable DVL-lock while the vehicle was at the surface and in GPS-satellite contact, and drove along the seafloor at 50-m altitude until it reached the feature to be mapped. The 740 m Mud Volcano, mapped on the final mission, 20220907m1, was too deep a target for DVL lock at the launch, so the AUV was spun down

from the surface in free-inertial while being aided by USBL fixes to reduce the drift in navigation.

Table 3.1. Successful AUV mission deployments on ARA13C. MAUV1 = the vehicle named “Mapper1”; MAUV2 = “Mapper2”. ARA05C Seismic Line 1 was collected in 2014

Mission	Route	Location	Vehicle	Launch Latitude	Launch Longitude
20220830m1	Rugous_Self_Edge_m1_v5	Shelf Edge Intact	MAUV2	-135.03167	70.833454
20220901m1	ShelfEdgeSlumpEast2022_m1_v3	Shelf Edge Failed	MAUV2	-136.021274	70.569027
20220902m1	MudVolcano420m_M1V10	420 m Mud Volcano	MAUV2	-135.29124	70.740215
20220906m1	Araon_05C_Line_1_m1_v7	ARA05 Seismic Line 1	MAUV2	-134.915262	70.855585
20220906m2	SW_SWL_2019_covreage_in_2022_m1_v2	Shelf Edge Intact	MAUV1	-135.181517	70.796342
20220907m1	MudVolcano740mRepeatM1V5	740 m Mud Volcano	MAUV2	-136.11251	70.784784

Ballast and trim were challenging due to the low salinity of the surface waters, particularly for MAUV1, for which two survey attempts failed despite acceptable “dunk-tests” at the surface (Table 3.2) because the AUV flight was unstable at depth. A third survey attempt for MAUV1 failed due to the Ranger1 USBL aiding feed not being utilized by the inertial navigation system (INS). Several missions were cancelled due to adverse weather conditions.

Table 3.2. Unsuccessful AUV missions on ARA13C

Mission	Route	Location	Vehicle	Reason
20220830m2	Araon_05C_Line_1_m1_v5	ARA05 Seismic Line 1	MAUV1	Aborted after the patch test. Vehicle ballasted nose-heavy?; subbottom very noisy.
20220901m2	ShelfEdgeSlump2022West_m1_v3	Shelf Edge Failed	MAUV1	Aborted, same ballasting problem
20220902m2	Ridge_south_rugous_shelf-edge_n1_v4	Shelf Edge Intact	MAUV1	Cancelled due to fog
20220903m1	MudVolcano740mRepeatM1V4	740 m Mud Volcano	MAUV1	Descent rate too slow; INS not acting on USBL aiding communications
20220911m1	Mackenzie_2022_m1_v5	West MacKenzie Trough	MAUV1	Cancelled due to current and wind
20220911m2	Mackenzie_2022_m2_v2	West MacKenzie Trough	MAUV2	Cancelled due to current and wind

Five of the six of the successful missions (Table 3.1) were conducted over places that had been surveyed previously with an MBARI AUV, which mapped in the vicinity in 2013, 2016, and 2017. The sixth, mission 22020906m1, was conducted to coincide with a seismic line collected by the IBRV Araon in 2014. Each mission was navigated together with the prior year’s surveys and respective ship-bathymetry (see Section 3.2.4, mbnadjust).

Three of the missions, 20220830m1, 20220906m1, and 20220906m2, were contiguous along the eastern shelf margin (Figure 3.11). Their navigation was adjusted together to become a region referred to here as “Shelf Edge Intact”. These missions were conducted over bathymetry data collected by the R/V Amundsen in 2010 as part of the Arctic Net Project and the CCGS Sir Wilfred Laurier in 2019, and as the ships were GPS-navigated, those data sets were used as regional base maps in the navigation adjustment process (see Section 3.2.4, mbnadjust). Comparisons of 2022 AUV missions with the prior data sets to determine differences that developed in the intervening years will be presented in Section 3.3.3.

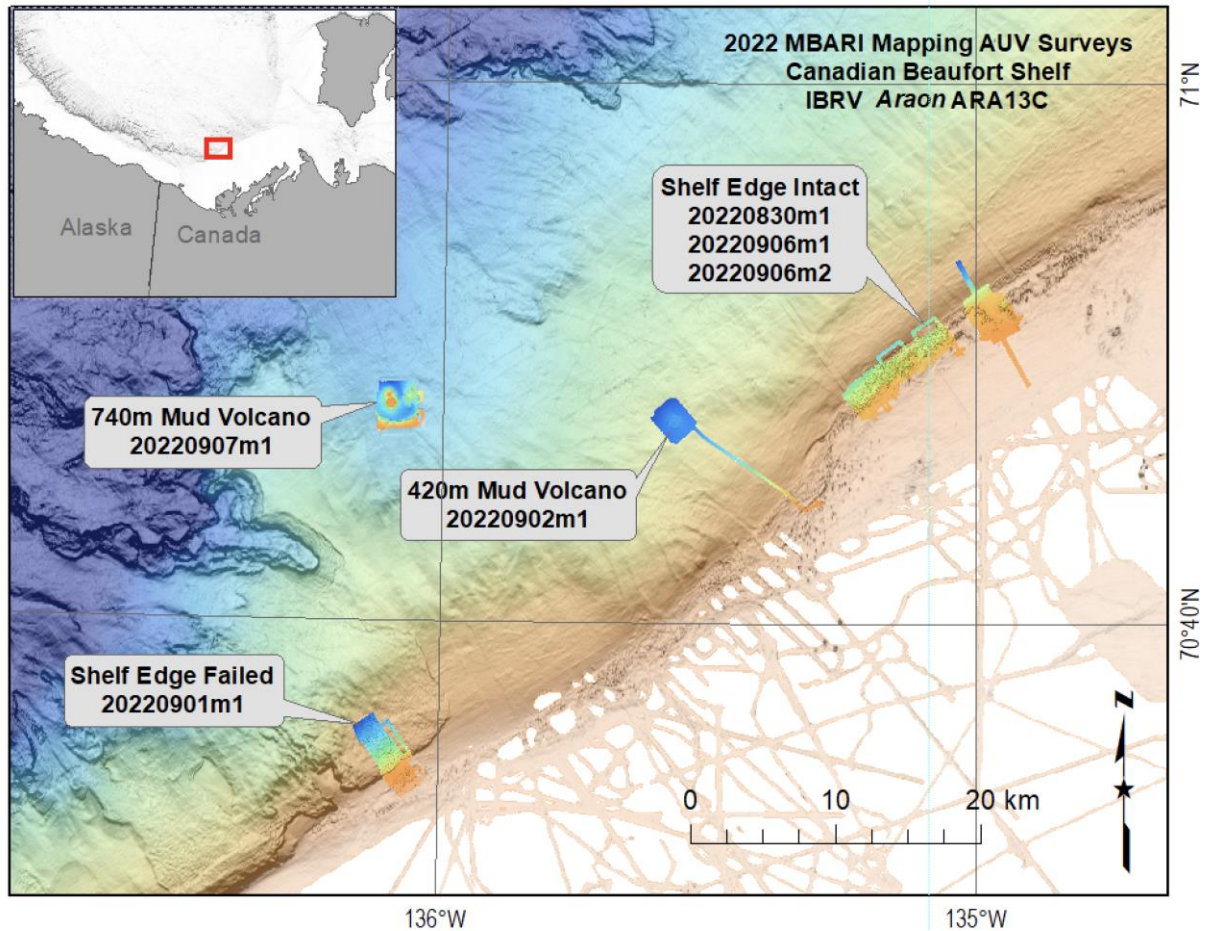


Figure 3.11. Map of 2022 ARA13C MBARI Mapping AUV coverage, indicating the region and mission names that will be referred to in the following sections. 2022 MBARI Mapping AUV bathymetry, with color ramps of the maximum to minimum depths of those grids, overlies regional bathymetry (faded) collected by the Arctic Net Project, the CCGS Sir Wilfred Laurier, and IBRV Araon.

3.3.2. Results From Each AUV Mission

A table of statistics from each mission and a series of maps are presented for each AUV mission. Bathymetry maps were gridded at 1-m resolution, with one shaded by slope and with navigation tracks overlaid, and another with 10-m contours overlaid. Maps of snippet multibeam backscatter (aka pseudo-sidescan), corrected and filtered (see Section 3.2.4, mbackangle), are shown with high-amplitudes dark. For each survey an example of the chirp subbottom profiler data has been chosen, and the location of the subbottom profile is indicated on the bathymetry map. On the profile plots, the signal returning from the seafloor is indicated, as are reflections from the sea surface and sea floor. Surface reflections are seen in the AUV-collected chirp profiles when the vehicle is operated in less than about 500 m water depth. During shallow water surveys, when the AUV is closer to the sea surface than the seafloor, the sea surface reflection would come before (above) the seafloor in the subbottom profile.

3.3.2.1. Mission 20220830m1 – Shelf Edge Intact (1)

Mission 20220830m1 was on the shelf edge. It is underlain by bathymetry from the CCGS Sir Wilfred Laurier. MiniROV dives M182, M183, M185, and M186, and coring stations ST23, ST24, ST28, and ST29 were sited in this area. The multibeam data collected during mission

20220830m1 with MAUV2 are summarized in Table 3.3. The sidescan and subbottom data correspond to the same time and spatial domain, but are organized in 38 sequential line files delineated by the waypoints in the AUV mission. Included below are representative maps of the multibeam bathymetry and multibeam backscatter imagery from mission 20220830m1 (Figures 3.12 to 3.14). Also included is an example of a subbottom profile section plot (Figure 3.15).

Table 3.3. Multibeam data statistics from Mapping AUV survey 20220830m1, which was conducted with MAUV2 in the region Shelf Edge Intact

MBARI MAUV2 Mission 20220830m1 Multibeam Data Totals:	
Number of Records:	194031
Bathymetry Data (1024 beams):	
Number of Beams:	176203279
Number of Good Beams:	147095278 83.48%
Number of Zero Beams:	0 0.00%
Number of Flagged Beams:	29108001 16.52%
Amplitude Data (1024 beams):	
Number of Beams:	176203279
Number of Good Beams:	147095278 83.48%
Number of Zero Beams:	0 0.00%
Number of Flagged Beams:	29108001 16.52%
Sidescan Data (2048 pixels):	
Number of Pixels:	397375488
Number of Good Pixels:	74727166 18.81%
Number of Zero Pixels:	0 0.00%
Number of Flagged Pixels:	322648322 81.19%
Navigation Totals:	
Total Time:	17.8723 hours
Total Track Length:	77.3762 km
Average Speed:	4.3294 km/hr (2.3402 knots)
Start of Data:	
Time:	08 30 2022 22:40:50.046386 JD242 (2022-08-30T22:40:50.046386)
Lon:	-135.031923392 Lat: 70.833493933 Depth: 61.3667 meters
Speed:	4.5423 km/hr (2.4553 knots) Heading: 131.2822 degrees
Sonar Depth:	61.3667 m Sonar Altitude: 0.0000 m
End of Data:	
Time:	08 31 2022 16:33:10.342173 JD243 (2022-08-31T16:33:10.342173)
Lon:	-135.065584660 Lat: 70.850541685 Depth: 159.4162 meters
Speed:	5.0336 km/hr (2.7209 knots) Heading: 61.4338 degrees
Sonar Depth:	107.2553 m Sonar Altitude: 51.9507 m
Limits:	
Minimum Longitude:	-135.186747021 Maximum Longitude: -135.017340809
Minimum Latitude:	70.812281438 Maximum Latitude: 70.857433401
Minimum Sonar Depth:	31.9808 Maximum Sonar Depth: 166.0701
Minimum Altitude:	33.0178 Maximum Altitude: 80.8941
Minimum Depth:	103.1164 Maximum Depth: 231.7732
Minimum Amplitude:	12.1257 Maximum Amplitude: 20503.7559
Minimum Sidescan:	0.0000 Maximum Sidescan: 6143.2822

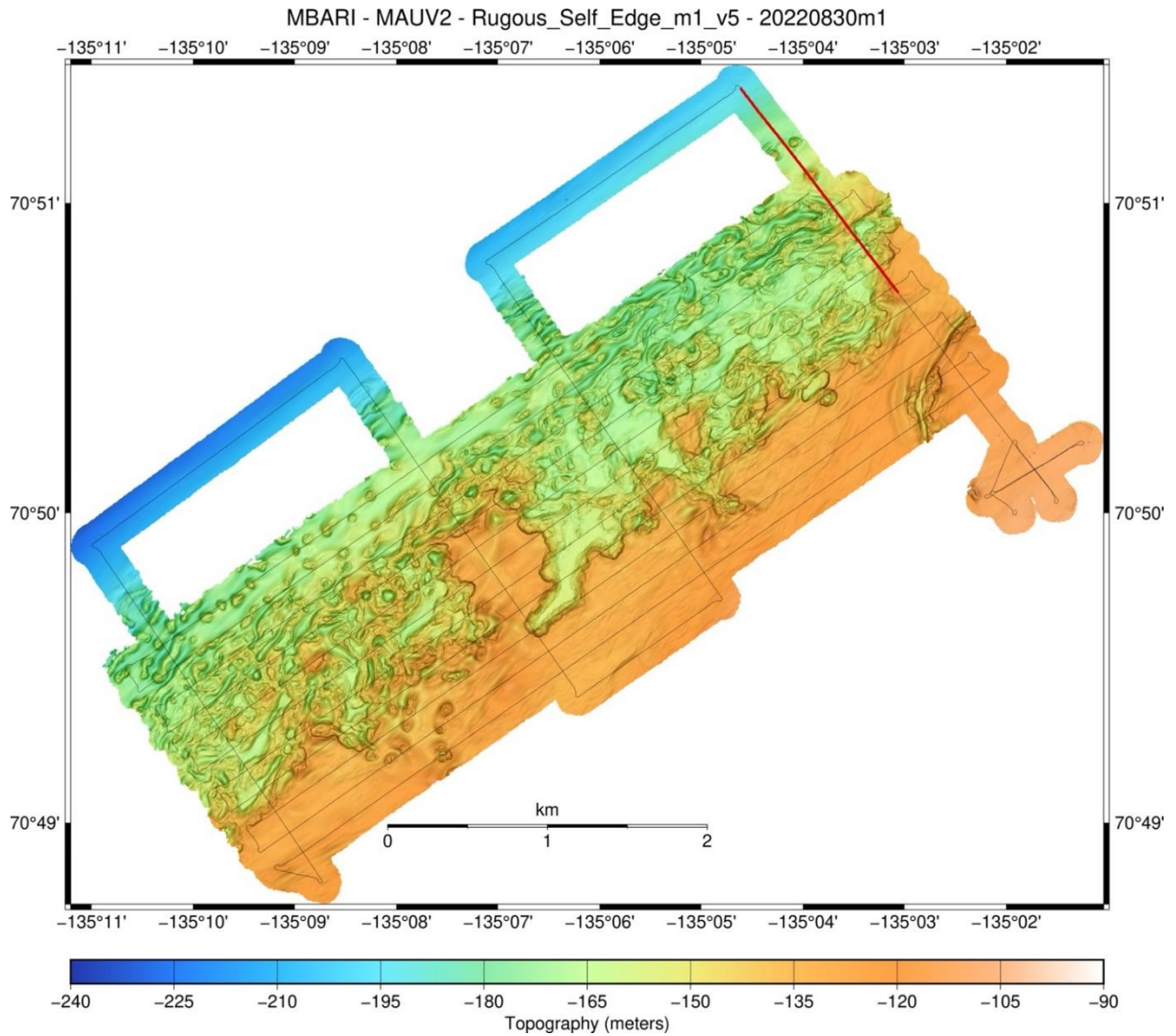


Figure 3.12. Mapping AUV 1-m resolution multibeam bathymetry from mission 20220830m1 displayed with slope magnitude shading overlain by the AUV tracklines. The red line indicates the location of the subbottom profile section shown in Figure 3.15.

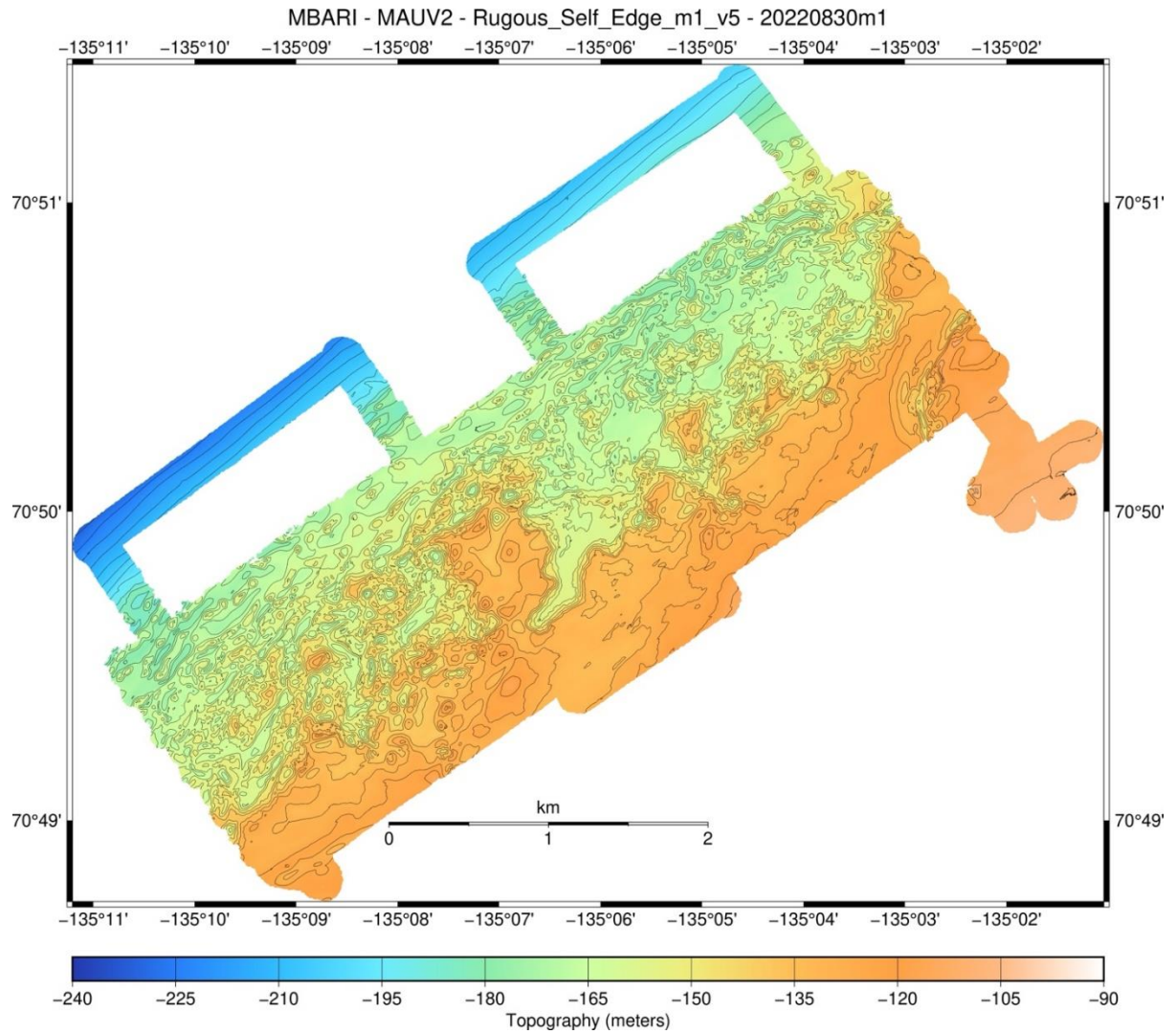


Figure 3.13. Mapping AUV 1-m resolution multibeam bathymetry from mission 20220830m1 displayed with 10-m contours.

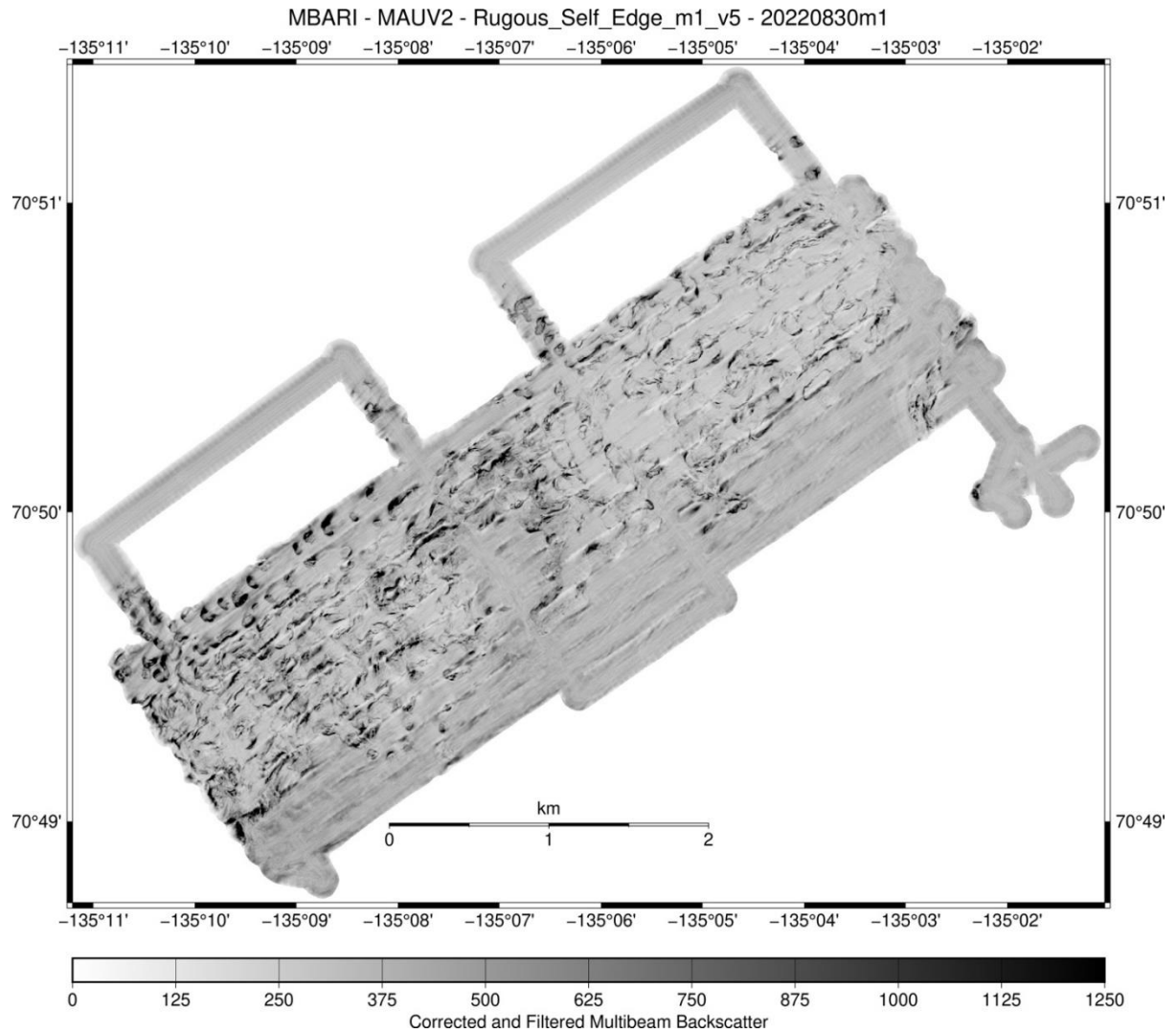


Figure 3.14. Mapping AUV 1-m resolution multibeam backscatter from mission 20220830m1. The backscatter has been corrected using an empirical amplitude-vs-grazing angle model and had a Gaussian smoothing filter applied. High amplitudes are shown dark.

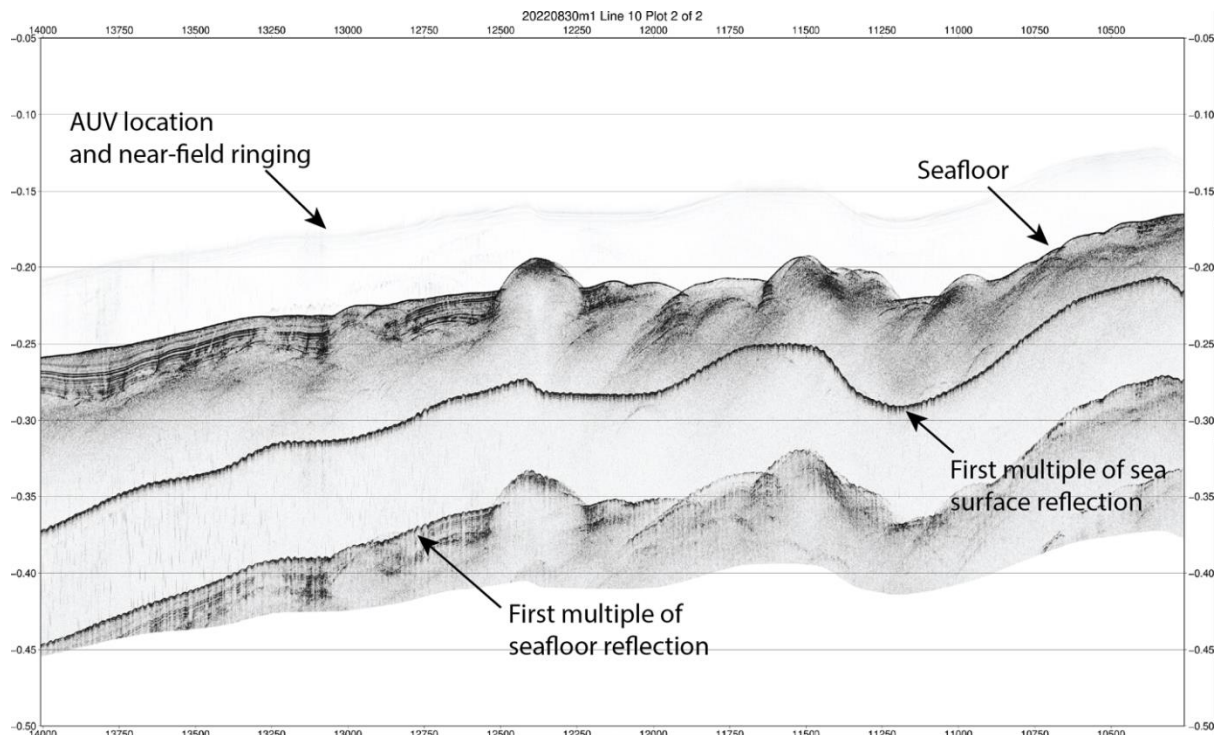


Figure 3.15. Mapping AUV chirp 1-6 kHz subbottom profiler data from mission 20220830m1. The section is shown “hung” from the AUV’s location in the water column, generally about 50-m above the seafloor. The location of this profile is shown by a red line on Figure 3.12. Arrows indicate locations of sub-seafloor and multiple reflections. Surface reflections are seen in the AUV-collected chirp profiles when the vehicle is operated in less than about 500 m water depth. During shallow water surveys, when the AUV is closer to the sea surface than the seafloor, the sea surface reflection would come before (above) the seafloor in the subbottom profile (not shown in this figure). Vertical scale is in seconds below sea level, two-way travel time.

3.3.2.2. Mission 20220901m1 – Shelf Edge Failed

Mission 20220901m1 was on a failed part of the shelf edge and the western-most of the surveys collected on ARA13C. MiniROV dive M188 and coring stations 11 and 12 were sited in this area. The multibeam data collected during mission 20220901m1 with MAUV2 are summarized in Table 3.4. The sidescan and subbottom data correspond to the same time and spatial domain, but are organized in 34 sequential line files delineated by the waypoints in the AUV mission. Included below are representative maps of the multibeam bathymetry and multibeam backscatter imagery from mission 20220901m1 (Figures 3.16 to 3.18). Also included is an example of a subbottom profile section plot (Figure 3.19).

Table 3.4. Multibeam data statistics from Mapping AUV survey 20220901m1, which was conducted with MAUV2 at the area Shelf Edge Failed

MBARI MAUV2 Mission 20220901m1 Multibeam Data Totals:	
Number of Records:	194482
Bathymetry Data (1024 beams):	
Number of Beams:	171910145
Number of Good Beams:	147518931 85.81%
Number of Zero Beams:	0 0.00%
Number of Flagged Beams:	24391214 14.19%
Amplitude Data (1024 beams):	
Number of Beams:	171910145
Number of Good Beams:	147518931 85.81%
Number of Zero Beams:	0 0.00%
Number of Flagged Beams:	24391214 14.19%
Sidescan Data (2048 pixels):	
Number of Pixels:	398299136
Number of Good Pixels:	76424075 19.19%
Number of Zero Pixels:	0 0.00%
Number of Flagged Pixels:	321875061 80.81%
Navigation Totals:	
Total Time:	17.9177 hours
Total Track Length:	86.2973 km
Average Speed:	4.8163 km/hr (2.6034 knots)
Start of Data:	
Time:	09 01 2022 22:21:55.805950 JD244 (2022-09-01T22:21:55.805950)
Lon:	-136.021321067 Lat: 70.569023218 Depth: 50.7461 meters
Speed:	5.4846 km/hr (2.9646 knots) Heading: 108.5901 degrees
Sonar Depth:	50.7461 m Sonar Altitude: 0.0000 m
End of Data:	
Time:	09 02 2022 16:16:59.448368 JD245 (2022-09-02T16:16:59.448368)
Lon:	-136.089368586 Lat: 70.594484054 Depth: 237.0944 meters
Speed:	4.7271 km/hr (2.5552 knots) Heading: 326.4460 degrees
Sonar Depth:	181.5491 m Sonar Altitude: 55.5462 m
Limits:	
Minimum Longitude:	-136.158239189 Maximum Longitude: -136.017264528
Minimum Latitude:	70.556911797 Maximum Latitude: 70.609197637
Minimum Sonar Depth:	40.4095 Maximum Sonar Depth: 260.7365
Minimum Altitude:	42.9619 Maximum Altitude: 90.7310
Minimum Depth:	63.8927 Maximum Depth: 318.7745
Minimum Amplitude:	23.2019 Maximum Amplitude: 37446.2266
Minimum Sidescan:	0.0000 Maximum Sidescan: 10695.1934

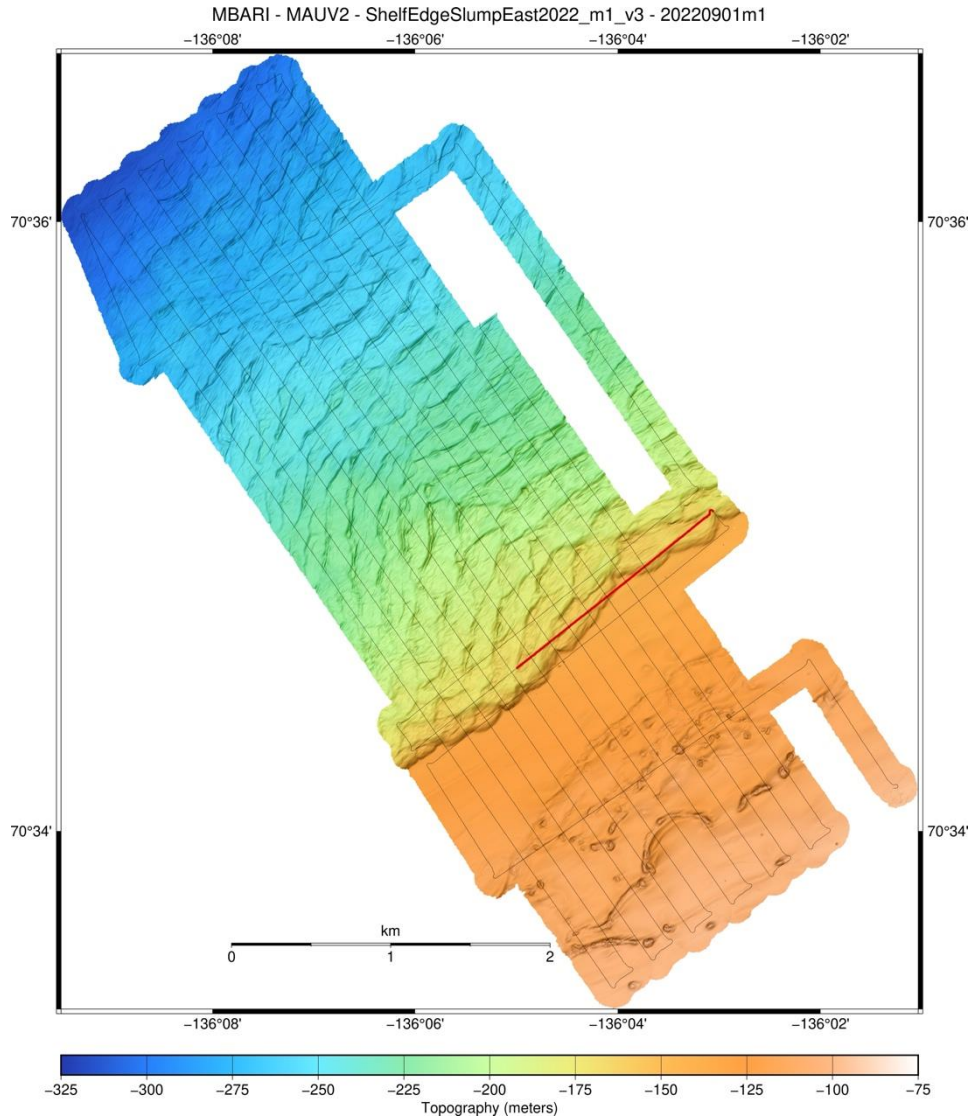


Figure 3.16. Mapping AUV 1-m resolution multibeam bathymetry from mission 20220901m1 displayed with slope magnitude shading overlain by the AUV tracklines. The red line indicates the location of the subbottom profile section shown in Figure 3.19.

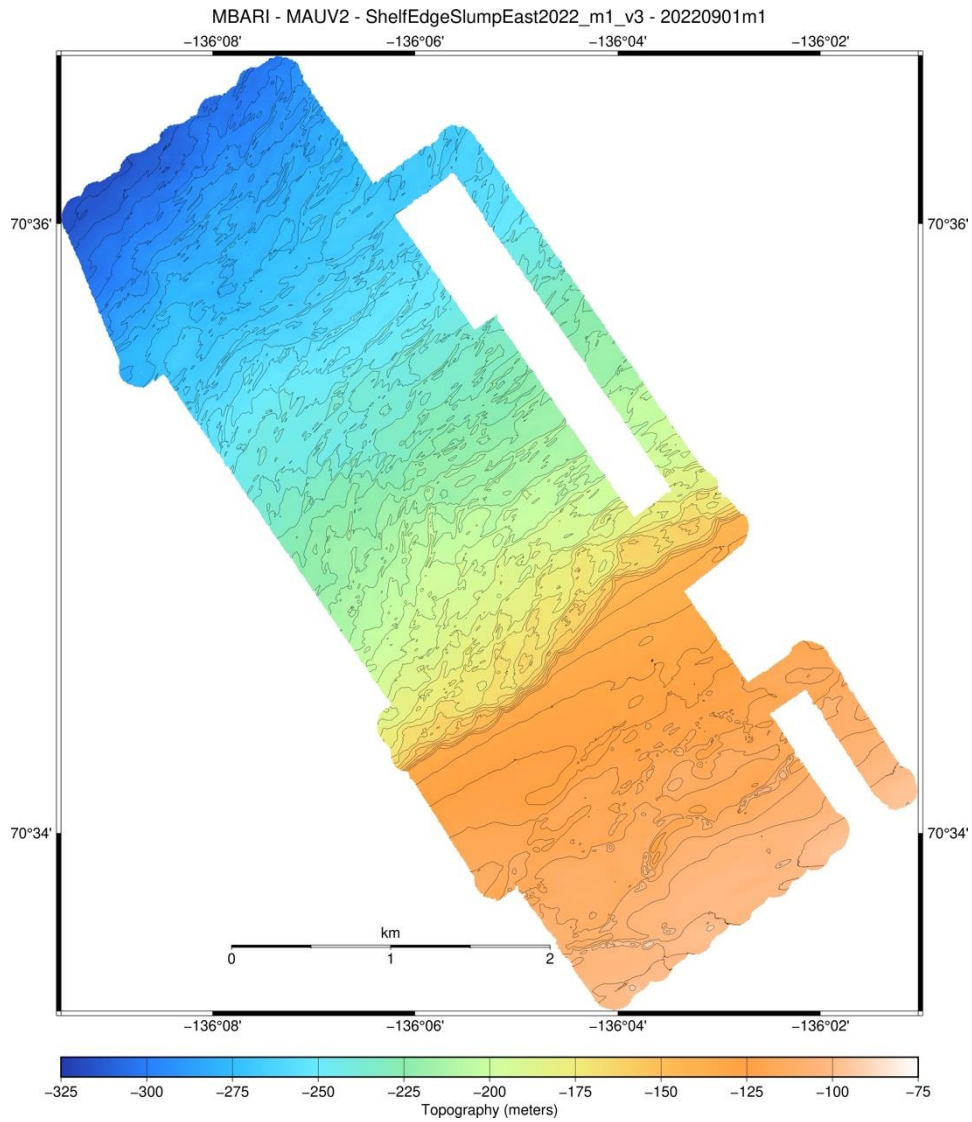


Figure 3.17. Mapping AUV 1-m resolution multibeam bathymetry from mission 20220901m1 displayed with 10-m contours.

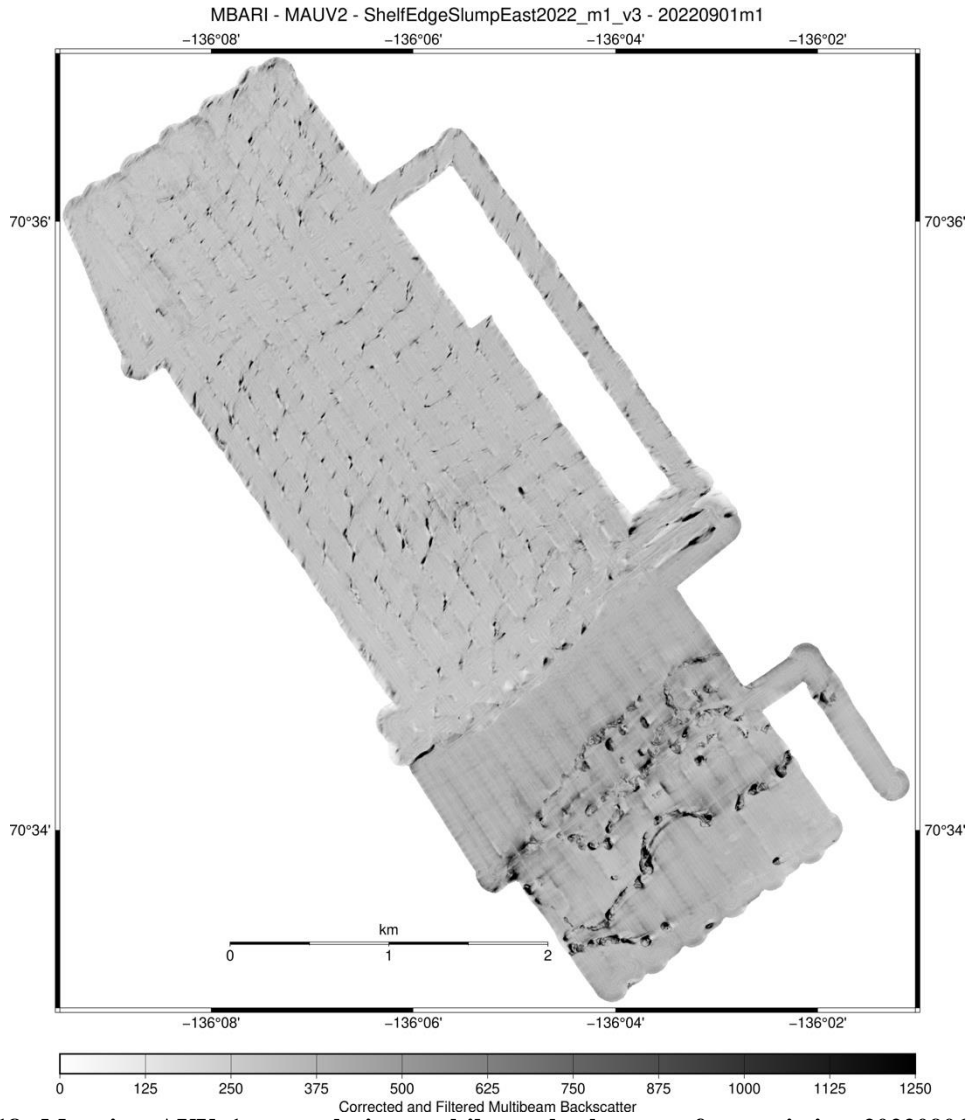


Figure 3.18. Mapping AUV 1-m resolution multibeam backscatter from mission 20220901m1. The backscatter has been corrected using an empirical amplitude-vs-grazing angle model and had a Gaussian smoothing filter applied. High amplitudes are shown dark.

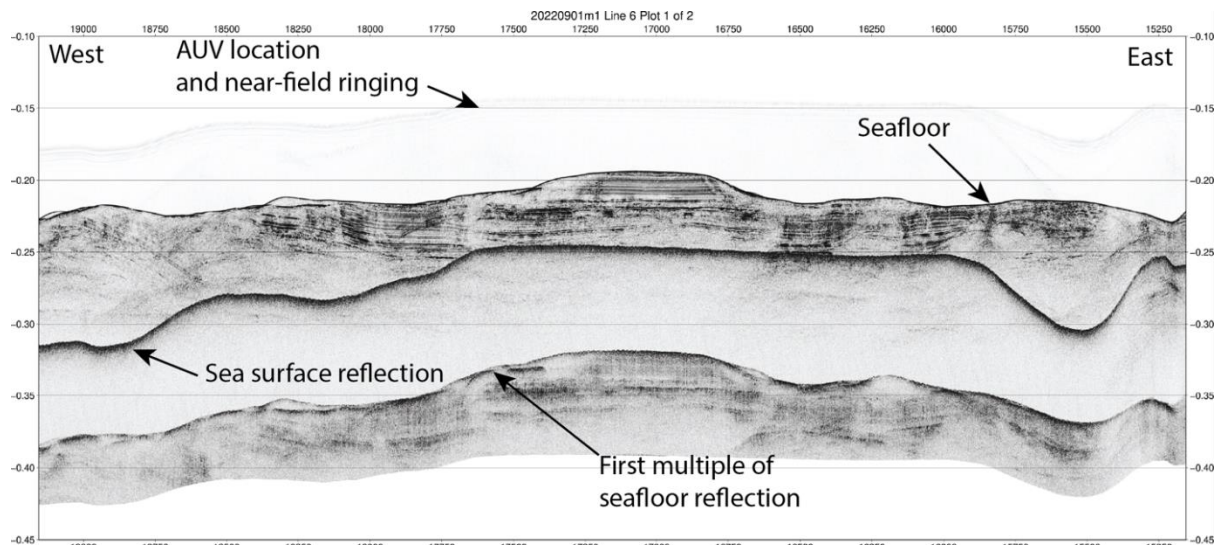


Figure 3.19. Mapping AUV chirp 1-6 kHz subbottom profiler data from mission 20220901m1. The section is shown “hung” from the AUV’s location in the water column, generally about 50-m above the seafloor. The location of this profile is shown as a red line on Figure 3.16. Arrows indicate locations of sub-seafloor and multiple reflections. Surface reflections are seen in the AUV-collected chirp profiles when the vehicle is operated in less than about 500 m water depth. During shallow water surveys, when the AUV is closer to the sea surface than the seafloor, the sea surface reflection would come before (above) the seafloor in the subbottom profile (not shown in this figure). Vertical scale is in seconds below sea level, two-way travel time.

3.3.2.3. Mission 20220902m1 – 420m Mud Volcano

Mission 20220902m1 surveyed the 420 m Mud Volcano. MiniROV dive M187 and coring stations ST15, ST16, ST17, ST25, and ST37 occurred at this site. The multibeam data collected during mission 20220902m1 with MAUV2 are summarized in Table 3.5. The sidescan and subbottom data correspond to the same time and spatial domain, but are organized in 77 sequential line files delineated by the waypoints in the AUV mission. Included below are representative maps of the multibeam bathymetry and multibeam backscatter imagery from mission 20220902m1 (Figures 3.20 to 3.22). Also included is an example of a subbottom profile section plot (Figure 3.23).

Table 3.5. Multibeam data statistics from Mapping AUV survey 20220902m1, which was conducted with MAUV2 at the 420 m Mud Volcano

MBARI MAUV2 Mission 20220902m1 Multibeam Data Totals:	
Number of Records:	194979
Bathymetry Data (1024 beams):	
Number of Beams:	171546012
Number of Good Beams:	152921058 89.14%
Number of Zero Beams:	0 0.00%
Number of Flagged Beams:	18624954 10.86%
Amplitude Data (1024 beams):	
Number of Beams:	171546012
Number of Good Beams:	152921058 89.14%
Number of Zero Beams:	0 0.00%
Number of Flagged Beams:	18624954 10.86%
Sidescan Data (2048 pixels):	
Number of Pixels:	399316992
Number of Good Pixels:	88559303 22.18%
Number of Zero Pixels:	0 0.00%
Number of Flagged Pixels:	310757689 77.82%
Navigation Totals:	
Total Time:	17.9646 hours
Total Track Length:	83.9834 km
Average Speed:	4.6749 km/hr (2.5270 knots)
Start of Data:	
Time:	09 03 2022 03:09:12.195017 JD246 (2022-09-03T03:09:12.195017)
Lon:	-135.290793409 Lat: 70.740368096 Depth: 9.3519 meters
Speed:	2.9458 km/hr (1.5923 knots) Heading: 74.1983 degrees
Sonar Depth:	9.3519 m Sonar Altitude: 0.0000 m
End of Data:	
Time:	09 03 2022 21:07:04.634586 JD246 (2022-09-03T21:07:04.634586)
Lon:	-135.563967165 Lat: 70.792145518 Depth: 417.9199 meters
Speed:	4.8397 km/hr (2.6160 knots) Heading: 99.7159 degrees
Sonar Depth:	398.1339 m Sonar Altitude: 19.7859 m
Limits:	
Minimum Longitude:	-135.609504062 Maximum Longitude: -135.285924034
Minimum Latitude:	70.735501638 Maximum Latitude: 70.806147817
Minimum Sonar Depth:	9.3519 Maximum Sonar Depth: 423.7399
Minimum Altitude:	0.0000 Maximum Altitude: 89.0768
Minimum Depth:	85.3716 Maximum Depth: 475.8737
Minimum Amplitude:	17.5739 Maximum Amplitude: 26856.9902
Minimum Sidescan:	0.0000 Maximum Sidescan: 11045.5176

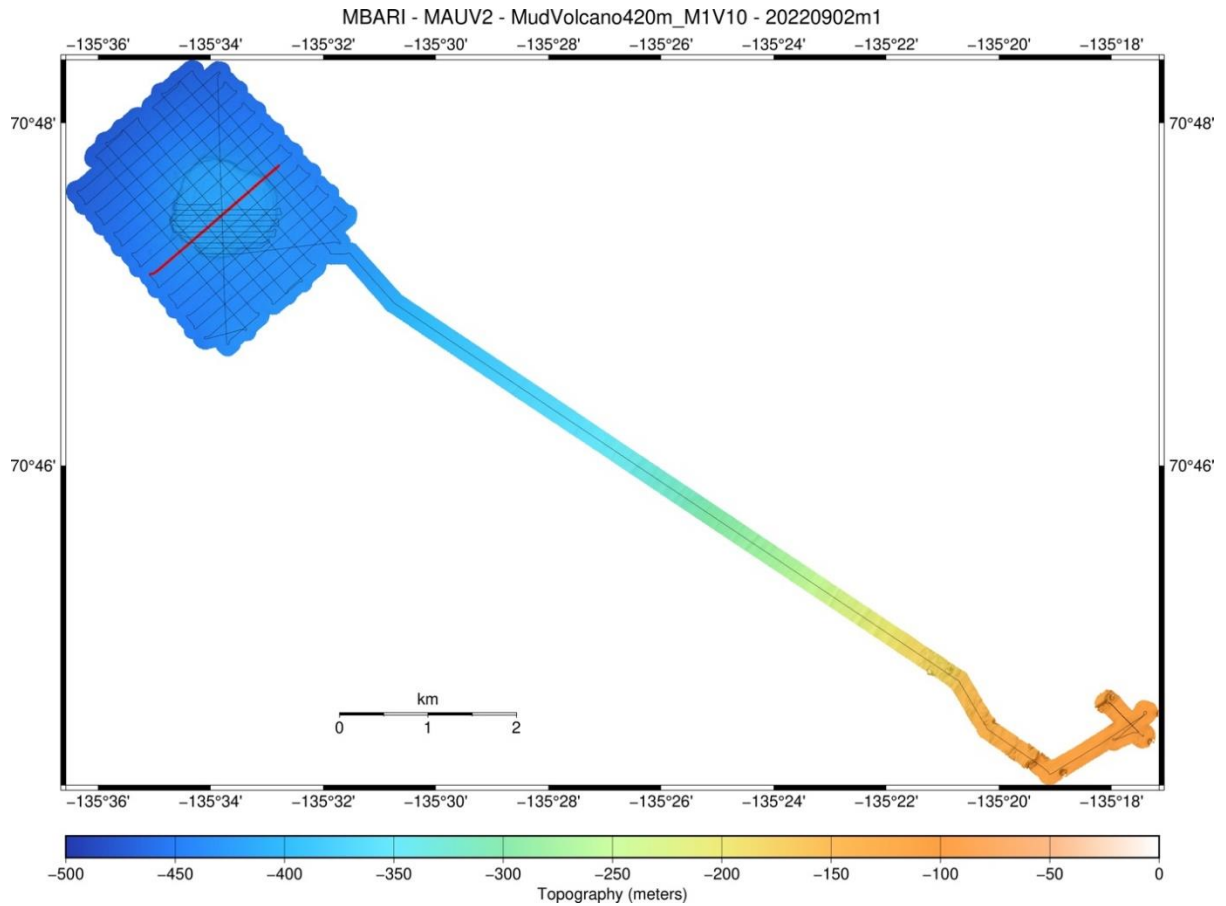


Figure 3.20. Mapping AUV 1-m resolution multibeam bathymetry from mission 20220902m1 displayed with slope magnitude shading overlain by the AUV tracklines. The red line indicates the location of the subbottom profile section shown in Figure 3.23.

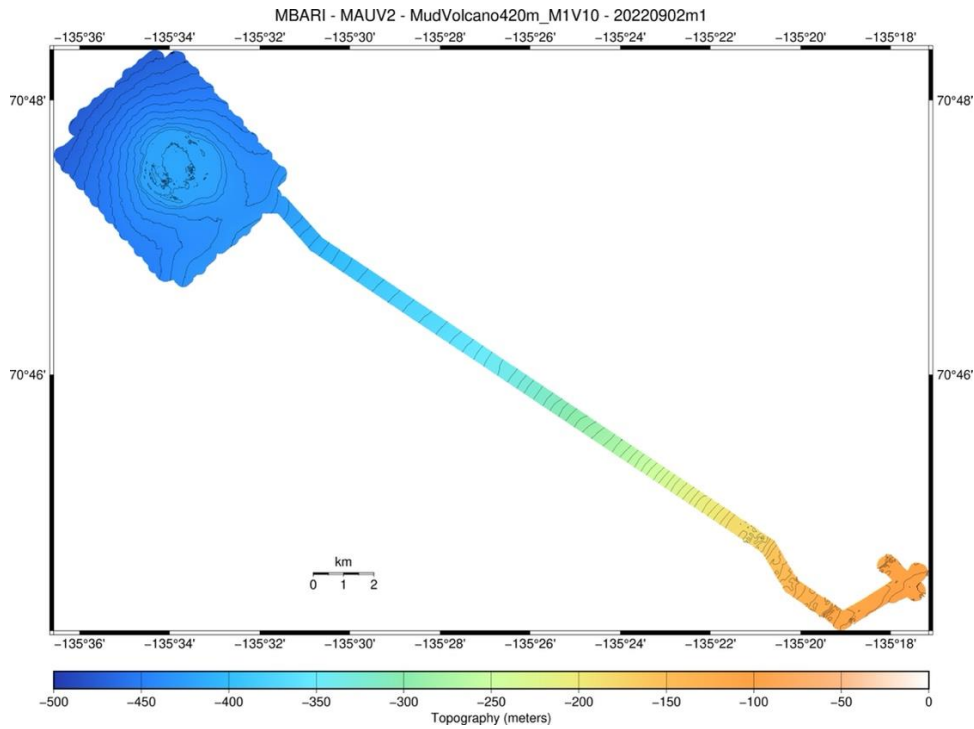


Figure 3.21. Mapping AUV 1-m resolution multibeam bathymetry from mission 20220902m1 displayed with 10-m contours.

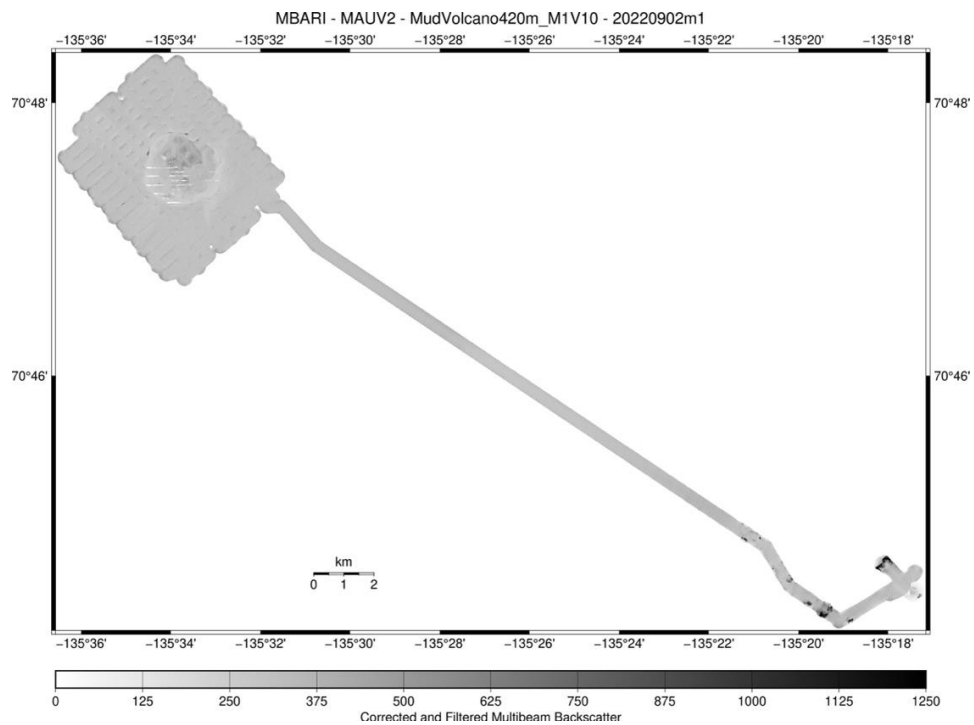


Figure 3.22. Mapping AUV 1-m resolution multibeam backscatter from mission 20220902m1. The backscatter has been corrected using an empirical amplitude-vs-grazing angle model and had a Gaussian smoothing filter applied. High amplitudes are shown dark.

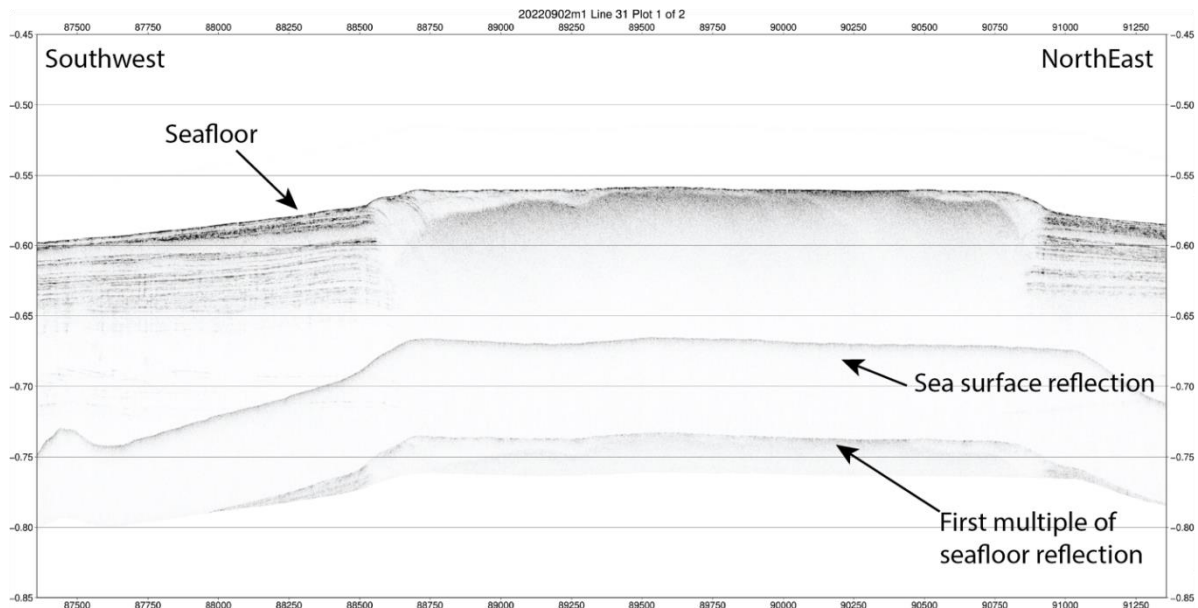


Figure 3.23. Mapping AUV chirp 1-6 kHz subbottom profiler data from mission 20220902m1. The section is shown “hung” from the AUV’s location in the water column, generally about 50-m above the seafloor. The location of this profile is shown as a red line on Figure 3.20. Arrows indicate locations of sub-seafloor and multiple reflections. Surface reflections are seen in the AUV-collected chirp profiles when the vehicle is operated in less than about 500 m water depth. During shallow water surveys, when the AUV is closer to the sea surface than the seafloor, the sea surface reflection would come before (above) the seafloor in the subbottom profile (not shown in this figure). Vertical scale is in seconds below sea level, two-way travel time.

3.3.2.4. Mission 20220906m1 – ARA05C Seismic Line 1; Shelf Edge Intact (2)

Mission 20220906m1 is the western-most survey in the Shelf Edge Intact region. It covers some of the shelf edge and has long transects over ARA05C Seismic Line 1. It is not underlain by bathymetry from the CCCG Sir Wilfred Laurier. MiniROV dive M189 and coring station ST20 were sited in this area. The multibeam data collected during mission 20220906m1 with MAUV2 are summarized in Table 3.6. The sidescan and subbottom data correspond to the same time and spatial domain, but are organized in 48 sequential line files delineated by the waypoints in the AUV mission. Included below are representative maps of the multibeam bathymetry and multibeam backscatter imagery from mission 20220906m1 (Figures 3.24 to 3.26). Also included is an example of a subbottom profile section plot (Figure 3.27).

Table 3.6. Multibeam data statistics from Mapping AUV survey 20220906m1, which was conducted with MAUV2 at the area Shelf Edge Intact

MBARI MAUV2 Mission 20220906m1 Multibeam Data Totals:	
Number of Records:	194600
Bathymetry Data (1024 beams):	
Number of Beams:	172131867
Number of Good Beams:	150009661 87.15%
Number of Zero Beams:	0 0.00%
Number of Flagged Beams:	22122206 12.85%
Amplitude Data (1024 beams):	
Number of Beams:	172131867
Number of Good Beams:	150009661 87.15%
Number of Zero Beams:	0 0.00%
Number of Flagged Beams:	22122206 12.85%
Sidescan Data (2048 pixels):	
Number of Pixels:	398540800
Number of Good Pixels:	79931635 20.06%
Number of Zero Pixels:	0 0.00%
Number of Flagged Pixels:	318609165 79.94%
Navigation Totals:	
Total Time:	17.9259 hours
Total Track Length:	86.8801 km
Average Speed:	4.8466 km/hr (2.6198 knots)
Start of Data:	
Time:	09 06 2022 22:21:35.612449 JD249 (2022-09-06T22:21:35.612449)
Lon:	-134.915293425 Lat: 70.855600588 Depth: 58.6787 meters
Speed:	4.7058 km/hr (2.5437 knots) Heading: 101.2390 degrees
Sonar Depth:	58.6787 m Sonar Altitude: 0.0000 m
End of Data:	
Time:	09 07 2022 16:17:08.871859 JD250 (2022-09-07T16:17:08.871859)
Lon:	-134.948921346 Lat: 70.869542901 Depth: 125.7715 meters
Speed:	4.8761 km/hr (2.6357 knots) Heading: 329.9634 degrees
Sonar Depth:	76.0918 m Sonar Altitude: 49.5845 m
Limits:	
Minimum Longitude:	-135.036650413 Maximum Longitude: -134.894670919
Minimum Latitude:	70.812903392 Maximum Latitude: 70.891510032
Minimum Sonar Depth:	28.4320 Maximum Sonar Depth: 230.3045
Minimum Altitude:	37.9721 Maximum Altitude: 78.6562
Minimum Depth:	68.6860 Maximum Depth: 286.0595
Minimum Amplitude:	22.6804 Maximum Amplitude: 32558.8848
Minimum Sidescan:	0.0000 Maximum Sidescan: 11501.6758

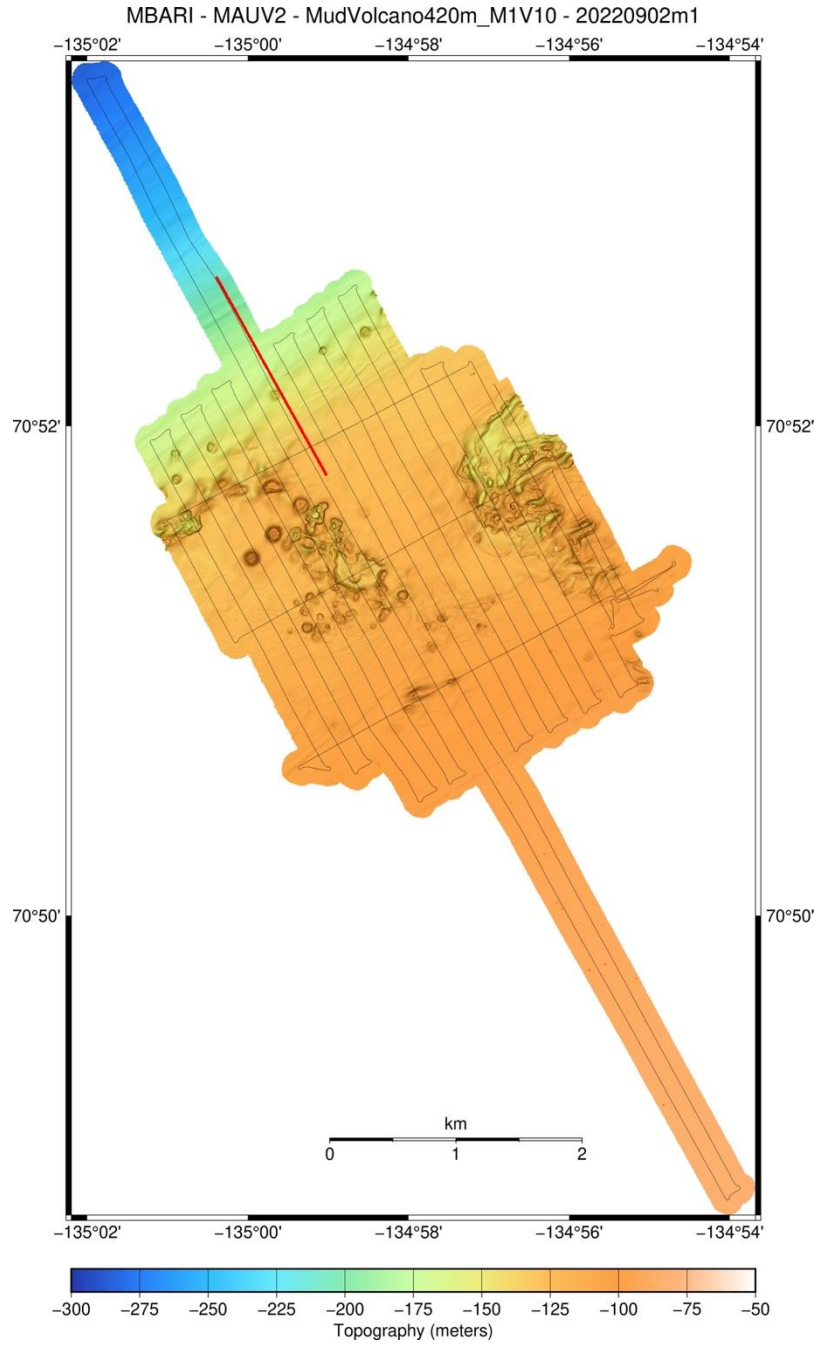


Figure 3.24. Mapping AUV 1-m resolution multibeam bathymetry from mission 20220906m1 displayed with slope magnitude shading overlain by the AUV tracklines. The red line indicates the location of the subbottom profile section shown in Figure 3.27.

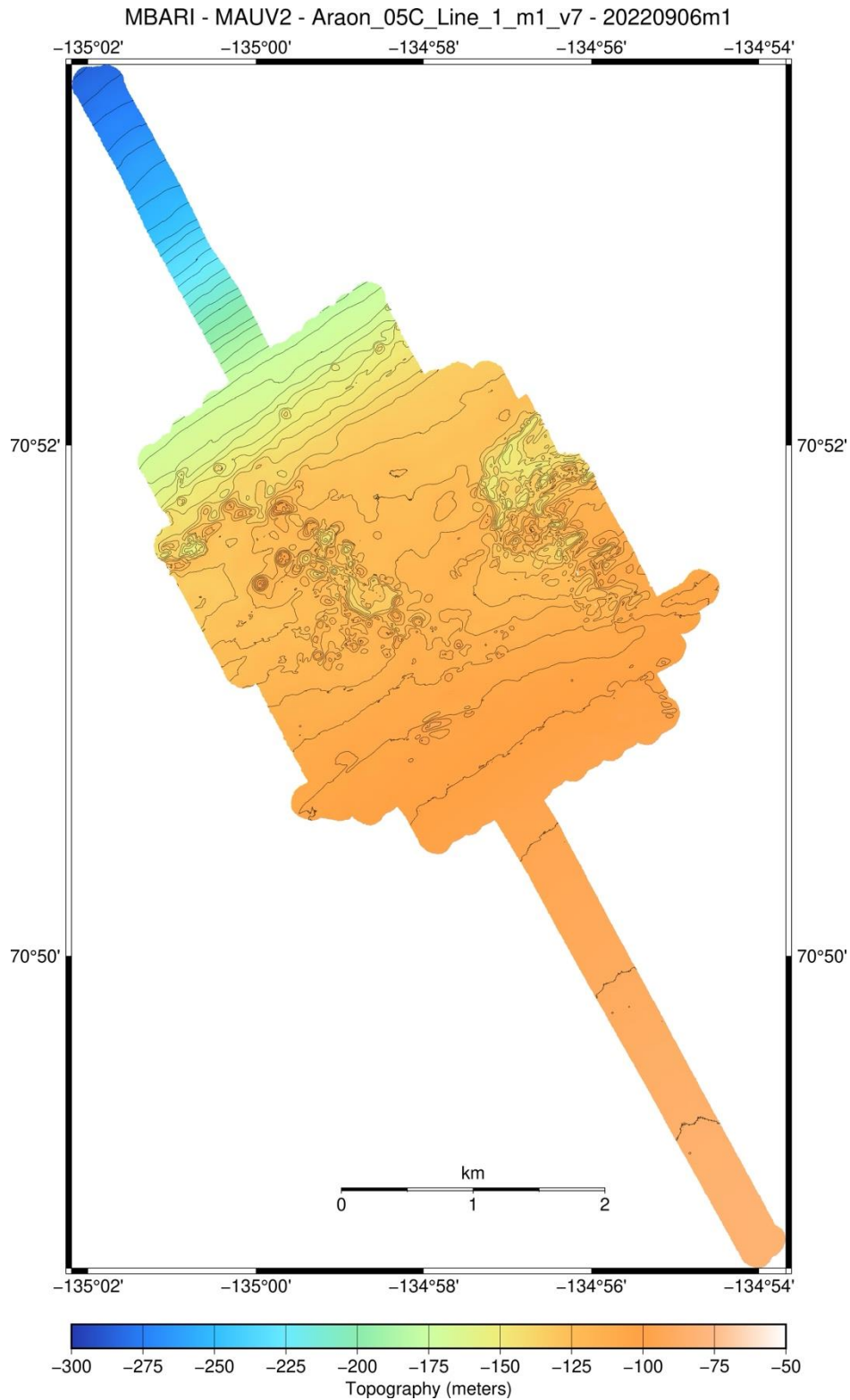


Figure 3.25. Mapping AUV 1-m resolution multibeam bathymetry from mission 20220906m1 displayed with 10-m contours.

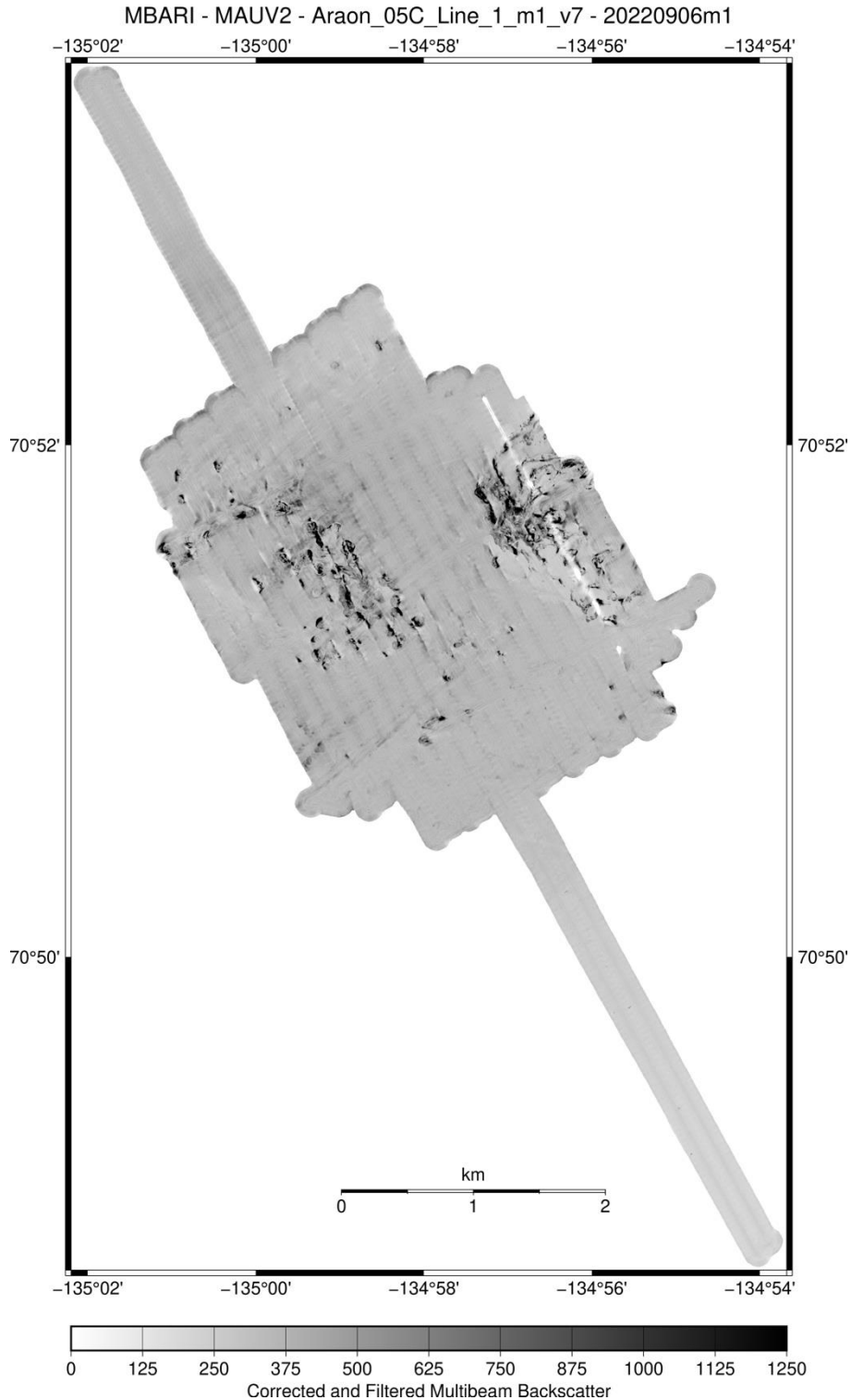


Figure 3.26. Mapping AUV 1-m resolution multibeam backscatter from mission 20220906m1. The backscatter has been corrected using an empirical amplitude-vs-grazing angle model and had a Gaussian smoothing filter applied. High amplitudes are shown dark.

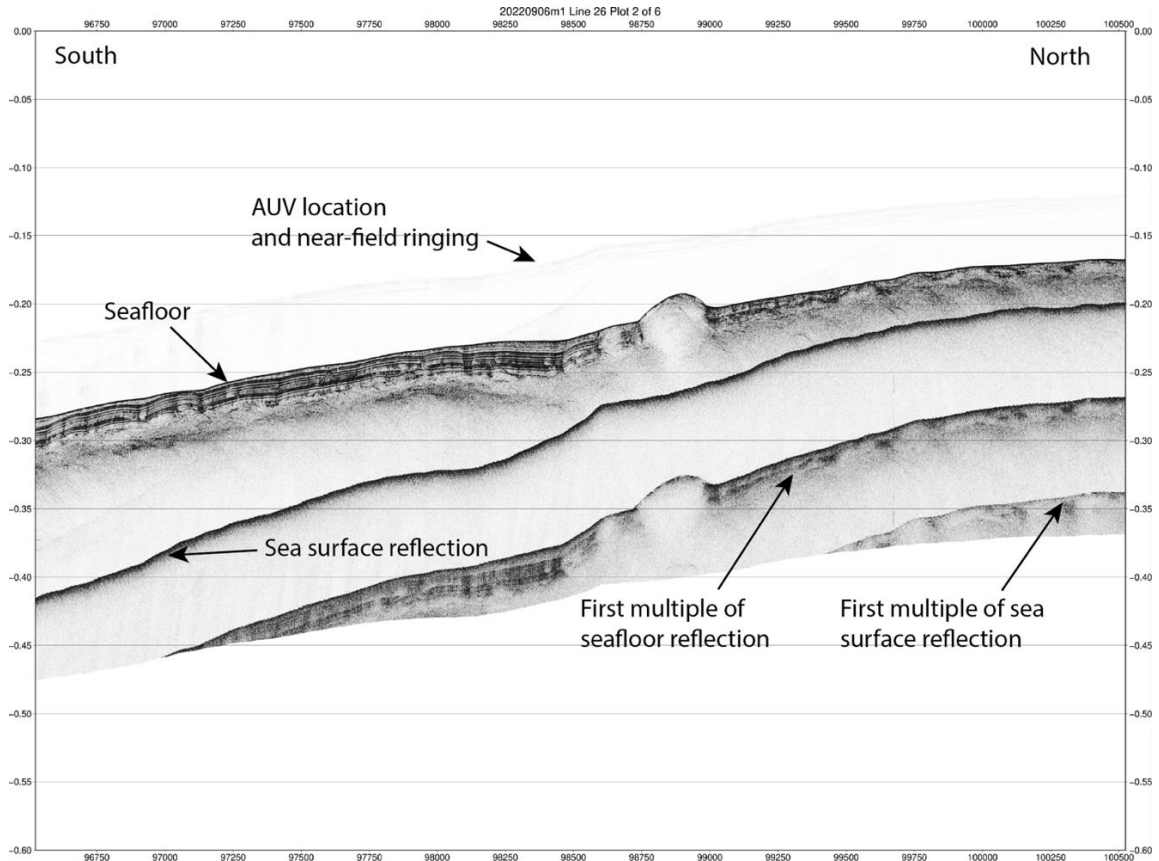


Figure 3.27. Mapping AUV chirp 1-6 kHz subbottom profiler data from mission 20220906m1. The section is shown “hung” from the AUV’s location in the water column, generally about 50-m above the seafloor. The location of this profile is shown as a red line on Figure 3.24. Arrows indicate locations of sub-seafloor and multiple reflections. Surface reflections are seen in the AUV-collected chirp profiles when the vehicle is operated in less than about 500 m water depth. During shallow water surveys, when the AUV is closer to the sea surface than the seafloor, the sea surface reflection would come before (above) the seafloor in the subbottom profile (not shown in this figure). Vertical scale is in seconds below sea level, two-way travel time.

3.3.2.5. Mission 20220906m2 –Shelf Edge Intact (3)

This mission was at the west end of the Shelf Edge Intact area. It was the third survey conducted along the intact part of the shelf edge, and the first successful mission with MAUV1. It is underlain by bathymetry from the CCGG Sir Wilfred Laurier. MiniROV dive M188 and coring stations ST11 and ST12 were sited in this area. The multibeam data collected during mission 20220906m2 with MAUV1 are summarized in Table 3.7. The sidescan and subbottom data correspond to the same time and spatial domain, but are organized in 50 sequential line files delineated by the waypoints in the AUV mission. Included below are representative maps of the multibeam bathymetry and multibeam backscatter imagery from mission 20220906m2 (Figures 3.28 to 3.30). Also included is an example of a subbottom profile section plot (Figure 3.31).

Table 3.7. Multibeam data statistics from Mapping AUV survey 20220906m2, which was conducted with MAUV1 at the west end of the area Shelf Edge Intact

MBARI MAUV1 Mission 20220906m2 Multibeam Data Totals:	
Number of Records:	192403
Bathymetry Data (1024 beams):	
Number of Beams:	173589287
Number of Good Beams:	140268221 80.80%
Number of Zero Beams:	0 0.00%
Number of Flagged Beams:	33321066 19.20%
Amplitude Data (1024 beams):	
Number of Beams:	173589287
Number of Good Beams:	140268221 80.80%
Number of Zero Beams:	0 0.00%
Number of Flagged Beams:	33321066 19.20%
Sidescan Data (2048 pixels):	
Number of Pixels:	394041344
Number of Good Pixels:	70592530 17.92%
Number of Zero Pixels:	0 0.00%
Number of Flagged Pixels:	323448814 82.08%
Navigation Totals:	
Total Time:	17.7699 hours
Total Track Length:	72.3971 km
Average Speed:	4.0741 km/hr (2.2022 knots)
Start of Data:	
Time:	09 06 2022 23:59:57.343025 JD249 (2022-09-06T23:59:57.343025)
Lon:	-135.181800134 Lat: 70.796231001 Depth: 61.5391 meters
Speed:	3.2687 km/hr (1.7669 knots) Heading: 313.1747 degrees
Sonar Depth:	61.5391 m Sonar Altitude: 0.0000 m
End of Data:	
Time:	09 07 2022 17:46:09.062822 JD250 (2022-09-07T17:46:09.062822)
Lon:	-135.228756489 Lat: 70.804726847 Depth: 169.0244 meters
Speed:	4.4246 km/hr (2.3917 knots) Heading: 321.7283 degrees
Sonar Depth:	112.3885 m Sonar Altitude: 55.8732 m
Limits:	
Minimum Longitude:	-135.250804417 Maximum Longitude: -135.141556353
Minimum Latitude:	70.792063726 Maximum Latitude: 70.827943342
Minimum Sonar Depth:	52.7665 Maximum Sonar Depth: 157.0131
Minimum Altitude:	0.0000 Maximum Altitude: 72.5396
Minimum Depth:	76.7917 Maximum Depth: 212.6376
Minimum Amplitude:	13.7808 Maximum Amplitude: 19644.4922
Minimum Sidescan:	0.0000 Maximum Sidescan: 4632.5654

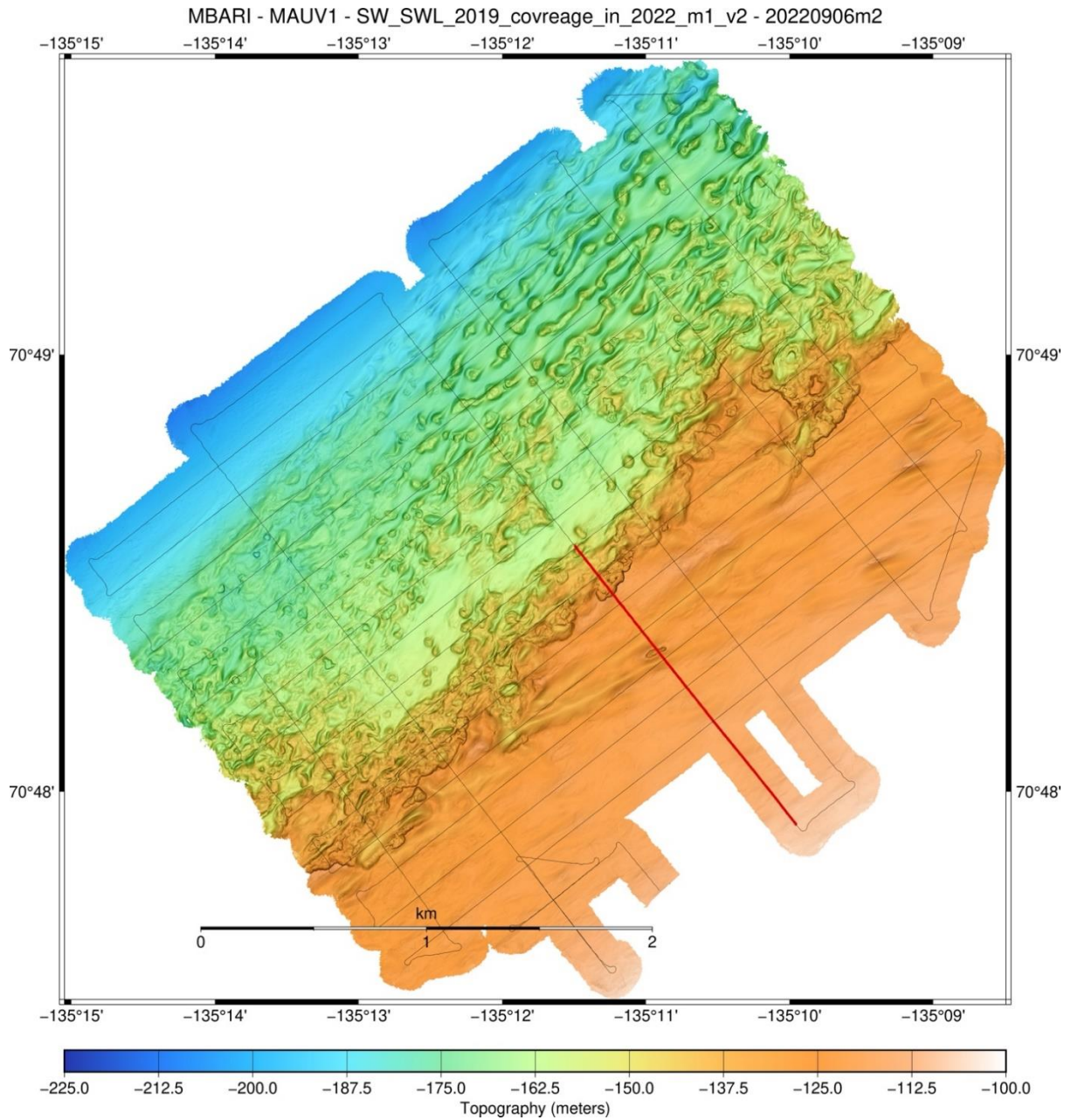


Figure 3.28. Mapping AUV 1-m resolution multibeam bathymetry from mission 20220906m2 displayed with slope magnitude shading overlain by the AUV tracklines. The red line indicates the location of the subbottom profile section shown in Figure 3.31.

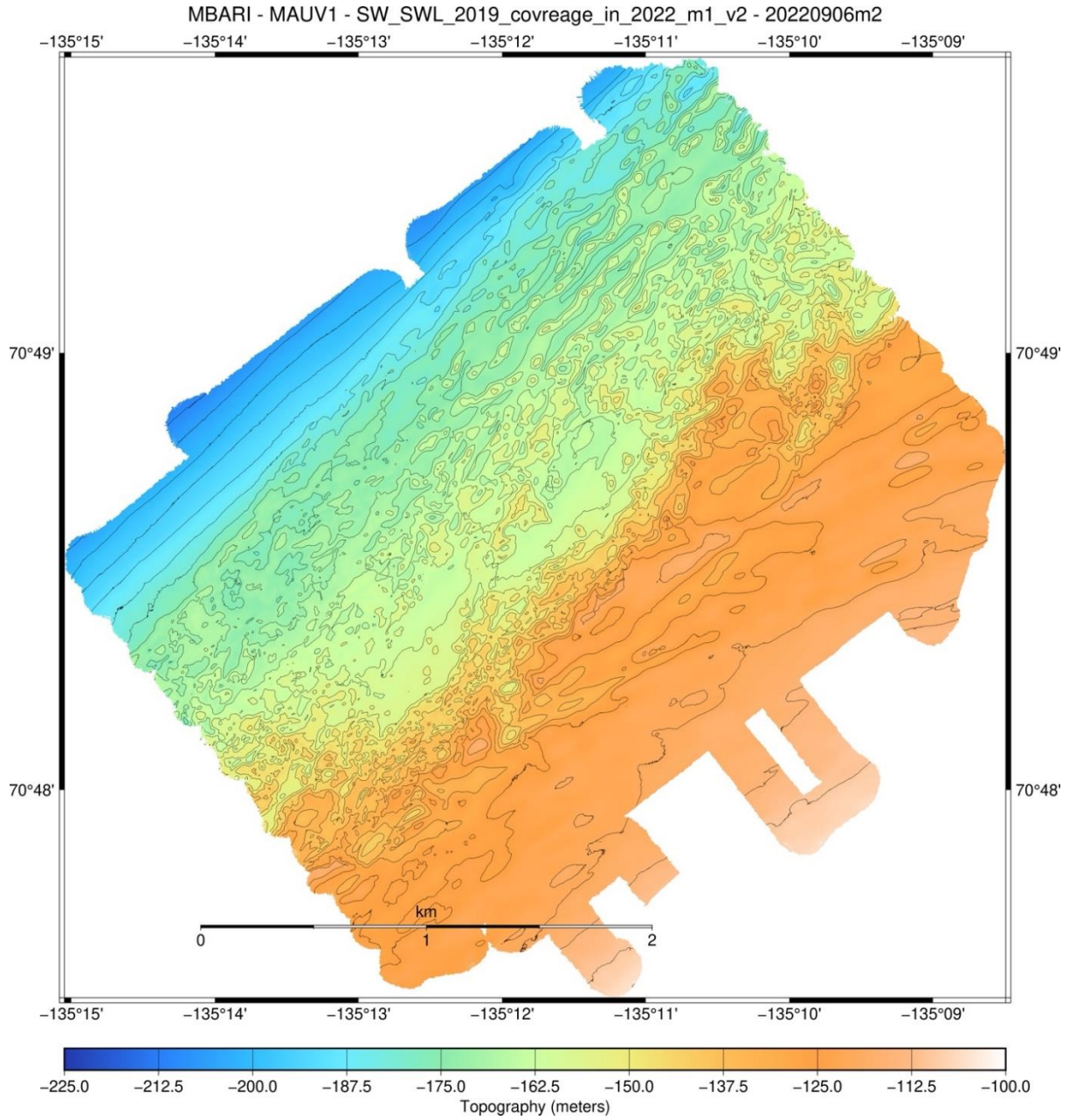


Figure 3.29. Mapping AUV 1-m resolution multibeam bathymetry from mission 20220906m2 displayed with 10-m contours.

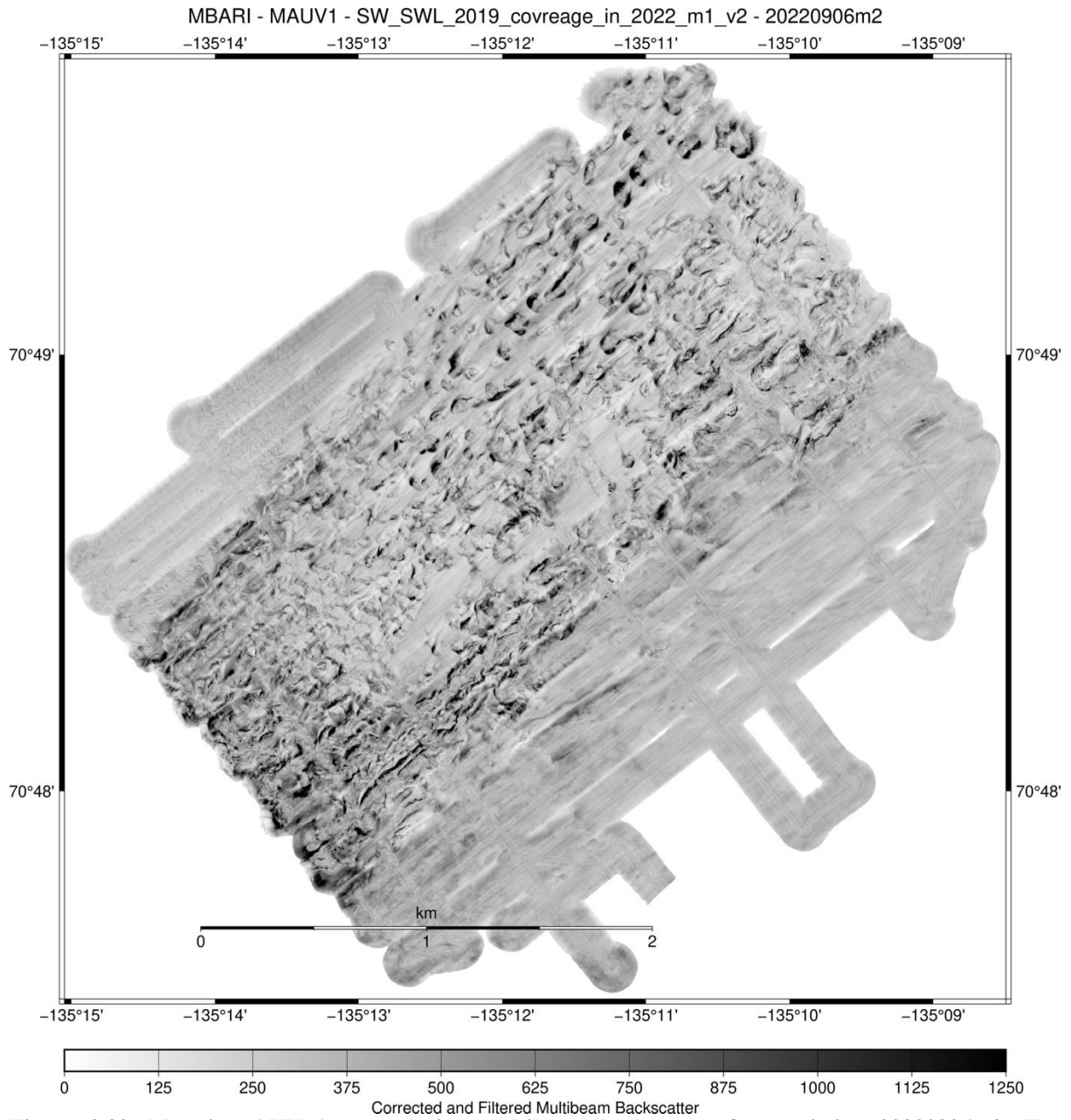


Figure 3.30. Mapping AUV 1-m resolution multibeam backscatter from mission 20220906m2. The backscatter has been corrected using an empirical amplitude-vs-grazing angle model and had a Gaussian smoothing filter applied. High amplitudes are shown dark.

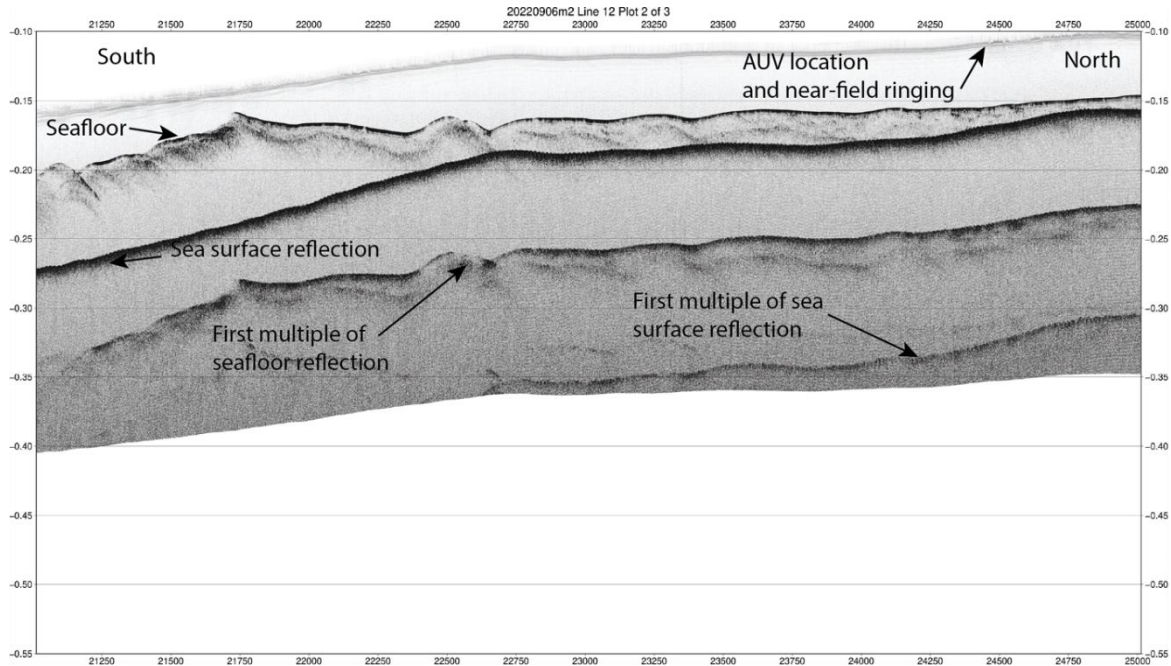


Figure 3.31. Mapping AUV chirp 1-6 kHz subbottom profiler data from mission 20220906m2. The section is shown “hung” from the AUV’s location in the water column, generally about 50-m above the seafloor. The location of this profile is shown as a red line on Figure 3.28. Arrows indicate locations of sub-seafloor and multiple reflections. Surface reflections are seen in the AUV-collected chirp profiles when the vehicle is operated in less than about 500 m water depth. During shallow water surveys, when the AUV is closer to the sea surface than the seafloor, the sea surface reflection would come before (above) the seafloor in the subbottom profile (not shown in this figure). Vertical scale is in seconds below sea level, two-way travel time.

3.3.2.6. Mission 20220907m1 –740 m Mud Volcano

This mission was conducted with MAUV2 at the 740 m Mud Volcano. As this site was deeper than the <130 m depth needed for the survey to begin with the vehicle in DVL bottom-lock while receiving GPS location, it was begun with a spin-down, the only one of the expedition. Coring stations ST19 and ST30 were sited in this area. The multibeam data collected during mission 20220907m1 with MAUV2 are summarized in Table 3.8. The sidescan and subbottom data correspond to the same time and spatial domain, but are organized in 45 sequential line files delineated by the waypoints in the AUV mission. Included below are representative maps of the multibeam bathymetry and multibeam backscatter imagery from mission 20220907m1 (Figures 3.32 to 3.34). Also included is an example of a subbottom profile section plot (Figure 3.35).

Table 3.8. Multibeam data statistics from Mapping AUV survey 20220907m1, which was conducted with MAUV2 at the 740 m Mud Volcano

MBARI MAUV2 Mission 20220907m1 Multibeam Data Totals:	
Number of Records:	172213
Bathymetry Data (1024 beams):	
Number of Beams:	151494277
Number of Good Beams:	131594836 86.86%
Number of Zero Beams:	0 0.00%
Number of Flagged Beams:	19899441 13.14%
Amplitude Data (1024 beams):	
Number of Beams:	151494277
Number of Good Beams:	131594836 86.86%
Number of Zero Beams:	0 0.00%
Number of Flagged Beams:	19899441 13.14%
Sidescan Data (2048 pixels):	
Number of Pixels:	352692224
Number of Good Pixels:	68201770 19.34%
Number of Zero Pixels:	0 0.00%
Number of Flagged Pixels:	284490454 80.66%
Navigation Totals:	
Total Time:	15.8650 hours
Total Track Length:	72.1705 km
Average Speed:	4.5490 km/hr (2.4589 knots)
Start of Data:	
Time:	09 08 2022 04:12:31.408145 JD251 (2022-09-08T04:12:31.408145)
Lon:	-136.112558360 Lat: 70.784955729 Depth: 622.6064 meters
Speed:	2.8468 km/hr (1.5388 knots) Heading: 347.4049 degrees
Sonar Depth:	622.6064 m Sonar Altitude: 0.0000 m
End of Data:	
Time:	09 08 2022 20:04:25.534313 JD251 (2022-09-08T20:04:25.534313)
Lon:	-136.054084767 Lat: 70.813642264 Depth: 771.4946 meters
Speed:	4.8831 km/hr (2.6395 knots) Heading: 8.5328 degrees
Sonar Depth:	720.1099 m Sonar Altitude: 51.3759 m
Limits:	
Minimum Longitude:	-136.128284644 Maximum Longitude: -136.033471255
Minimum Latitude:	70.783683379 Maximum Latitude: 70.814777367
Minimum Sonar Depth:	622.6064 Maximum Sonar Depth: 740.3408
Minimum Altitude:	0.0000 Maximum Altitude: 121.4148
Minimum Depth:	731.3676 Maximum Depth: 791.1033
Minimum Amplitude:	32.9335 Maximum Amplitude: 11694.6611
Minimum Sidescan:	0.0000 Maximum Sidescan: 3520.0542

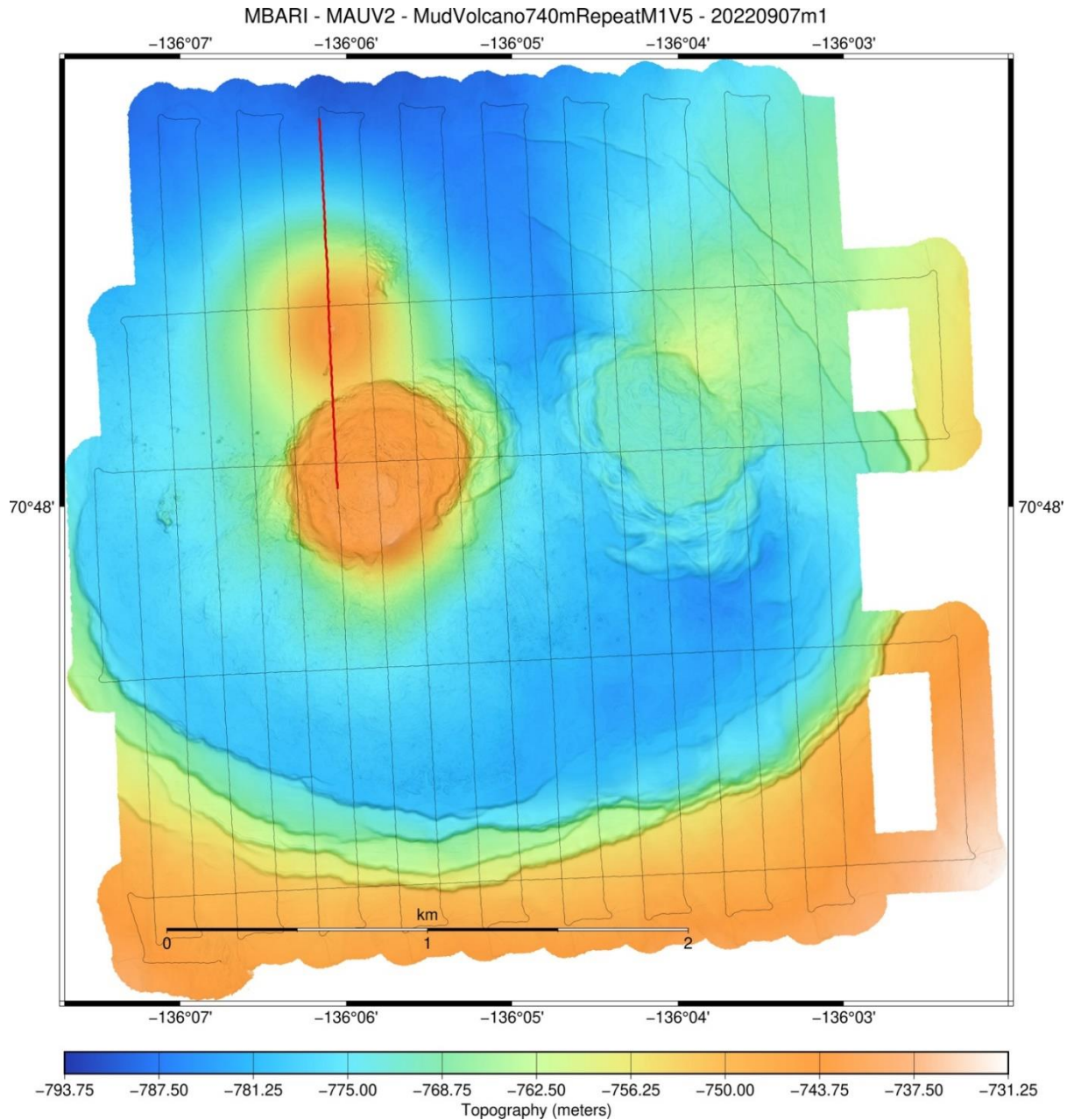


Figure 3.32. Mapping AUV 1-m resolution multibeam bathymetry from mission 20220907m1 displayed with slope magnitude shading overlain by the AUV tracklines. The red line indicates the location of the subbottom profile section shown in Figure 3.35.

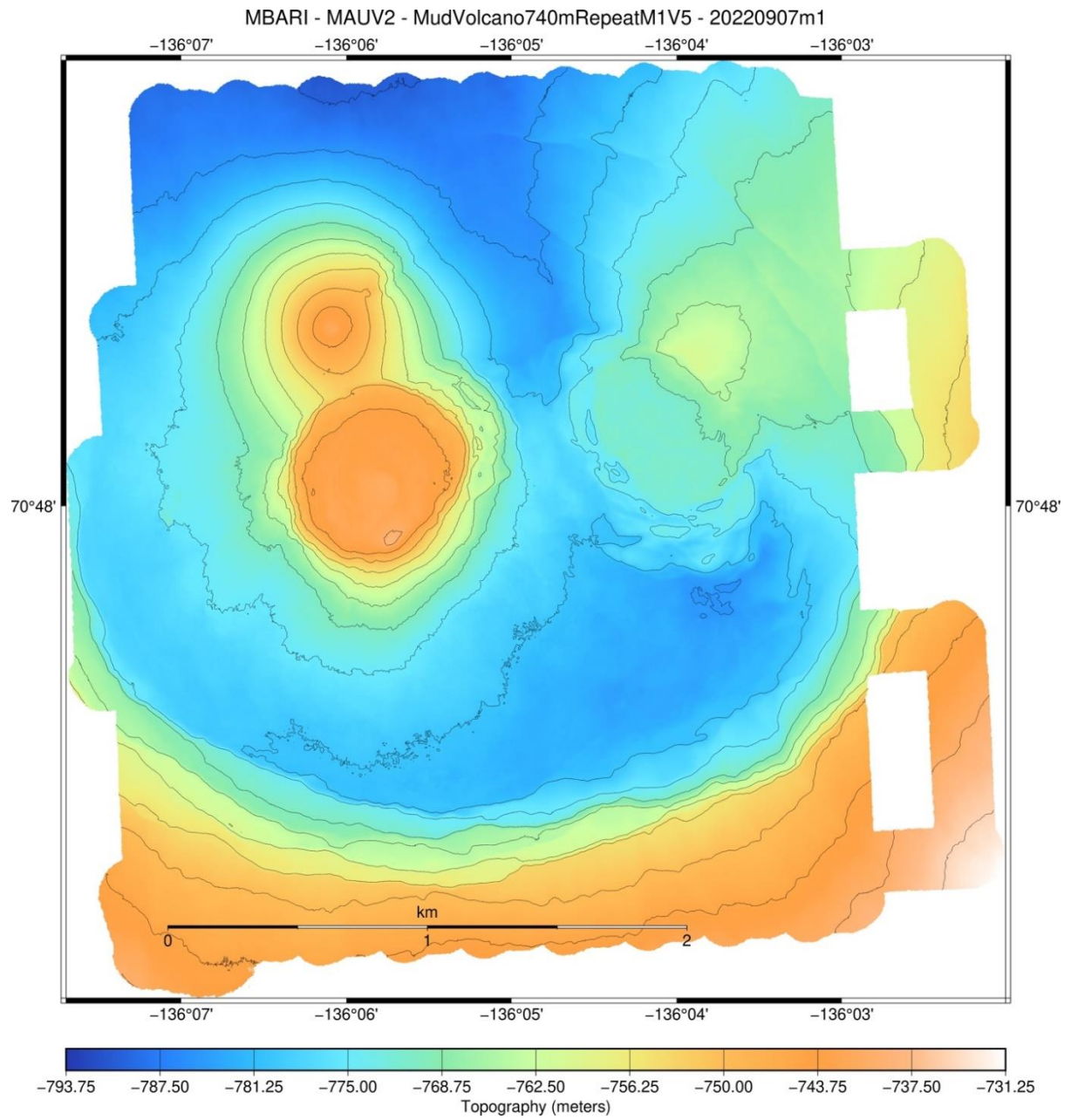


Figure 3.33. Mapping AUV 1-m resolution multibeam bathymetry from mission 20220907m1 displayed with 10-m contours.

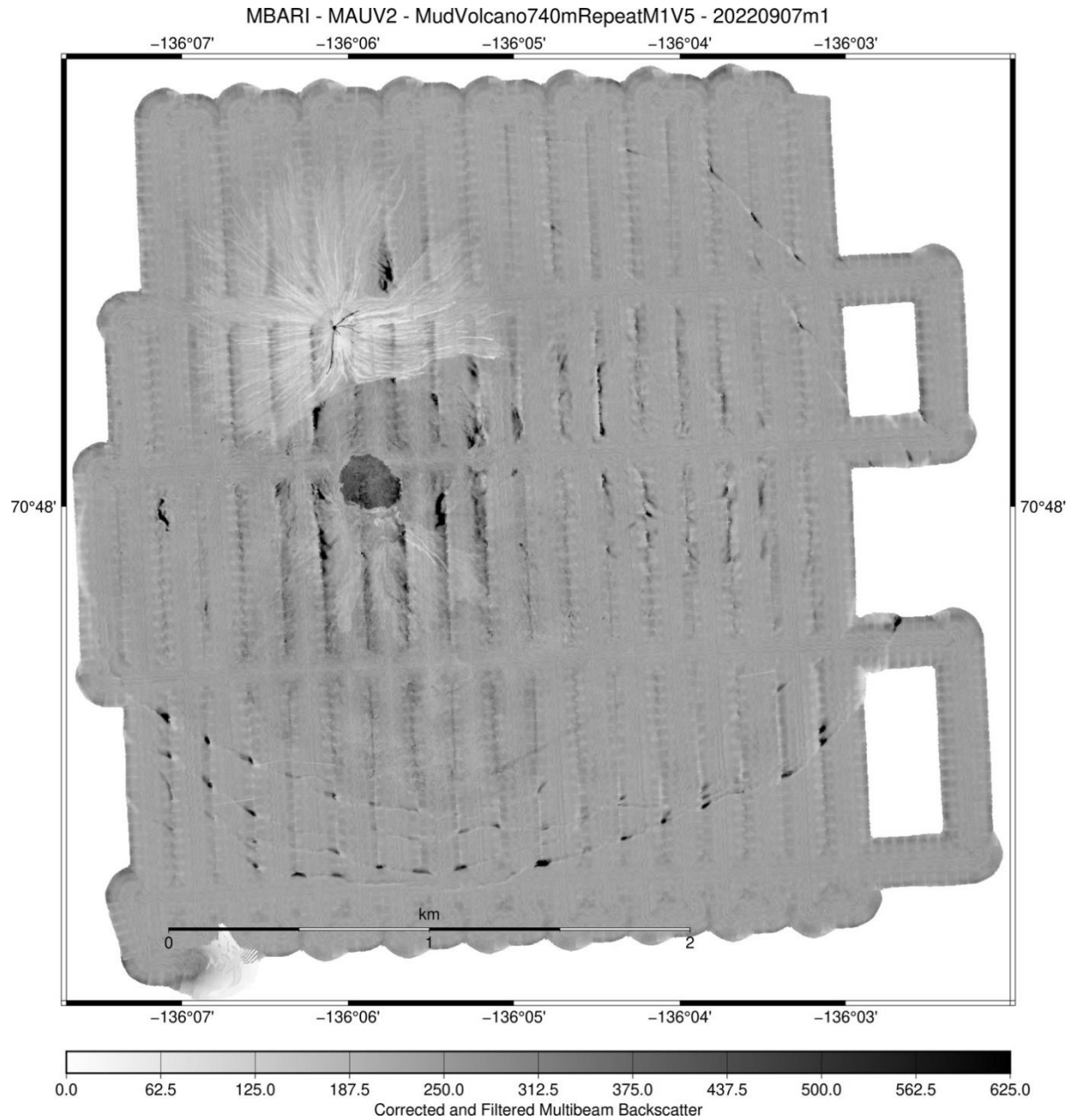


Figure 3.34. Mapping AUV 1-m resolution multibeam backscatter from mission 20220907m1. The backscatter has been corrected using an empirical amplitude-vs-grazing angle model and had a Gaussian smoothing filter applied. High amplitudes are shown dark.

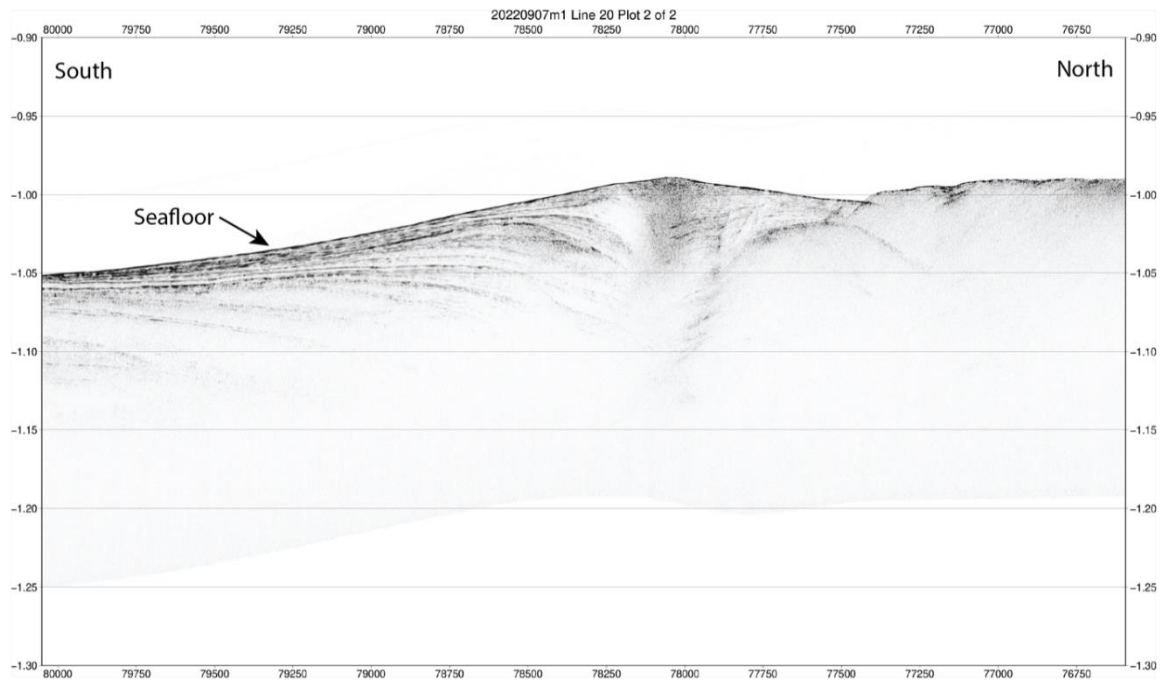


Figure 3.35. Mapping AUV chirp 1-6 kHz subbottom profiler data from mission 20220907m1. The section is shown “hung” from the AUV’s location in the water column, generally about 50-m above the seafloor. The location of this profile is shown as a red line on Figure 3.32. Vertical scale is in seconds below sea level, two-way travel time.

3.3.3. Differencing of Bathymetry by Region

Bathymetry from the MBARI Mapping AUV surveys conducted in 2022 were navigation-adjusted with and compared against AUV surveys collected in 2013, 2016, and 2017 and ship-based surveys in 2010 and 2019, as appropriate. Adjustments between the mission data file sections were made only in the X-Y plane during navigation processing, with a single vertical offset applied between each survey to accommodate for air pressure (weather) effects and calibration differences. As the ships were GPS-navigated, their data sets were used as regional base maps in the navigation adjustment process (see Section 3.2.4, *mbnavadjust*). The difference maps were produced by gridding the bathymetry data at the same latitude-longitude bounds and grid-cell resolution, and subtracting each of the prior grids from the 2022 grids with a Generic Mapping Tools (GMT) *grdmath* statement. For this report, differences between AUV data collected on this expedition and only the most recently collected bathymetry are included. The source bathymetry maps and difference maps are presented in the following sections, organized by feature name (Figure 3.11). Differences that developed in the intervening years are displayed such that areas that subsided are in cool colors of the color ramp, and areas that infilled or built up are in warm colors, and areas of little change are in greens. Note that data artifacts due to imperfect vehicle attitude bias correction or navigation adjustment, or impacts by poor weather on the ship data, are large relative to the signal at this scale. The fundamental limit to the interpretation of the differences is about 20 cm in the vertical dimension, and there are large artifacts and errors in these maps at this preliminary stage of the processing.

3.3.3.1. Shelf Edge Intact

The intact eastern shelf edge was surveyed on missions 20220830m1, 20220906m1 and 20220906m2. As the missions were contiguous along the eastern shelf margin (Figure 3.11), their navigation was adjusted together to become a region referred to here as “Shelf Edge Intact”. The western two 2022 AUV surveys were conducted over ground surveyed by MBARI AUVs in the years 2013 and 2017, on missions 20131002m1 and 20170910m1, however the most recent survey was collected by the ship CCGS Sir Wilfred Laurier in 2019. The terrain covered by the eastern mission, 20220906m1, had not been mapped by AUV before, but had been surveyed by the R/V Amundsen as part of the Arctic Net Project in 2010. The 2022 Mapping AUV bathymetry maps are presented in Figure 3.36 and Figure 3.37. The prior 2019 (Figure 3.38) and 2010 ship-collected bathymetry data (Figure 3.39) are shown at the same 2-m resolution and map scale as the AUV data. Comparisons of 2022 AUV missions with the prior data sets are presented in Figure 3.40 and Figure 3.41.

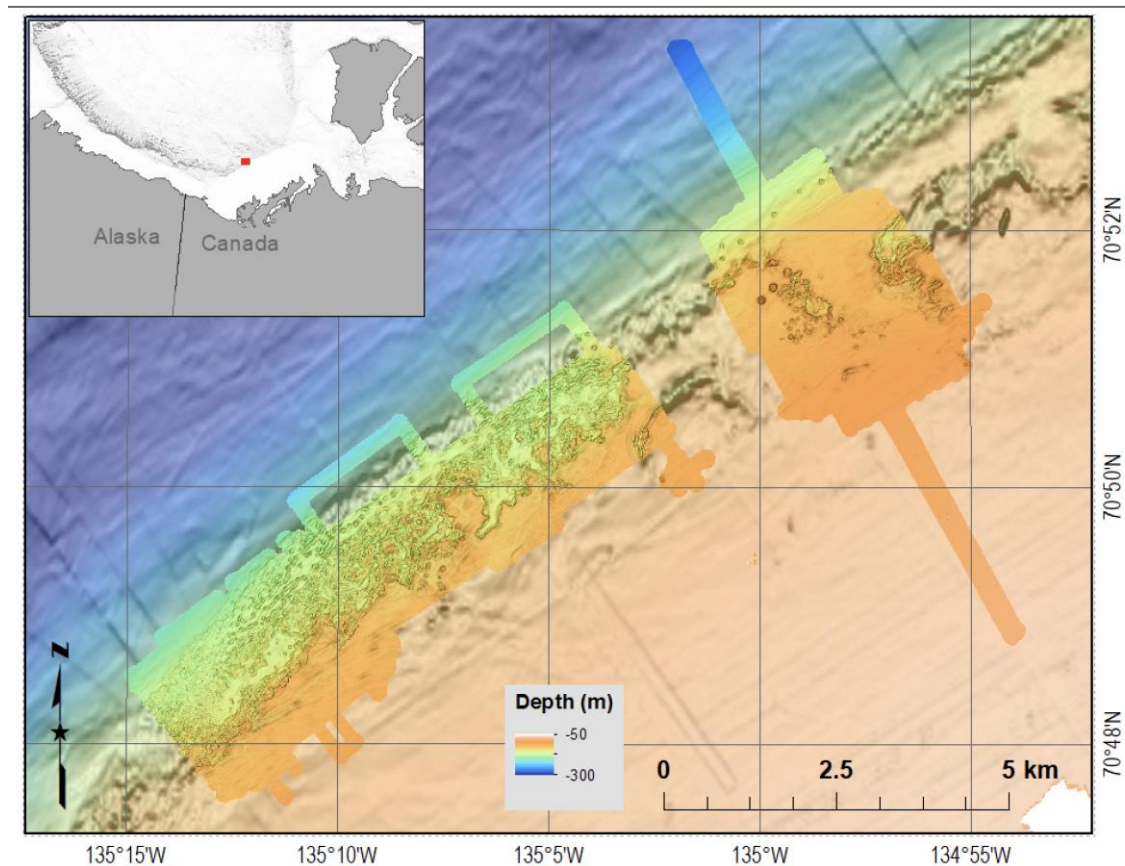


Figure 3.36. Missions 20220830m1, 20220906m1 and 20220906m2 are collectively referred to as “Shelf Edge Intact”. Their bathymetry is shown over bathymetry collected by the Arctic Net Project through 2010 and the CCGS Sir Wilfred Laurier in 2019. The inset map shows where the main map is located in the Canadian Beaufort Sea of the Arctic Ocean.

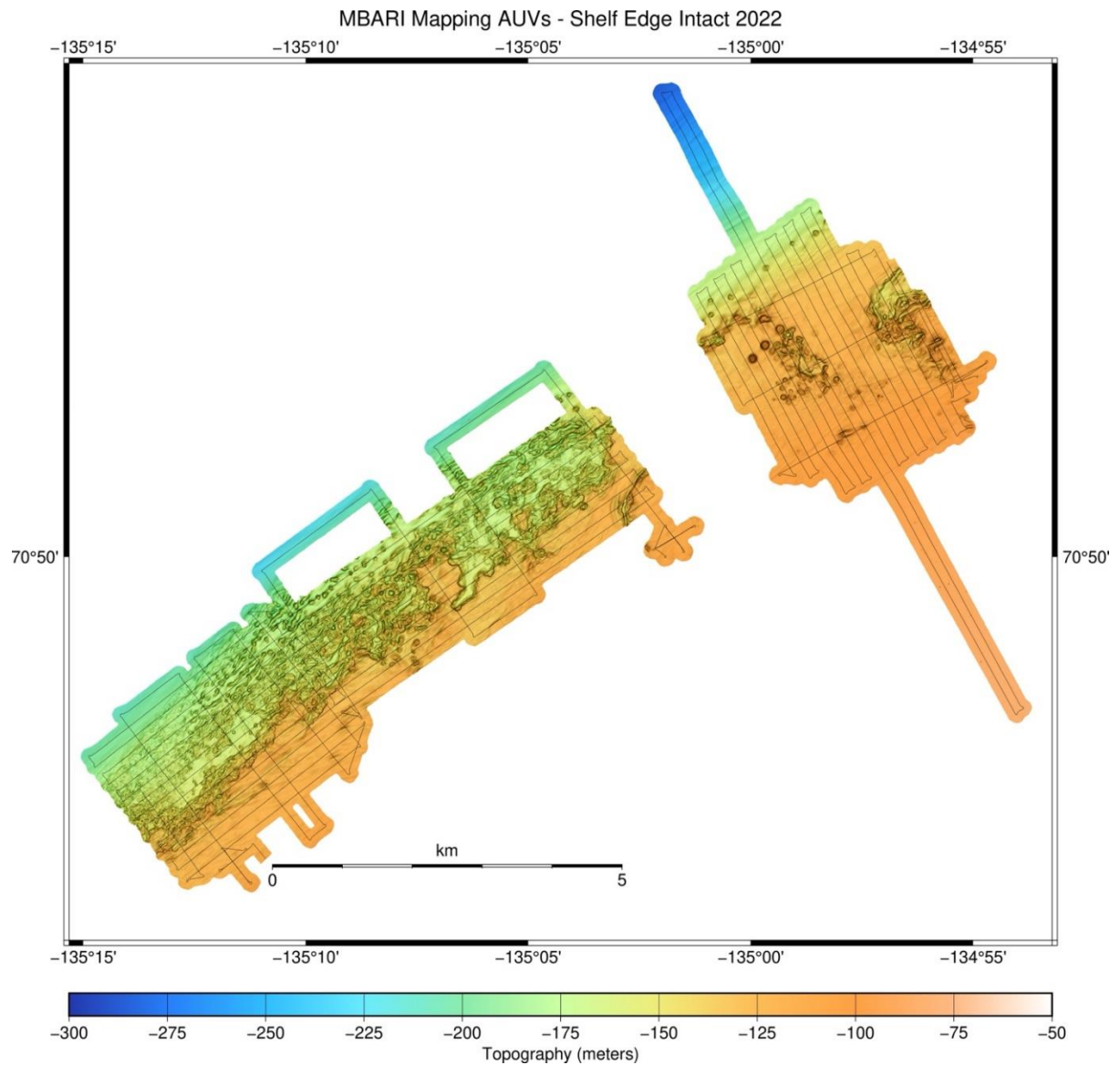


Figure 3.37. Bathymetry from AUV missions 20220830m1 (center), 20220906m1 (to the east) and 20220906m2 (to the west) with AUV navigation tracklines superimposed, gridded at 2-m horizontal resolution.

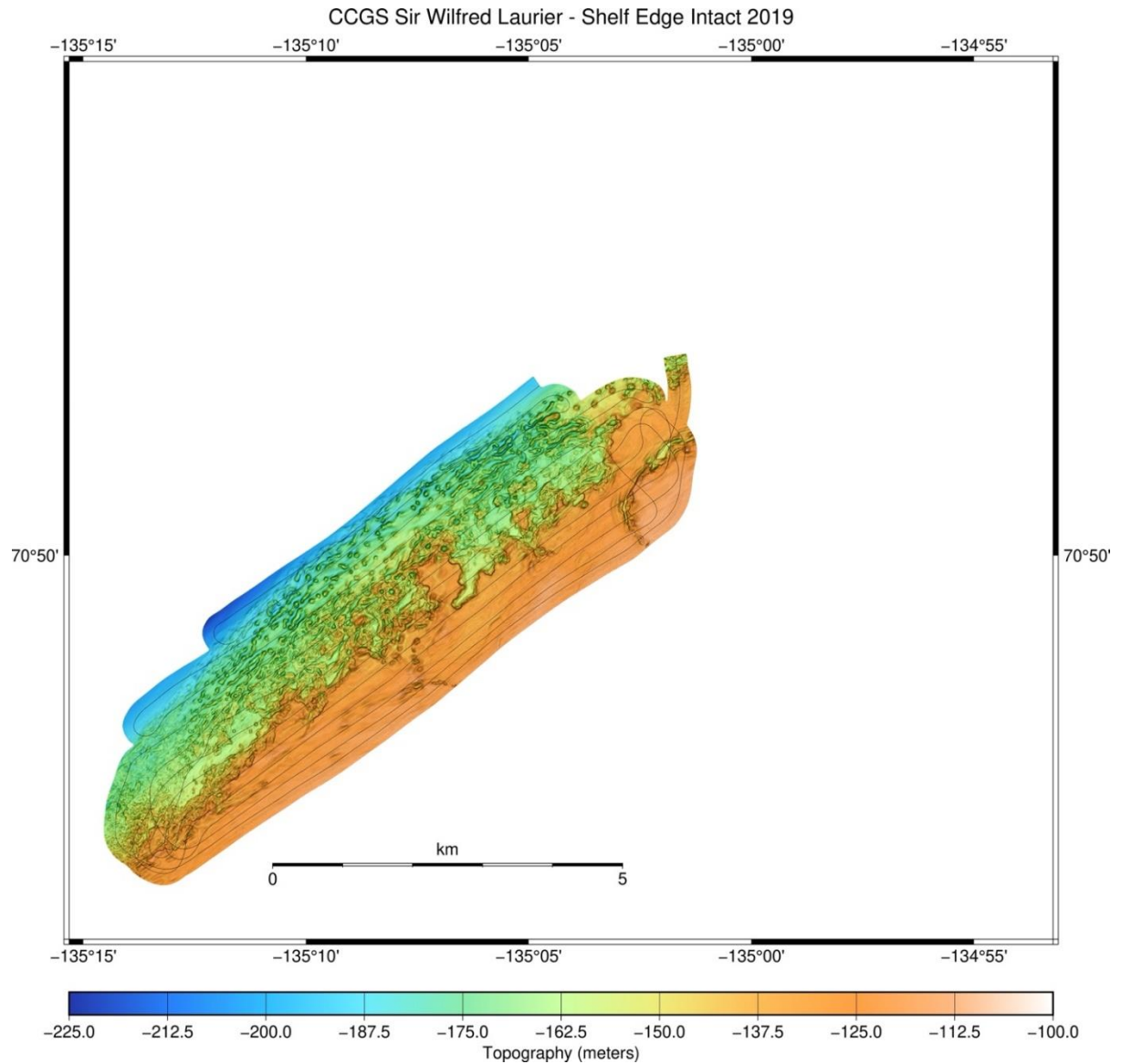


Figure 3.38. Bathymetry from the 2019 survey by the CCGS Sir Wilfred Laurier with its navigation tracklines superimposed, gridded at 2-m horizontal resolution, and shown at the same scale as Figure 3.37. Note that the area covered by AUV mission 20220906m1 was not included in this survey.

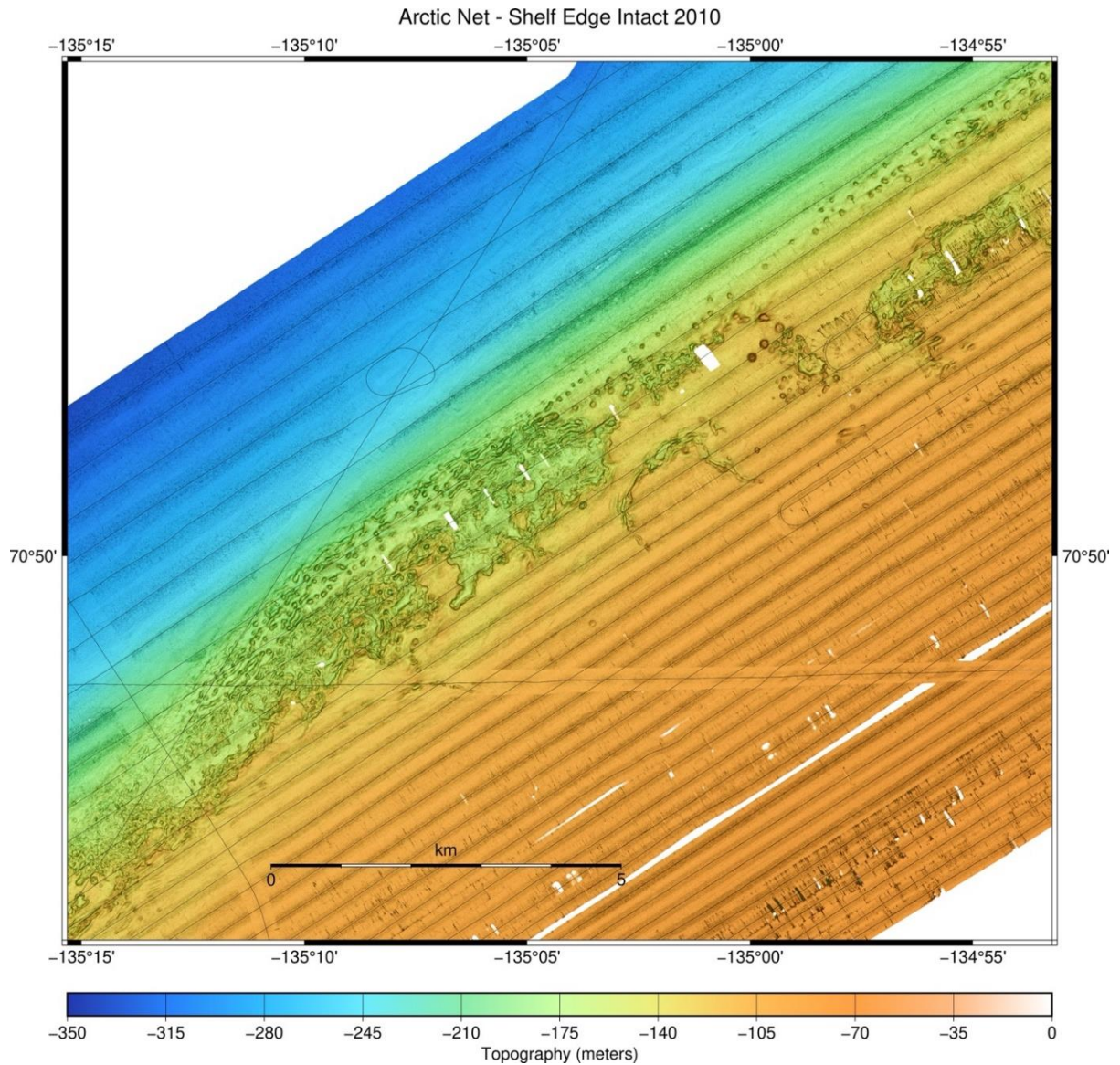


Figure 3.39. Bathymetry from the 2010 survey by the R/V Amundsen with its navigation tracklines superimposed, gridded at 2-m horizontal resolution, and shown at the same scale as Figure 3.37. All three 2022 “Shelf Edge Intact” AUV missions were conducted over ground covered by this 2010 survey.

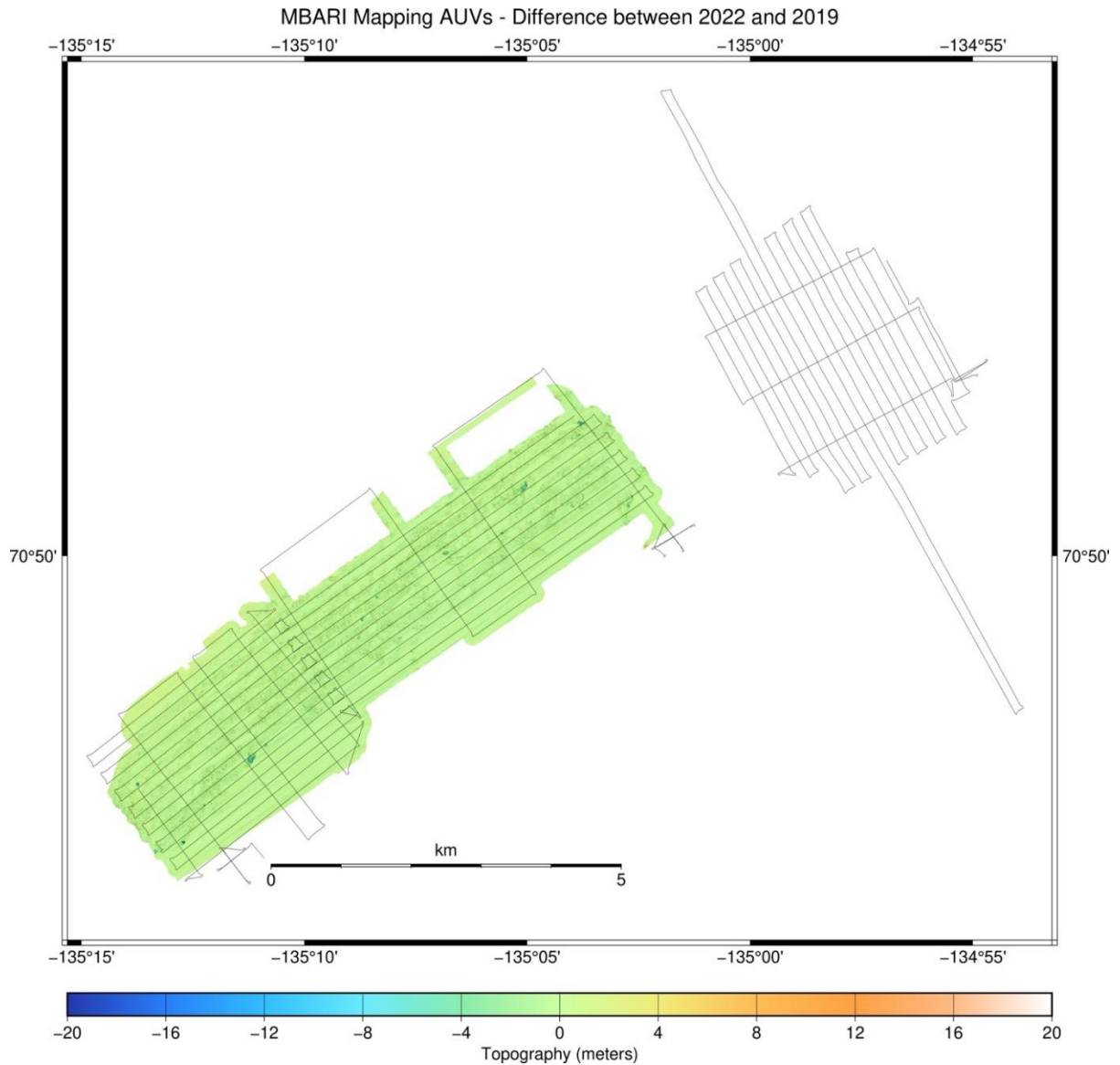


Figure 3.40. Difference in the Shelf Edge Intact area between 2022 AUV missions and the bathymetry collected by the CCGS Sir Wilfred Laurier in 2019, shown with AUV navigation tracklines superimposed and at the same scale as Figure 3.37. The difference maps are gridded at 2-m horizontal resolution, and the color ramp shows negative differences to -20 m in the cool colors and positive changes to +20 m in the warm colors, with no change as light green. As the ground under the eastern survey, 20220906m1, had not been covered in 2019, the difference grid results there are null.

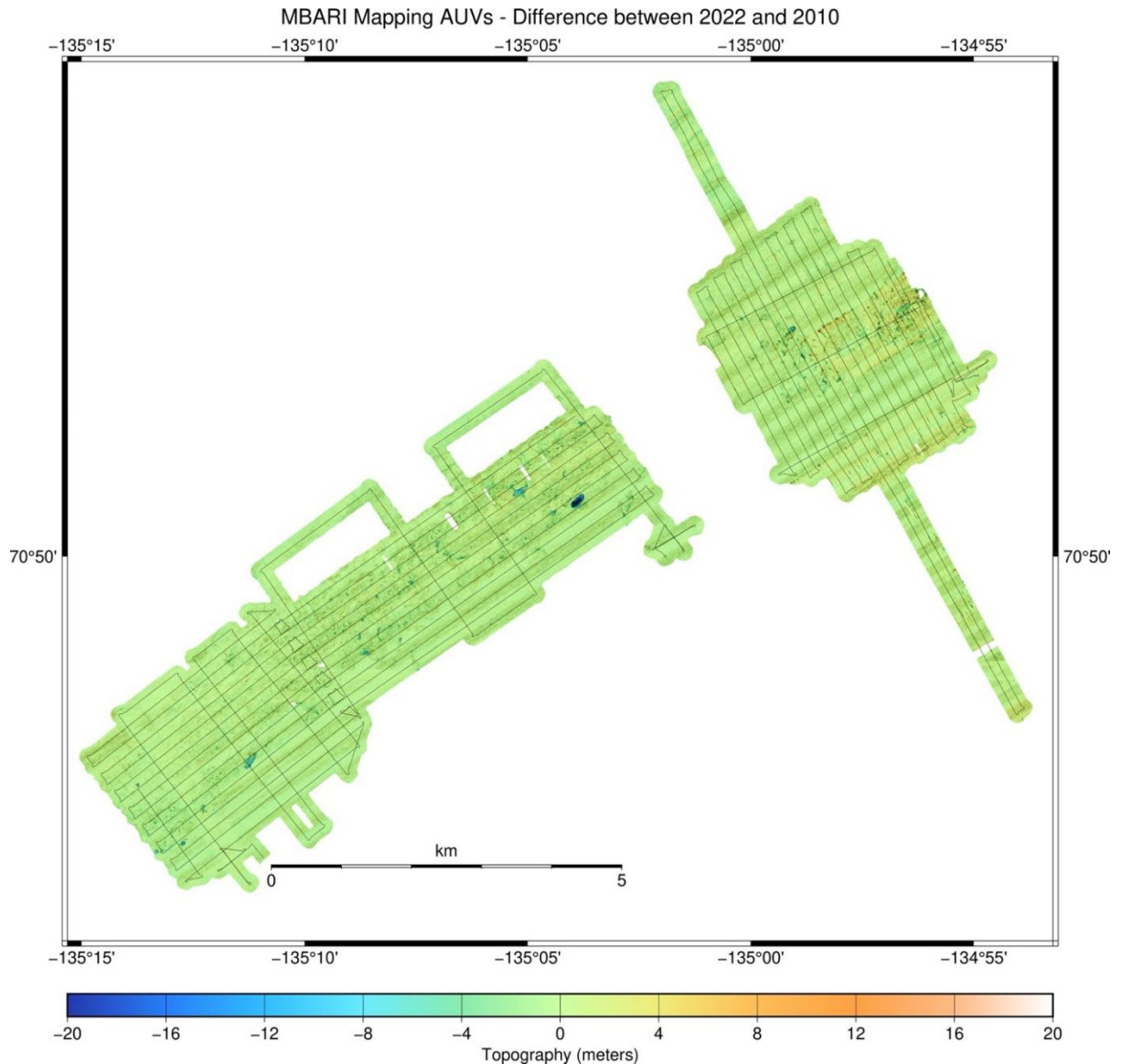


Figure 3.41. Difference in the Shelf Edge Intact area between 2022 AUV missions and the bathymetry collected by the R/V Amundsen in 2010, shown with AUV navigation tracklines superimposed and at the same scale as Figure 3.37. The difference maps are gridded at 2-m horizontal resolution, and the color ramp shows negative differences to -20 m in the cool colors and positive changes to +20 m in the warm colors, with no change as light green.

3.3.3.2. Shelf Edge Failed

The western-most AUV survey of 2022 was 20220901m1 on a slump in the margin of the Canadian Beaufort Shelf, in a region referred to here as Shelf Edge Failed. Prior AUV surveys of this feature were conducted in 2013 and 2016 on missions 20131007m1, 20160927m2 and 20160927m2, however 20160927m2 had little coverage that overlapped with the 2022 survey. All of the surveys were navigation-adjusted together, with ship-collected data as a reference grid, but only the 2022 and most recent (2016) AUV data are presented here, in Figures 3.42 through 3.44.

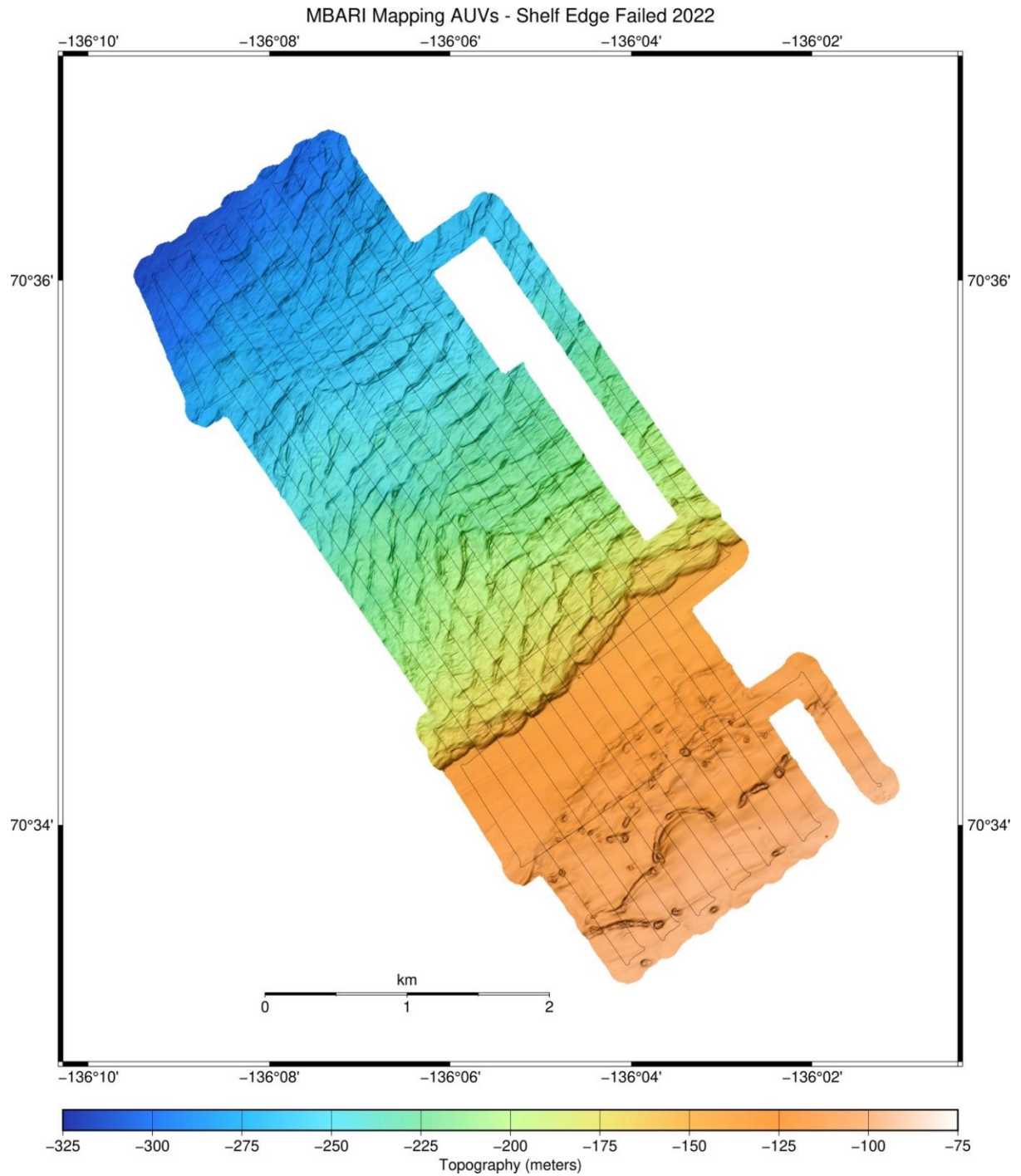


Figure 3.42. Bathymetry from 2022 AUV mission 20220901m1 with AUV navigation tracklines superimposed, gridded at 2-m horizontal resolution.

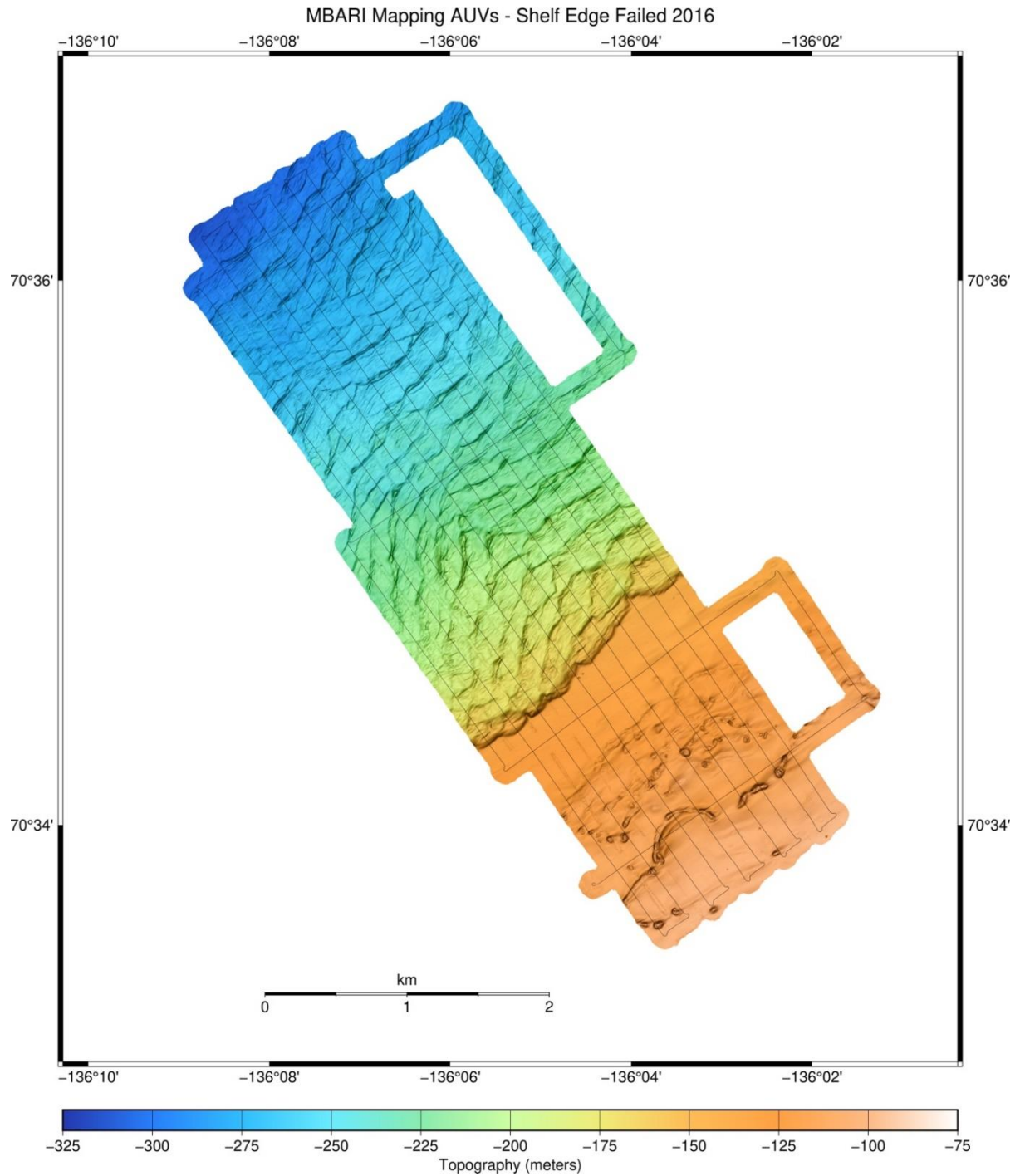


Figure 3.43. Bathymetry from 2016 AUV mission 20160927m1 with AUV navigation tracklines superimposed, gridded at 2-m horizontal resolution, and shown at the same scale as Figure 3.42.

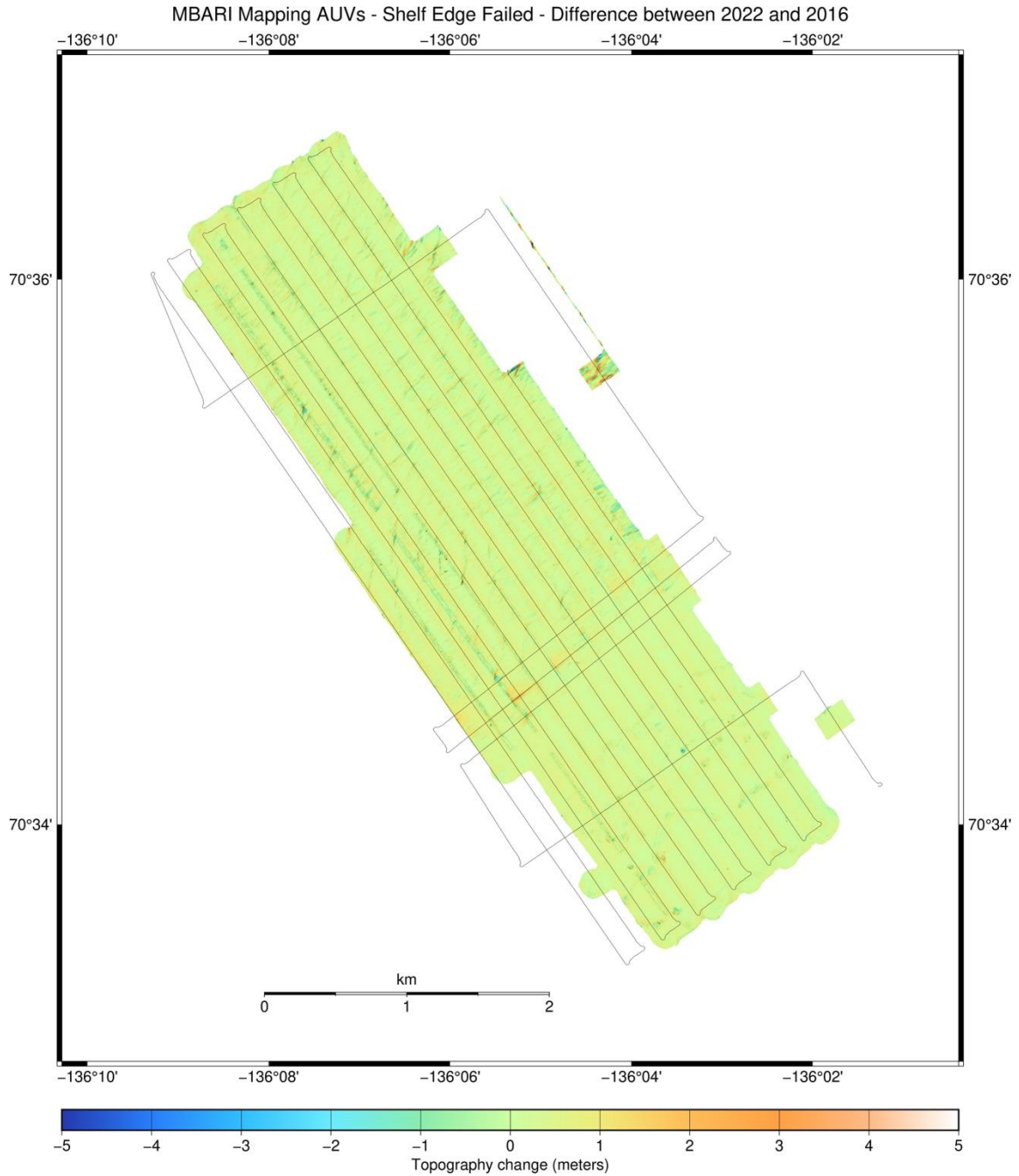


Figure 3.44. Difference in the Shelf Edge Failed area between 2022 and 2016 AUV missions, shown with AUV navigation tracklines superimposed and at the same scale as Figure 3.42. The difference map is gridded at 2-m horizontal resolution, and the color ramp shows negative differences to -5 m in the cool colors and positive changes to +5 m in the warm colors, with no change as light green.

3.3.3.3. 420 m Mud Volcano

Mission 20220902m1 was on a mud volcano at about 420 m depth. Prior AUV surveys of this feature were conducted in 2013, 2016, and 2017 on missions 20131005m1, 20160926m1 and 20170908m1. All of the surveys were navigation-adjusted together, with ship-collected data as a reference grid, but only the 2022 and most recent (2017) AUV data will be presented here, in Figures 3.45 through 3.47.

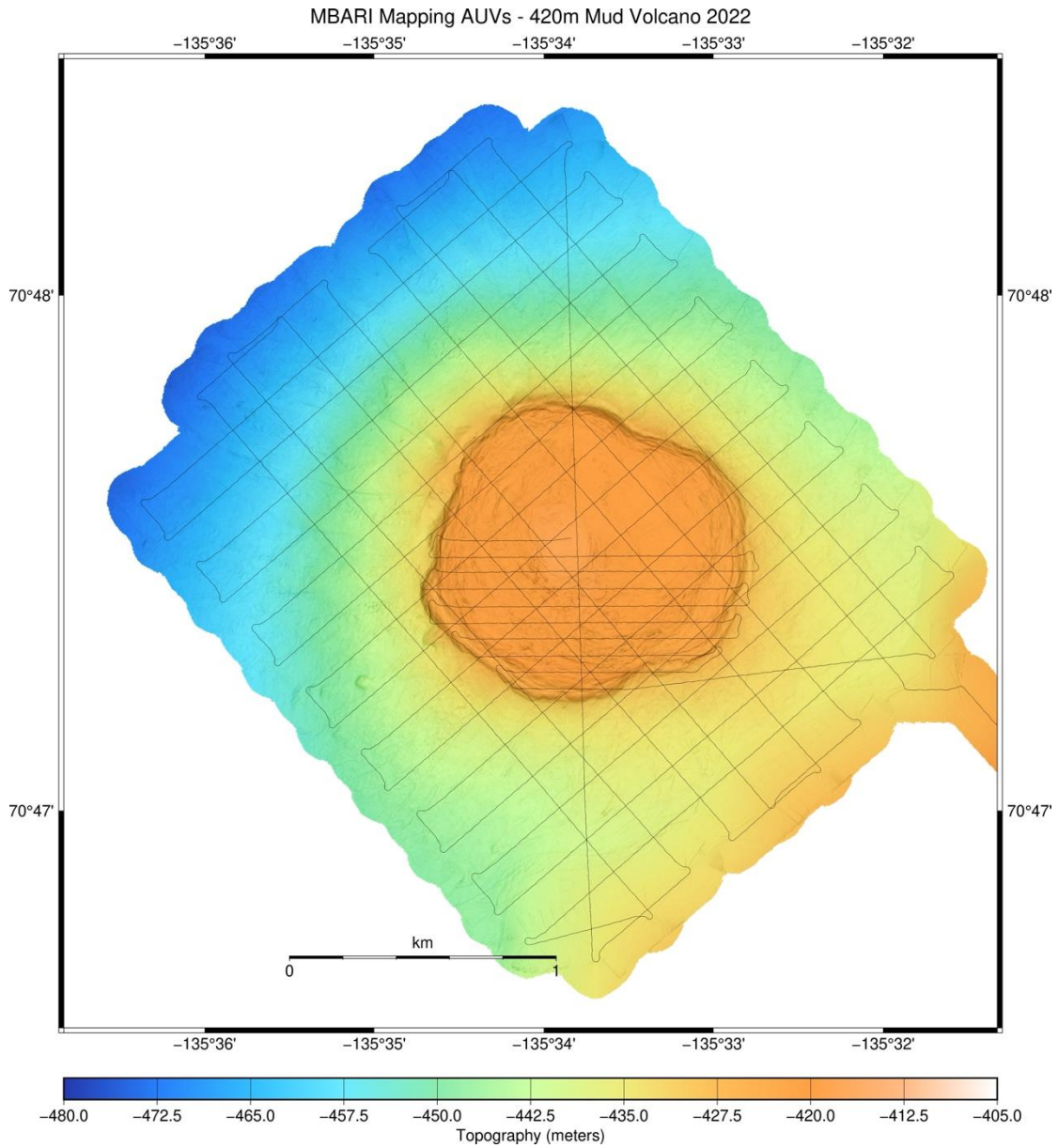


Figure 3.45. Bathymetry from 2022 AUV mission 20220902m1 at the 420 m Mud Volcano with AUV navigation tracklines superimposed, gridded at 2-m horizontal resolution.

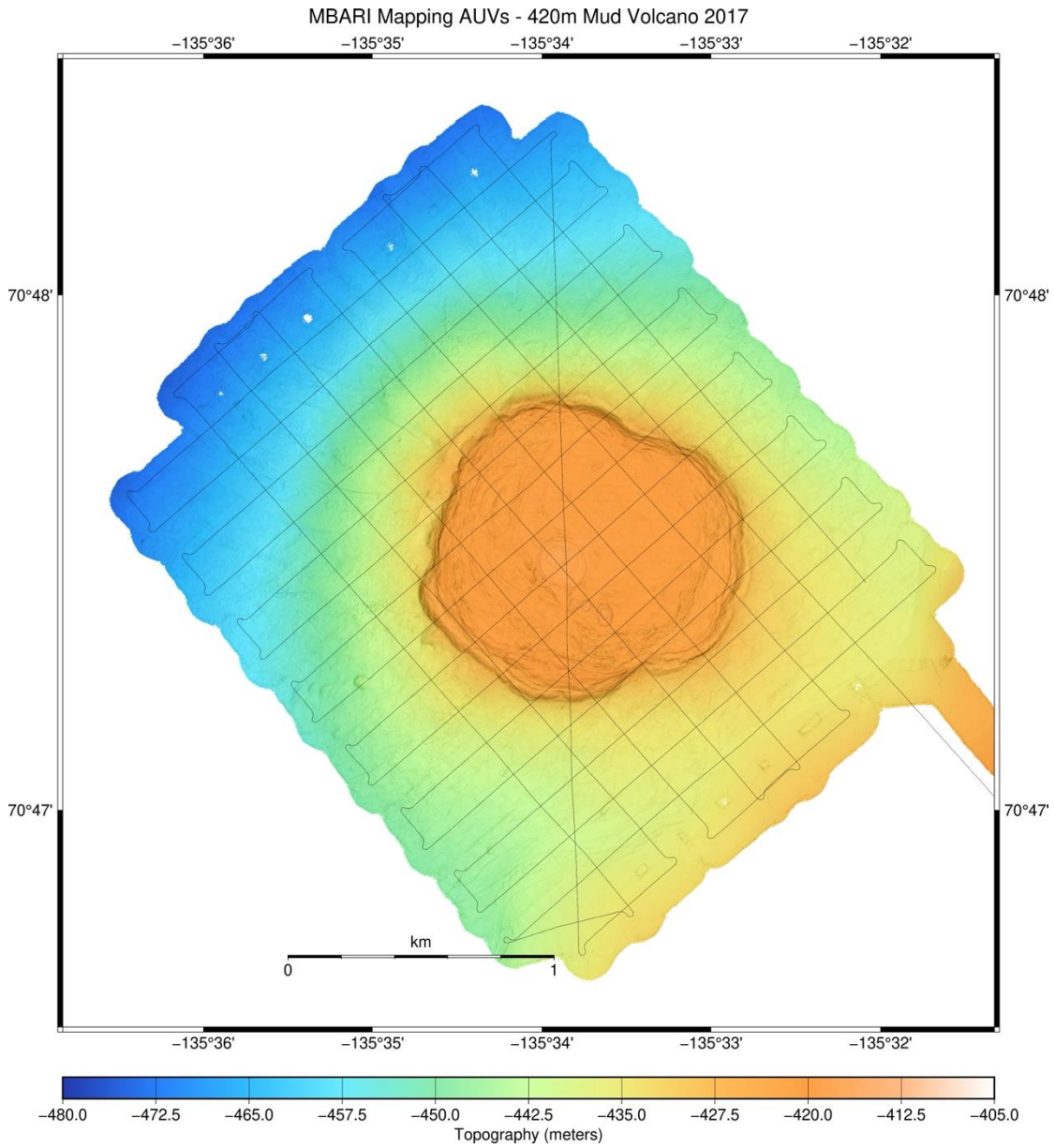


Figure 3.46. Bathymetry from the 2017 survey at the 420 m Mud Volcano, 20170908m1, shown at the same scale as Figure 3.45.

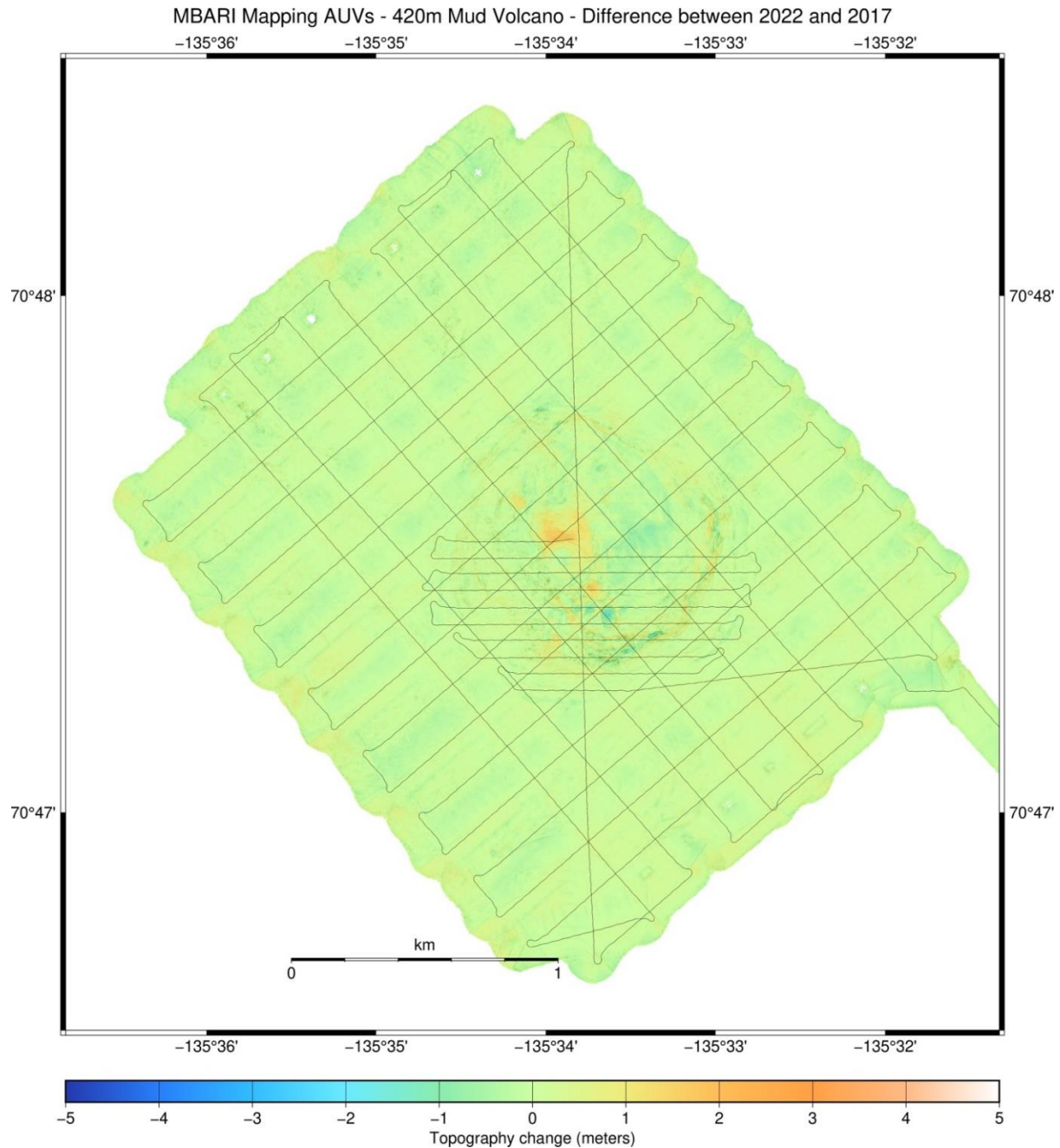


Figure 3.47. Difference in the 420 m Mud Volcano area between 2022 and 2017 AUV missions, shown with AUV navigation tracklines superimposed and at the same scale as Figure 3.45. The difference map is gridded at 2-m horizontal resolution, and the color ramp shows negative differences to -5 m in the cool colors and positive changes to +5 m in the warm colors, with no change as light green.

3.3.3.4. 740 m Mud Volcano

Mission 20220907m1 was on a mud volcano at about 740 m depth. Prior AUV surveys of this feature were conducted in 2013 and 2016 on missions 20131004m1 and 20160928m2. The surveys were navigation-adjusted together, with ship-collected data as a reference grid, but only the 2022 and most recent (2016) AUV data will be presented here, in Figures 3.48 through 3.50.

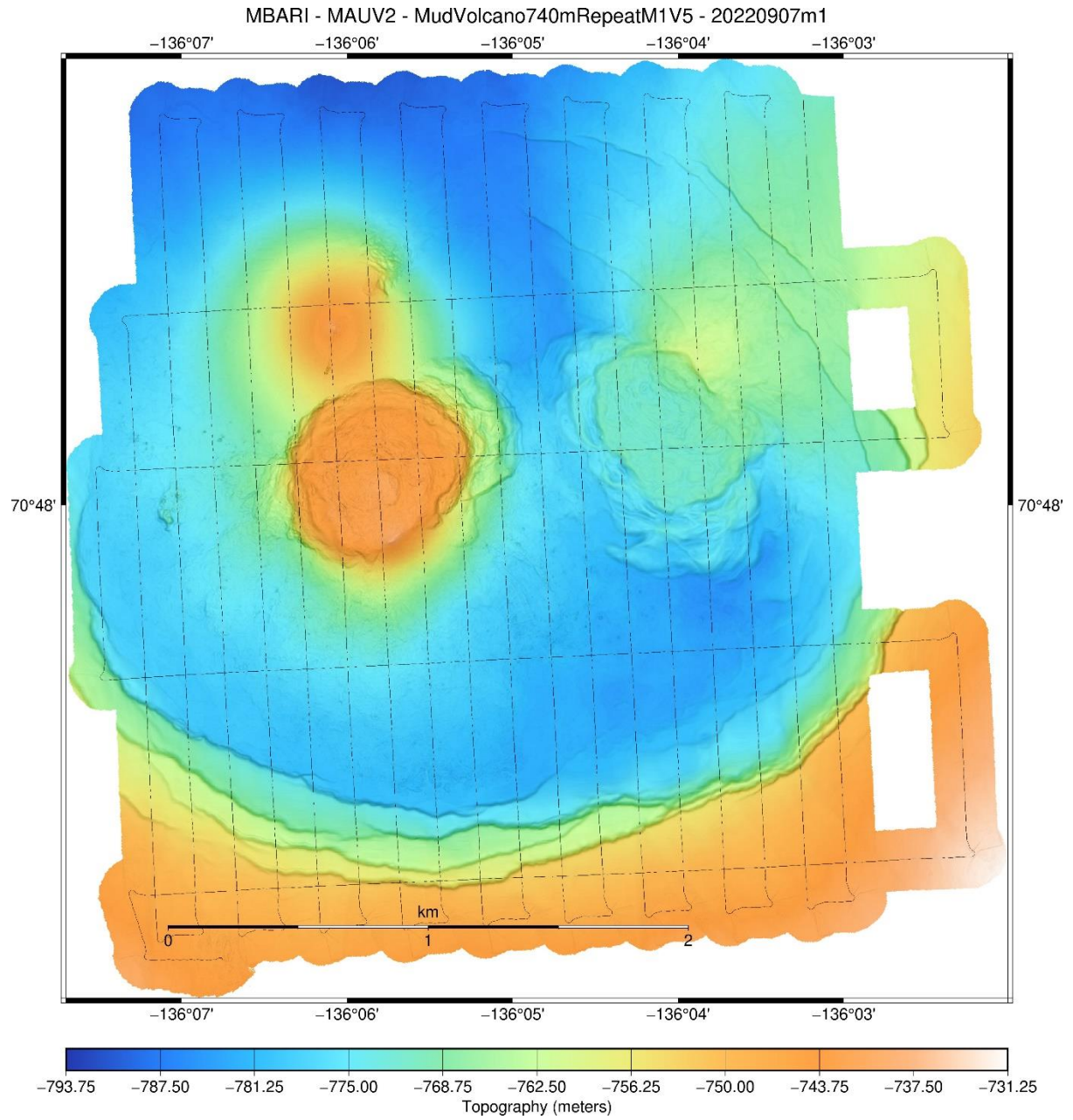


Figure 3.48. Bathymetry from 2022 AUV mission 20220907m1 at the 740 m Mud Volcano, gridded at 2-m horizontal resolution.

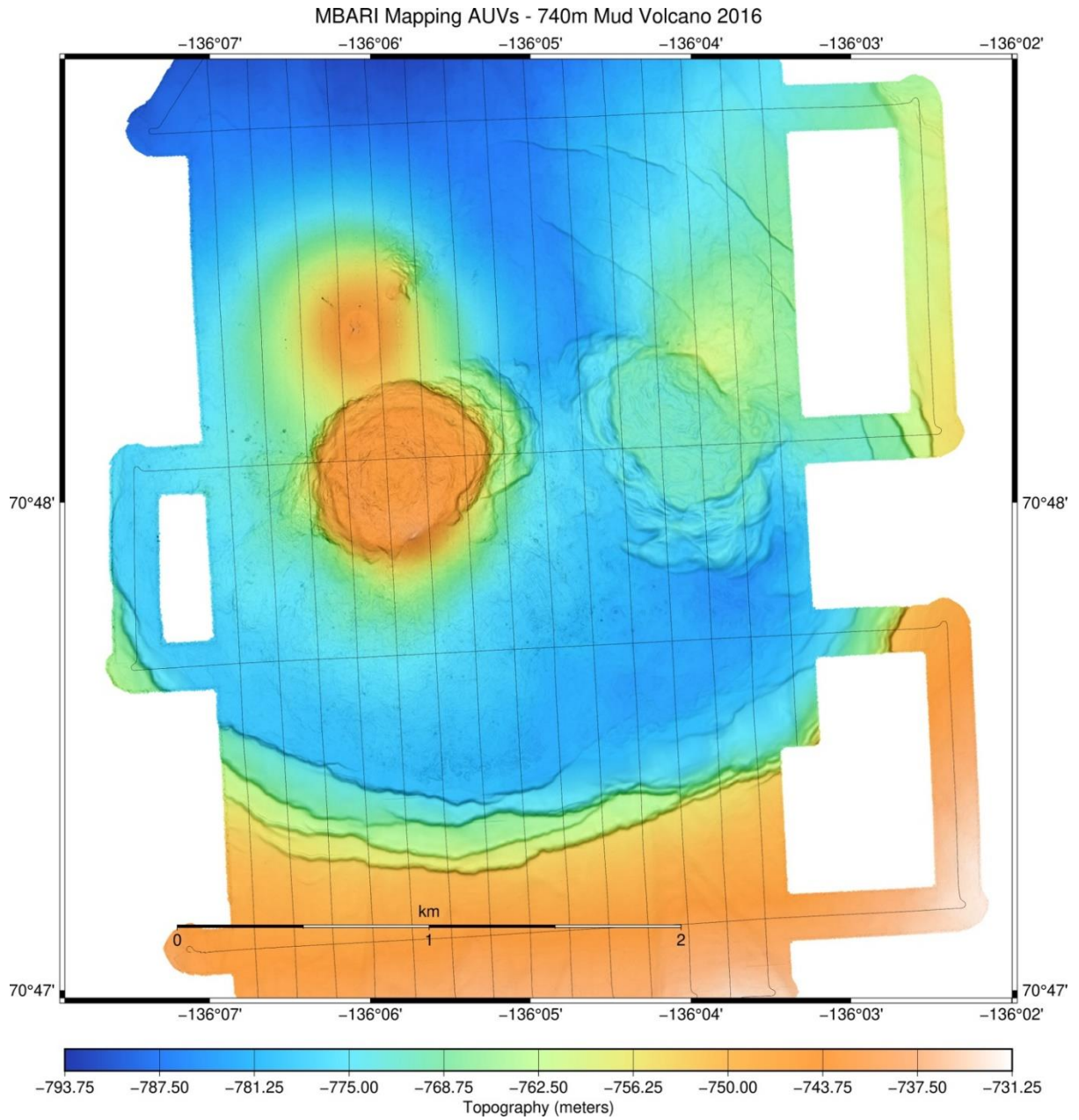


Figure 3.49. Bathymetry from the 2016 survey at the 740 m Mud Volcano, 20160928m2, shown at the same scale as Figure 3.48.

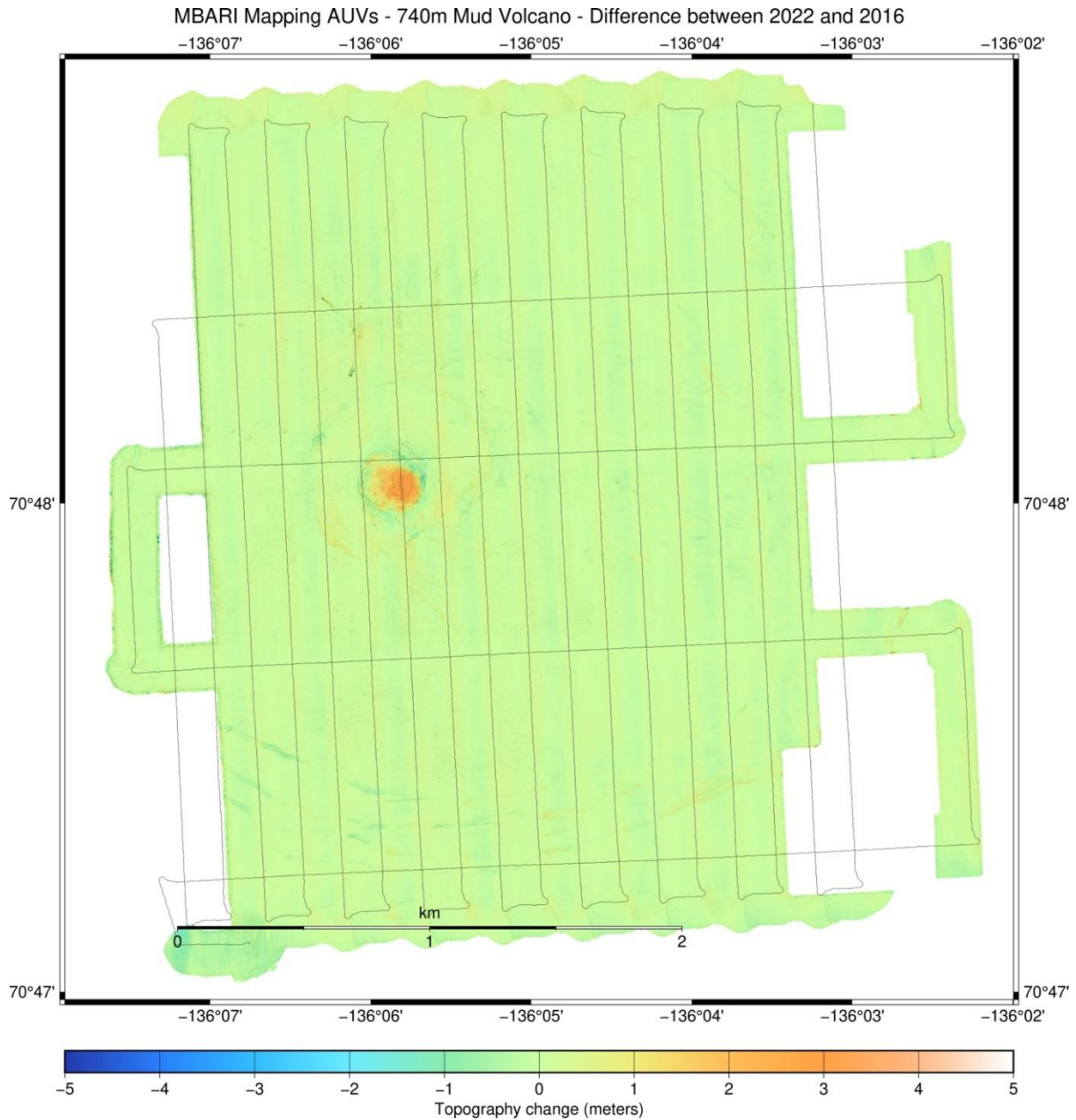


Figure 3.50. Difference in the 740 m Mud Volcano area between 2022 and 2016 AUV missions, shown with AUV navigation tracklines superimposed and at the same scale as Figure 3.48. The difference map is gridded at 2-m horizontal resolution, and the color ramp shows negative differences to -5 m in the cool colors and positive changes to +5 m in the warm colors, with no change as light green.

Acknowledgements

The AUVs were operated by Randy Prickett, Jordan Caress, Tanner Poling of the MBARI Autonomous Systems Group, and MBARI Electrical Engineer Eric Martin. Primary funding for the MBARI ROV and AUV operations was provided by the David and Lucile Packard Foundation, with supplemental funding provided by the US Naval Research Labs. We thank our Korean colleagues and the Captain and crew of the IBRV Araon for the opportunity to join them in exploring the geology of the Arctic Ocean.

References

- Caress, D.W., and Chayes, D. N. 1996. Improved processing of Hydrosweep DS Multibeam Data on the R/V Maurice Ewing, *Marine Geophysical Researches*, 18, 631-650.
- Caress, D.W., Thomas, H., Kirkwood, W. J., McEwen, R., Henthorn, R., Clague, E. A., Paull, C. K., Paduan, J. and Maier, K. L. 2008. High-Resolution Multibeam, Sidescan, and Subbottom Surveys Using the MBARI AUV D. Allan B. Marine Habitat Mapping Technology for Alaska, J.R. Reynolds and H.G. Greene (eds.) Alaska Sea Grant College Program, University of Alaska Fairbanks.
- Caress, D. W., Chayes, D. N. and Ferreira, C. 2022. MB-System Seafloor Mapping Software: Processing and Display of Swath Sonar Data. Version 5.7.9, Open source software.

ARA13C Cruise report

Chapter 4. MiniROV Diving

C. K. Paull, E. Lundsten, D. W. Caress, R. Gwiazda, D. Graves and F. Flores

4.1. Introduction

During ARA13C a detailed visual inspection and precise sampling of the seafloor was conducted on 9 dives of MBARI's MiniROV. The MiniROV dives were all located in areas where MBARI's mapping autonomous underwater vehicles (AUV) had surveyed in previous years, in areas planned for AUV mapping in this cruise in 2022, or along multichannel seismic lines to provide ground truth calibration. These observations provide a basic understanding of the seafloor conditions at these sites.

4.2. MiniROV System

4.2.1. MiniROV Specifications

MBARI's MiniROV is a portable, low cost, 1,500-meter inspection class system compact fly away ROV capable of operating with a small dedicated crew (2-3 people) on ships of opportunity around the world. The MiniROV was designed and built at MBARI specifically for this purpose. The vehicle is capable of light duty work functions such as limited sampling, video transects, instrument deployment and recovery (with a 120-pound instrument payload), and is outfitted with the following suite of core instruments: HD camera, scanning sonar, lasers, LED lights and CTD (Table 4.1). In addition, the vehicle has bolted on tool skids for mission specific payload and sampling requirements.

Table 4.1 MiniROV Specifications & Instrumentation

Depth rating = 1500 meters
Vehicle type = Electric
Dimensions = ~ 48" L x 35" W x 24" H
Weight in air = ~ 800 pounds
Science payload = 120 pounds
Power Requirements = 3 phase 208VAC (5kW)
Thrusters = (6x) ~.75hp electric DC brushless

Auxiliary instrument power & available voltages

- ~1kW
- 240, 48, 24, 12, and 5 VDC

Auxiliary Video & Data

- (2) spare single mode fibers
- RS-232 serial ports
- (2) spare video channels

Core Instrumentation

- Insite Mini Zeus HDTV video camera
- (2) DSPL HDTV cameras
- Insite IT1000 low light B&W camera
- Imagenex 881-A scanning sonar
- CTDO
- (6) Main LED lights (5,000 lumens each)
- 5 function ECA manipulator arm
- ROWE 1.2 MHz DVL
- Valeport Depth/Altimeter sensor
- Camera/light tilt platform
- PNI 3-axis digital compass
- Swing arm
- Sampling drawer

ROV Auto Functions

- Auto Depth
- Auto Heading
- Observation mode (MBARI mode)
- Advanced Navigation mode (Dynamic station keeping)

Smart Clump

- DSPL HDTV camera
- Camera tilt platform
- Auto heading (2) Thrusters
- PNI 3-axis digital compass
- LED light (5000 lumens)
- Niskin water sampler
- O2 sensor
- Valeport Depth/Altimeter sensor
- Analog video camera
- Spare RS-232 serial channels

Umbilical = 1,700 meter .625" OD

Umbilical Winch

Aluminum construction
 Variable speed Electric drive motor
 Power requirements = 220VAC (4Kw)
 Dimensions = ~ 60"x 60"x60"

4.2.2 MiniROV operations off the IBRV Araon

The MiniROV control room used on this expedition was built within a 8' by 20' shipping container. The container was designed to also carry two AUVs during the pre-and post-cruise shipping. The container was outfitted to also serve as a workshop to coordinate AUV operations. The control room was positioned on the aft deck of the IBRV Araon in Incheon for the transit and first legs of the 2022 expedition.

Two additional 20' shipping containers shipped to Korea contained the ROV, tether winch, and eight ROPAKs with assorted miscellaneous equipment necessary for both AUV and ROV operation as well as the science gear needed to process samples and to make measurements on shipboard. The contents of these two containers were unloaded in Incheon and stored out of the weather in various places on the IBRV Araon. These components were then used to prepare the ROV during the transit from Barrow, Alaska to the operating area in Canada.

The MiniROV was launched off the IBRV Araon's starboard rail, forward of the main crane (Figures 4.1, 4.3 and 4.4).

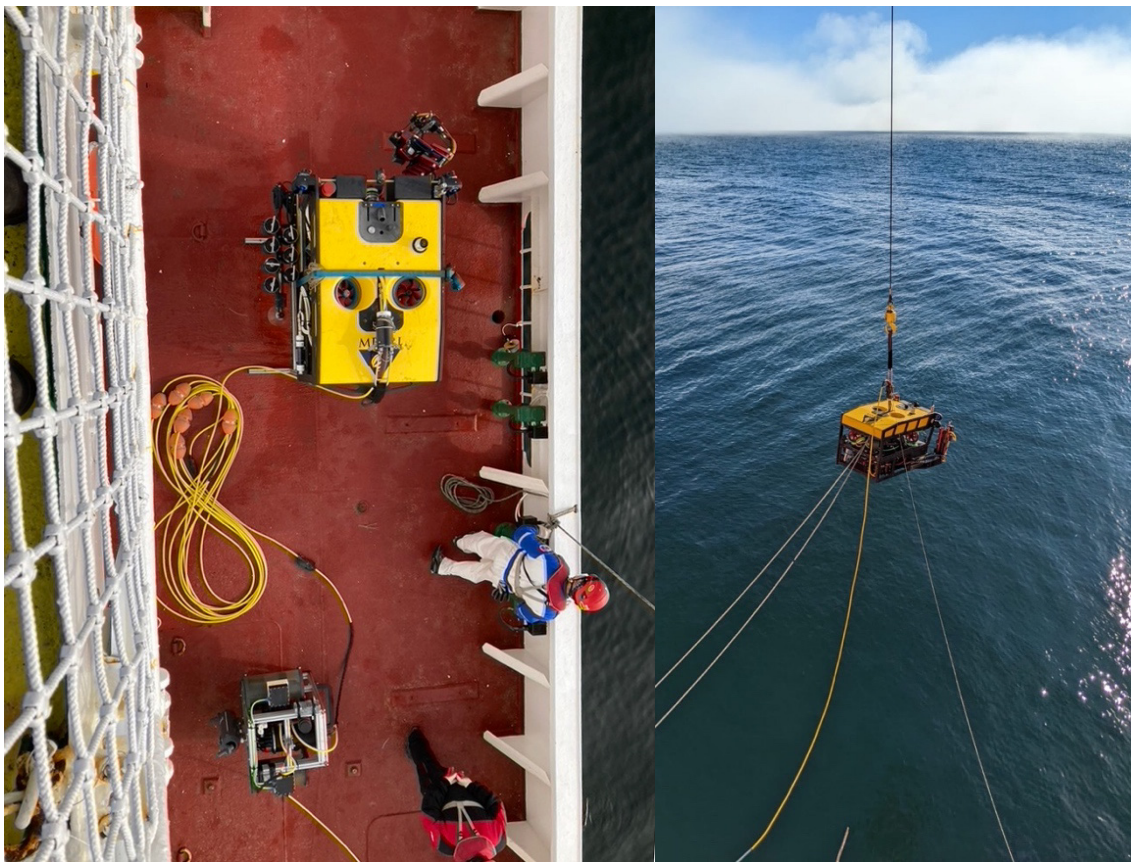


Figure 4.1. Left: MiniROV, coiled tether with orange floats, and smart clump weight ready to launch over the starboard rail. Right: MiniROV getting launched with tether and tag lines stretched to the ship. Note the red manipulator arm on the right, the quiver of push cores is stowed on the opposite side of ROV. Photos courtesy of Monterey Bay Aquarium Research Institute.

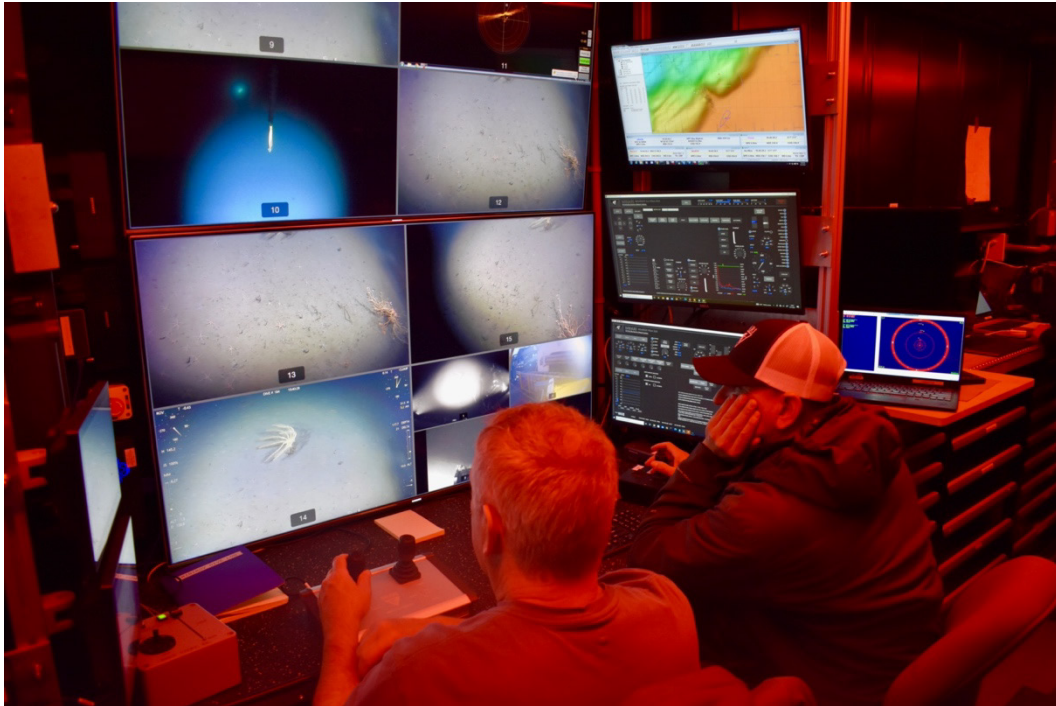


Figure 4.2. Image shows the ROV command center in the control room. Note the multiple screens showing the main digital video image, video from multiple small HD cameras, USBL tracking displays, ROV control interface, and the scanning sonar display. Photo courtesy of Monterey Bay Aquarium Research Institute.

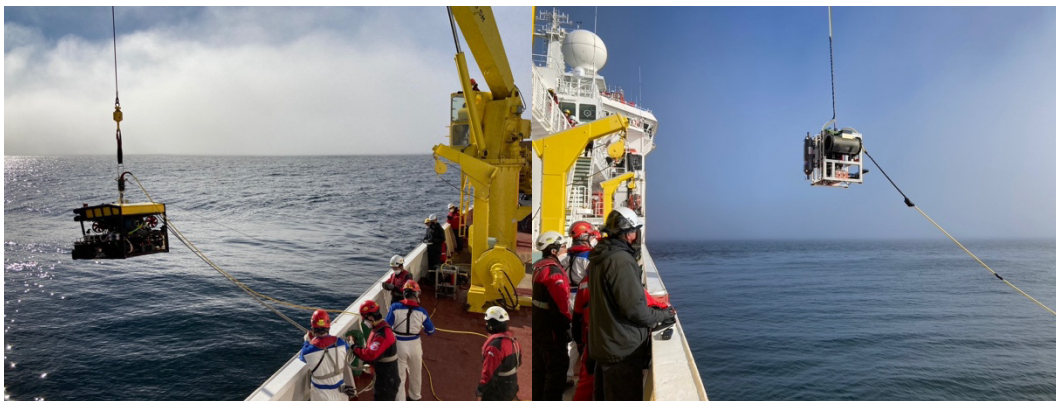


Figure 4.3. shows images of the MiniROV and smart clump weight being deployed. The ROV is lifted using a whip from the crane and connected to the top of the ROV using a latch, which will not release under a load. However, when the ROV is floating in the water, the latch is released using a pull string. Photos courtesy of Monterey Bay Aquarium Research Institute.



Figure 4.4. Photos showing the smart clump (cube shaped device) and turning block (wheel and cable) on the deck used to feed the tether to the ROV. The winch is shown in the foreground with the turning block suspended from the crane in the background. After the ROV is launched the tether between the ship and the clump weight is passed through the turning block suspended below the crane. The winch was operated using control box with instructions communicated via hand held radio from the control room. Photos courtesy of Monterey Bay Aquarium Research Institute.

4.2.3. ROV data types

Video images were recorded continuously during all dives (Table 4.2, Figure 4.2). The video usually has two red dots on the images. These are from parallel laser beams, which are 13.49 cm apart, and provide a scale bar independent of the zoom on the camera.

Detailed seafloor sampling during the ARA13C cruise was achieved using the mechanical manipulator arm on the MiniROV (Table 4.3). The arm allowed solid objects to be picked up off the seafloor. Samples were placed in a retractable drawer to ensure secure transit and recovery.

The MiniROV is also equipped to take up to seven push cores on each dive. The core tubes are carried in quivers mounted onto a swing arm. The swing arm is stowed against the port side of the ROV during normal operations but is swung out in front of the ROV into the field of view and in reach of the ROV's mechanical arm when collecting samples. The push core tubes are 20 cm long, and 8 cm in diameter. Porewater and sediment samples were sub-sampled from the cores after each dive and tubes were re-used. In order to ensure unique sample names, the samples are labeled with both MBARI's ROV dive number (i.e., M182) and the core tube number (PsC-3).

The MiniROV carried a temperature probe, mounted on the manipulator arm so the probe can be positioned over an area of interest. When actuated, the probe advances up to 30 cm into the sediment. This probe has a temperature range of -3.00 to + 24.00°C.

The ROV also carried a CTD sensor built into the vehicle body and a CT sensor attached to the temperature probe on the manipulator arm. The data from the CT sensor on the arm was only logged occasionally.

For this expedition a system for extracting Radium (Ra) from bottom waters was installed in the ROV. This system consists of a peristaltic pump that is turned on when the ROV was on the bottom and off where the vehicle left the bottom. The pump passed 1.5 liters per minute through a canister filled with MnO₂-coated fibers that efficiently extract the Ra from the waters

flowing through the canister. Subsequently, the activity of ^{223}Ra , and ^{224}Ra scavenged on the fibers are measured in a delayed-coincidence counter system (Moore and Arnold, 1996). The ROV was capable of collecting two samples per dive.

4.3. Results / Highlights

4.3.1. Summary of MiniROV dive sites

The main objective of the ROV program was to investigate areas that have experienced large morphological changes over the course of a few years along the shelf edge (Figure 4.5). All ROV sites along the shelf edge were first surveyed with multibeam sonars in 2010 by the CCGS Amundsen. The morphological changes are revealed by comparing repeated multibeam mapping surveys covering the same areas. The survey comparisons include surveys that were conducted as long as 12 years apart and as short as 3 years apart. The mapping platforms are surface-ship multibeam systems and high resolution autonomous underwater mapping vehicles (AUVs). The morphological changes expressed as newly formed depressions or as the lateral retreat of scarps. It is hypothesized that the morphological changes are due to the melting of relict permafrost at depth. Bathymetric surveys conducted during this cruise (ARA13C) allowed the detection of newly developed depressions over the last three years.

The depressions were colloquially referred to with shorthand names, which will be used throughout this chapter. ROV-01/M182 was in the depression called “Giant Hole” which was identified by comparing 2010 and 2019 surveys, and discussed in Paull et al., 2022. ROV-02/M183, was at a neighboring depression, called “Old Hole”, which was surveyed three times in the period 2010-2022 and showed no changes. ROV-03/M184 was below and across the headwall of a landslide scarp along the shelf edge where a suspected depth change turned out to be an artifact in the mapping data. ROV-04/M185 was in the “Ice hole”. This site was revealed by comparing the AUV survey conducted in this cruise (ARA13C) with the surface ship bathymetry collected by CCGS Sir Wilfred Laurier three years earlier in 2019. This dive was the first time ever that permafrost ice was discovered exposed in an underwater outcrop. ROV-05/M186 explored the “Collapse Ridge Hole”, a ridge that became a depression between 2019 and 2022. ROV-07/M188, was at a site named “Station 11”. At this site ice resembling the ice observed in ROV-04/M185 was recovered from a gravity core. During this dive several exposures of ice at the bottom of a scarp at approximately the same depth were discovered. ROV-08/M189 explored two PLFs located on the rim of an existing depression along a seismic line collected by a previous expedition of the IBRV Araon. Attempts were made during this dive to find the source of water column anomalies observed in the echosounder of the ship during this cruise (ARA13C).

There were two dives that pursued other objectives: ROV-06/M187 was on an active mud volcano at 420 mwd, that has been repeatedly mapped with an AUV since 2013, and showed an upwards expansion of 2.5 m at its center since 2019. This dive located the sites where a thermal probe pierced the volcano in three tests conducted during this cruise to measure heat flow in the mud volcano. ROV-09/M190 was the deepest dive at 890 mwd. This dive was at the “890 m Orange Mounds”. Shimmering water was seen emanating from one of the many orange mounds protruding from the seafloor at around 889 mwd, revealing the site of a deep-water spring along the slope.

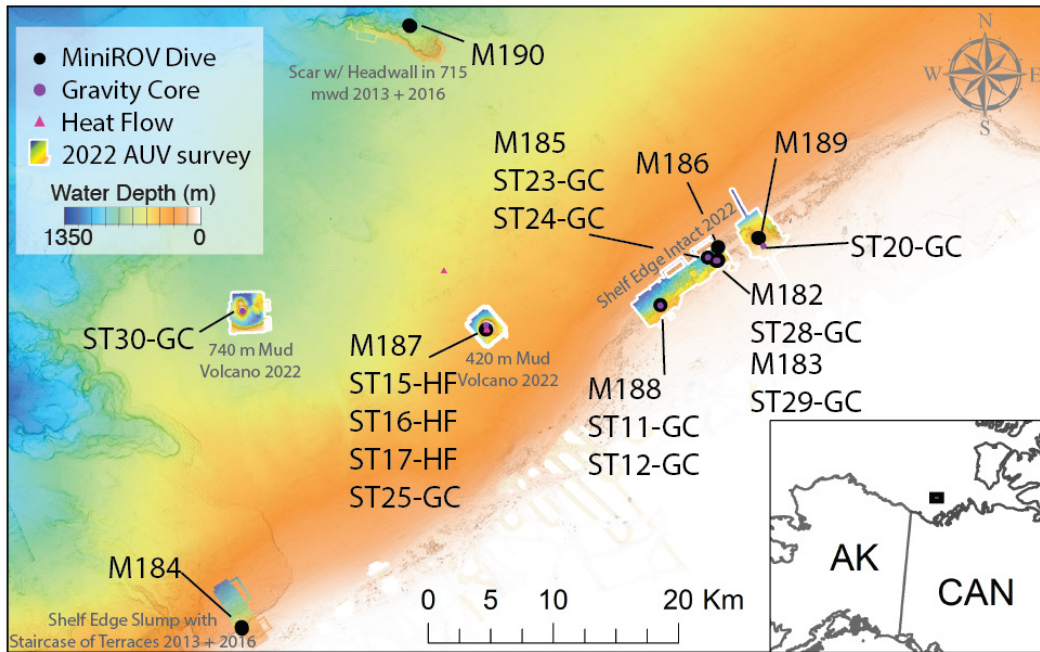


Figure 4.5. Map with the locations of MiniROV dives conducted during ARA13C in 2022, of gravity core and heat flow stations, and names of AUV mapping surveys.

4.3.2. ARA13C ROV-01

MBARI Dive M182 Tuesday August 30th, 2022

The objective of this dive is to explore the depression discovered by comparing the surface-ship bathymetry surveys conducted by CCGS Amundsen in 2010 and by the CCGS Sir Wilfrid Laurier in 2019 (Figure 4.6). The AUV survey conducted on this expedition indicates nominal change between 2019 and 2022.

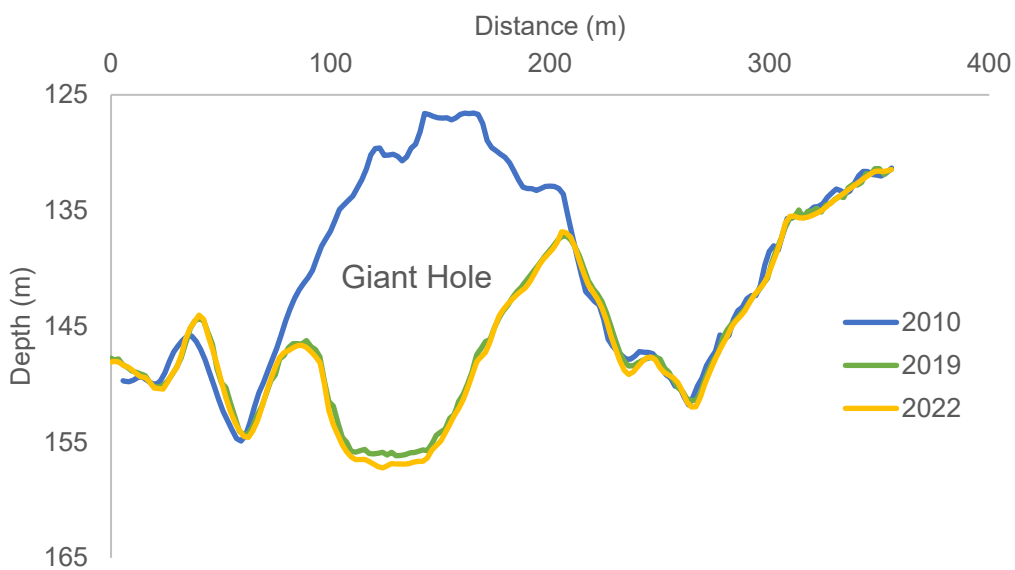
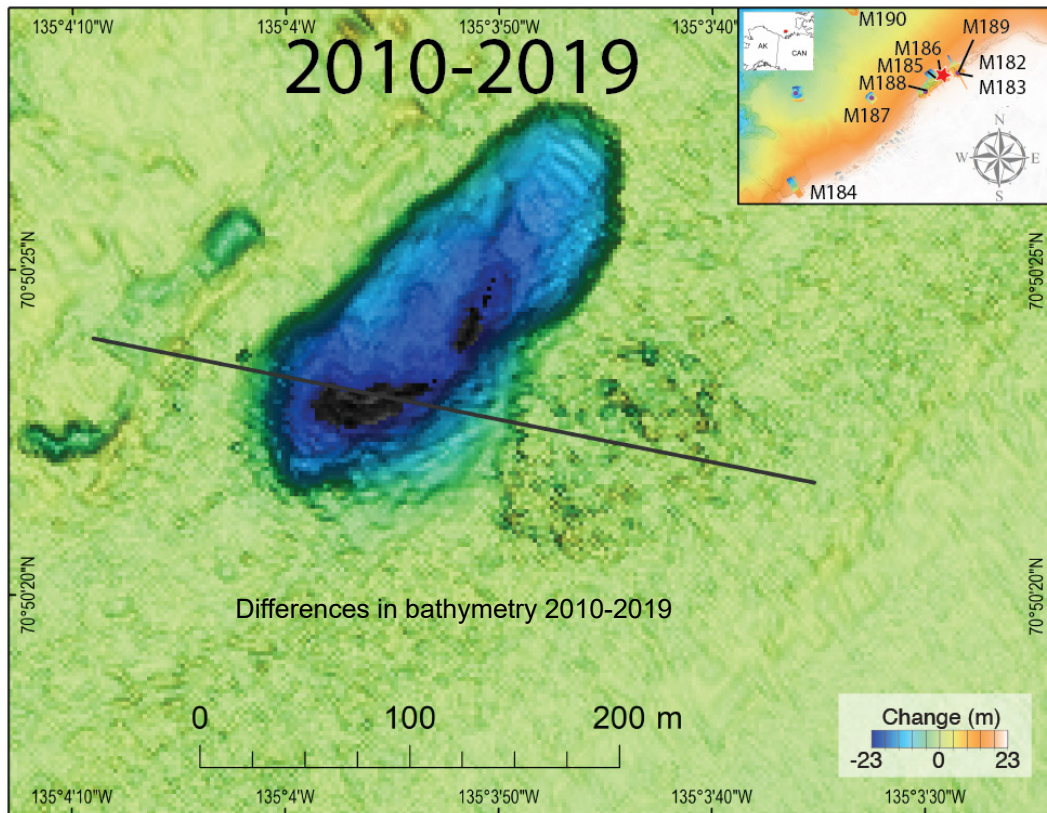


Figure 4.6. Differences in bathymetry 2010-2019 illustrated in map and profile views.

The location of this dive is colloquially referred to as the “Giant Hole”, and is described in Paull et al., 2022, PNAS paper.

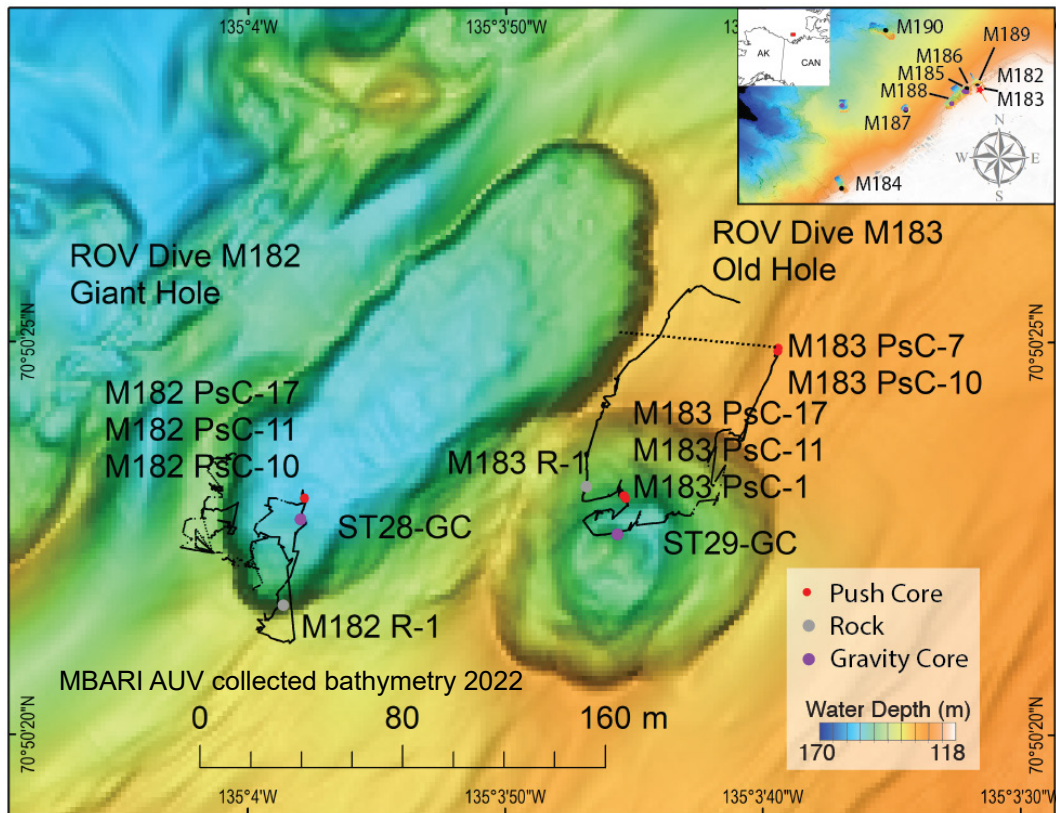


Figure 4.7. MBARI AUV collected bathymetry 2022 with details of Dives M182 and M183

The ROV reached bottom at 154 mwd along the sloping SW side of an oval shaped hole (Figure 4.7). The slope was composed of scattered clay clasts and numerous brittle stars. Upslope from this location towards west, north-west, the slope became increasingly steep, reaching $>60^\circ$. It was composed of an undraped massive gray surface, apparently broken along conchoidal fractures, leaving angular, near vertical faces with sharp edges. The surface morphology consisted of downslope oriented grooves or gullies spaced $\sim 1\text{-}2$ m apart with intervening ridges (Figure 4.8). No sessile organisms were seen on the steep sidewalls.



Figure 4.8. Downslope oriented grooves or gullies spaced $\sim 1\text{-}2$ m apart with intervening ridges. Photo courtesy of Monterey Bay Aquarium Research Institute.

At 151 mwd one small orange-stained spot ~10 cm in diameter was seen (Figure 4.9). Similar colored stains are often attributed to precipitation of iron oxides (limonite?) and were common on ROV-09/M190.



Figure 4.9. Orange-stained spot ~10 cm in diameter. Photo courtesy of Monterey Bay Aquarium Research Institute.

At 146 mwd the upper edge of the crater appeared on the sonar. The ROV zigzagged along the sharply defined edge of the crater, which was sharply defined. The seafloor outside the crater is composed of a series of ~10 cm high, ~1-2 m wavelength rounded laterally continuous ridges which are either parallel or slightly oblique to the edge of the crater (Figure 4.10). The sonar showed the crests of some of the ridges were spaced up to ~3 m apart.



Figure 4.10. Laterally continuous ridges which are either parallel or slightly oblique to the edge of the crater. Photo courtesy of Monterey Bay Aquarium Research Institute.

The ROV went ~20 m past the rim of the crater. No talus or accumulations of sediment was noted on the seafloor outside the depression. Abundant sessile organisms (e.g., soft corals) were seen attached to the seafloor outside the depression (Figure 4.11).



Figure 4.11. Sessile organisms (e.g., soft corals) attached to the seafloor outside the depression. Photo courtesy of Monterey Bay Aquarium Research Institute.

Returning to the edge of the crater the ridges seen on the seafloor outside the crater were observed to truncate abruptly. Where the orientation of the ridge was oblique to the rim of the crater, an upturned sharp ridge was observed (Figure 4.12).



Figure 4.12. Upturned ridge at the edge of the crater. Photo courtesy of Monterey Bay Aquarium Research Institute.

No sessile organisms were seen attached to the sidewalls, except for a few tubeworms whose lower ends appear to be exposed immediately under the rim along the truncated sidewall of the crater (Figure 4.13).



Figure 4.13. Tubeworms whose lower ends appear to be exposed immediately under the rim along the truncated sidewall of the crater. Photo courtesy of Monterey Bay Aquarium Research Institute.

The ROV flew to the north back into the crater to position the smart clump to collect a Niskin bottle sample above the lowest spot in the depression. The Niskin bottle attached to the clump weight was triggered at 152.4 mwd, 4 m above bottom. The ROV then moved across the seemingly flat crater floor stopping to collect push cores M182 PsC-17, M182 PsC-11 and M182 PsC-10 in 152.6 mwd (Figure 4.14). These push cores were taken near the sites where the Station 28 gravity core (ST28-GC) was subsequently collected. The push cores were entirely composed of mud, which occurred both as angular clasts and as a soft matrix between the clasts. Fauna on the floor of the basin consisted of brittle stars, numerous crabs, and flatfish. No attached sessile organisms were observed on the crater floor.



Figure 4.14. The ROV collecting push cores. Photo courtesy of Monterey Bay Aquarium Research Institute.

The ROV then transited toward the southwest edge of the crater along a gently upward sloping crater floor. As the flank of the crater was approached, the smooth surface of the basin was interrupted by occasional furrows with smooth rounded grooves, estimated to be <1 m wide and a few m long flanked by elevated sides (Figure 4.15). Similar features have been seen frequently in ROV dives in this region in 2010, 2012, 2013, 2016, and 2017. Better examples of these recurring features are seen in subsequent dives. Previously we have described these morphological features as whale marks (Jin et al., 2018), in part as we believed that the seafloor in the Beaufort Sea area was relatively untouched. An on-going investigation into the origins of these features by Lonny Lundsten of MBARI's video laboratory questioned whether there are any whale species known to inhabit the CBS which are of an appropriate size to make these marks. However, these features are of a size and shape similar to trawl marks left by the doors of otter trawls. We have also learned that there has been trawling in the CBS (e.g., Majewski et al., 2013 and references within). A similar discovery of surprisingly frequent trawl marks was also made north of Svalbard (<https://polarjournal.ch/en/2022/12/07/bottom-trawls-leave-scars-in-seabed-north-of-svalbard/>), another Arctic area where little fishing pressure was previously assumed. Thus, these recurring features are now tentatively being referred to as trawl marks in this report.



Figure 4.15. The smooth surface of the basin was interrupted by occasional furrows with smooth rounded grooves. Photo courtesy of Monterey Bay Aquarium Research Institute.

In 149 mwd, the first angular talus was observed (Figure 4.16). Rock sample M182 R-1 was collected here. It was composed of sticky cohesive clay. The amount and size of the angular gray talus increased as the ROV began to ascend the steep wall. No sessile organisms were observed on the wall.



Figure 4.16. Angular talus. Photo courtesy of Monterey Bay Aquarium Research Institute.

Subtle color variations were detected on the surface of the side wall suggesting different surface exposure ages, with a slightly more yellow/orange hue apparently on the older surfaces (Figure 4.17).



Figure 4.17. Subtle color variations on the surface of the side wall. Photo courtesy of Monterey Bay Aquarium Research Institute.

The exposed face of the upper wall was massive, with no floating clasts, suggesting it is a diamicton. The slope steepened, reaching an average slope of 45° (based on the multibeam) for the last 7 m. In some places the face of the side wall was nearly vertical. Based on the ROV sonar, the edge of the crater was at 139.9 mwd. The upper rim of the crater was sharply defined and laterally indented with 1 to 2 m wide scallops, noticed as the ROV moved laterally along the edge of the crater to the east for ~ 10 m (Figure 4.18).

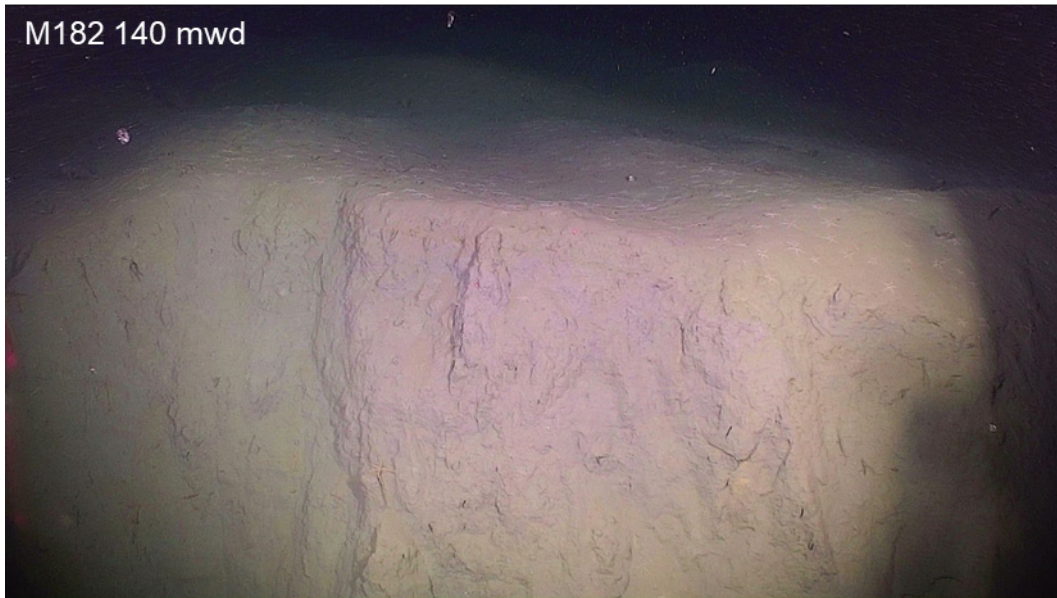


Figure 4.18. The upper rim of the crater was sharply defined. Photo courtesy of Monterey Bay Aquarium Research Institute.

The ROV ascended after transiting southeast outside the crater for ~30 m.

Key observations:

- The lack of any indication of surface alteration extending beyond the sharply defined rim and near vertical walls on the uppermost rim of the depression is consistent with the crater being a sinkhole collapse feature.
- The lighter colors on the exposed surface of the steep wall which have the most angular faces suggest smaller secondary failures have occurred on the walls of the crater.
- The existence of an apron of sediment drape below the exposed wall and fining of sediment with distance away from the apron suggest that sediment has accumulated in the interior of the depression on-top of the initial collapse surface.

4.3.3. ARA13C ROV-02

MBARI Dive M183 Wednesday August 31st, 2022

The dive target was a circular depression colloquially referred to as “The Old Hole” which was surveyed three times over the course of 12 years. The first bathymetric survey was conducted by the CCGS Amundsen in 2010. It was surveyed again by the CCGS Sir Wilfried Laurier in 2019, and by the mapping AUV during this cruise (ARA13C), three years later in 2022 (Figure 4.19). When the grids from the three surveys are compared chronologically, no changes are detected in the morphology of the hole over the course of the 12 years encompassed by these surveys.

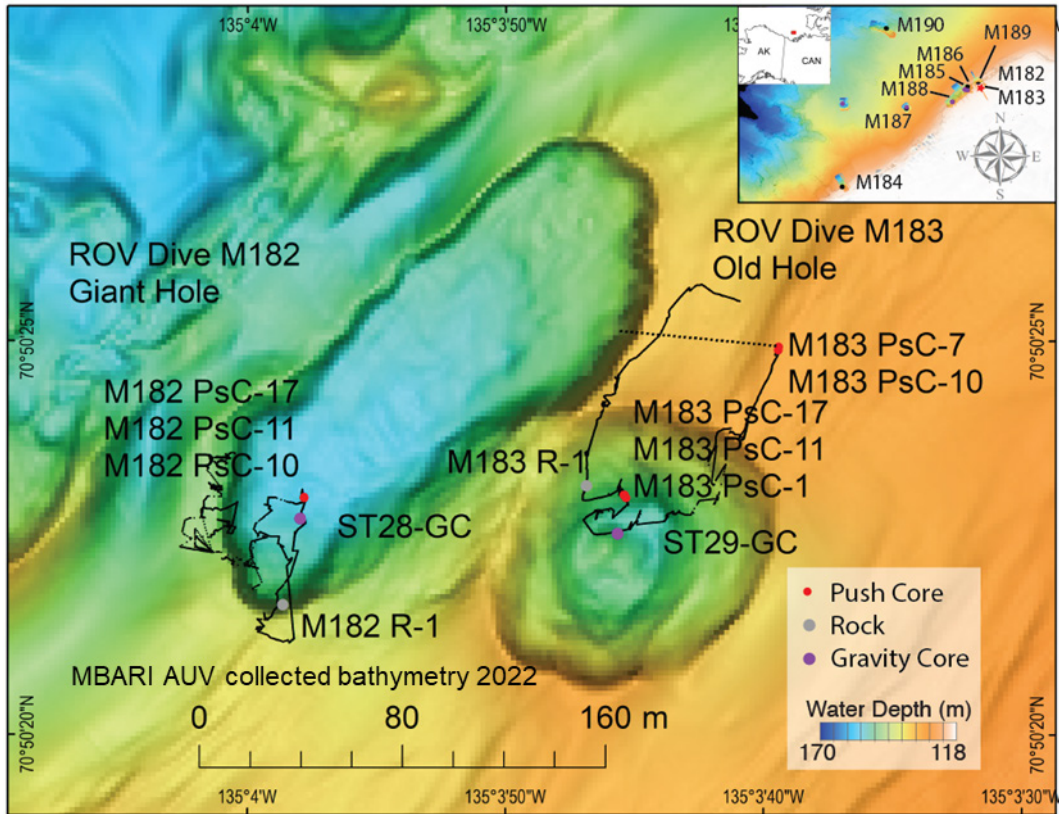


Figure 4.19. MBARI AUV collected bathymetry 2022 with details of Dives M182 and M183

The objective of this dive is to contrast the morphology of this depression of unknown age (“Old Hole”) with a newly formed depression (“Giant Hole”, described in Paull et al. 2022, PNAS paper) that was surveyed in ROV-01/M182. Both depressions are separated by a swale, with the old depression (“Old Hole”) located to the SE of the new depression (“Giant Hole”).

The ROV landed NW and outside of the depression (“Old Hole”) at 127.4 m water depth and transited towards the depression edge. The sonar showed ridges with up to 6 m wavelength upon approaching the depression rim. The seafloor was covered with fauna consisting of both sessile and mobile organisms (Figure 4.20). One potential trawl mark was seen before reaching the depression.

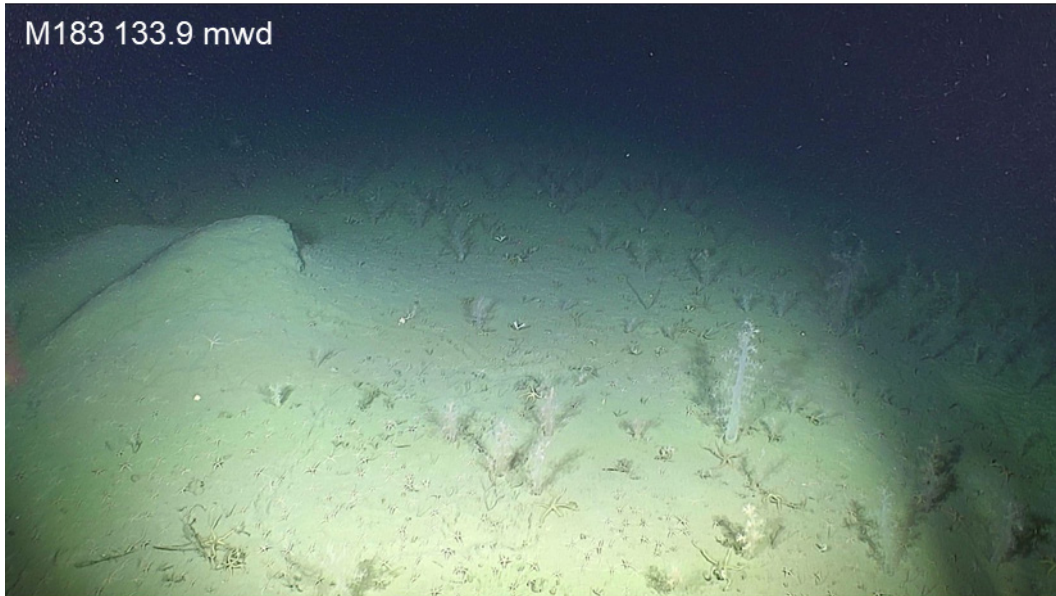


Figure 4.20. Seafloor covered with fauna consisting of both sessile and mobile organisms. Photo courtesy of Monterey Bay Aquarium Research Institute.

The upper edge of the depression is rounded and slopes at $\sim 45^\circ$. Fauna seen on the flank includes some sessile sea pens, numerous brittle stars, some basket stars and an occasional rattail like fish (4.21).



Figure 4.21. Fauna observed on the flank. Photo courtesy of Monterey Bay Aquarium Research Institute.

Some rounded ledges suggesting old failures within the drape that covers the side wall were seen while descending along the flank of the crater (Figure 4.22). No outcropping strata were observed.

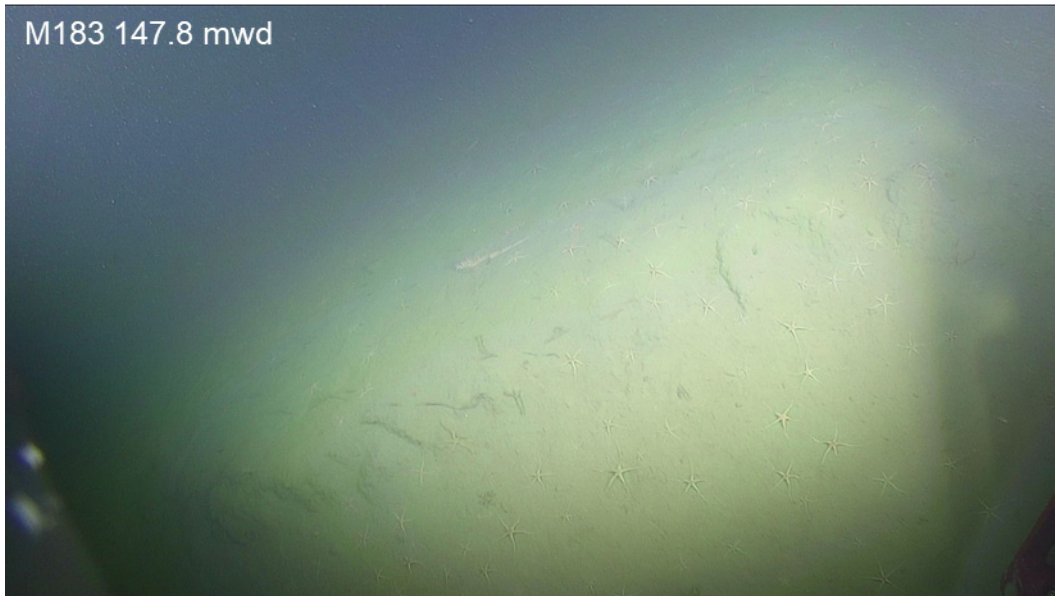


Figure 4.22. Rounded ledges suggesting old failures. Photo courtesy of Monterey Bay Aquarium Research Institute.

The bottom of the hole is largely sediment draped and not of uniform depth. The ROV started at 135 mwd when it arrived at the crater floor and reached 152 mwd at the deepest point of the transit over the depression floor. As the ROV moved into deeper parts of the hole, the water became increasingly murky. When approaching the deepest point, a rock with a small crinoid (?) attached was sampled (M183 R-1) (Figure 4.23). The rock was visually examined on deck and judged to be a rounded chert cobble, presumably a dropstone.



Figure 4.23. Rock with a small crinoid (?) attached. The rock was collected by the ROV (M183 R-1). Photo courtesy of Monterey Bay Aquarium Research Institute.

A Niskin bottle attached to the clump weight was triggered at 142.5 m water depth. Push cores M183 PsC-11, M183 PsC-17, & M183 PsC-1 were taken at the deepest point of the depression at 152.2 m (Figure 4.24). Pilots noted that the seafloor was firmer compared to the seafloor in the newly formed depression (“Giant Hole”) visited on ROV-01/M182. This

judgment was based on the resistance of the seafloor to penetration and extraction by the push cores. The visibility near the bottom of the depression was very poor.

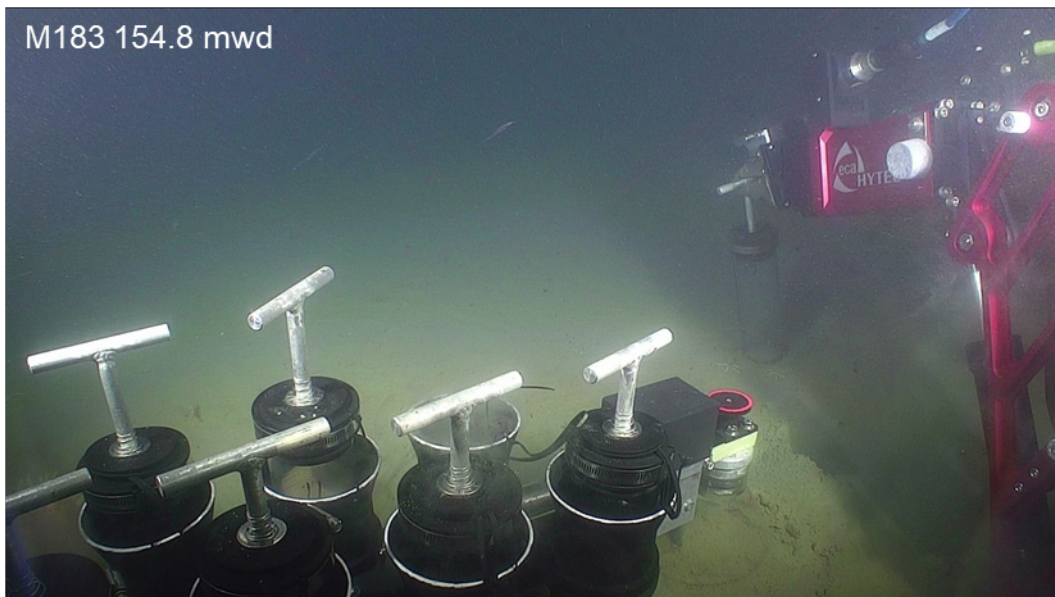


Figure 4.24. Push were cores taken within the depression. The visibility near the bottom of the depression was very poor. Photo courtesy of Monterey Bay Aquarium Research Institute.

In the center of the “Old Hole” there is a slightly elevated area that is ~20 m in diameter and ~5 m in height (Figure 4.25). It is heavily sediment-draped, but the rounded edges of occasional sediment-draped blocks are exposed on the floor at random orientations.

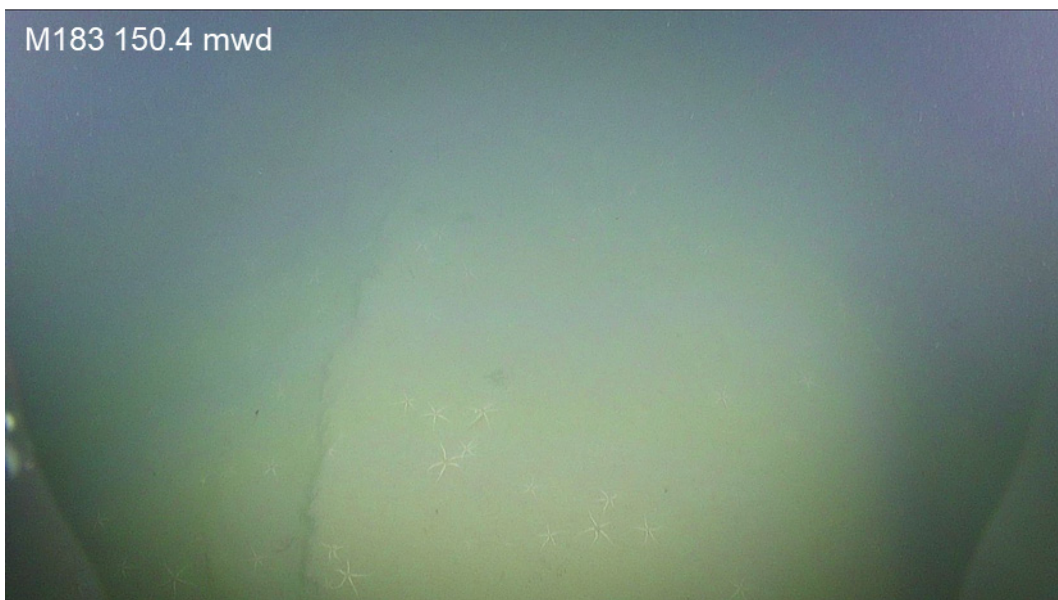


Figure 4.25. Slightly elevated area in the center of the “Old Hole”. Photo courtesy of Monterey Bay Aquarium Research Institute.

The ROV returned to the north wall of the depression and ascended along the flank farther east from the point where it had descended. The average slope angle was ~30°. No outcropping beds were seen. As the ROV continued its ascent the water clarity improved and more sessile organisms were observed colonizing the slope (Figure 4.26).

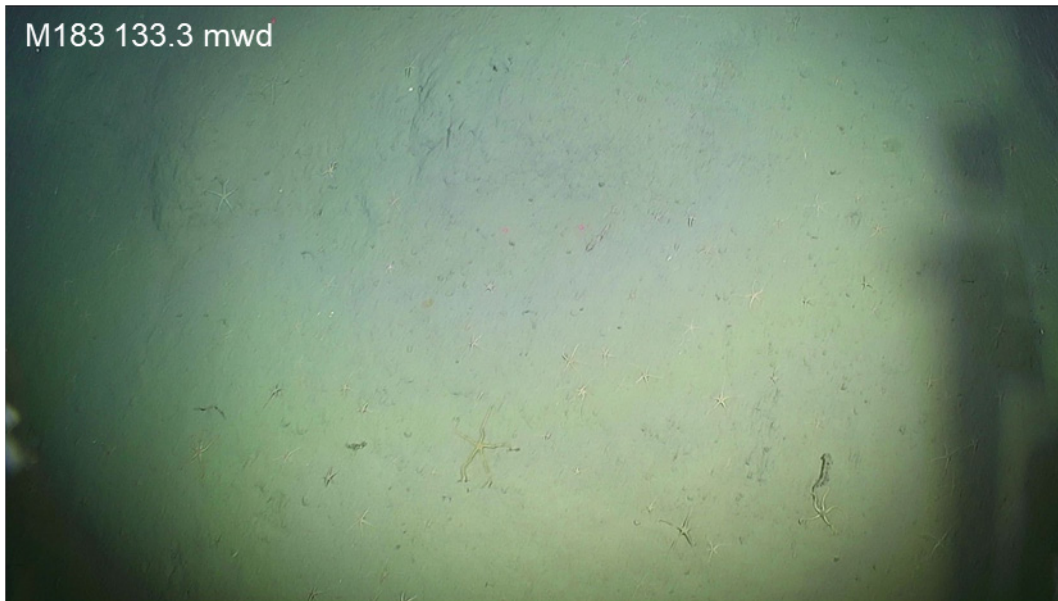


Figure 4.26. Sessile organisms observed colonizing the slope. Photo courtesy of Monterey Bay Aquarium Research Institute.

Two distinctive indentations and a somewhat smaller hole ~10 cm behind them were seen as the ROV reached the upper rim of the crater (Figure 4.27). The indentations have near vertical ~30 cm high semicircular backwalls with a radius of ~15 cm across. The color of the walls inside the depressions is darker than the sediment outside them. The floors of the indentations align horizontally with a break in the slope on the adjacent face which suggests the base of the holes is a bedding surface. Their slightly grayer sediment in the interior compared to the surrounding sediment suggests the surfaces of the hole were exposed comparatively recently. The origin of these holes (biological vs geological) is unknown.

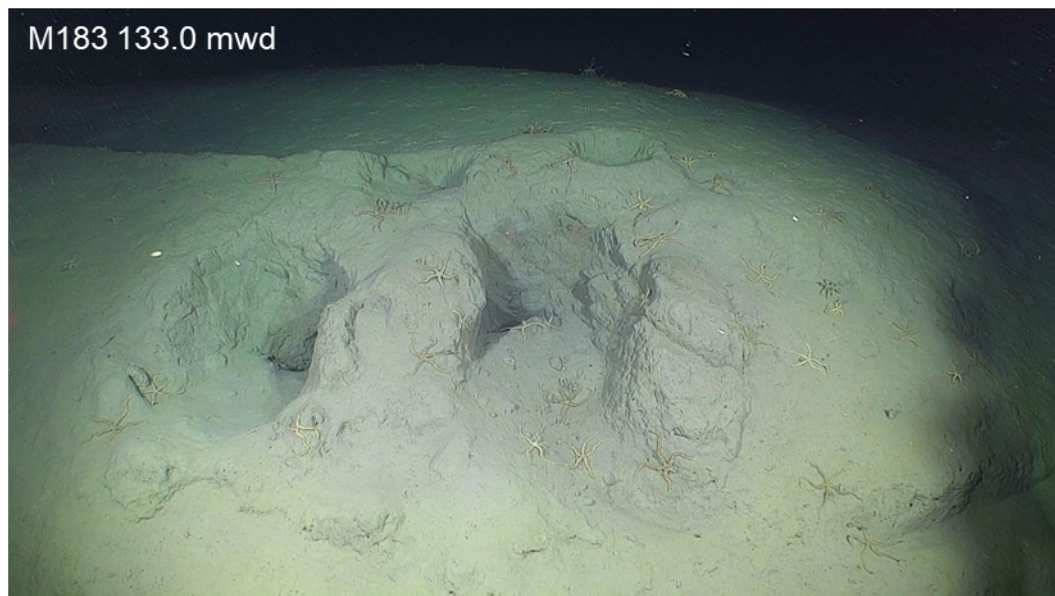


Figure 4.27. Distinctive indentations seen as the ROV reached the upper rim of the crater. Photo courtesy of Monterey Bay Aquarium Research Institute.

Based on the AUV map, the “Old Hole” appears to truncate a ~60 m wide, 0.5 m high, NE-SW oriented ridge that exists on both the NE and SW side of the Old Hole. The ROV followed the ridge ~30 m to the NE. The ridge was not discernable in ROV sonar. Push cores M183 PsC-7 and M183 PsC-10 were taken on a site that was judged to be on the ridge based on distance and direction traveled by the ROV since it had left the crater rim (Figure 4.28).

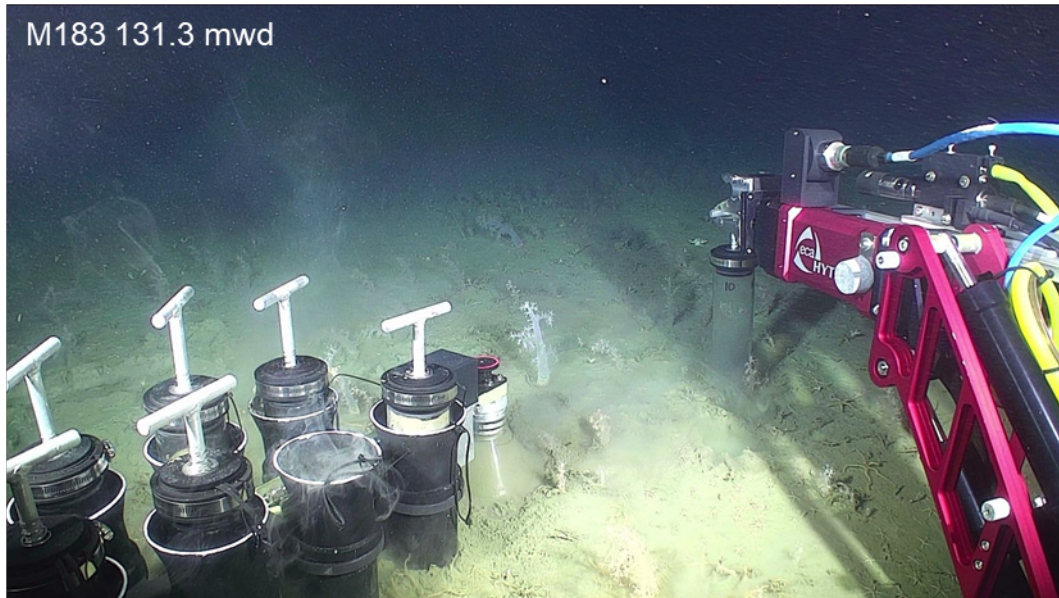


Figure 4.28. Push cores taken on a site that was judged to be on the ridge based on distance and direction traveled by the ROV. Photo courtesy of Monterey Bay Aquarium Research Institute.

After these cores were collected, the USBL navigation failed. However, the ROV proceeded westward towards the “Giant Hole”. The seafloor surface between both depressions is smooth, colonized with communities of both sessile and mobile fauna (Figure 4.29).



Figure 4.29. Seafloor colonized with communities of both sessile and mobile fauna. Photo courtesy of Monterey Bay Aquarium Research Institute.

An elongated depression was encountered. The dimensions were ~ 3 m long and ~ 1 m wide with a ~30 cm deep indentation on one end and a ~30 cm linear mound at the other end that is cut through the middle by a smooth groove (Figure 4.30). A similar feature, presumably a trawl mark, was seen earlier in this dive. Otherwise, the seafloor surface transited by the ROV was unremarkable all the way to the edge of the “Giant hole”.



Figure 4.30. Elongated depression ~ 3 m long and ~ 1 m wide. Photo courtesy of Monterey Bay Aquarium Research Institute.

The upper edge of the “Giant Hole” was reached at 131 mwd. The edge marks an abrupt transition from the surrounding flat seafloor outside the crater into a very steep wall, which based on the multibeam data, had an average slope of 50° in the upper 7 m. The massive exposed face walls had angular vertical edges, suggesting jointing (Figure 4.31). Sediment drape was absent. A faint horizontal lineation ~15 cm below the break in slope suggests the existence of a thick sedimentary layer that was truncated by the formation of the hole.



Figure 4.31. Massive exposed face walls with angular vertical edges. Photo courtesy of Monterey Bay Aquarium Research Institute.

By 140 mwd accumulations of talus started to be seen covering some of the side walls of the depression (Figures 4.32 and 4.33).

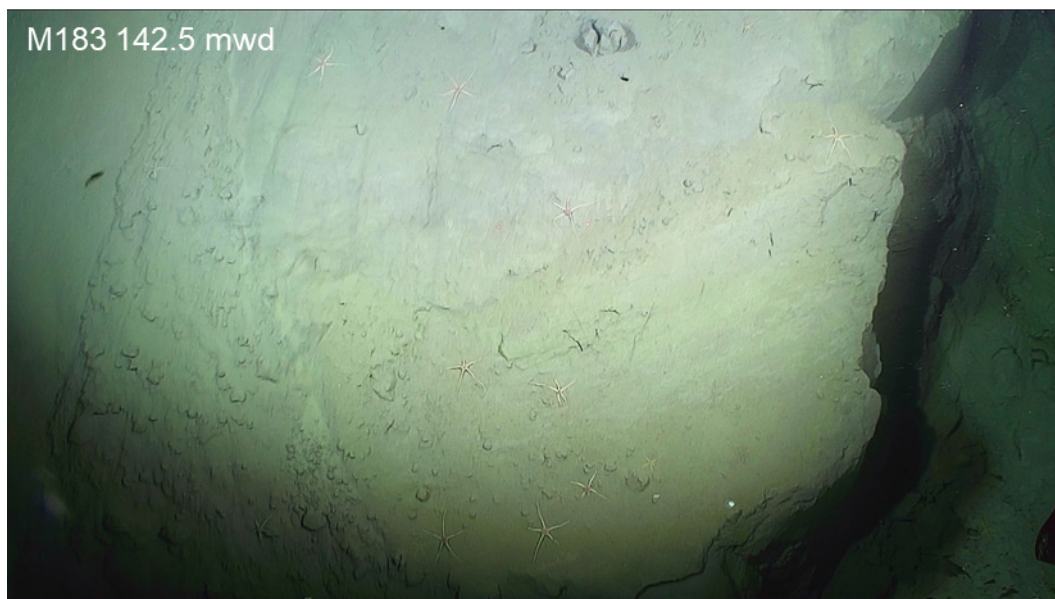


Figure 4.32. Accumulation of talus on a side wall. Photo courtesy of Monterey Bay Aquarium Research Institute.

At 146 mwd jumbled angular talus blocks of fresh appearance were noticed protruding from the seafloor (Figure 4.34).

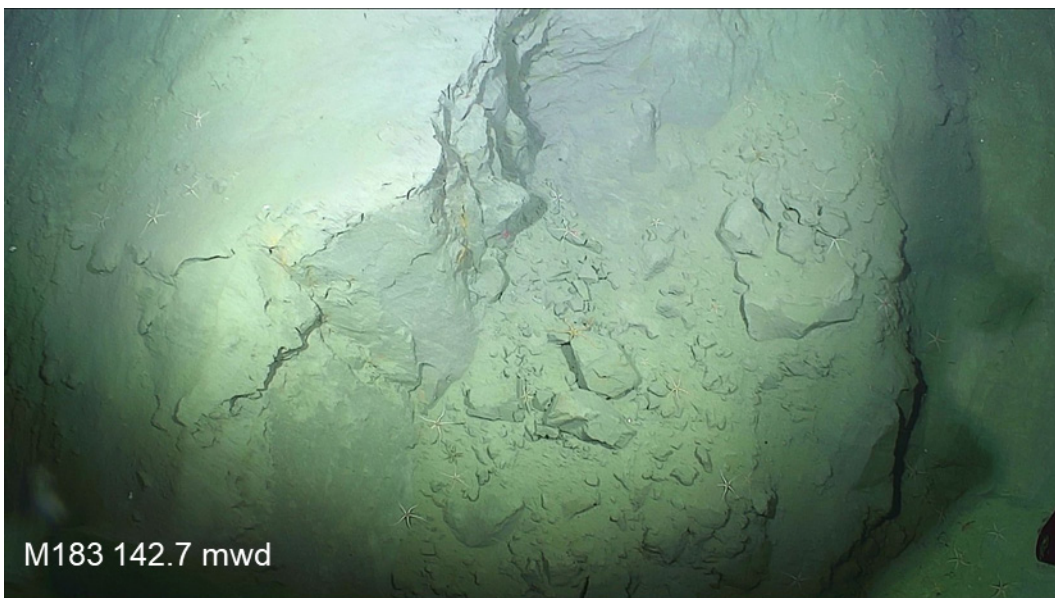


Figure 4.33. Angular talus blocks. Photo courtesy of Monterey Bay Aquarium Research Institute.

Dive ended just immediately after, before reaching the flat floor of the “Giant Hole”

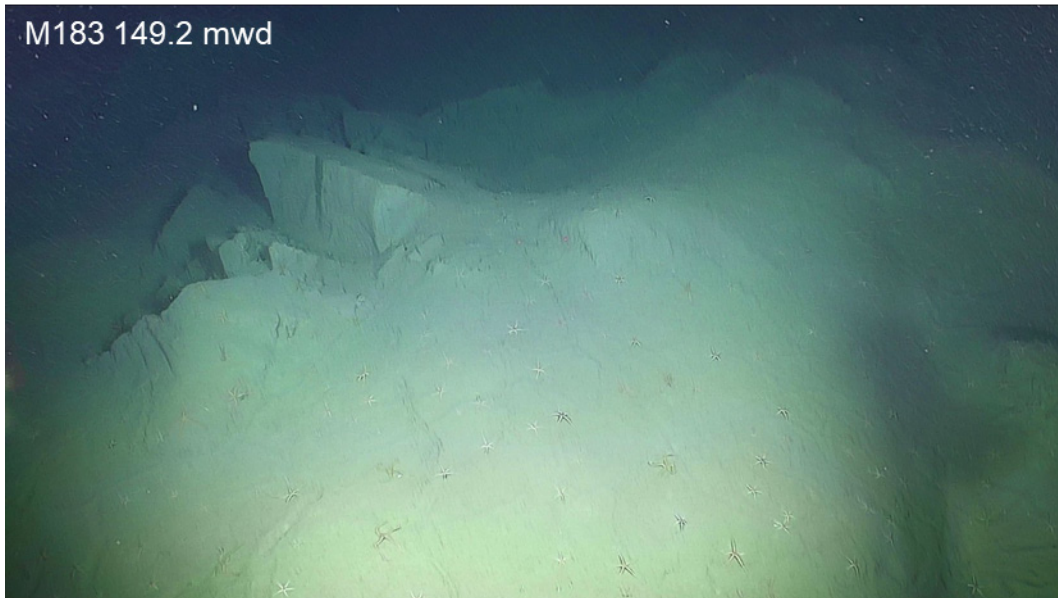


Figure 4.34. Angular talus blocks on the seafloor. Photo courtesy of Monterey Bay Aquarium Research Institute.

Impression:

The morphology observed in the “Giant Hole” on ROV-01/M182, and at the end of ROV-02/M183, differ significantly from the morphology of the “Old Hole” where the ROV spent most of the time during this dive, ROV-02/M183. The “Giant Hole” has steep faces on its upper flanks, composed of massive outcrops broken along angular faces. In contrast, the adjacent “Old Hole” has less-steep sides, lacks outcropping exposures, and has a very weathered talus. Thus, consistent with the repeat mapping data, the visual observations indicate that the “Giant Hole” is younger than the adjacent “Old Hole”, and it is still experiencing secondary failures along its steep walls.

4.3.4. ARA13C ROV-03

MBARI Dive M184, Thursday September 1st, 2022

This dive was conducted in the upper section of a scarp created by a landslide on the upper continental slope, below the shelf edge (Figure 4.35). A comparison between bathymetry grids collected by MBARI’s mapping AUV in 2013 and in 2016 showed a possible -3.7 m depth change near the headwall of the landslide.

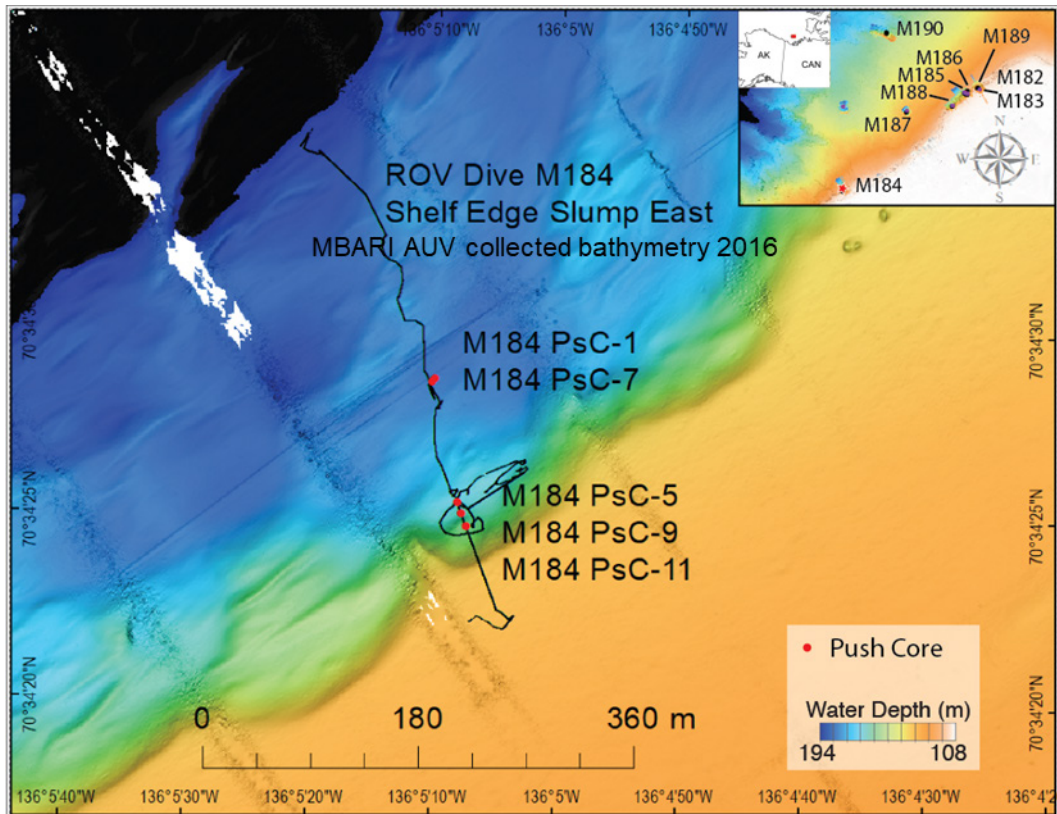


Figure 4.35. MBARI AUV collected bathymetry 2016 with details of Dive M184

However, there was considerable uncertainty as to whether this depth change was an artifact due to errors associated with the collected bathymetry or whether the depth change indeed took place. The objective of this dive was to inspect the seafloor at 136.08548° W and 70.57345° N in 150 m water depth where the possible depth change may have taken place. Regrettably, the ROV dive took place before the 2022 AUV survey was conducted during this expedition, which subsequently showed this feature to be an artifact.

The ROV reached the seafloor on the slope at 177.5 mwd and during the course of the dive followed a 147° course, ascending along the slope and finishing on the shelf edge above the scarp. This course took the ROV along a morphology that multibeam data and Chirp lines show is part of a large landslide scar.

The seafloor was covered in smooth sediment traversed by animal tracks and trails and is well colonized by sessile and mobile fauna (Figure 4.36). Push cores M184 PsC-17 and M184 PsC-1 were taken in 169 mwd.

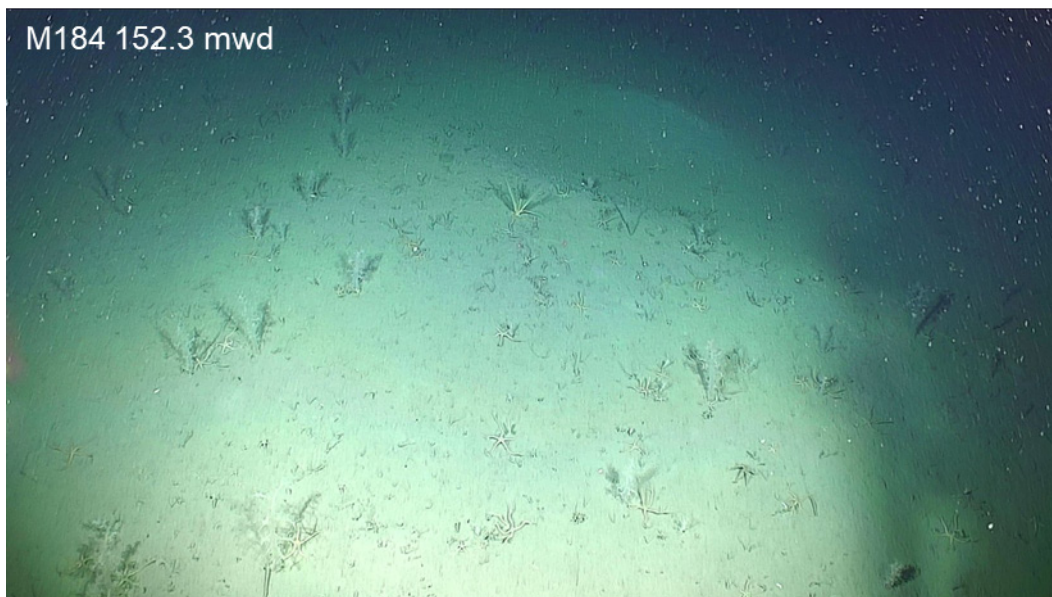


Figure 4.36. Seafloor colonized by sessile and mobile fauna. Photo courtesy of Monterey Bay Aquarium Research Institute.

The AUV multibeam and Chirp survey data show that the dive crossed a couple of ridges and troughs that were created when blocks of the wall were rotated along strike by the slumping. The existence of the ridges was confirmed by the subtle depth changes and faint lineations observed on the ROV sonar. However, they were not discernable in the ROV images alone.

Seven instances of distinct elongated depressions with raised edges, which could be sediment depressions left by trawl fishing were seen (Figure 4.37). These features were oriented at seemingly random directions, suggesting they are not associated with the slump scarp ridges. Otherwise, the seafloor was largely unremarkable.

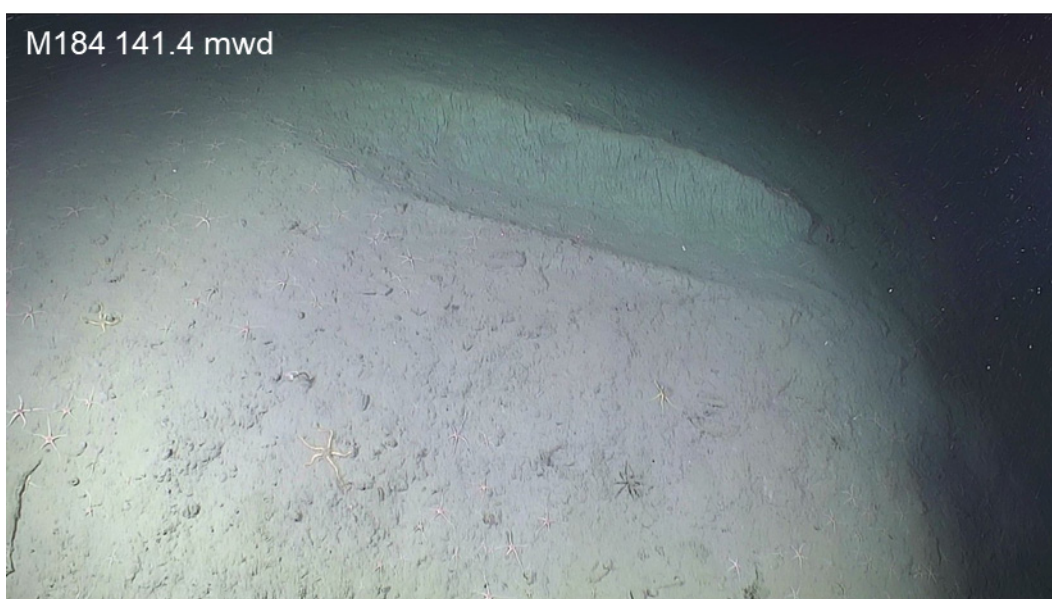


Figure 4.37. Elongated depression with raised edges. Photo courtesy of Monterey Bay Aquarium Research Institute.

A Niskin bottle was fired at 138.3 mwd, ~9 m off the bottom, shortly before arriving at the site of interest. At the site of interest, the ROV landed on a relatively flat bench below the headwall, composed of smoothly-textured seafloor. It was no different from the texture of the seafloor seen over most of the transect up to this depth. The site of interest is just below the change in slope associated with the headwall of the slide scar. Push cores M184 PsC-5, M184 PsC-9, and M184 PsC-11 were collected here in 152.8 mwd (Figure 4.38).

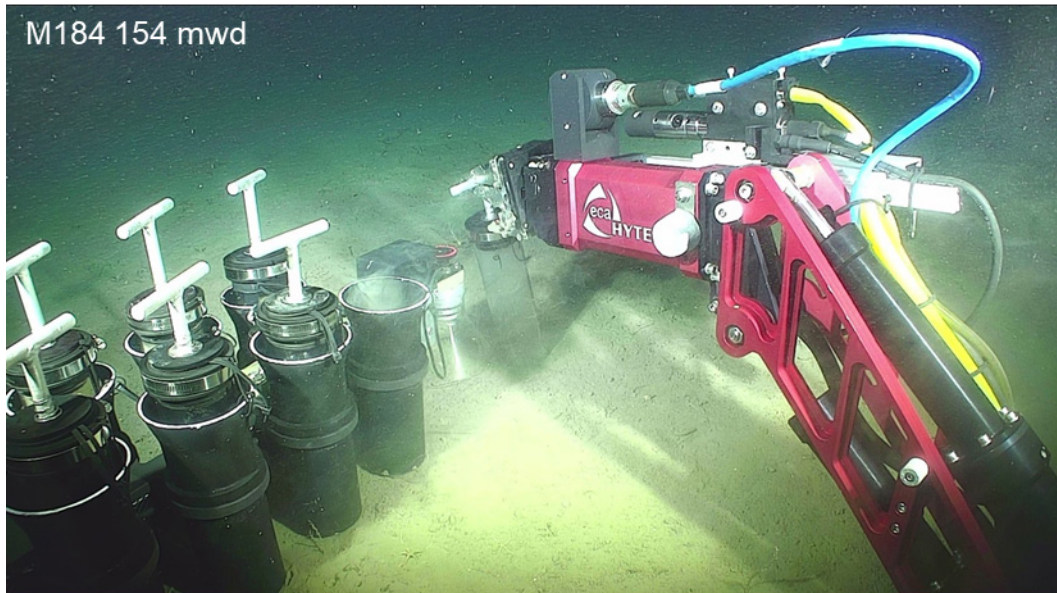


Figure 4.38. Push cores taken below the change in slope associated with the headwall of the slide scar. Photo courtesy of Monterey Bay Aquarium Research Institute.

The transect continued up the headwall. Between 147 and 132 mwd some faint laminations, indicating outcropping beds, were seen (Figure 4.39). In addition, the surface of the wall displayed a rougher surface, which suggests some small clumps of sediment were eroding out of the exposed face.



Figure 4.39. Faint laminations on the headwall indicating outcropping beds. Photo courtesy of Monterey Bay Aquarium Research Institute

Some mud clasts were noticed. Attempts to sample the rounded mud clasts at 141.8 m with the manipulator arm failed because they were too soft to pick up, showing they were locally-derived mud clasts. The upper edge of the headwall scarp was reached at 131 mwd (Figure 4.40). Again, no distinctive changes in the morphology were noted. Dive ended at 130.1 mwd.

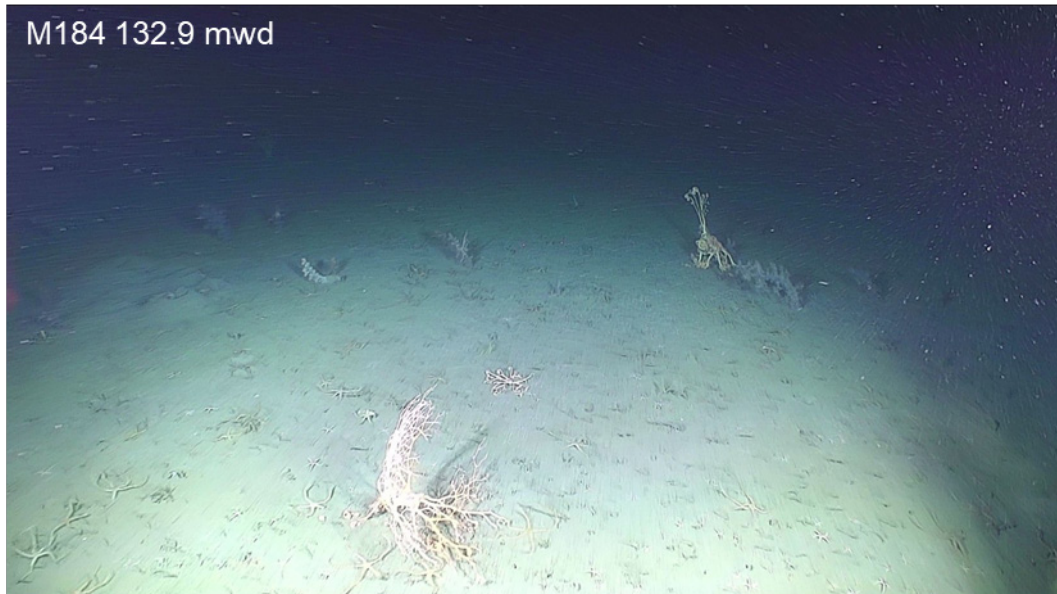


Figure 4.40. Seafloor at the upper edge of the headwall scarp. Photo courtesy of Monterey Bay Aquarium Research Institute.

4.3.5. *ARA13C ROV-04*

MBARI Dive M185, Friday September 2nd, 2022

The dive target was an area that got deeper by up to 7.75 m over the course of ~3 years (Figure 4.41). This change was detected by comparing the surface-ship bathymetry collected by the CCGS Sir Wilfred Laurier in 2019, and by MBARI's mapping AUV in 2022 during this cruise (ARA13C) (Figure 4.42). The new depression is 125 m long and 25 m wide. The greatest depth change was detected adjacent to a crescent-shaped scarp on the eastern side of the new depression where the water depth is now 161 m. The new depression, which colloquially was named "Ice hole", is located in an area that previously was the flank of a ridge, but large sections along the ridge's eastern flank have collapsed. The objective of the dive was to explore this newly formed feature. Ice was subsequently recovered from the gravity core collected at Station 23 (ST23-GC), located in the center of the new depression.

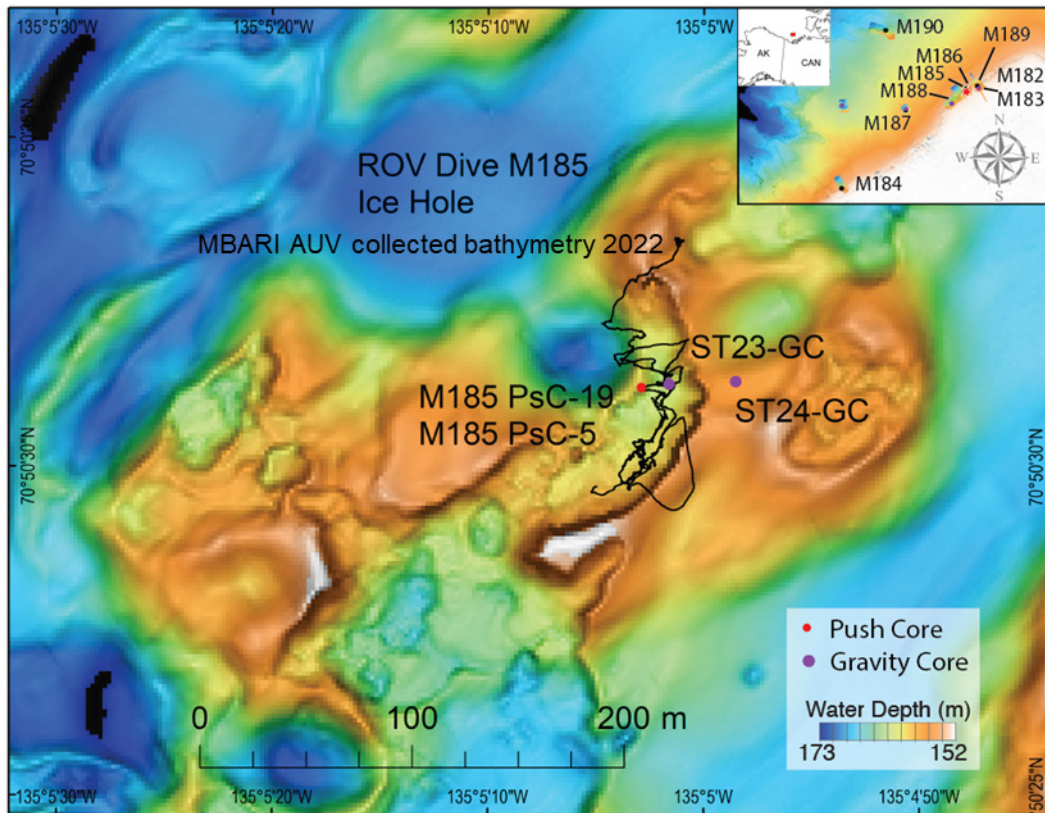


Figure 4.41. MBARI AUV collected bathymetry 2022 with details of Dive M185

Inaccurate calibration of the ship's USBL system may have led to errors (up to 10 meters) in the accuracy of the location of the ROV during the dive.

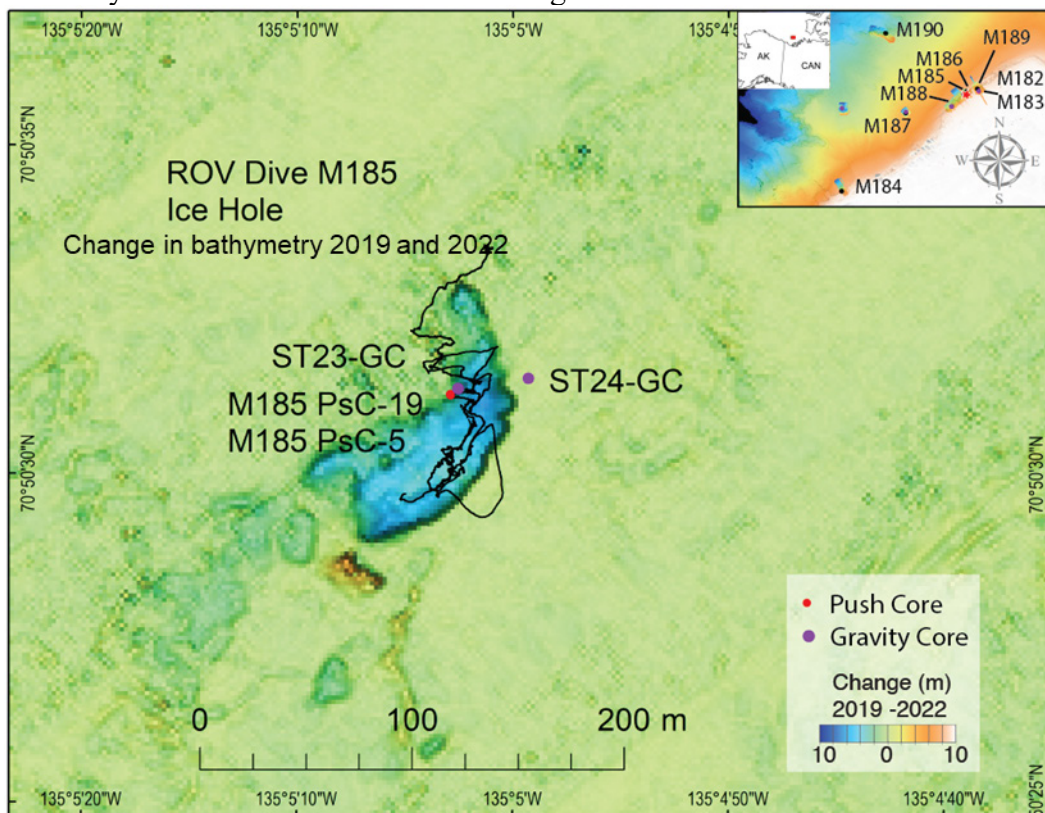


Figure 4.42. Change in bathymetry between 2019 and 2022 with details of Dive M185

The ROV reached the seafloor at 157 mwd, about 50 m north of the new depression and crossed a narrow ridge before reaching the edge of the depression. Outside the new depression, the seafloor was smooth and colonized with sessile organisms (soft corals). Before reaching the depression, billowing plumes of turbid water were encountered (Figure 4.43). The flow of sediment plumes out of the depression was not due to disturbances associated with the ROV thrusters. Similar dense sediment clouds flowed past the ROV multiple times during the dive. Later on, it was concluded that the turbid clouds of sediment were being carried over the bottom by the north west flowing current as a result of fine sediment lofted from cascading debris falling off the sidewalls of the depression.

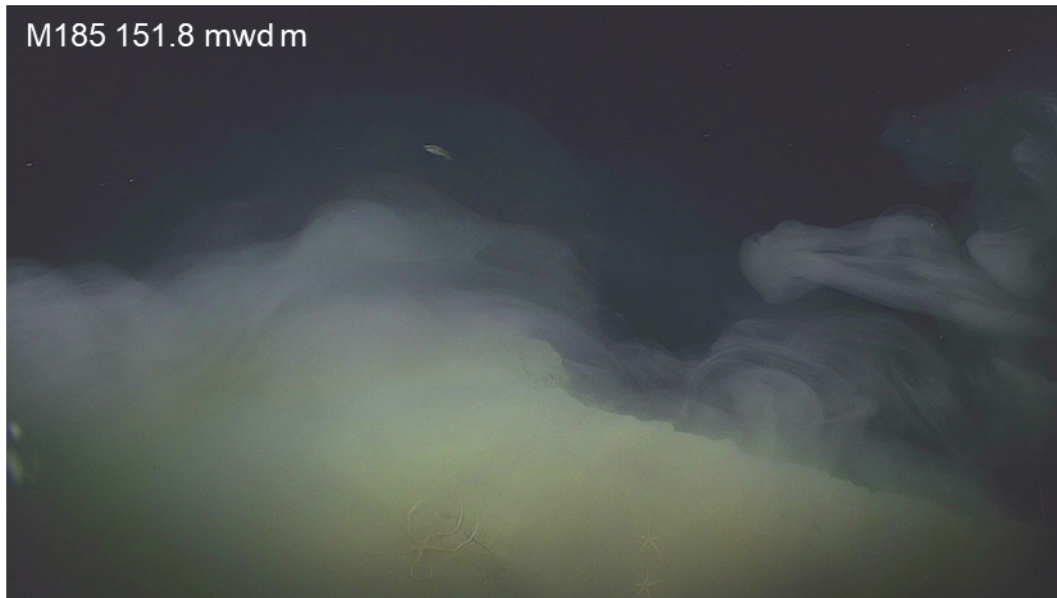


Figure 4.43. Billowing plumes of turbid water. Photo courtesy of Monterey Bay Aquarium Research Institute.

The following images are not provided in chronological order, but aim to illustrate the most salient features observed in this dive. The images come from the time intervals with the best visibility.

The contact between the seafloor surface outside the depression and side wall of the depression was usually a single sharply defined abrupt transition (Figure 4.44).

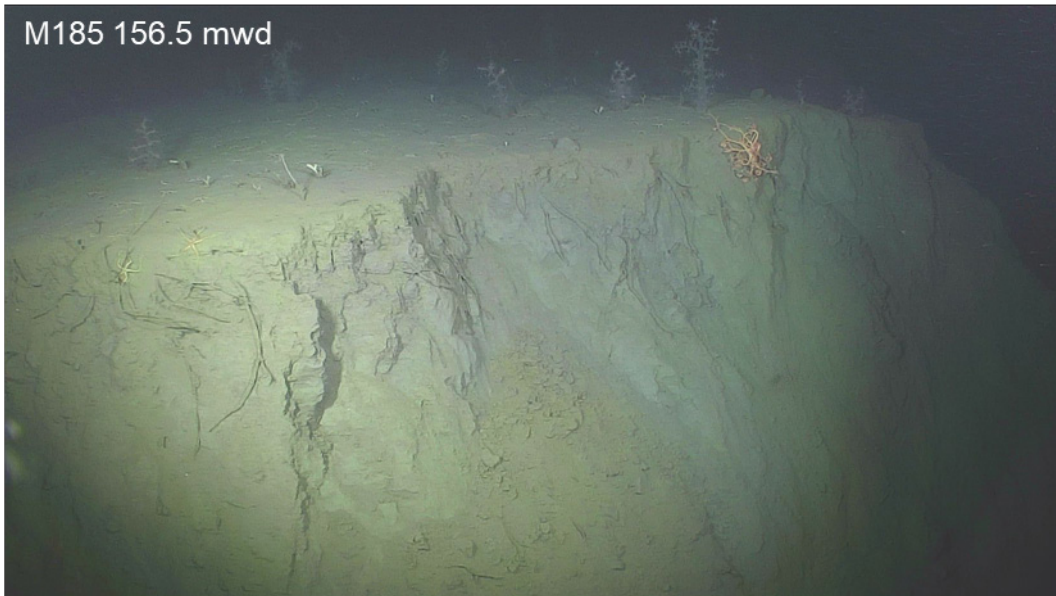


Figure 4.44. Contact between the seafloor surface outside the depression and side wall of the depression. Photo courtesy of Monterey Bay Aquarium Research Institute.

Occasionally one or two similarly aligned crown cracks with up to ~10 cm down-steps were observed (Figure 4.45). These cracks suggested incipient failure blocks forming up to 2 m back from the exposed face of the depression.

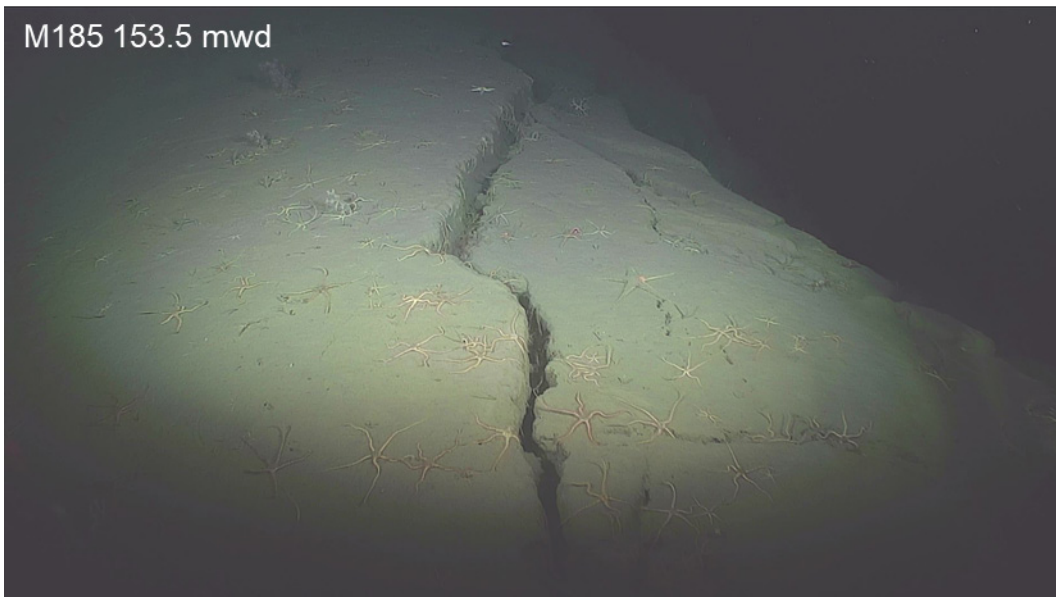


Figure 4.45. Crown cracks with up to ~10 cm down-steps. Photo courtesy of Monterey Bay Aquarium Research Institute.

No indications of rubble or accumulations of sediment were seen above the rim. Soft corals extended to the edge of the depression, and the lower ends of tubeworms were exposed along the truncated edge at the top of the scarp (Figure 4.46).

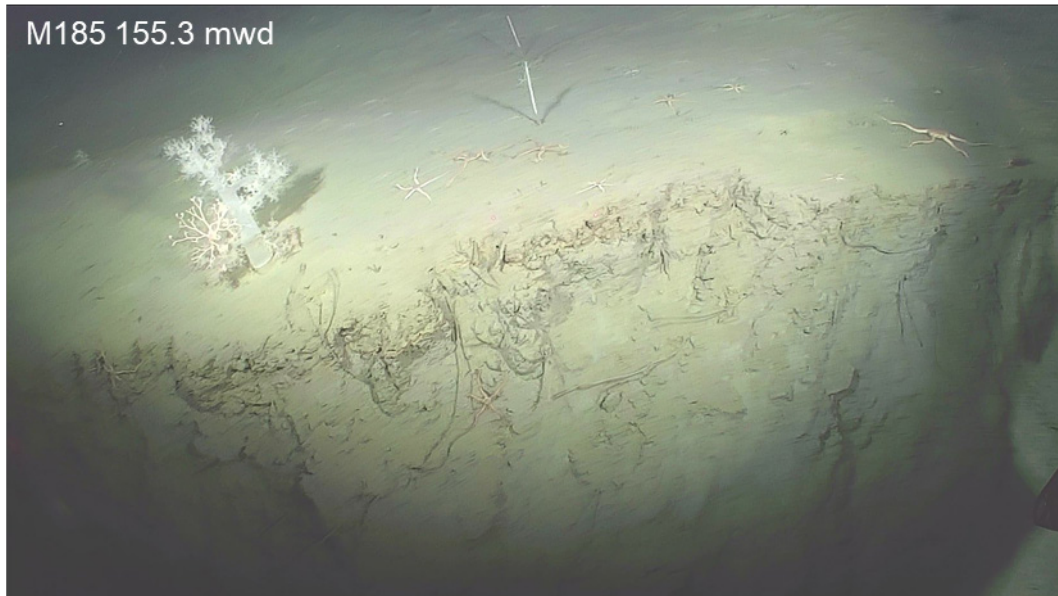


Figure 4.46. The lower ends of tubeworms were exposed along the truncated edge of the depression. Photo courtesy of Monterey Bay Aquarium Research Institute.

The exposed face on the side of the depression slopes at angles between 45° and 90° . The upper section of the sidewall was composed of massive gray cohesive mud broken along irregularly oriented surfaces (Figure 4.47). Down-slope oriented gullies spaced 0.5 to 1 m apart fluted the face of the side wall.

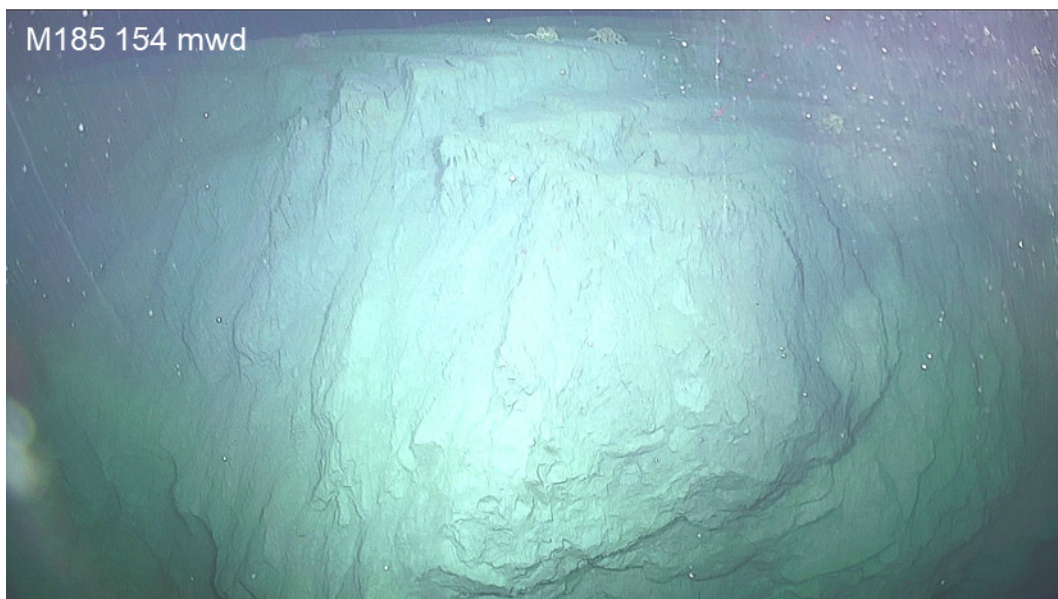


Figure 4.47. Sidewall composed of massive gray cohesive mud broken along irregularly oriented surfaces. Photo courtesy of Monterey Bay Aquarium Research Institute.

Small pieces of sediment were seen crumbling off the steep walls of the depression and funneled into these fluted gullies. The gullies led downslope to sediment fans composed of material of varying sizes (Figure 4.48). In places, the fans coalesced downslope into sediment aprons covering the intact massive strata on the exposed wall.

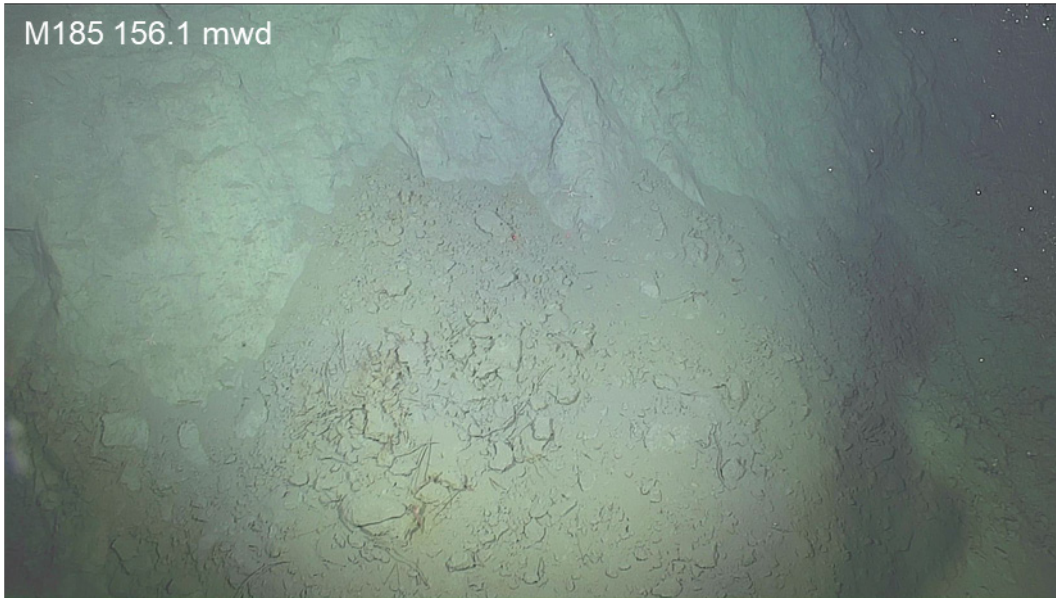


Figure 4.48. Sediment fans composed of material of varying sizes. Photo courtesy of Monterey Bay Aquarium Research Institute.

The presence of overhangs at the bottom of the intact cohesive massive mudstone was observed where the sediment aprons were not as developed (Figure 4.49). The wall overhang was characteristically deeper than ~2 m from the rim of the depression. Where visible, the overhangs extended laterally for several meters. Other indented ledges were observed below the top undercut.

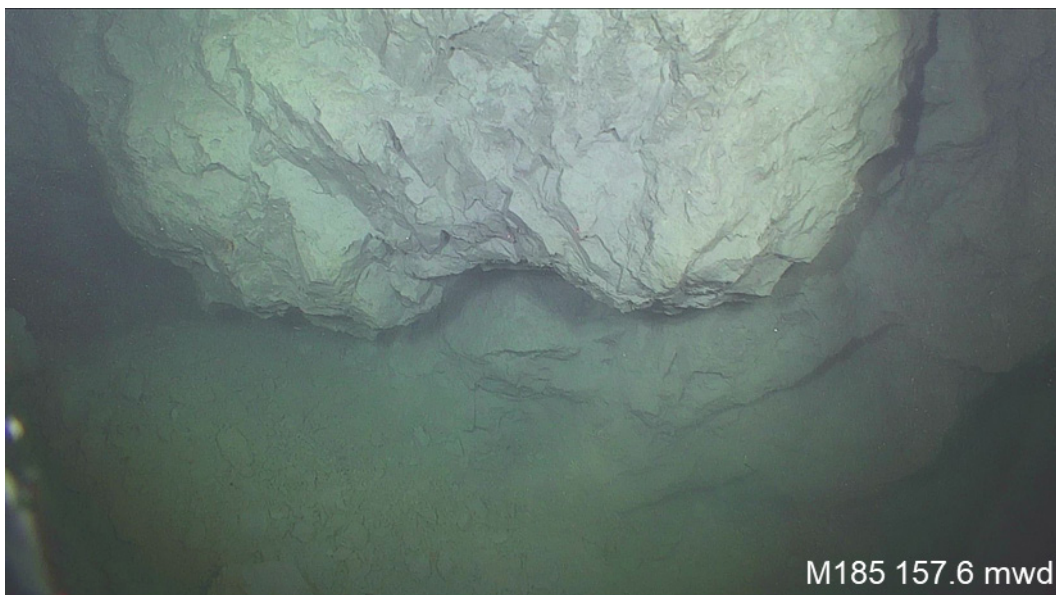


Figure 4.49. Overhangs at the bottom of the intact cohesive massive mudstone. Photo courtesy of Monterey Bay Aquarium Research Institute.

A horizontal gap between 15 and 30 cm tall, was observed at the base of the top overhang (Figure 4.50). How far the gap extended underneath the overhanging wall could not be determined, but exceeded one meter.

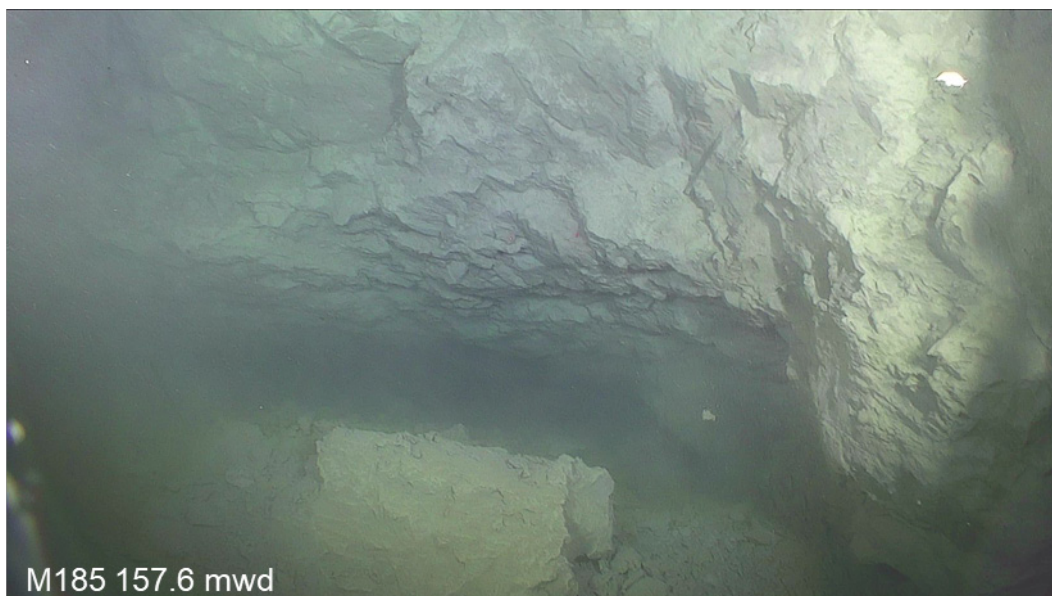


Figure 4.50. Horizontal gap between 15 and 30 cm tall, observed at the base of the top overhang. Photo courtesy of Monterey Bay Aquarium Research Institute.

Dark horizons of variable thickness were seen in three places. In the first observation, the horizon was a distinct darker bed. The contact with the overlying massive sediment above was sharp. Underneath the black layer there was an undercut void (Figure 4.51).



Figure 4.51. Dark horizon in sharp contact with the overlying massive sediment. Photo courtesy of Monterey Bay Aquarium Research Institute.

The second appearance of dark material consisted of a massive block, at least 90 cm thick, sticking out from the wall (Figure 4.52). The surface was hard, as the manipulator arm was unable to scratch it or break its edges off. We infer that the block is massive permafrost.



Figure 4.52. Massive block of dark material at least 90 cm thick, sticking out from the wall. Photo courtesy of Monterey Bay Aquarium Research Institute.

The ice block displayed sharply tilted internal layering (Figure 4.53).



Figure 4.53. Internal layering of the ice block. Photo courtesy of Monterey Bay Aquarium Research Institute.

Nearby massive black ice was observed, its thickness reached at least one meter. Small suspended inclusions at different depths in the transparent ice moved relative to each other as the viewing orientation changed, confirming the observed material was ice. Objects seen through the ice, such as the clamp of the ROV arm, appeared offset when behind the ice, indicating the light traveled through a material with a different index of refraction (e.g., transparent ice) (Figure 4.54).

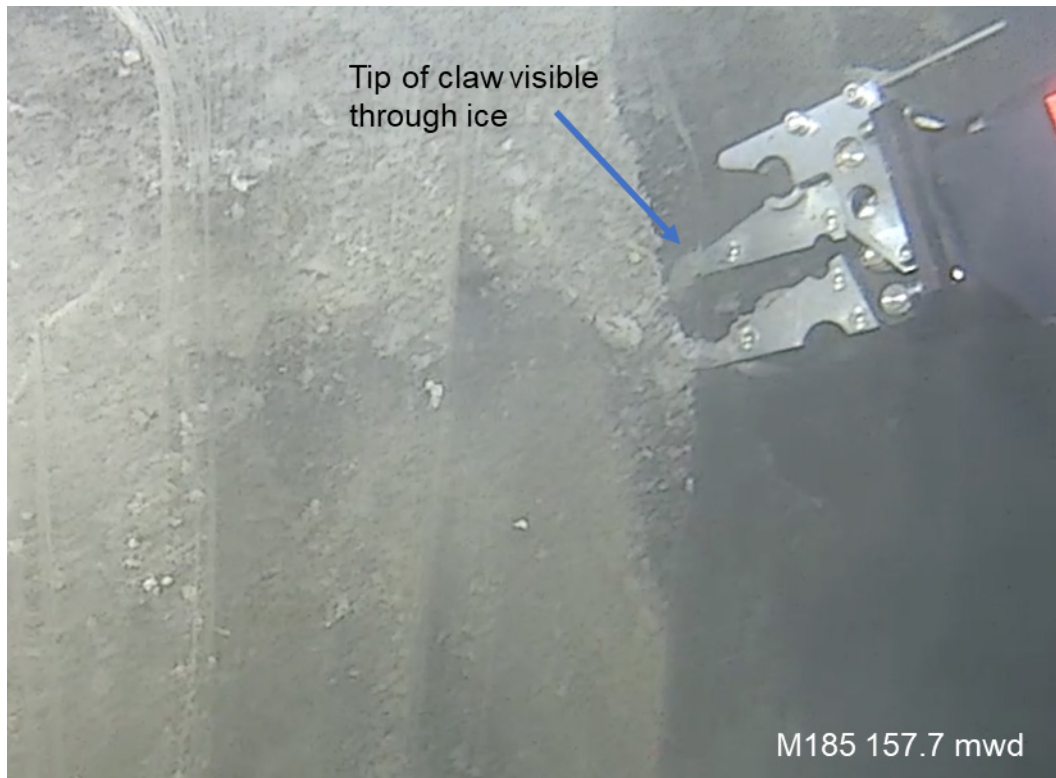


Figure 4.54. Objects seen through the ice, such as the clamp of the ROV arm, appeared offset when behind the ice. Photo courtesy of Monterey Bay Aquarium Research Institute.

Occasionally, the laser beam from the ROV showed two reflected dots from the same beam, one from the surface of the ice and another one from an inclusion within the ice (Figure 4.55).

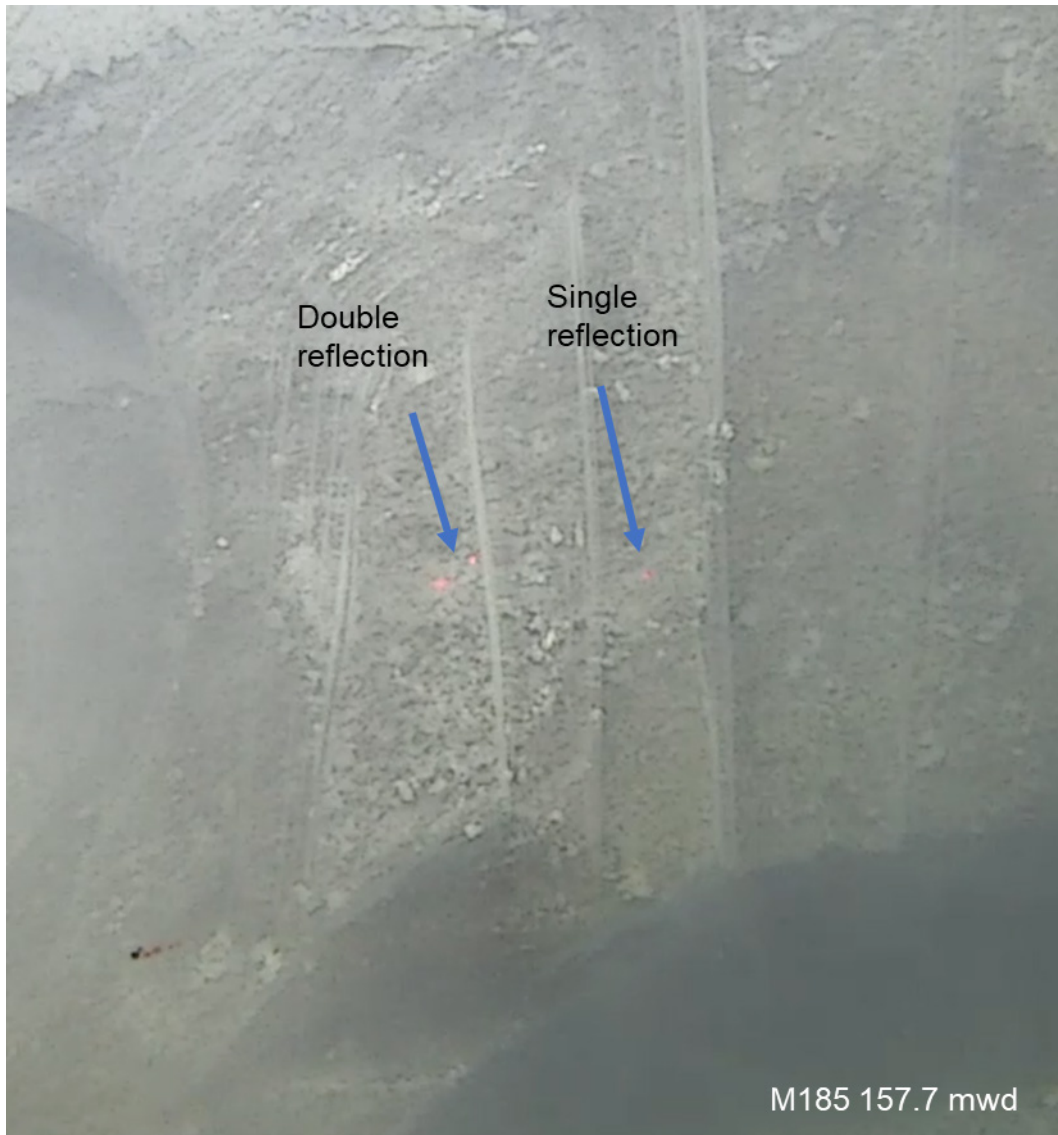


Figure 4.55. Laser beam from the ROV showed two reflected dots from the same beam. Photo courtesy of Monterey Bay Aquarium Research Institute.

Rivulets of sediment were seen continuously descending along thin vertical channels formed on the surface of the ice (Figure 4.56).

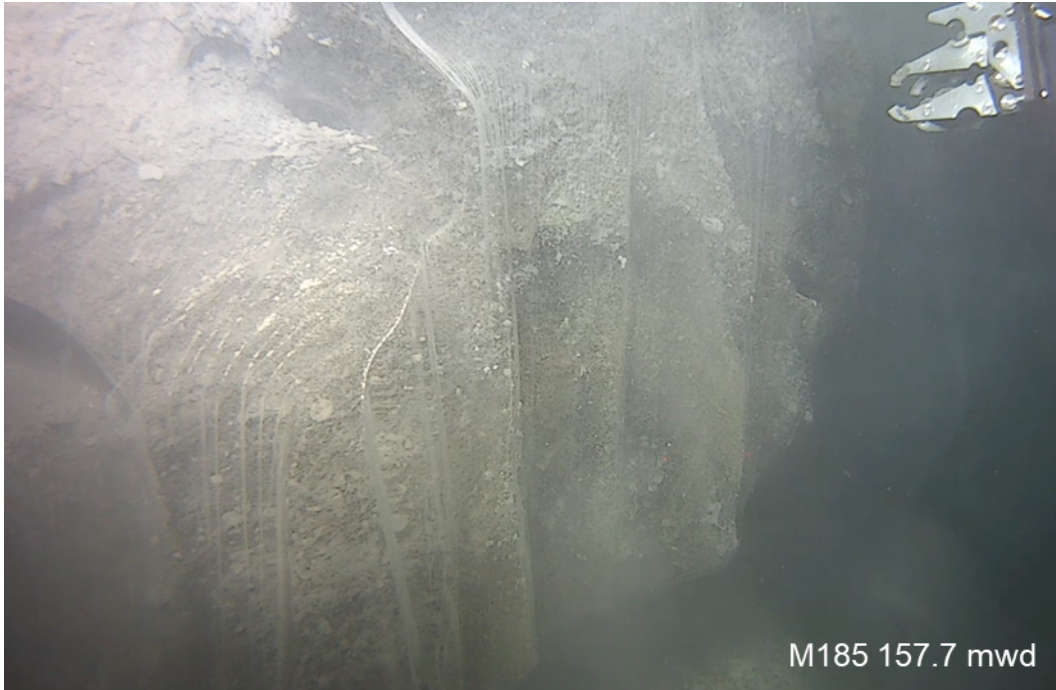


Figure 4.56. Rivulets of sediment were seen continuously descending on the surface of the ice. Photo courtesy of Monterey Bay Aquarium Research Institute.

The third area with exposures of ice was seen first as a black patch which was on a sediment covered ledge (Figure 4.57). The edges of the patch were covered with chips of the mudstone which have come from the actively crumbling scarp wall above.



Figure 4.57. Black patch on a sediment covered ledge. Photo courtesy of Monterey Bay Aquarium Research Institute.

A few meters further to the SE the ice layer reemerged from the sediment cover. Here the exposed black-appearing ice layer was seen again clearly under an overhang in the scarp wall.

In the middle of the ice exposure there is a sediment covered ledge, but the ice appears to be over 50 cm thick (Figure 4.58).

Two push cores (M185 PsC-5 and M185 PsC-19) were taken in 160 mwd at sites which we believe is associated with the largest depth change measure by the 2019 SWL survey and the 2022 AUV survey.

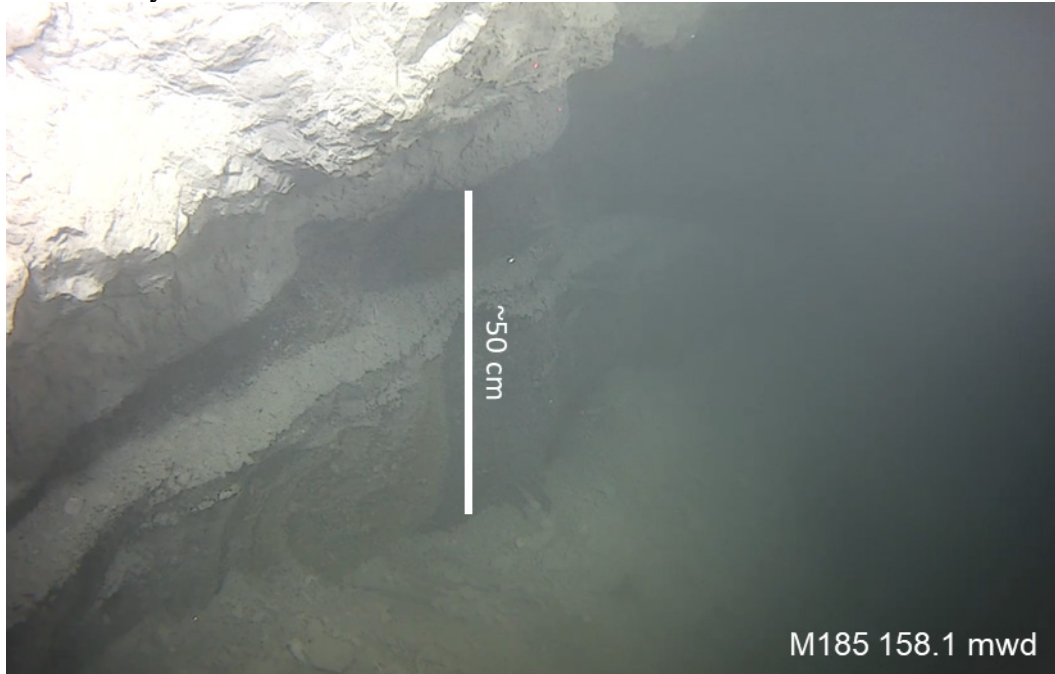


Figure 4.58. Ice exposure appears to be over 50 cm thick. Photo courtesy of Monterey Bay Aquarium Research Institute.

Key observations:

- The ongoing crumbling of the walls suggests that the collapse that created the new depression has occurred recently.
- The numerous small failures on the wall indicate that the present walls of the depression are unstable and are continuing to erode at a fast pace.
- The hardness and translucent character of the black material suggest it consists of layers of segregated permafrost ice.
- The ice contained opaque inclusions floating in the transparent ice matrix.
- At the ambient conditions the ice is exposed to (i.e., -1.198°C temperature and 33.51 ppt salinity) the ice is unstable and it will melt. Thus, undercuts and subsurface void space may be attributed to the decomposition of permafrost horizons.
- The undercutting observed on the side walls suggests that ice melting leaves the sidewalls susceptible to further collapse.
- The on-going failures in the overlying gray mudstones may be caused by receding support underneath due to melting of the underlying ice.

4.3.6. ARA13C ROV-05

MBARI Dive M186, Sunday September 4th, 2022

The dive target was a newly developed seafloor depression. This depression was identified by comparing the surface-ship bathymetry collected by the CCGS Sir Wilfred Laurier in 2019, and bathymetry collected in 2022 during this cruise (ARA13C) by the mapping AUV (Figure 4.59).

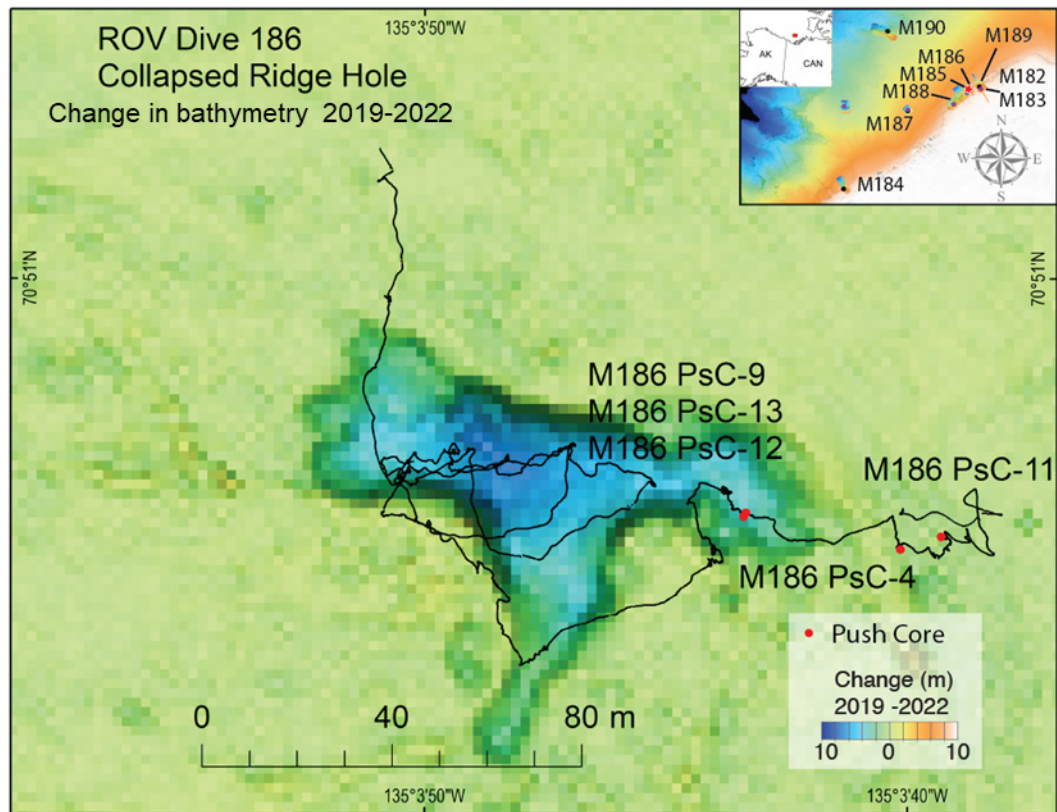


Figure 4.59. Change in bathymetry between 2019 and 2022 with details of Dive M186

The new depression developed along what was previously the crest of a 100 m long smooth ridge. The depression is colloquially referred to as “Collapsed Ridge Hole”. The greatest detected change in depth is -9 m.

The crest has now turned into a 25 m wide trough surrounded on both sides by scarps that are up to 4 and 3 m high on the NNE and SSW sides, respectively (Figure 4.60). The surface of the new trough has a complex morphology consisting of oval shaped holes encircled by small-scale ridges. Similar morphologies are seen on the crests of many other ridges in this area. The objective of the dive was to explore this newly formed depression.

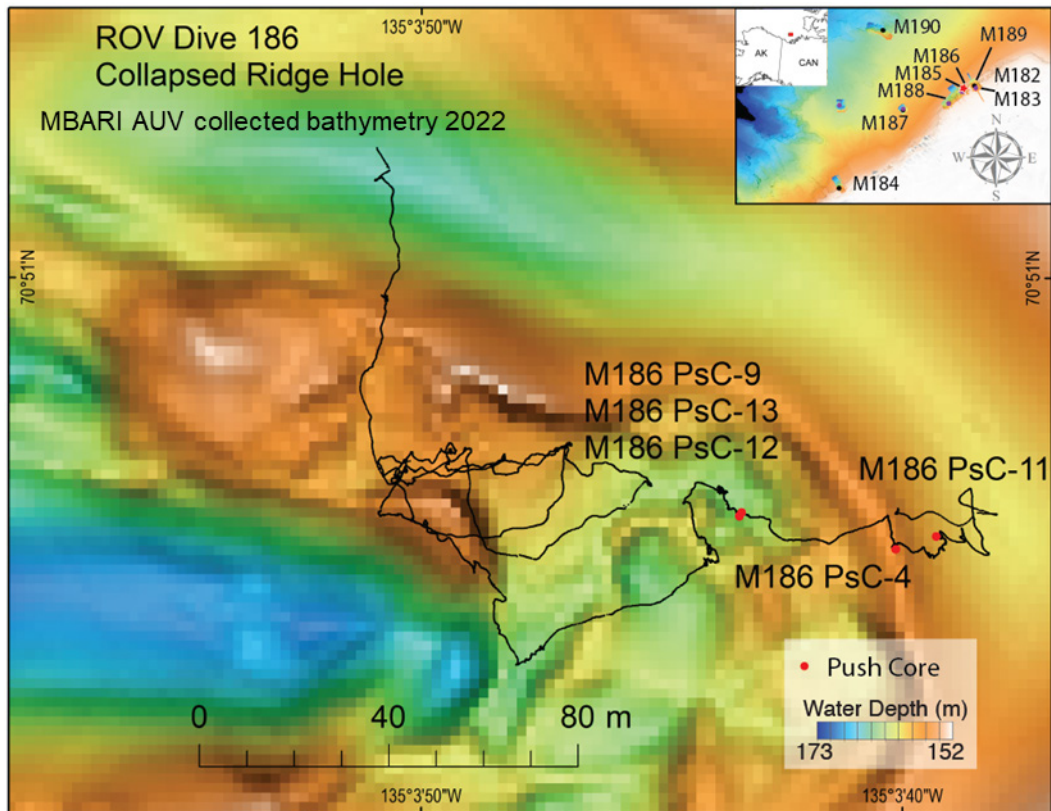


Figure 4.60. MBARI AUV collected bathymetry 2022 with details of Dive M186

The ROV landed above the northern flank, outside the depression and encountered a gently sloping surface, colonized by sessile organisms (e.g., soft corals and sea pens) (Figure 4.61).



Figure 4.61. Gently sloping surface, colonized by sessile organisms. Photo courtesy of Monterey Bay Aquarium Research Institute.

The side wall scarp on the east-northeast side of the trough was sharply defined and transitioned abruptly to a steep slope (Figure 4.62). In places, there were secondary 5-10 cm high scarps with down-dropped blocks extending a meter or two from the edge.



Figure 4.62. Side wall scarp on the east-northeast side of the trough. Photo courtesy of Monterey Bay Aquarium Research Institute.

The scarp face is composed of massive cohesive muds typically sloping at $>45^\circ$. The face of the scarp is grooved with channels that extend downslope. At the bottom of the channels small sediment fans coalesce into an apron that covers the base of the outcrop. In places, trails of fine sediment were seen moving down these channels. Sediment descent along the channels was also seen to be triggered by minimal water column disturbances created by the ROV motion. The continuous downward flow of fine sediment along the scarp wall suggests the exposed face is actively weathering (Figure 4.63).

While transiting through the depression floor, only a few sediment clouds, not attributable to disturbances produced by the ROV, were noticed. The lower frequency of unexplained sediment clouds in the “Collapse Ridge Hole” (i.e., ROV-05/M186) is in sharp contrast to the other depression (“Ice Hole” ROV-04/M185). This contrast suggests that the rate of side walls crumbling in “Collapse Ridge Hole” is less than in the “Ice Hole”. While the formation of both of these depressions occurred sometime within the 2019 to 2022 time interval, the “Collapsed Ridge Hole”, ROV-05/M186, is older than the “Ice Hole”.

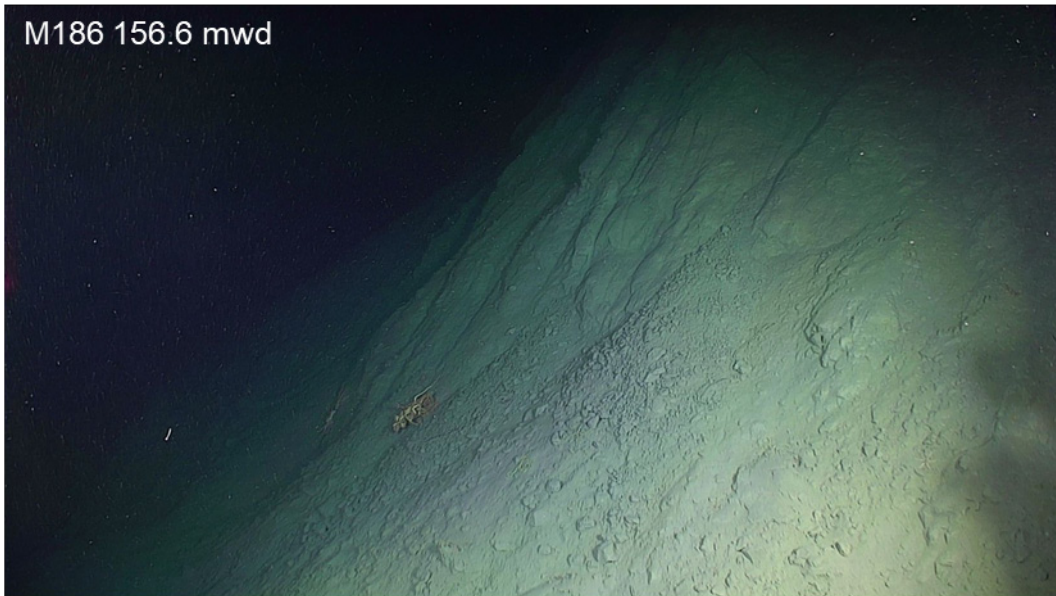


Figure 4.63. Continuous downward flow of fine sediment along the scarp wall. Photo courtesy of Monterey Bay Aquarium Research Institute.

The surface of the scarp displays a variety of textures and colors. In some places, the wall surface is smooth, with a rounded texture. In other places, lower in the scarp, the surface of the scarp displays an irregular surface and is lighter in color (Figure 4.64). The talus blocks below these latter sections of the wall are distinctively angular. Since the scarp started to develop in 2019 at the earliest, the different degrees of weathering along this depression wall indicate that the scarp is continuing to undergo active defacement. The rate of deterioration of the mud face is fast enough for secondary failures to start to develop within the three year long period.



Figure 4.64. The surface of the scarp displays a variety of textures and colors. Photo courtesy of Monterey Bay Aquarium Research Institute.

While transiting through the depression floor, only a few sediment clouds, not attributable to disturbances produced by the ROV, were noticed. The lower frequency of unexplained sediment clouds in the “Collapse Ridge Hole” (i.e., ROV-05/M186) is in sharp contrast to the

other depression (“Ice Hole” ROV-04/M185). This contrast suggests that the rate of side walls crumbling in “Collapse Ridge Hole” is less than in the “Ice Hole”. While the formation of both of these depressions occurred sometime within the 2019 to 2022 time-interval, the “Collapsed Ridge Hole”, ROV-05/M186, is older than the “Ice Hole”.

The bottom of the depression is typically draped with a veneer of soft sediment (Figure 4.65). Pieces of debris of variable size are scattered over the depression floor and covered in fine sediment. When not covered by sediment and exposed, some of the debris blocks have rounded edges. Circles of crumbled material surrounding the blocks on the floor suggest they are disintegrating in place. No sessile organisms were seen colonizing the depression floor.

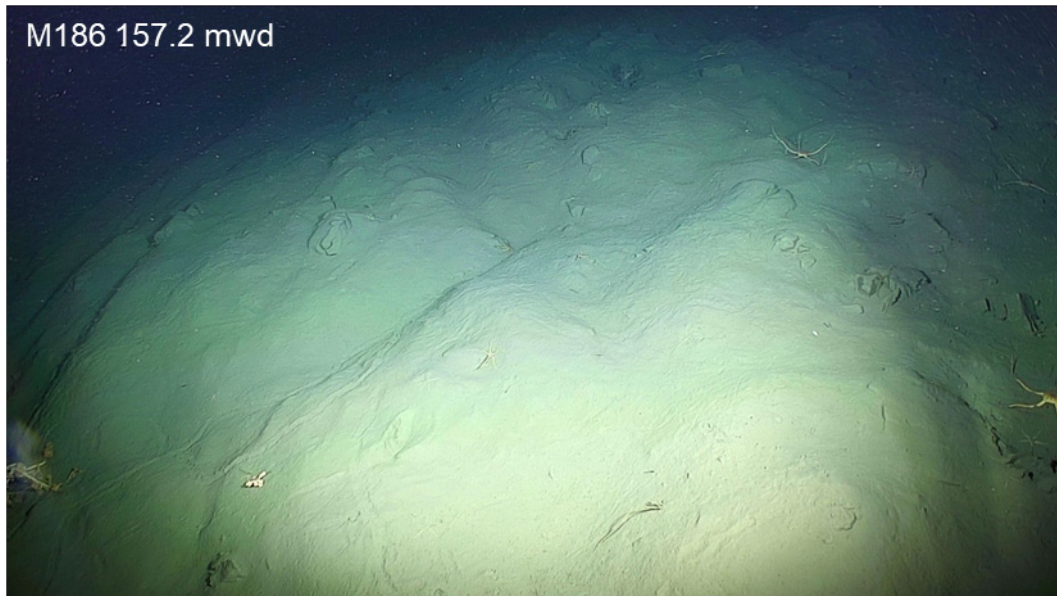


Figure 4.65. The bottom of the depression is typically draped with a veneer of soft sediment. Photo courtesy of Monterey Bay Aquarium Research Institute.

The seafloor surface within the collapsed depression shows a considerable amount of local topography. Generally, these bottom textures occur in patches with abrupt boundaries. For example, the image below shows a small local fault scarp where one side is down-dropped (Figure 4.66). The surface of the down-dropped block is flatter in contrast to the more irregular topography on the higher block. In addition, a linear depression runs along the fault trace but the sediment failures along the fault scarp do not continue onto the adjacent block.

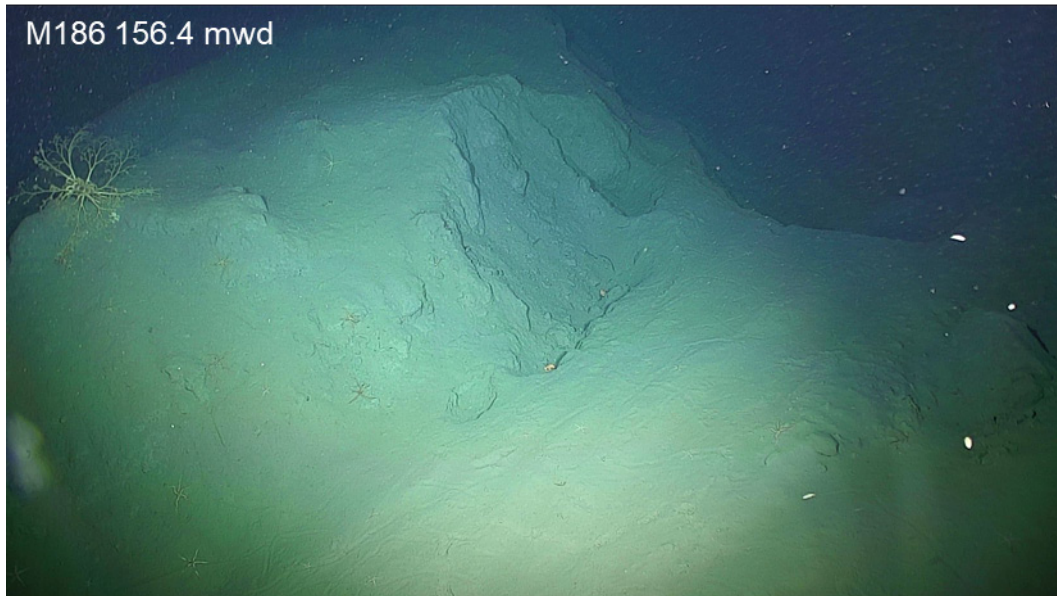


Figure 4.66. Small local fault scarp. Photo courtesy of Monterey Bay Aquarium Research Institute.

Collapse holes were seen within sediment aprons below some scarps (Figure 4.67). However, layers of hard black material, interpreted to be segregated permafrost ice, such as those seen on ROV-04/M185, and subsequently on ROV-07/M188, were not observed on this dive (ROV-05/M186).

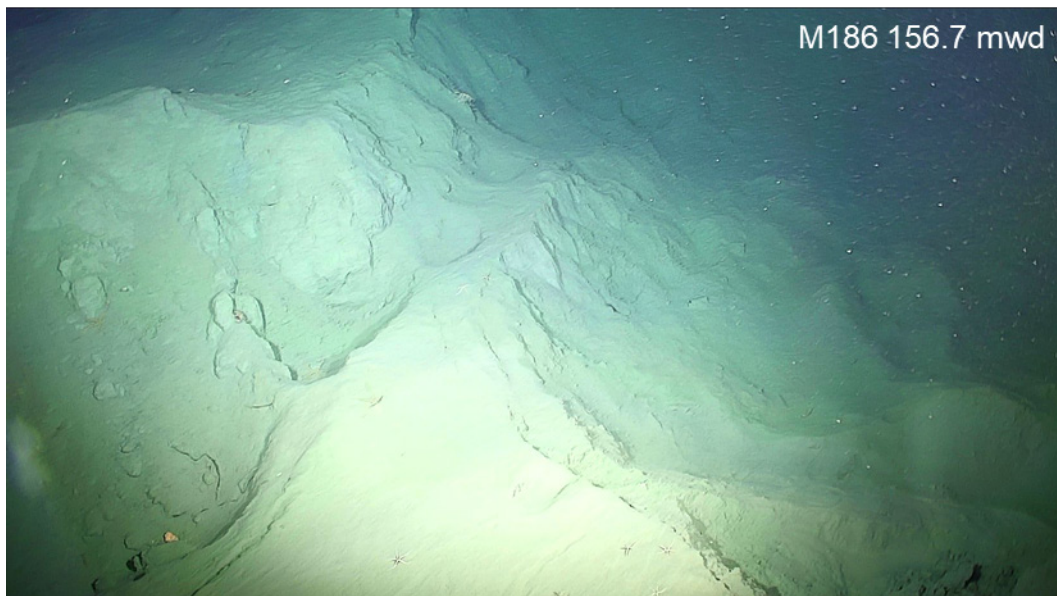


Figure 4.67. Collapse holes within sediment aprons. Photo courtesy of Monterey Bay Aquarium Research Institute.

During a southern transect the ROV crossed a ~30 m long section of the seafloor that has shown no change between 2019 and 2022. This area was colonized with sessile organisms (i.e., soft corals). On the eastern edge of the colonized patch, the lower ends of tubeworms were exposed along the top of a small scarp, suggesting a post-2019 failure (Figure 4.68).

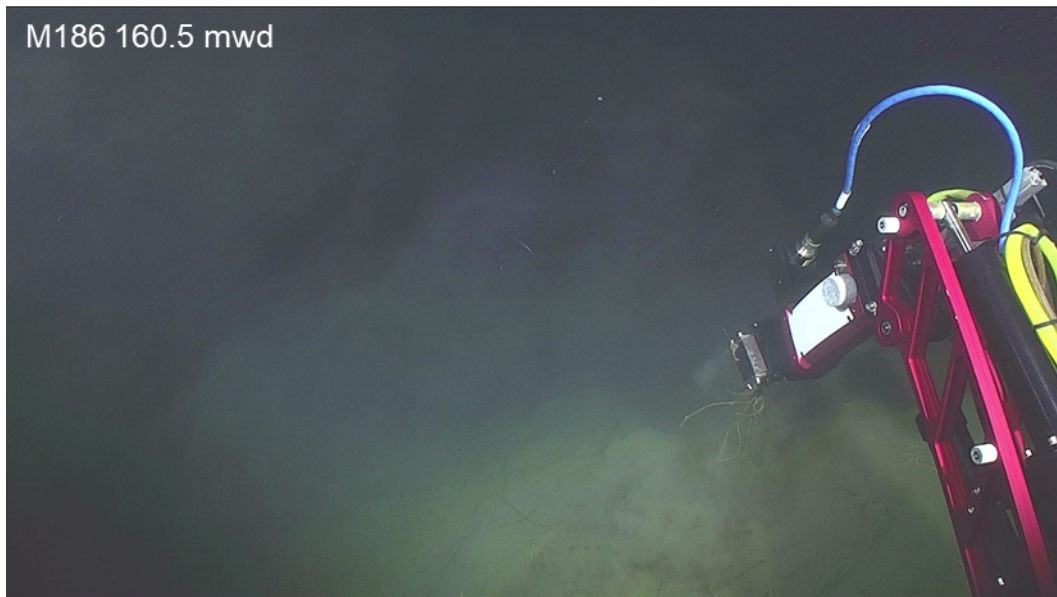


Figure 4.68. Sample collection via the ROV arm. Photo courtesy of Monterey Bay Aquarium Research Institute.

In order to be able to compare pre- and post- failure sediment, push cores were taken at two locations: Push cores M186 PsC-9, M186 PsC-13 and M186 PsC-12 were taken within the new depression, and M186 PsC-4 and M186 PsC-11 outside the depression.

4.3.7. ARA13C ROV-06

MBARI dive M187, Sunday September 4th, 2022

This dive site is on the top of a mud volcano located in 420 mwd (Figure 4.69). The dive objectives were to sample tubeworms and microbial communities, and to inspect the seafloor expression left by the heat probe (ST15-HF, ST16-HF, ST17-HF) at the penetration sites where heat flow measurements were conducted on this cruise (see Chapter 6).

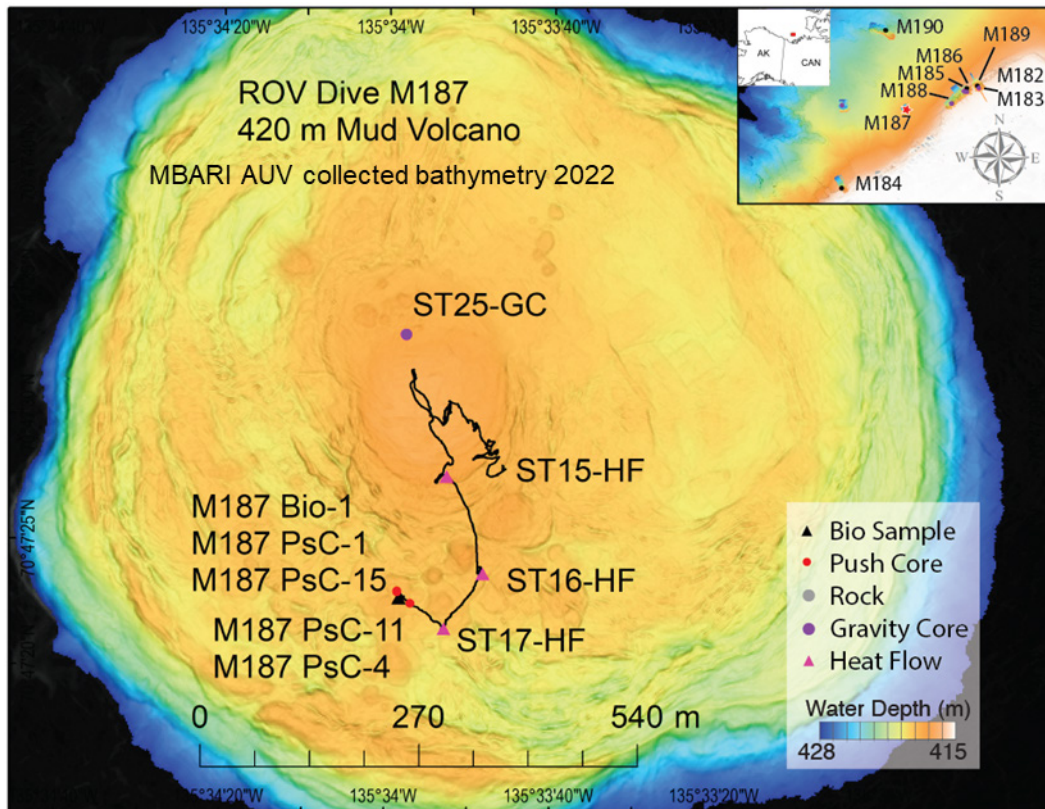


Figure 4.69. MBARI AUV collected bathymetry 2022 with details of Dive M187

This mud volcano was surveyed four times (2013, 2016, 2017, and during this cruise ARA13C in 2022) with a mapping AUV: A comparison between the bathymetric grids of 2022 and 2017 shows an area approximately at the center of the volcano that rose 2.5 m over the 5-year time period (See Chapter 3) (Figure 4.70).

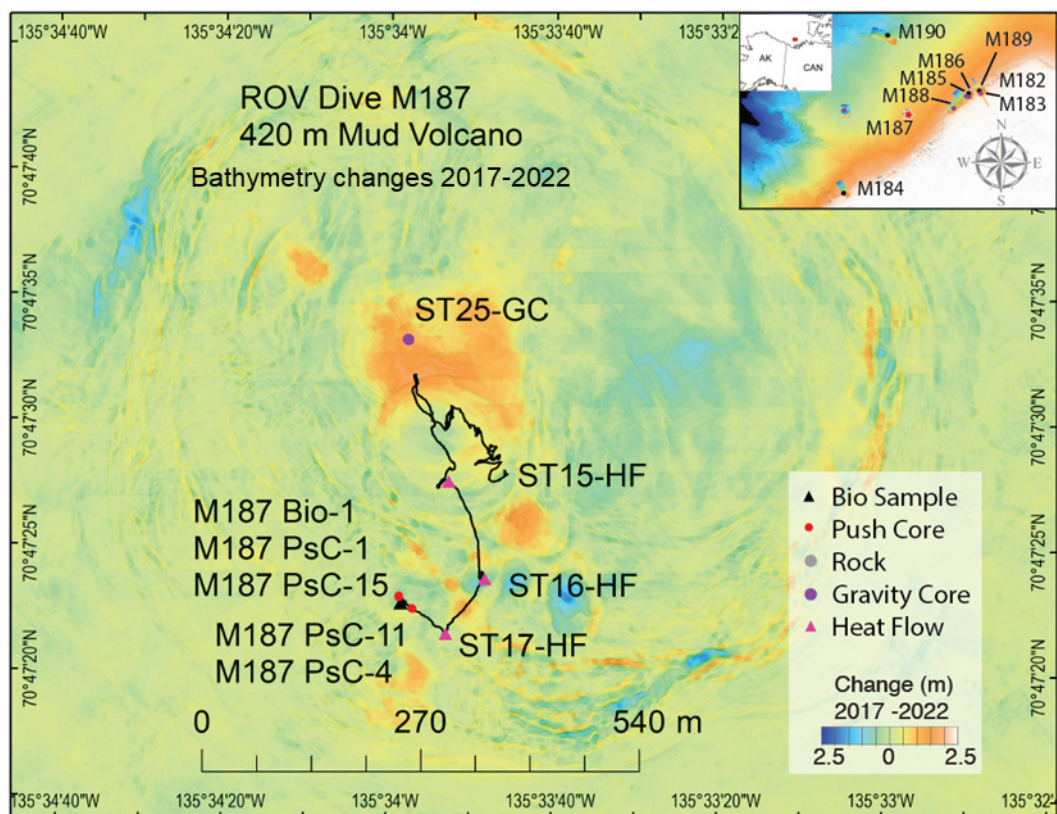


Figure 4.70. Change in bathymetry between 2017 and 2022 with details of Dive M187

Additional aims of this dive were to explore the different floor textures that develop in this dynamic environment. Previous work has shown that mud flows leave distinct seafloor textural expressions with different degrees of organism colonization depending on the time lapse since the last eruption (Paull et al. 2015). Areas that have been stable for long periods are extensively colonized by tubeworms. Resampling tubeworms to better understand their chemosynthetic endosymbionts was a priority of the dive (Lee, Y.M., et al., 2019; Lee, D.-H., 2019). An additional dive objective was to locate the gas source (and sample, if possible), creating water column anomalies over this site detected by the IBRV Aaron's EK echosounder system.

The ROV landed at 420.9 mwd at a site extensively colonized by tubeworms. The presence of patches of black sediment rimmed with white bacterial mats was also noted upon landing.

Samples were taken in 421.2 mwd for microbial analysis of the tube worm colonies (Figure 4.71). The manipulator arm was used to sample tubeworms, which reached up to 30 cm long. Push cores M187 PsC-1 and M187 PsC-15 were also taken nearby. M187 PsC-1 was from within the tube worms and showed roots of the worm extended from below the core tube. Push core M187 PsC15 was taken ~0.3 m away, but in an area without visible tubeworms.

A set of two push cores were also taken at 420.9 mwd for microbial analysis. M187 PsC-11 and M187 PsC-4 were both taken in the middle of bacterial mat patches.

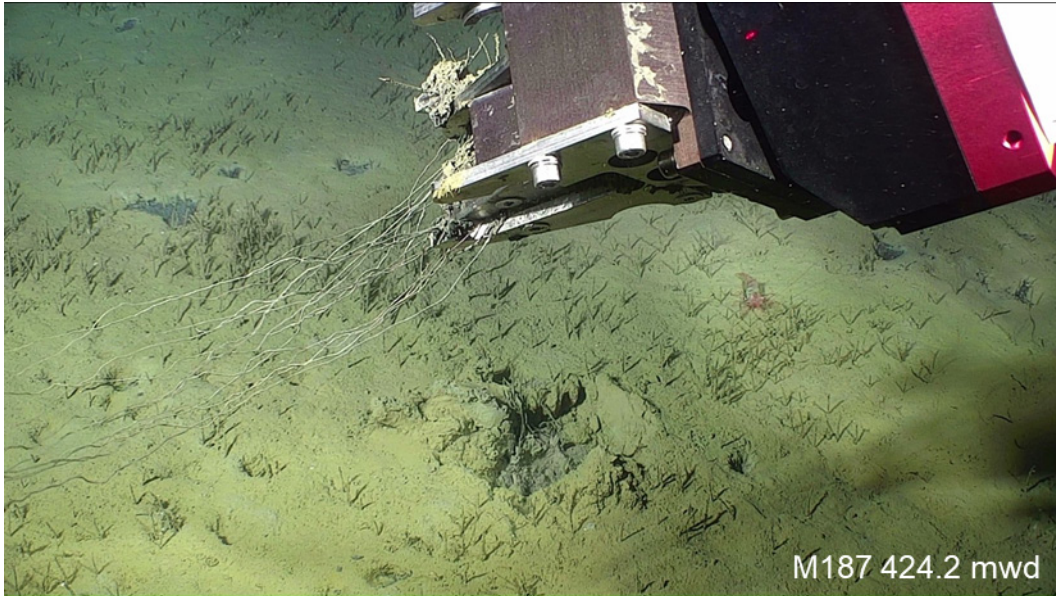


Figure 4.71. Samples taken for microbial analysis of tube worm colonies. Photo courtesy of Monterey Bay Aquarium Research Institute.

A variety of seafloor textures were transited by the ROV during this dive. The textures included: established tubeworms colonies on old mudflows, lumpy uncolonized seafloor, bacterial mats, short discontinuous linear ridges, dimpled seafloor and colonized ridges (Figure 4.72).

A set of two push cores were also taken at 420.9 mwd for microbial analysis. M187 PsC-11 and M187 PsC-4 were both taken in the middle of bacterial mat patches.

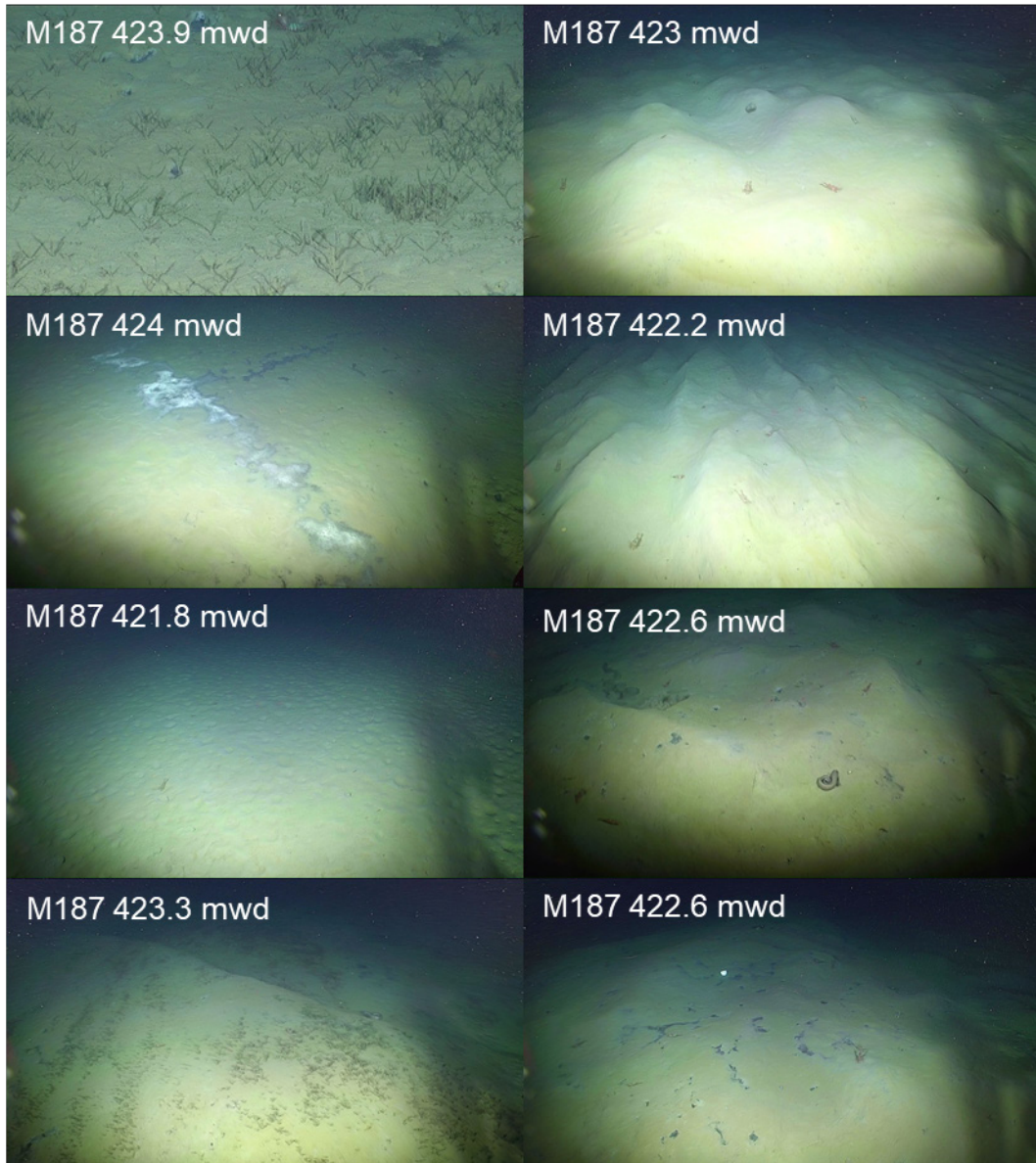


Figure 4.72. Seafloor textures transited by the ROV during dive M187. Photos courtesy of Monterey Bay Aquarium Research Institute.

The ROV proceeded towards the site of temperature gradient measurements conducted during this cruise (Figure 4.73). The heat probe used in these measurements is a series of thermistors attached to a barrel connected to a heavy weight. Three sites were penetrated by the probe that made successive temperature gradient measurements of the subsurface down to 50 m below the seafloor. The points of impact and penetration of the probe were found by following signs of fresh rubble and the imprint in the sediment left by the extra few meters of cable paid out at the end of the tests (Figure 4.74).

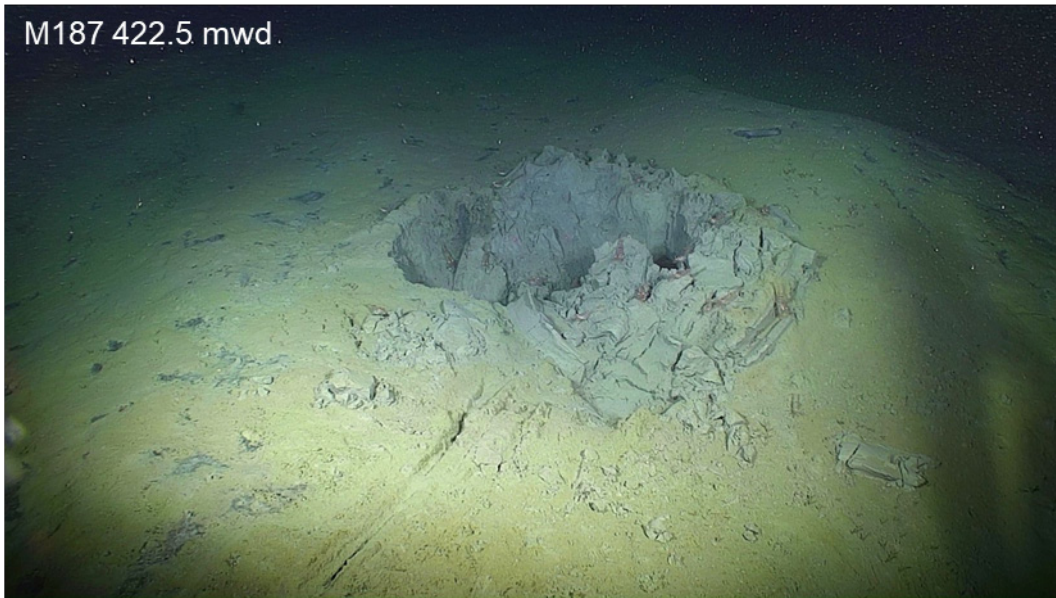


Figure 4.73. Site of temperature gradient measurements conducted during this cruise. Photo courtesy of Monterey Bay Aquarium Research Institute.

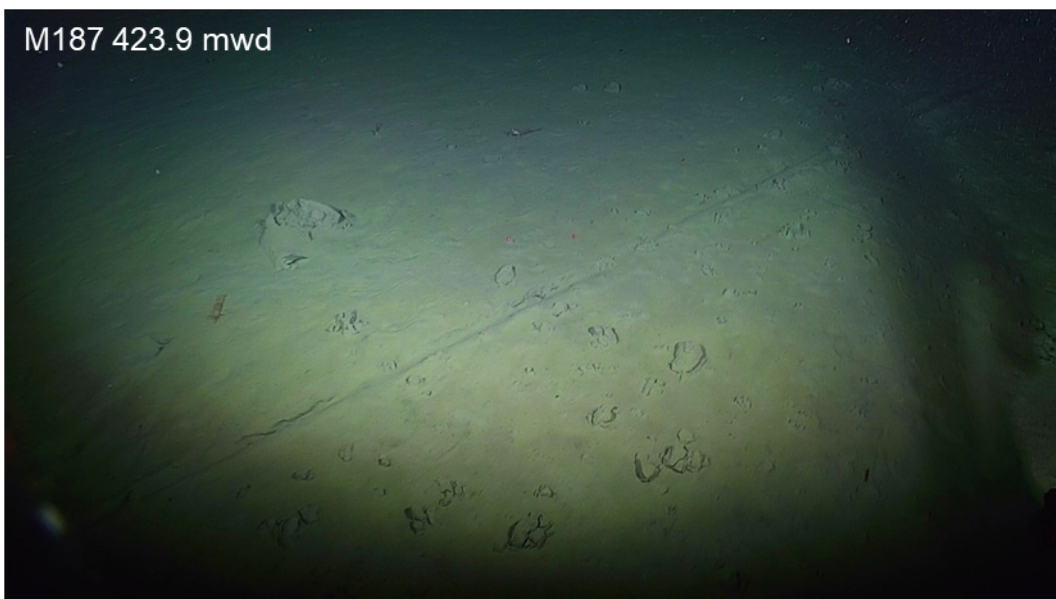


Figure 4.74. Signs of fresh rubble and the imprint in the sediment left by the extra few meters of cable. Photo courtesy of Monterey Bay Aquarium Research Institute.

The thermal probe of the ROV was inserted into the sediment rim of the hole created by the heavy weight of the gradient thermal probe at site ST17-HF (Figure 4.75). The temperature above the hole was 0.5°C and 0.78°C at an estimated sediment depth of ~ 20 cm.

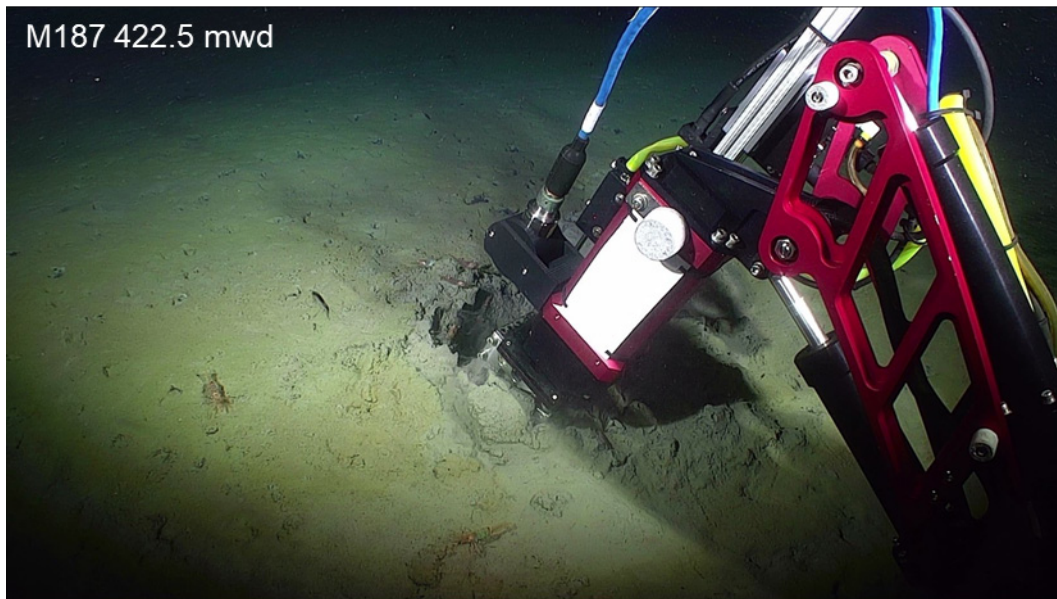


Figure 4.75. The thermal probe of the ROV was inserted into the sediment rim of the hole created by the heavy weight of the gradient thermal probe at site ST17-HF. Photo courtesy of Monterey Bay Aquarium Research Institute.

4.3.8. *ARA13C ROV-07*

MBARI Dive M188, Monday September 5th

This dive was conducted at a site where significant bathymetry changes were detected when comparing the multibeam surveys collected by CCGS Amundsen in 2010 and by CCGS Sir Wilfred Laurier 2019 (Figure 4.76). This recently developed depression was documented in Paull et al. 2022. The change in depth was seen along a scarp that marks the southern edge of the denuded terrain. Earlier in the expedition, Station11-GC captured ice 60 cm below the seafloor, motivating this ROV dive.

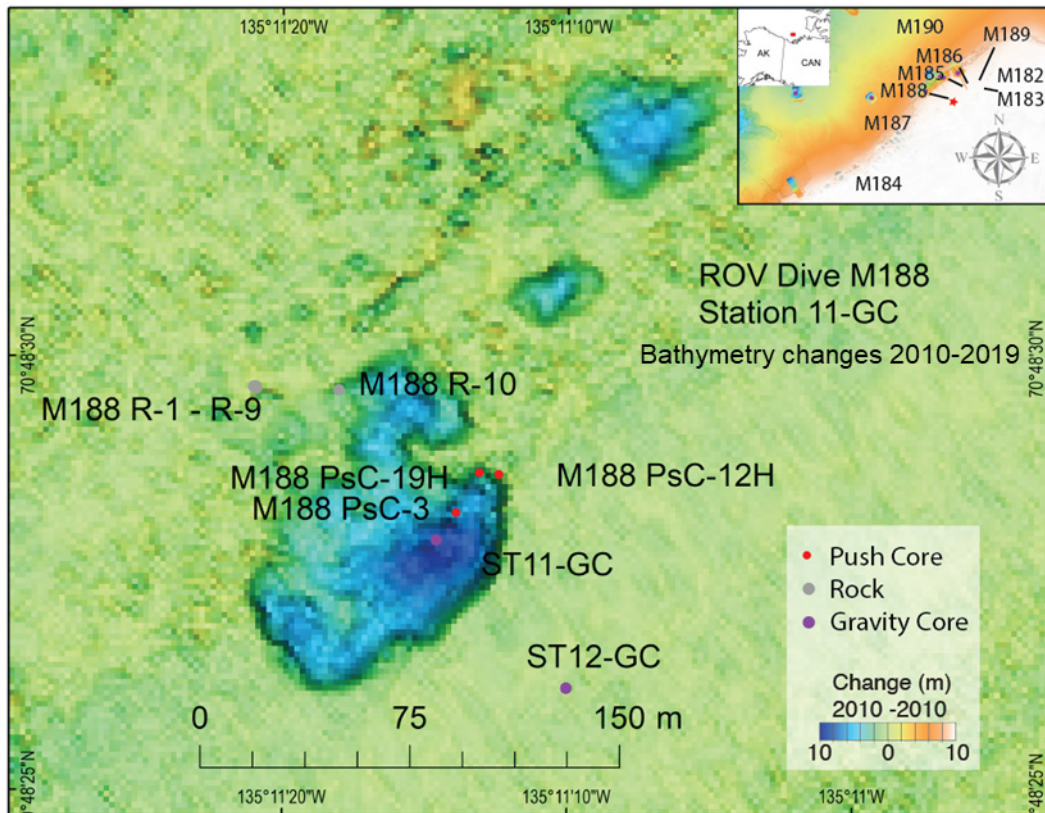


Figure 4.76. Change in bathymetry between 2010 and 2019 with details of Dive M188

This ROV dive (ROV-07/M188) took place before navigation corrected data from the 2022 AUV survey of this area were available. Post-dive, based on the AUV 2019 and 2022 surveys, it was determined that new depth changes have taken place over the last three years just northeast of where the scarp retreat occurred between 2010 and 2019 (Figure 4.77).

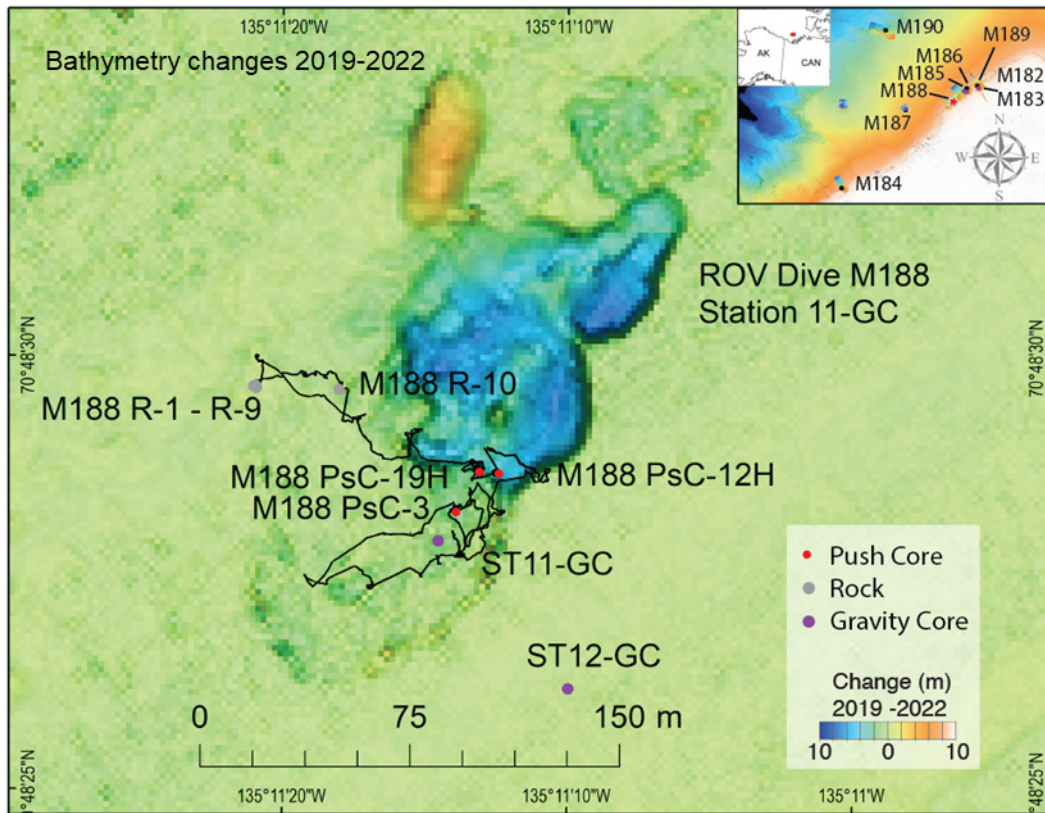


Figure 4.77. Change in bathymetry between 2019 and 2022 with details of Dive M188

This ROV dive covered the south scarp developed in the time period 2010-2019. The ROV took place between 118- and 141-meter water depths, making a transect up the slope to the headwall, and returning back down slope to explore the face of the scarp along strike to the SW (Figure 4.78).

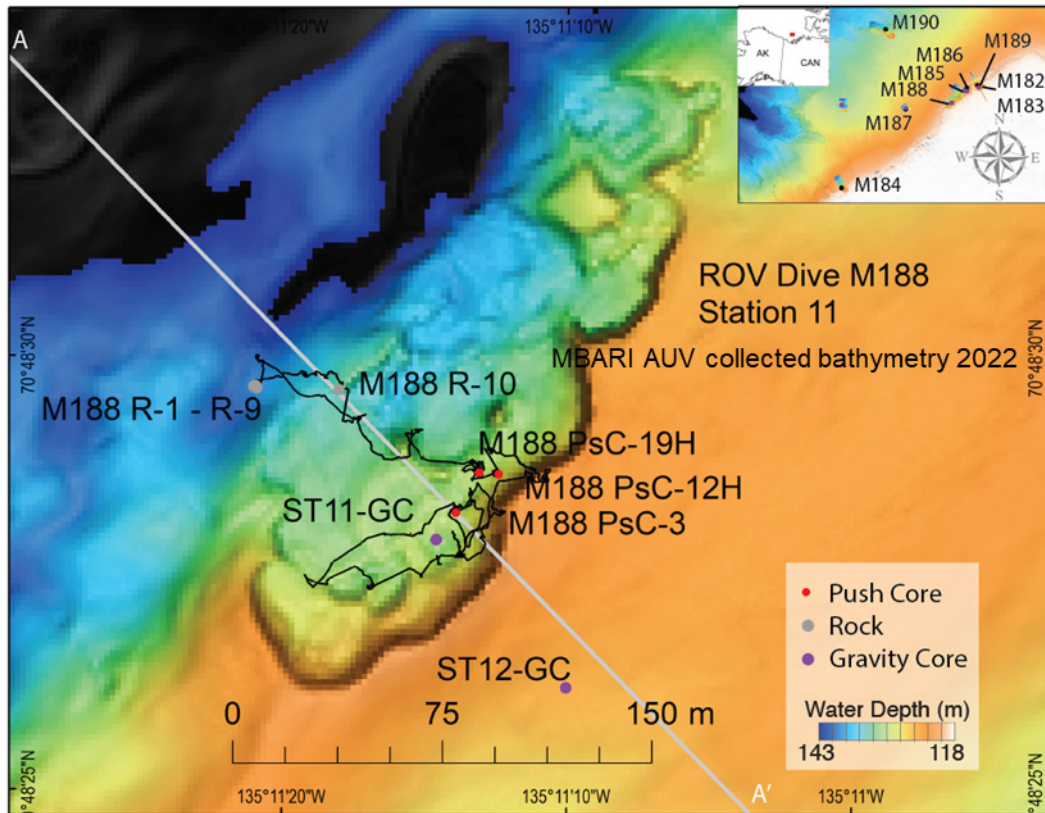


Figure 4.78. MBARI AUV collected bathymetry 2022 with details of dive M188

An IBRV Araon Chirp profile (Figure 4.79) was collected on the 2022 cruise that ran from the layered sediments on the upper slope, over the entire denuded zone (Paull et al., 2022), across a slope failure scarp (the target of this dive) and onto the undulating surface of the continental shelf. This profile shows the relationship of the ST11-GC and ST12-GC sites to the undulating diffuse reflector that is truncated by the scarp. Ice was sampled in ST11-GC and observed during the miniROV near where M188 PsC-3 was taken.

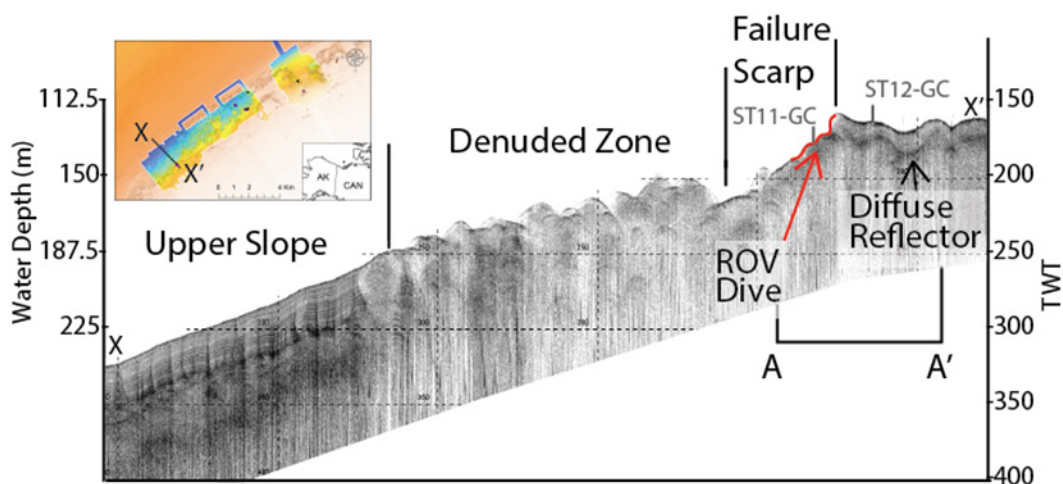


Figure 4.79. IBRV Araon Chirp profile collected on the 2022 cruise that ran from the layered sediments on the upper slope

The observations made on this dive are described by ascending depth rather than in sequential order.

Lower on the slope there were a number of ~1 m wide rounded grooves with pushed up sides interpreted to be a trawl mark (Figure 4.80). These features are seen within an otherwise smooth seafloor surface.

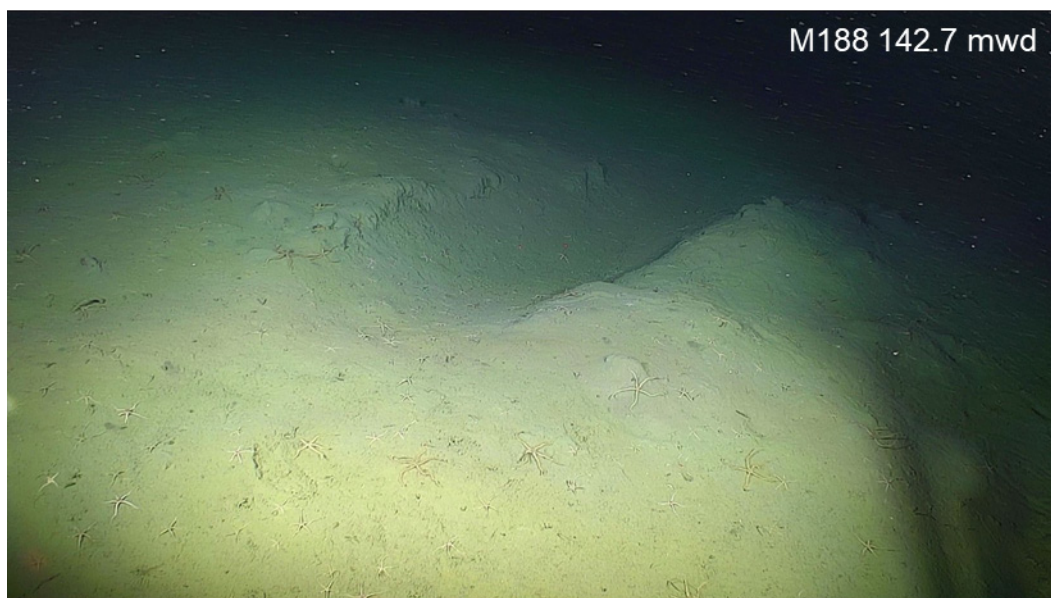


Figure 4.80. Rounded grooves with pushed up sides interpreted to be a trawl mark. Photo courtesy of Monterey Bay Aquarium Research Institute.

At 141 mwd a tongue of rubble was seen, which appeared to be a slide deposit (Figure 4.81). It contained numerous hard rounded pebbles and cobbles (Figure 4.82). Eight rock samples were collected at ~140 mwd. After recovery, these were judged to be chert cobbles.

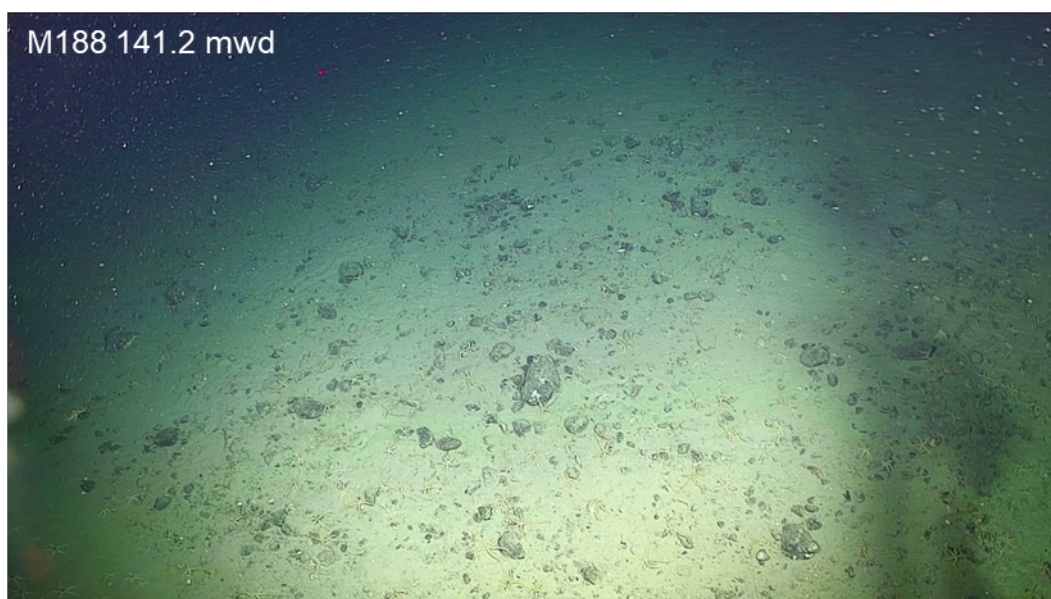


Figure 4.81. Tongue of rubble with numerous hard rounded pebbles and cobbles. Photo courtesy of Monterey Bay Aquarium Research Institute.



Figure 4.82. Hard rounded pebbles and cobbles at 141.4 mwd. Photo courtesy of Monterey Bay Aquarium Research Institute.

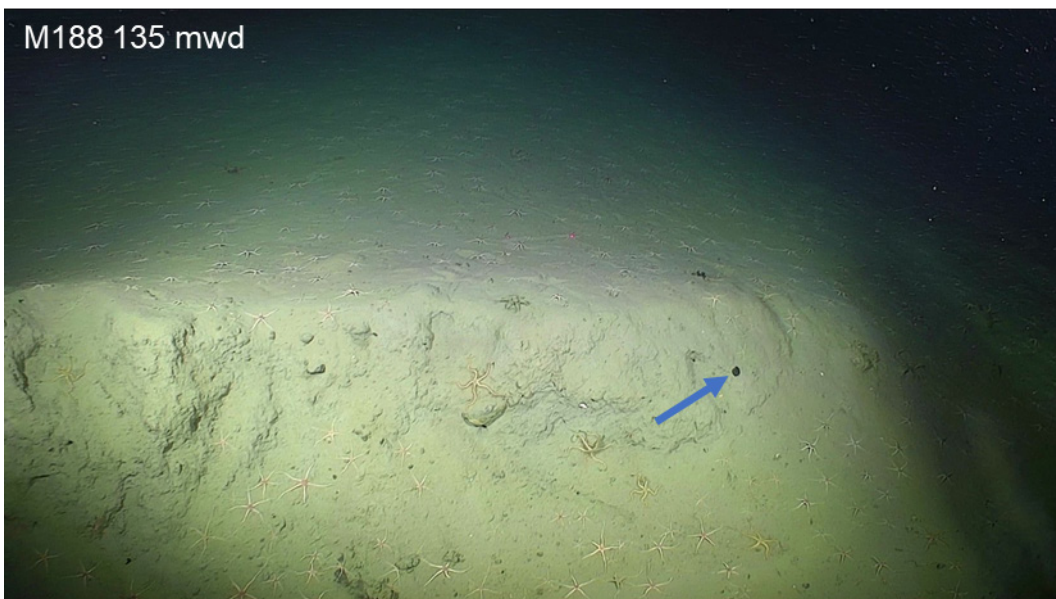


Figure 4.83. Deposits containing multiple angular clasts and large boulders. Photo courtesy of Monterey Bay Aquarium Research Institute.

In ~130 mwd there are deposits containing multiple angular clasts including large boulders suggesting this is part of a large debris flow deposit (Figure 4.83). There are also numerous depressions (Figure 4.84). There are no indications that these depressions have been cut by surface erosion as a result of downslope channeling. Instead, these depressions might be interpreted as being collapse features.

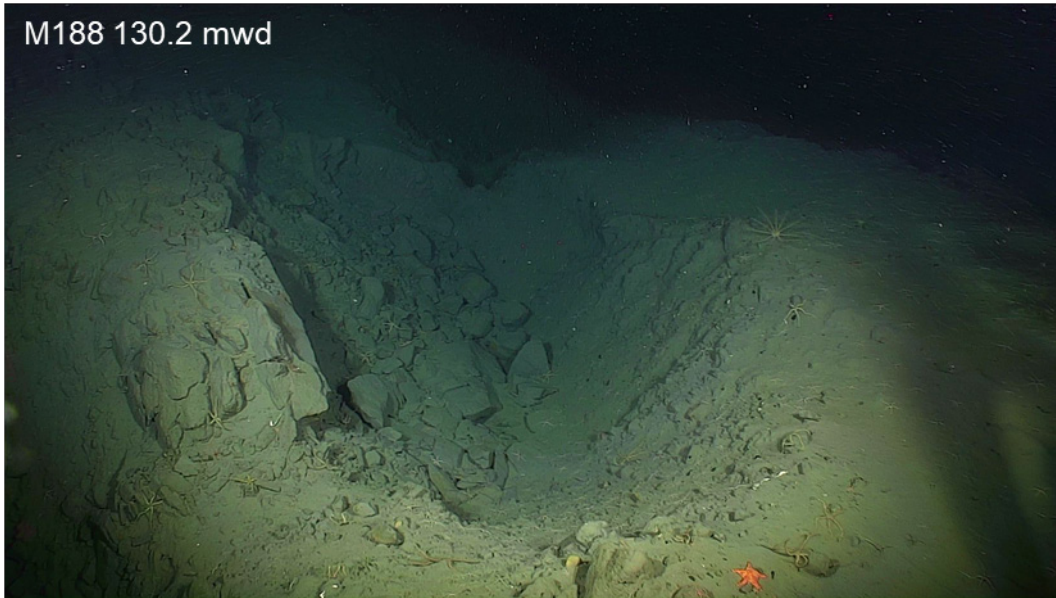


Figure 4.84. Depression that might be interpreted as being a collapse feature. Photo courtesy of Monterey Bay Aquarium Research Institute.

Closed smaller depressions are common within the surface of the debris (129 mwd) (Figure 4.85).



Figure 4.85. Small depressions within the surface of the debris. Photo courtesy of Monterey Bay Aquarium Research Institute.

Distinctive black areas, interpreted to be the surface of exposed segregated ice horizons, were seen in several holes in the 129 to 130 m depth range (Figure 4.86). The appearance of the ice is similar to the ice seen in ROV-04/M185.



Figure 4.86. Black areas, interpreted to be the surface of exposed segregated ice horizons. Photo courtesy of Monterey Bay Aquarium Research Institute.

The texture of the ice visible in the ROV camera, is also similar to ice captured in the gravity core from nearby (ST11-GC) at the same water depth (130 mwd) (Figure 4.87).



Figure 4.87. Ice captured in the gravity core. Photo courtesy of Korea Polar Research Institute.

The whole round section of the ice from Station 11-GC was cut in half with a hacksaw. The ice was 4 cm thick, transparent and had opaque inclusions (Figure 4.88).



Figure 4.88. Ice was 4 cm thick, transparent and had opaque inclusions. Photo courtesy of Monterey Bay Aquarium Research Institute.

Open voids were seen under the exposed face of the ice (Figure 4.89). The manipulator arm was unable to make a visible scratch on the surface of the ice using either a push core tube or its titanium arm. Horizontal push cores were taken in the gray sediment above the exposed ice for ^{14}C dating.

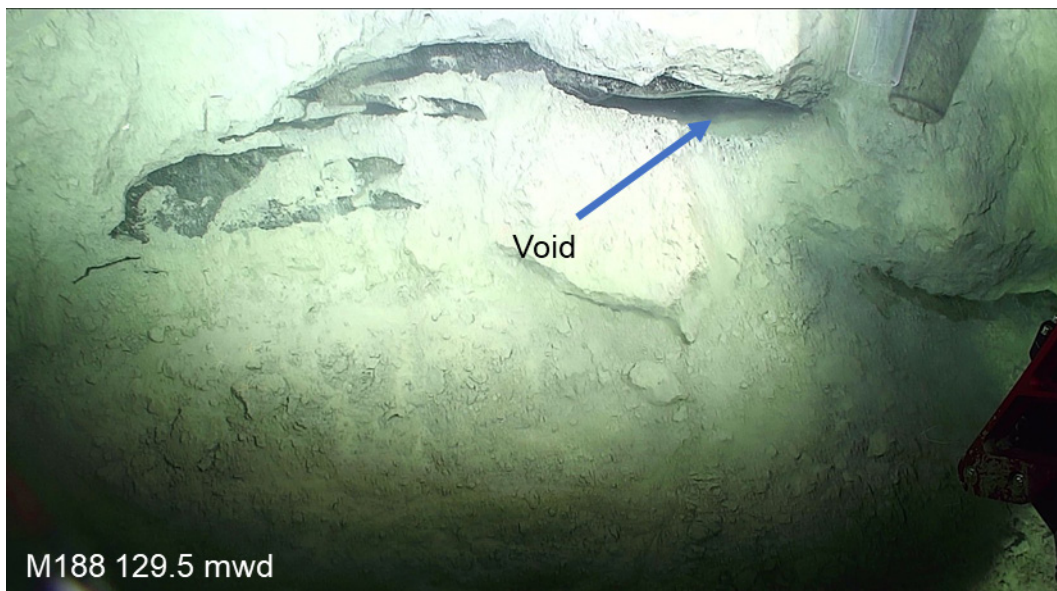


Figure 4.89. Open void under the exposed face of the ice. Photo courtesy of Monterey Bay Aquarium Research Institute.

At another exposure, thin rivulets of fine sediment slowly flowed across the slanting surface of the ice (Figure 4.90). At an abrupt change in the orientation of the ice face, sediment was

observed to flow over a small overhang and cascade straight downward. Based on the distance between the laser beams, it is estimated that the thickness of the exposed ice is >20 cm.



Figure 4.90. Rivulets of fine sediment slowly flowed across the slanting surface of the ice. Photo courtesy of Monterey Bay Aquarium Research Institute.

A water sample (M188-W1) was taken with the hope of capturing some of the water produced by the melting of the ice, which is unstable at the temperature and salinity of bottom waters (see ROV-04/M185 dive) (Figure 4.91). The sampling device consisted of a 50 cc evacuated cylinder connected to a plastic inverted funnel through an on/off valve. The valve is mechanically turned when the manipulator arm squeezes two metal plates.



Figure 4.91. A water sample (M188-W1) was taken with the hope of capturing some of the water produced by the melting of the ice. Photo courtesy of Monterey Bay Aquarium Research Institute.

Black patches of ice were observed in several nearby holes (Figure 4.92). The surface of the ice in these holes are all in water depths between 129 and 130 m. All these exposures might be part of a laterally continuous ice layer.

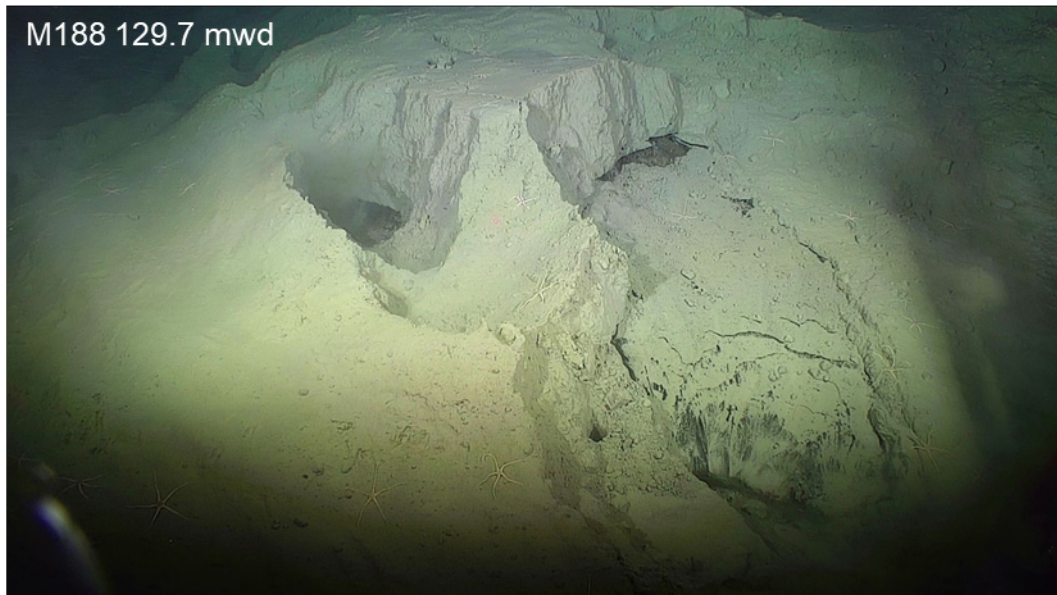


Figure 4.92. Black patches of ice observed in several holes. Photo courtesy of Monterey Bay Aquarium Research Institute.

At ~128 mwd the ROV arrived at an area not covered in rubble, consisting of massive sediment cut by steeply dipping fractures (Figure 4.93). The exposed surface could be part of a huge boulder composed of intact strata.

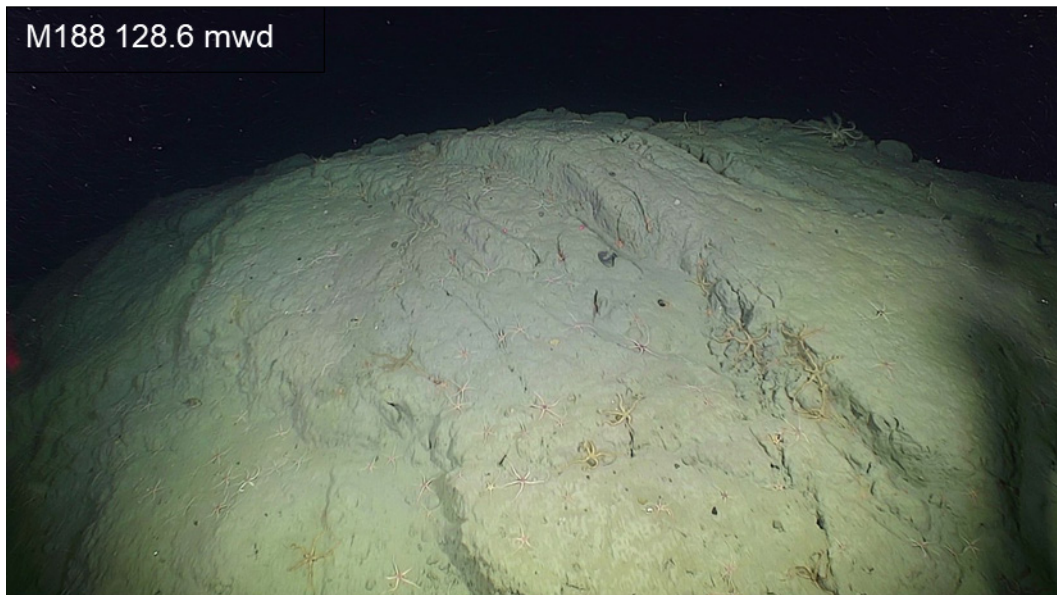


Figure 4.93. Massive sediment cut by steeply dipping fractures. Photo courtesy of Monterey Bay Aquarium Research Institute.

Moving further upslope above <125 mwd, the face of the scarp steepened, becoming near vertical in places, with occasional overhangs (Figure 4.94). Faint lineations running along the escarpment face suggest some thick bedding within the otherwise massive outcrop surface.



Figure 4.94. Scarp face with overhang. Photo courtesy of Monterey Bay Aquarium Research Institute.

Truncated beds with sharply defined edges are visible at 120 mwd (Figure 4.95). However, a smaller step ~3 m away from the exposed scarp face suggests this is a slightly down-dropped block of strata near the top of the main scarp.

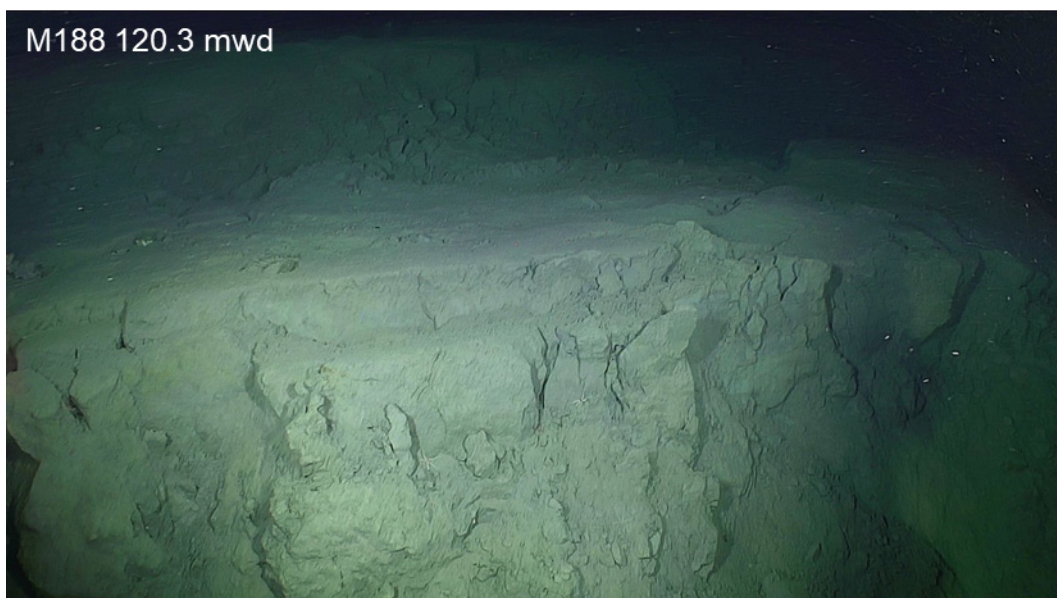


Figure 4.95. Truncated beds with sharply defined edges. Photo courtesy of Monterey Bay Aquarium Research Institute.

In 119 mwd an open crown crack was observed (Figure 4.96). Sessile organisms were seen on the surface to the south. ROV sonar indicated the top of the escarpment had been reached and that there were no more down-dropped blocks in front of the ROV to the south.

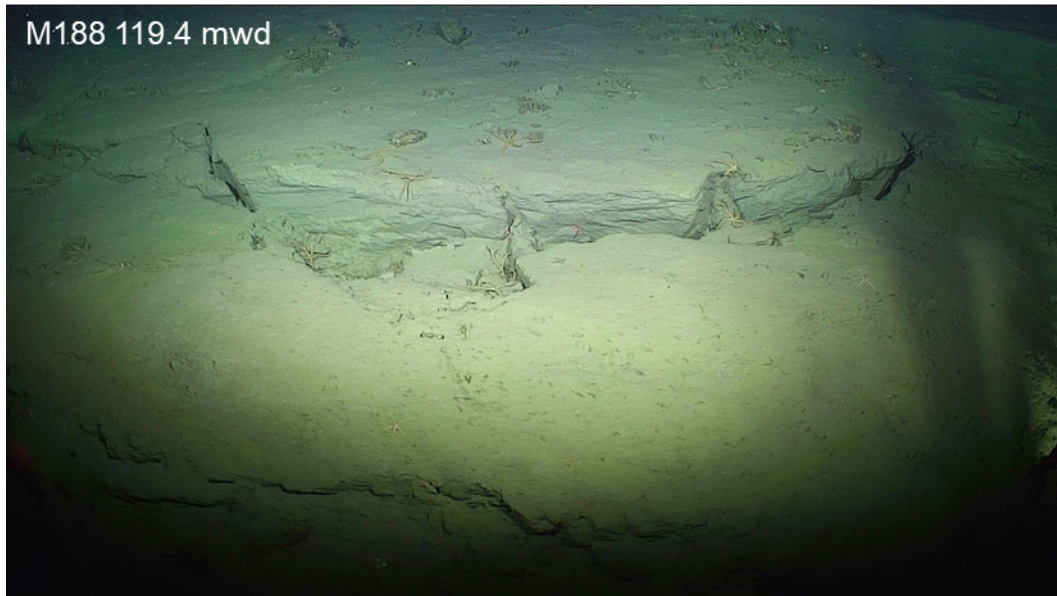


Figure 4.96. Open crown crack observed at 119 mwd. Photo courtesy of Monterey Bay Aquarium Research Institute.

4.3.9. ARA13C ROV-08

MBARI Dive M189, Wednesday September 7th, 2022

This dive was located along the multichannel seismic (MCS) profile ARA05C Line 1, collected during IBRV Araon's 2014 cruise in the region (Figure 4.97). This MSC line crosses two pingo-like features (PLFs) which are aligned north-south and separated by a narrow trough. On a previous crossing of this area by the IBRV Araon during this cruise (ARA13C), a water column anomaly was observed in the EK80 sonar over the southernmost PLF. A few hours prior to the dive, a high-resolution grid was obtained from the mapping AUV to assist in the design of the ROV route. A goal of this ROV dive was to explore these PLF's. Another goal was to find the source of the water column anomaly observed in the EK80 sonar such that any potential gas could be sampled.

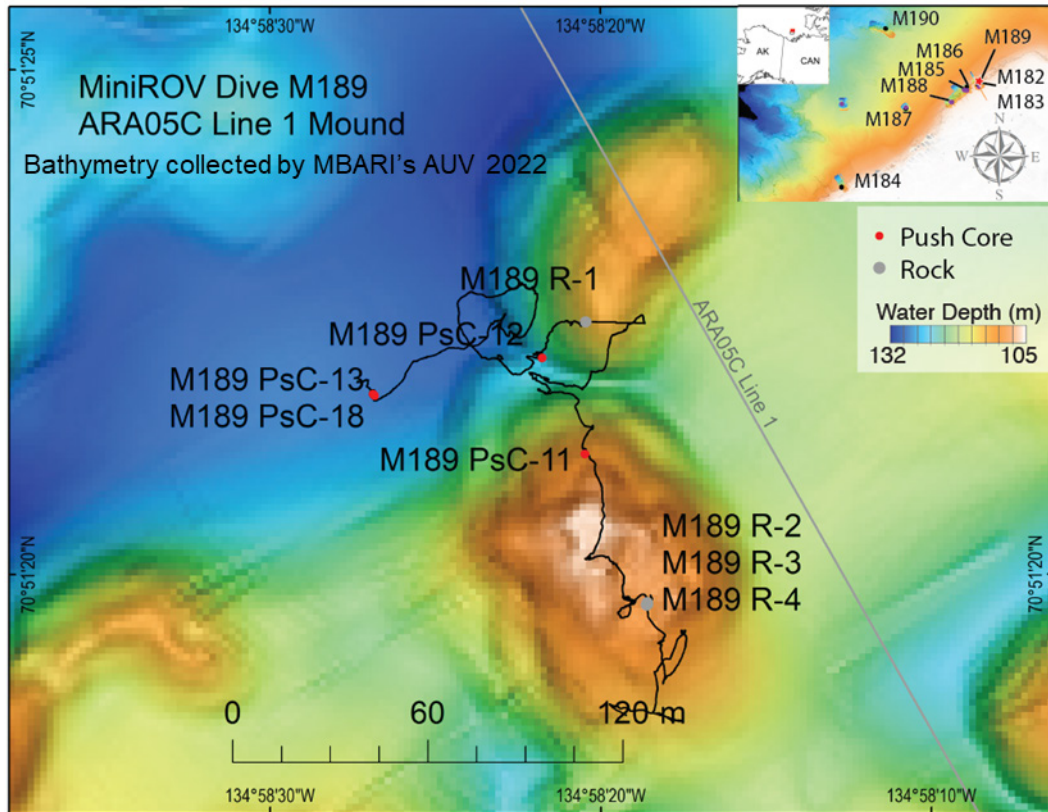


Figure 4.97. MBARI AUV collected bathymetry 2022 with details of Dive M189

The ROV landed in a depression at 130 mwd where there were abundant sessile organisms colonizing the seafloor. Two push cores were taken (M189 PsC-13 and M189 PsC-18) for the purpose of ^{210}Pb dating. Multiple ~ 1 m wide \times ~ 3 m long grooves were seen. These elongated indents on the seafloor with pushed-up small ridges are hypothesized to be trawl marks (Figure 4.98). Sessile organisms were observed both on top and within these features, suggesting these depressions were not fresh.



Figure 4.98. Elongated indents on the seafloor with pushed-up small ridges are hypothesized to be trawl marks. Photo courtesy of Monterey Bay Aquarium Research Institute.

As the ROV moved SSE upslope on the side of the depression, the slope increased to $>20^\circ$. The seafloor was entirely sediment-covered up to 124.5 m, where a ledge, which appeared to be a horizontal bed, protruded through the sediment cover (Figure 4.99). A push core (M189 PsC-12) was collected in 124.5 m, on the ledge, with the intent of ^{14}C -dating this horizon, and thus may provide a stratigraphic control for the MCS line.

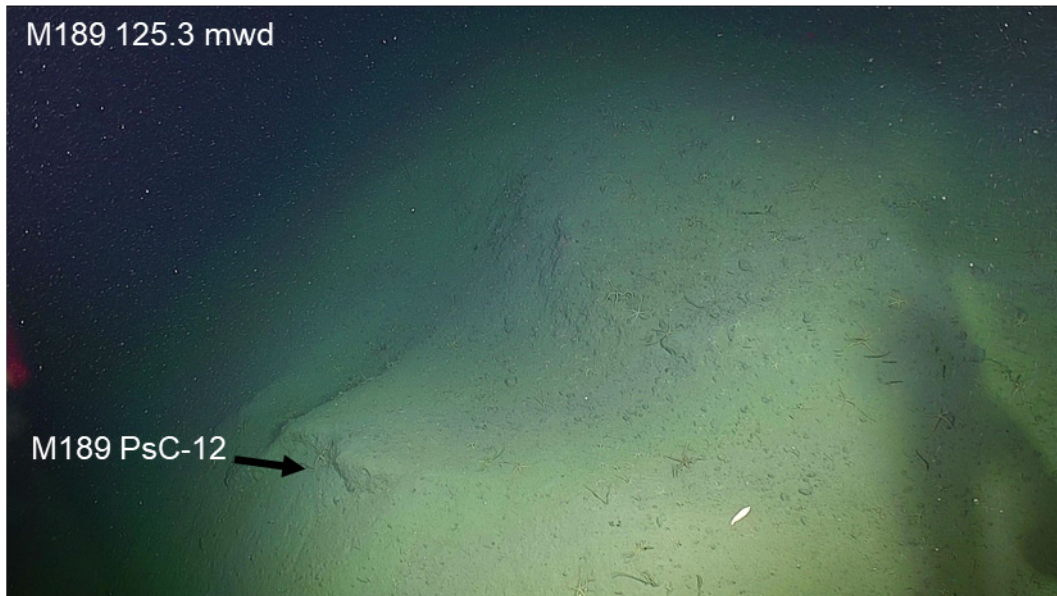


Figure 4.99. Ledge protruding through the sediment cover. Photo courtesy of Monterey Bay Aquarium Research Institute.

At 116 mwd some cobbles, with lithologies different from the locally-derived mudstone, were seen. Sample M189 R-1 collected at this depth was determined to be chert. More cobbles were seen suspended in a sediment matrix 1 meter above (115 mwd), on the slope wall. The cobbles were of varied shapes and sizes. The presence of similar pebbles and cobbles supported by a fine-grained sediment matrix were present to the top of the northern PLF at 113 mwd and along the flanks and crest of the southern PLF as well. Besides the scattered cobbles, the only morphologic features of note were a series of ~ 1 m wide, ~ 4 m long troughs (trawl mark) (Figure 4.100).



Figure 4.100. Scattered cobbles and a series of ~1 m wide, ~ 4 m long troughs. Photo courtesy of Monterey Bay Aquarium Research Institute.

From the top of the northern PLF, the ROV proceeded to the south, to the trough between the two PLF's and then ascended to the crest of the southern PLF. In the trough, the ROV stopped to sample the material in a patch of debris where a push core (M189 PsC-11) and four rocks were collected (M189 R-1, M189 R-2, M189 R-3, M189 R-4) (Figure 4.101). Upon inspection on the deck, they were judged to be of basalt, sandstone and chert lithologies.



Figure 4.101. Patch of debris where a push core (M189 PsC-11) and four rocks were collected. Photo courtesy of Monterey Bay Aquarium Research Institute.

The topography on the crest of the southern PLF contained meter-scale grooves and circular depressions and ridges (Figure 4.102).

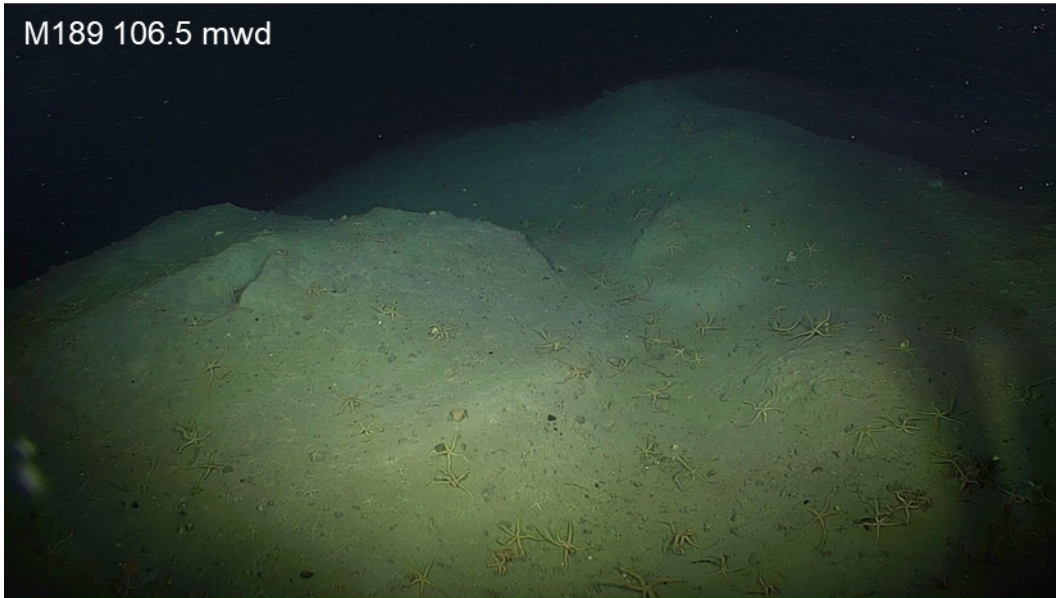


Figure 4.102. Meter-scale grooves and circular depressions and ridges. Photo courtesy of Monterey Bay Aquarium Research Institute.

In addition, a few small depressions ~20 cm deep and ~0.5 m across with slightly elevated ridges were seen near the top (Figure 4.103).



Figure 4.103. Small depression ~20 cm deep and ~0.5 m. Photo courtesy of Monterey Bay Aquarium Research Institute.

No evidence of gas venting was seen during the dive. Moreover, the EK80 sonar on the IBRV Araon, which was run during the dive, also did not detect any water column anomalies.

4.3.10. ARA13C ROV-09

MBARI Dive M190, Thursday September 8th, 2022

The targets of this dive were orange mounds discovered within a slide scar on previous MiniROV dives in 2013 (M21) and 2016 (M80) (Figure 4.104). Shimmering water was seen emerging from one mound in 2013 (Paull et al., 2021). These features were seen at ~890 mwd on the previous dives. The goals of the ROV-09/M190 dive were to collect a sample of the venting waters, to sample the orange precipitates for microbiology, and to investigate the geographic lateral extent of these features along the scarp face at 890 mwd.

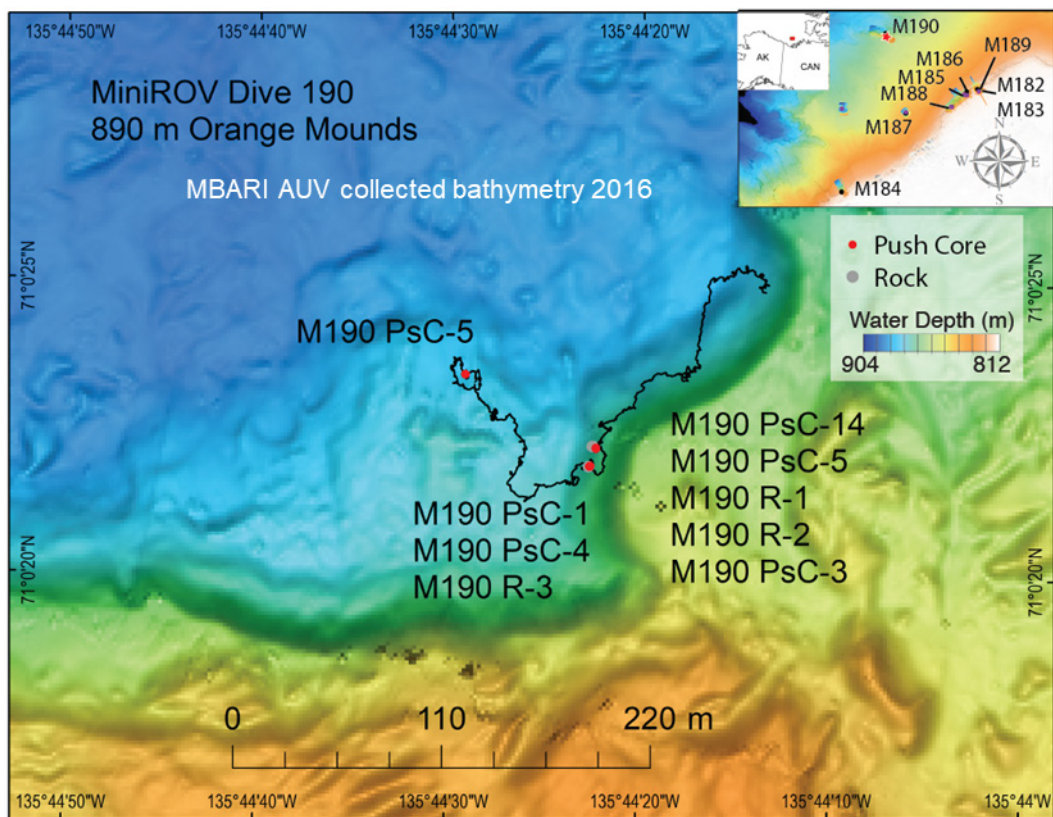


Figure 4.104. MBARI AUV collected bathymetry 2016 with details of Dive M190

The ROV landed at 879 mwd on an estimated 20° slope with a smooth surface except for an occasional rubble clast. The first orange-stained patch was seen at 887.7 mwd and had little to no surface relief (Figure 4.105).



Figure 4.105. Orange-stained patch. Photo courtesy of Monterey Bay Aquarium Research Institute.

Continuing laterally at 889 mwd, an elevated orange mound was encountered. The main concretion was ~45 cm wide and stood ~20 cm tall above a ~1 m wide pedestal (Figure 4.106). Before the surface was disturbed, the base of the mound was largely covered with a drape of gray sediment. However, cracks in its surface indicated that the gray drape overlaid a dark orange colored material below.



Figure 4.106. Elevated orange mound. Photo courtesy of Monterey Bay Aquarium Research Institute.

On top of this broad pedestal the width of the mound expands. The brightest yellow and lighter orange areas occurred on the underside and outer edge of the mound (Figure 4.107). Before the area was disturbed, shimmering water was seen rising in front of the crinoid that was attached to the top of the mound. The water appeared to be coming from the bright yellow upwards-pointing knob that protruded from the very top of the mound. In contrast, a gray dusting of sediment covered the rest of the dark orange mound top. This suggests that flow intensity and color of precipitate are related: rising waters flow upwards and emanate in the

locations with the lightest coloration. There, as they meet bottom waters, they presumably produce a precipitate that builds up into a mound. Thus, the most active mound growth site is where the bright yellow material is found. The dark orange areas would be the sites where flow has ceased.

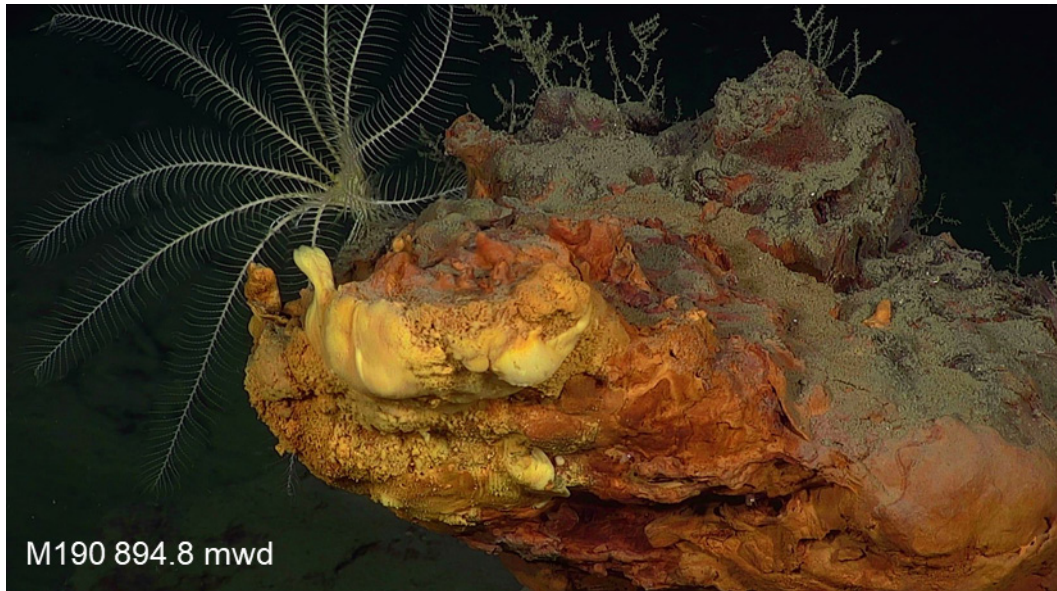


Figure 4.107. Bright yellow material on the underside and outer edge of the mound. Photo courtesy of Monterey Bay Aquarium Research Institute.

When a temperature probe with 0.01° C resolution was positioned near the shimmering water, no clear increase in temperature was noted (Figure 4.108). However, when the temperature probe was inserted ~10 cm into the base of the mound, the temperature shifted from 0.35° to 0.30° C. After >5 minutes the probe was extracted and the temperature returned to 0.35°C. This suggests that the water flowing through the mound is colder than the temperature of bottom seawater.

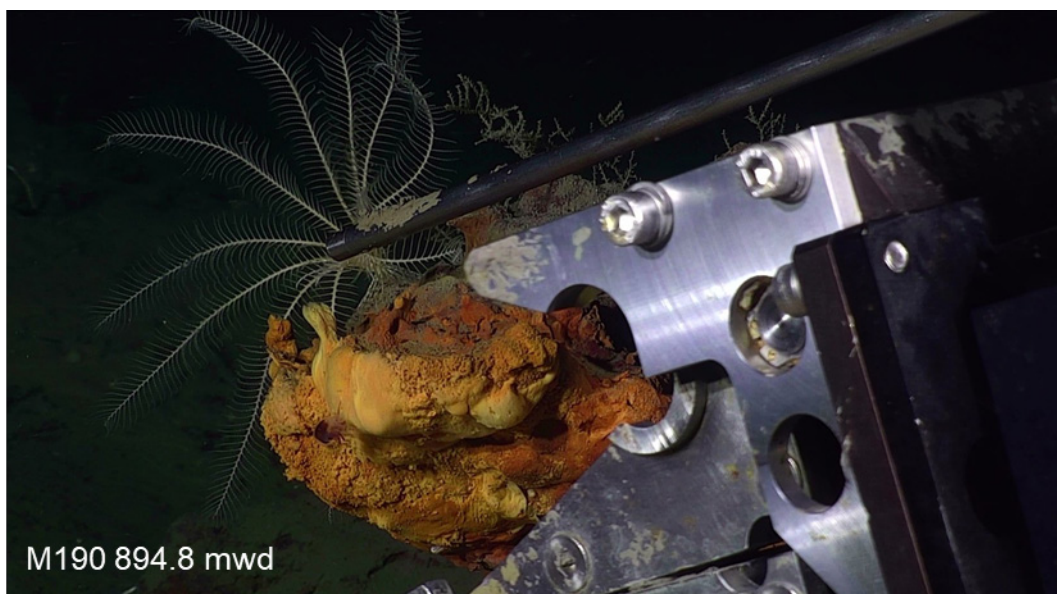


Figure 4.108. Temperature probe positioned near the shimmering water. Photo courtesy of Monterey Bay Aquarium Research Institute.

A sampling device designed to collect rising water or gas with an overturned funnel was used to attempt to collect the emanating waters (water sample M190-W1). The top of the funnel is connected via a solenoid valve and through a one-way check valve into an evacuated cylinder. The funnel was placed over the site of the shimmering waters and the solenoid valve activated. A sudden shaking of the funnel indicated that the valve opened. The valve was then closed. However, when the water sample was retrieved on deck, the volume of collected water was at most a third of the cylinder capacity. The sample contained some orange dusting. It is not clear at this point if the water sampling was successful. A failure in the one-way check valve is suspected.

An attempt was made to take a push core on top of the mound, but most of the overhanging edge fell off as the push core made contact with the mound. This demonstrated the fragile nature of the orange concretions. Push cores M190 PsC-14, M190 PsC-6, and M190 PsC-1 were taken to capture the orange material that had fallen off. After collecting the orange material, the bottoms of these cores were pushed into the underlying gray sediment to prevent the orange material from falling out of the core tubes. Three concretions were carefully picked up with the ROV manipulator arm and placed in the ROV drawer (M190 R-1 and M190 R-2).

The ROV moved ~5 m away from the orange mound to collect (M190 PsC-3) at 894.6 mwd in the typical gray sediments characteristic of the area. This core was taken as a potential background core for ^{210}Pb dating. It also served to sample the white worm (?) seen near the sculpin in the following image (Figure 4.109).



Figure 4.109. Core M190 PsC-3 was taken for ^{210}Pb dating. It also served to sample the white worm (?) seen near the sculpin. Photo courtesy of Monterey Bay Aquarium Research Institute.

Another orange concretion was found nearby. This concretion had a sculpin sitting on the flat concretion surface, presumably guarding a brood of eggs. The mound again had a substantial overhanging edge (Figure 4.110).



Figure 4.110. Orange concretion with overhanging edge. Photo courtesy of Monterey Bay Aquarium Research Institute.

Throughout the rest of the dive, the ROV moved between scattered orange concretions in 889 to 895 mwd, on a generally west then north west course. The intent was to assess the variations in the appearance and spatial distribution concretions, and to see if shimmering water could be found at other mounds. Typically, mounds were found within ~15 m or less from each other. This suggests that they are very abundant in this area. However, shimmering water was not seen again.

M190 R-3 was collected from one of these orange mounds in 887.3 mwd. This was followed by collecting M190 PsC-1, which captured some bright yellow material that broke off the mound when the M190 Rx-3 sample was taken and sampled the sediment at the base of the mound.

The degree of sediment coverage on top of the concretions varied (Figure 4.111). Most of the concretions had at least one approximately horizontal overhang layer. Most of the concretions were also located at the edge of small ledges. Several concretions appeared to have spurs that grew upwards. All of them stood proud above the seafloor demonstrating that their rate of growth exceeded the rate of burial by hemipelagic sedimentation.

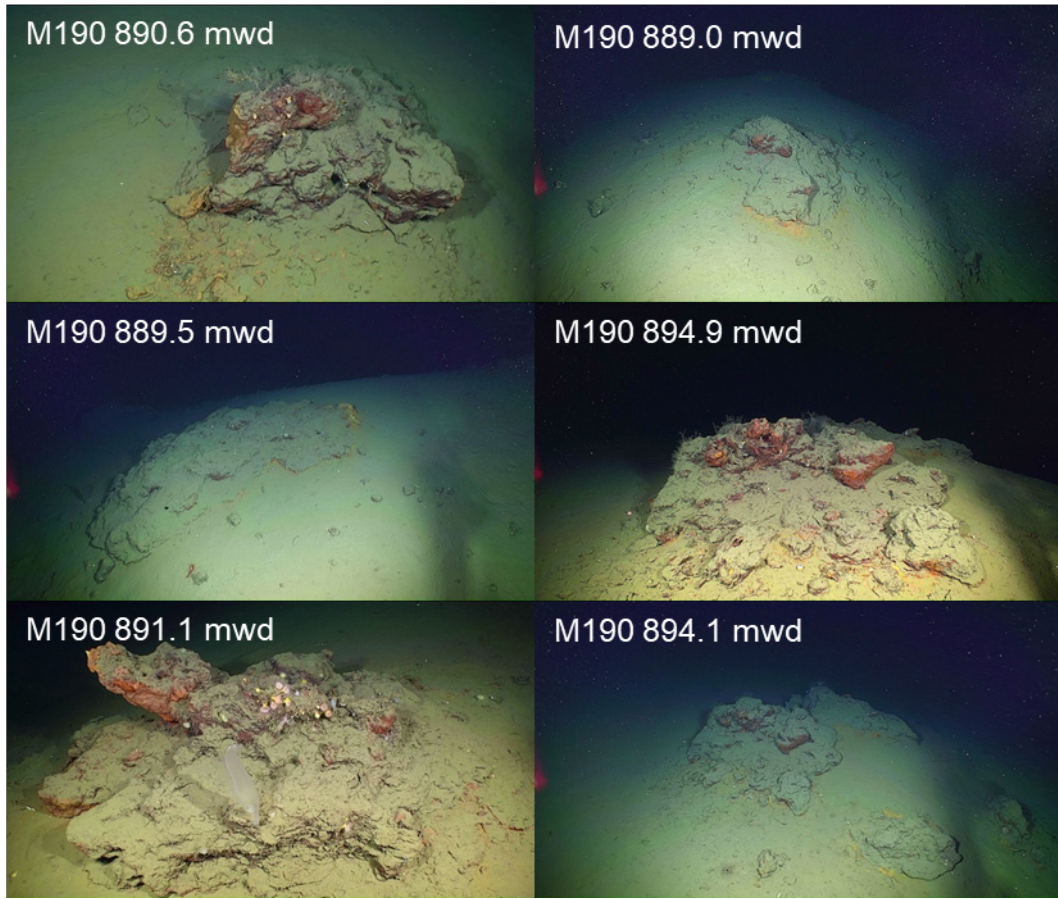


Figure 4.111. The degree of sediment coverage on top of the concretions varied. Photos courtesy of Monterey Bay Aquarium Research Institute.

At the end of dive, another push core M190 PsC-5 in 889 mwd was taken to evaluate the sedimentation rate of the background sediment by means of the ^{210}Pb method.

Table 4.2. ROV Dive List

KOPRI ROV Station	MBARI Dive Number	Date	Dive Name	Multibeam Survey Area (2010 Amundsen, 2019 SWL -are ship based)	Comment	Nearby Stations
01	M182	8/30/22	Giant Hole	2010 Amundsen +2019 SWL + Shelf Edge Intact 2022 (AUV)	Large Oval Hole	ST28-GC
02	M183	8/31/22	Old Hole	2010 Amundsen +2019 SWL + Shelf Edge Intact 2022 (AUV)	Adjacent round hole	ST29-GC
03	M184	9/1/22	Shelf Edge Slump East	2010 Amundsen + Shelf Edge Slump with Staircase of Terraces 2013 + 2016 (AUV)	Scalloped bathy, no hole	
04	M185	9/2/22	Ice Hole	2010 Amundsen + 2019 SWL + Shelf Edge Intact 2022 (AUV)	7 m hole, undercut ice layer	ST23-GC ST24-GC

05	M186	9/3/22	Collapsed Ridge Hole	2010 Amundsen + 2019 SWL + Shelf Edge Intact 2022 (AUV)	Curved-collapsed ridge NE Shelf Edge Intact 2022	
06	M187	9/4/22	Mud Volcano 420 m	2010 Amundsen + 420 m Mud Volcano 2013 + 2016 + 2017 +2022 (AUV)	Surveys 4 times	ST15-HF ST16-HF ST17-HF ST25-GC
07	M188	9/5/22	ST11	2010 Amundsen + 2019 SWL + Shelf Edge Intact 2022 (AUV)	ST11-GC and ST12-GC core site	ST11-GC ST12-GC
08	M189	9/7/22	ARA05C Line 1 mound	2010 Amundsen + Shelf Edge Intact 2022 (AUV)	Small pingo in ~120mwd	ST20-GC (nearby)
09	M190	9/8/22	890 m Orange Mounds	2010 Amundsen + Scar w/ Headwall in 715 m 2013 + 2016 (AUV)	Many orange mounds with shimmering water	

Table 4.3. Samples collected during all ROV dives during ARA13C

Dive	Sample	Depth (m)	Sample Type	Date (GMT)	Time (GMT)	Latitude	Longitude
M182	On bottom		Note	8/30/22	17:08:39	70.839878	-135.066797
M182	Ra-1 on	151.7	Radium	8/30/22	17:47:01	70.839677	-135.06679
M182	N-1	152	Niskin water	8/30/22	18:25:00	70.839729	-135.066065
M182	PsC-17	156.2	Push Core	8/30/22	18:37:00	70.839723	-135.066052
M182	PsC-11	153.2	Push Core	8/30/22	18:43:01	70.839722	-135.066055
M182	PsC-10	156.2	Push Core	8/30/22	18:47:00	70.839725	-135.066052
M182	R-1	149.2	Rock	8/30/22	19:10:00	70.839346	-135.066279
M182	Ra-1 off		Radium	8/30/22	19:57:00	70.839596	-135.066483
M182	End		Note	8/30/22	20:00:01	70.839402	-135.066602
M183	PsC-7	129	Push Core	8/31/22	0:02:01	70.840245	-135.060954
M183	PsC-10	129	Push Core	8/31/22	0:07:01	70.840257	-135.06095
M183	End	146.8	Note	8/31/22	0:38:01	70.840257	-135.06095
M183	Ra-1 off	9	Radium	8/31/22	0:57:00	70.840257	-135.06095
M183	On bottom	127.8	Note	8/31/22	21:41:00	70.840418	-135.06137
M183	Ra-1 on	127.7	Radium	8/31/22	21:42:01	70.840418	-135.06137
M183	R-1-crinoid	152	Rock	8/31/22	22:22:01	70.839766	-135.063014
M183	N-1	146.5	Niskin water	8/31/22	22:33:00	70.839757	-135.062676
M183	PsC-11	152.2	Push Core	8/31/22	22:40:00	70.839734	-135.062615
M183	PsC-17	152.2	Push Core	8/31/22	22:48:00	70.839734	-135.062606
M183	PsC-1	152.2	Push Core	8/31/22	22:54:01	70.839723	-135.062592
M184	On bottom	117.5	Note	9/1/22	16:47:01	70.57648	-136.088928
M184	Ra-1 on	176	Radium	9/1/22	16:57:01	70.576318	-136.089003
M184	PsC-17	169	Push Core	9/1/22	17:48:01	70.574638	-136.086095

M184	PsC-1	169	Push Core	9/1/22	17:54:01	70.57461	-136.08616
M184	N-1		Niskin water	9/1/22	18:55:00	70.573517	-136.084939
M184	PsC-5	152.9	Push Core	9/1/22	19:08:00	70.573713	-136.085533
M184	PsC-9	152.7	Push Core	9/1/22	19:17:00	70.573631	-136.08544
M184	PsC-11	152.8	Push Core	9/1/22	19:22:00	70.573532	-136.085325
M184	End	130.1	Note	9/1/22	19:55:00	70.57285	-136.08431
M184	Ra-1 off	126	Radium	9/1/22	20:00:01	70.572824	-136.084795
M185	On bottom	156	Note	9/2/22	21:18:00	70.842622	-135.083644
M185	Ra-1 on	158	Radium	9/2/22	21:33:01	70.842293	-135.084515
M185	PsC-19	160	Push Core	9/2/22	22:09:01	70.841998	-135.084133
M185	PsC-5	160	Push Core	9/2/22	22:13:00	70.842002	-135.084135
M185	N-1	155.3	Niskin water	9/2/22	22:22:00	70.842006	-135.084125
M185	Ra-1 off	152.6	Radium	9/3/22	0:52:01	70.841665	-135.084018
M185	End	152.6	Note	9/3/22	0:53:01	70.84167	-135.084013
M186	On bottom	156.5	Note	9/3/22	16:30:00	70.849969	-135.064096
M186	Ra-1 on	158.7	Radium	9/3/22	17:16:00	70.849641	-135.062896
M186	Bio-1	160.5	Bio	9/3/22	18:05:00	70.84946	-135.062251
M186	N-1	155.5	Niskin water	9/3/22	18:20:00	70.849594	-135.062132
M186	PsC-9	162	Push Core	9/3/22	18:30:00	70.849557	-135.062039
M186	PsC-13	162	Push Core	9/3/22	18:37:01	70.849551	-135.062051
M186	PsC-12	162	Push Core	9/3/22	18:40:01	70.84955	-135.062052
M186	PsC-4	155.1	Push Core	9/3/22	18:56:00	70.849488	-135.061149
M186	PsC-11	157.5	Push Core	9/3/22	19:13:01	70.849512	-135.060916
M186	Ra-1 off		Radium	9/3/22	19:21:01	70.849505	-135.06075
M186	End		Note	9/3/22	19:23:00	70.849512	-135.060751
M187	On bottom		Note	9/4/22	16:47:18	70.789655	-135.566198
M187	Ra-1 on	420	Radium	9/4/22	16:47:18	70.789655	-135.566198
M187	Bio-1	420	Bio	9/4/22	16:48:01	70.789653	-135.566204
M187	PsC-1	421.2	Push Core	9/4/22	16:59:01	70.789727	-135.566271
M187	PsC-15	421.2	Push Core	9/4/22	17:05:00	70.789718	-135.566267
M187	PsC-11	420.8	Push Core	9/4/22	17:18:01	70.789593	-135.565826
M187	PsC-4	420.9	Push Core	9/4/22	17:24:00	70.789591	-135.565819
M187	Temp probe	420.9	Temp probe	9/4/22	17:28:01	70.789595	-135.565814
M187	Temp probe	420.9	Temp probe	9/4/22	17:30:01	70.789591	-135.56582
M187	Temp probe	420.9	Temp probe	9/4/22	17:32:01	70.789592	-135.565812
M187	Temp probe	420.9	Temp probe	9/4/22	17:36:01	70.789596	-135.565812
M187	Temp probe	419	Temp probe	9/4/22	17:44:00	70.789503	-135.565374
M187	Temp probe	420	Temp probe	9/4/22	18:12:00	70.789947	-135.563558
M187	Temp probe	420	Temp probe	9/4/22	18:16:00	70.789936	-135.563562
M187	Temp probe	420	Temp probe	9/4/22	18:18:01	70.789936	-135.563562
M187	Temp probe	420	Temp probe	9/4/22	18:23:00	70.790012	-135.563564

M187	N-1	406.8	Niskin water	9/4/22	20:51:02	70.7912	-135.563711
M187	Ra-1 off	420	Radium	9/4/22	21:04:00	70.791085	-135.562638
M187	End	420	Note	9/4/22	21:05:01	70.791086	-135.562694
M188	On bottom	132.9	Note	9/6/22	16:27:46	70.808147	-135.188073
M188	Ra-1 on	132.9	Radium	9/6/22	16:32:00	70.808137	-135.18813
M188	R-1	140.2	Rock	9/6/22	16:46:01	70.808232	-135.189137
M188	R-2	140.2	Rock	9/6/22	16:48:01	70.808234	-135.189145
M188	R-3	140.2	Rock	9/6/22	16:50:00	70.808237	-135.189143
M188	R-4	140.2	Rock	9/6/22	16:52:00	70.808239	-135.189148
M188	R-5	140.2	Rock	9/6/22	16:53:01	70.808237	-135.189155
M188	R-6	140.2	Rock	9/6/22	16:54:00	70.808237	-135.189158
M188	R-7	140.2	Rock	9/6/22	16:55:01	70.808238	-135.189162
M188	R-8	140.2	Rock	9/6/22	16:57:01	70.808239	-135.189158
M188	R-9	140.2	Rock	9/6/22	16:58:01	70.808237	-135.189167
M188	R-10	133.8	Rock	9/6/22	17:20:01	70.808226	-135.188333
M188	Temp probe	129.1	Temp probe	9/6/22	17:53:00	70.807961	-135.186991
M188	Temp probe	129.1	Temp probe	9/6/22	17:59:00	70.807957	-135.186985
M188	Temp probe	129.1	Temp probe	9/6/22	18:03:00	70.807957	-135.186966
M188	PsC-19H	129	Push Core	9/6/22	18:19:01	70.807962	-135.186966
M188	Temp probe	129.2	Temp probe	9/6/22	18:30:00	70.807984	-135.187071
M188	PsC-12H	128.6	Push Core	9/6/22	18:54:01	70.807957	-135.186774
M188	PsC-3	128.6	Push Core	9/6/22	19:54:01	70.807834	-135.187191
M188	W-1	129.5	Water	9/6/22	20:28:01	70.807696	-135.187168
M188	Ra-1 off	126.5	Radium	9/6/22	20:31:01	70.807722	-135.18716
M188	N-1	118.4	Niskin water	9/6/22	20:34:01	70.80777	-135.187225
M189	On bottom	129.9	Note	9/7/22	20:40:00	70.856087	-134.974265
M189	Ra-1 on	131	Radium	9/7/22	20:50:01	70.856091	-134.97419
M189	PsC-13	131.1	Push Core	9/7/22	20:54:01	70.856048	-134.974122
M189	PsC-18	131.1	Push Core	9/7/22	20:58:00	70.856052	-134.974137
M189	PsC-12	124.6	Push Core	9/7/22	21:38:00	70.856152	-134.972714
M189	R-1	116.3	Rock	9/7/22	21:59:01	70.85625	-134.972347
M189	PsC-11	125.4	Push Core	9/7/22	22:42:00	70.855887	-134.972356
M189	R-1	105.6	Rock	9/7/22	23:12:01	70.855477	-134.971833
M189	R-2	105.6	Rock	9/7/22	23:14:00	70.855477	-134.971831
M189	R-3	105.6	Rock	9/7/22	23:16:01	70.855473	-134.97183
M189	R-4 crinoid	105.6	Rock	9/7/22	23:17:00	70.855471	-134.971837
M189	N-1	101.5	Niskin water	9/7/22	23:36:01	70.855319	-134.971698
M189	Ra-1 off	105.7	Radium	9/7/22	23:36:01	70.855319	-134.971698
M189	End		Note	9/7/22	23:37:00	70.855279	-134.971765
M190	On bottom	876	Note	9/8/22	14:12:00	71.00693	-135.737128
M190	Ra-1	888.9	Radium	9/8/22	14:58:01	71.006182	-135.739546

M190	Temp probe	888.9	Temp probe	9/8/22	15:00:01	71.006175	-135.739547
M190	Temp probe	888.9	Temp probe	9/8/22	15:02:00	71.006179	-135.739536
M190	Temp probe	888.9	Temp probe	9/8/22	15:07:01	71.006181	-135.739534
M190	Temp probe	888.9	Temp probe	9/8/22	15:24:00	71.006175	-135.739513
M191	Temp probe	888.9	Temp probe	9/8/22	15:26:30	71.006169	-135.739515
M190	W-1	888.3	Water	9/8/22	16:16:00	71.00616	-135.73957
M190	PsC-14	888.7	Push Core	9/8/22	16:21:00	71.006164	-135.739538
M190	PsC-6	888.7	Push Core	9/8/22	16:32:00	71.006161	-135.739512
M190	R-1	888.9	Rock	9/8/22	16:43:01	71.006172	-135.739553
M190	R-2	888.9	Rock	9/8/22	16:45:00	71.006172	-135.739564
M190	Temp probe	889	Temp probe	9/8/22	16:50:16	71.006169	-135.739553
M190	PsC-3	888.9	Push Core	9/8/22	17:10:00	71.006164	-135.739512
M190	N-1	871.2	Niskin water	9/8/22	17:22:00	71.006075	-135.73966
M190	R-3	887.2	Rock	9/8/22	17:37:00	71.006077	-135.739614
M190	PsC-1	887.2	Push Core	9/8/22	17:40:00	71.006078	-135.739602
M190	PsC-4	887.2	Push Core	9/8/22	17:43:00	71.006079	-135.739591
M190	PsC-5	889.8	Push Core	9/8/22	18:45:00	71.006505	-135.741418
M190	Ra-1 off	889.8	Radium	9/8/22	18:48:01	71.00651	-135.741446
M190	End	889.8	Note	9/8/22	18:49:00	71.006502	-135.741439

References

- Jin, Y.K., Côté, M.M., Paull, C.K. and King, E.L., 2018. 2017 Korea-Canada-U.S.A. Beaufort Sea (offshore Yukon and Northwest Territories) research program: 2017 Araon expedition (ARA08C) cruise report; Geological Survey of Canada, Open File 8406, 206 p.
- Lee, Y.M., Noh, H-J., Lee, D-H., Kim, J-H., Jin, Y.K. and Paull, C.K., 2019. Bacterial endosymbiont of *Oligobrachia* sp. (Frenulata) from an active mud volcano in the Canadian Beaufort Sea. *Polar Biology*, 8 p.
- Lee, D.-H., Lee, Y.M., Kim, J.H., Jin, Y.K. Paull, C., Niemann, H., Kim, J.-H. and Shin, K.-H., 2019. Discriminative biogeochemical signatures of methanotrophs in different chemosynthetic habitats at an active mud volcano in the Canadian Beaufort Sea. *Scientific Reports*, <https://doi.org/10.1038/s41598-019-53950-4>.
- Majewski, A.R., Rhiggins-Lynn, B., Lowdon, M.K., Williams, W.J., and Reist, J.D., 2013, Community composition of demersal marine fishes on the Canadian Beaufort Shelf and at Herschel Island, Yukon Territory, *J. Mar. Syst.*, v. 127, p. 55-64, [10.1016/j.jmarsys.2013.05.012](https://doi.org/10.1016/j.jmarsys.2013.05.012).
- Moore, W.S. and R. Arnold, 1996. Measurement of ^{223}Ra and ^{224}Ra in coastal waters using a delayed-coincidence counter. *Journal of Geophysical Research*, 101(C1), 1321-1329.
- Paull, C.K., Dallimore, S.R., Caress, D.W., Lundsten, E., Anderson, K., Melling, H., Jin, Y.K., Duchense, M.J., Kang, S-G. Kim, S., Riedel, M., King, E.L. and Lorensen, T., 2021. A 100-km wide slump along the upper slope of the Canadian Arctic was likely preconditioned for failure by brackish pore water flushing. *Marine Geology*, 435.
- Paull, C.K., Dallimore, S., Jin, Y.K., Caress, D.W., Lundsten, E., Gwiazda, R., Anderson, K., Hughes Clarke, J., Youngblut, S. and Melling H., 2022. Rapid seafloor changes associated with the degradation of Arctic submarine permafrost. *Proceeding of the National Academy of Sciences*, 119 (12) e2119105119.
- Paull, C.K., Dallimore, S.R., Caress, D.W., Gwiazda, R., Melling, H., Riedel, M., Jin, Y.K., Hong, J.K., Graves, D., Sherman, A., Lundsten, E., Anderson, K., Lundsten L., Villinger, H., Kopf, A., Johnson, S., Vrjenhoek, R., Conway, K., Neelands, P. and Cote, M., 2015, Active mud volcanoes on the continental slope of the Canadian Beaufort Sea, *Geochemistry, Geophysics, Geosystems*, v. 16, p. 2797-3342.

ARA13C Cruise report

Chapter 5. Sediment coring

J.-H. Kim, Y. M. Lee, H.-S. Moon, Y. Ahn, J. Obelcz, S.-R. Seong, M. Walton, R. Gwiazda, H. T. H. Nguyen, S. Lee, J. Mok

5.1. Introduction

The cryosphere (e.g., ice sheet, permafrost, and glaciers) in Arctic regions is sensitive to global climate changes through geological time, which has immense consequences on the environment and ecosystem. Recently, the cryosphere extent in Arctic regions has been shrinking due to rapid temperature increases compared to those in other regions. Therefore, the cryosphere melting significantly influences the marine (bio/geo) chemistry and ecosystems in the Arctic region.

5.1.1. Permafrost, shelf edge morphology, and freshening background

Over the last two decades, our understanding of the geologic processes taking place on the Beaufort Shelf and downslope to 1,000 m water depth has expanded considerably. It is now well established that the shelf east of the Mackenzie River is underlain by thick (600 – 700 m maximum thickness) relict permafrost and gas hydrate deposits (both below and within the permafrost) that formed during periods of glaciation and undergo a presently undetermined amount of degradation during interglacial periods. While the precise northern limit of the relict permafrost is not known, reconstruction of the present-day northern permafrost limit is based on subsurface geophysical data, core logs, core samples from the shelf, and thermal modelling.

The morphology of the shelf edge and upper slope includes nearly ubiquitous gravity mass failure-generated scarps that parallel the shelf edge, narrow ridges protruding from the seafloor, and of several meter deep depressions. Repeat high-resolution AUV mapping indicates that the new sinkhole-like-depressions form within the 3- to 4-year long time intervals between multibeam mapping surveys (Paull et al., 2022). A proposed explanation for why the shelf edge is undergoing extremely rapid morphological changes is that the northern limit of the permafrost is receding. A hypothesis is that warm groundwaters ascending from depth at these locations can either thaw the relict permafrost, promoting the formation of collapse depressions, or freeze and expand to form linear ridges and mounds that resemble pingos on land (pingo-like features, or PLFs). Whether thawing or freezing occurs is dependent on subtle variations in the temperature and salinity of the ground waters. The chloride (Cl⁻) concentration and isotopic composition of pore water are useful tools for understanding the hydrological processes leading to morphological changes. The hypothesis is supported in recognizing decreasing downcore Cl⁻ concentrations in pore water from cores collected during the ARA08C cruise in 2017 on seabed mounds at the shelf edge suggesting a freshwater dilution sourced from depth (Gwiazda et al., 2018).

On the Yukon Shelf, west of the Mackenzie Trough, our knowledge about the presence of relict permafrost is more limited. Indeed, the mere existence of relict permafrost under the shelf in this area has not been proven. Nevertheless, both flanks of the Mackenzie Trough exhibit a morphology similar to that observed along the shelf edge. This suggests that upward advecting

groundwaters may be similarly impacting the seafloor there through freezing and thawing. Exploring sites with different morphologies along the shelf edge on the western side of this trough with MiniROV observation, high resolution AUV repeat mapping, coring, and chemical analysis of pore water will be essential for elucidating the mechanisms that create this unusual morphology. Given the similarity between the shelf edge morphologies on both sides of the Mackenzie Trough, the ascent of groundwaters to surficial sediment along the shelf edge on the west Mackenzie Trough is a reasonable hypothesis to test with the multiple chemicals, sedimentological, and dating approaches targeted by the ARA13C cruise.

5.1.2. Microbial background

Marine sediments are the largest organic carbon reservoirs, supporting a rich and diverse benthic microbial community (Kallmeyer et al., 2012). In addition, sediments in coastal areas are important for organic matter (OM) retention, transformation and mineralization (McGovern et al., 2020). Benthic microorganisms play key roles in biochemical cycles through diverse metabolisms including the oxidation of OM, production of methane and other hydrocarbons, the removal of sulfates, and iron oxidation (Whitman et al., 1998; Glöckner et al., 2012; Kallmeyer et al., 2012; Rubin-Blum et al., 2014). The composition and function of benthic microbial communities are known to be affected by environmental factors including salinity gradient and availability of nutrients (Yang et al., 2016; Li et al., 2021; Zhang et al., 2021). Recent studies on the benthic microbial communities that have been performed in the coastal areas of the Beaufort Sea, Greenland, Svalbard, and Alaska have also revealed the close relationship between microbial communities and organic matter or salinity (Garneau et al., 2009; Hauptmann et al., 2016; Sipler et al., 2017; Delpech et al., 2021; Walker et al., 2021). Since the change in OM and salinity in the coastal environment generally reflects the significant increase of terrestrial sources driven by climate change, characterization of microbial communities in the Arctic Ocean is important for understanding and predicting the response and functional changes of microbial communities (McClelland et al., 2011).

Activity of Mud Volcanos (MV) in the CBS, discovered about a decade ago, has been demonstrated from study of three slope-situated examples (MV282, MV420, and MV740 at water depths of 282 m, 420 m, and 740 m) (Paull et al., 2015). Bacterial and archaeal communities involved in methane oxidation and geochemical characteristics have been investigated on MV420 according to visually discriminative chemosynthetic fields (Lee et al., 2019). Methanotrophic groups were differentiated according to the availability of electron acceptors affected by the benthic chemosynthetic communities such as bacterial mat and Siboglinadae tubeworms and upward methane flux, implying that the monitoring of methanotrophic groups can be an indirect indicator of methane flux.

Pore water, gas, mineralogy, biomarkers, and composition of microbial communities provide direct/indirect information for the marine (bio/geo) chemistry because their properties change in response to the source and diagenesis within the sediment column of the marine system. We have collected 45 cores in the Beaufort Sea during the ARA13C cruise to further investigate pore water, gas, mineralogy, biomarkers, and microbiology properties. Our sediment coring goals are 1) to find new or relict ice to confirm the linkage between permafrost thaw and rapid morphological change, 2) to identify the source and diagenesis of pore water and gas chemistry, 3) to investigate correlation between the seawater dissolved organic matter (DOM) and that accumulated in sediment pore water, 4) to characterize DOM properties and interaction between DOM and microbial communities in sediment, 5) to identify microbe-mediated methane oxidation at MVs according to the methane flux or benthic chemosynthetic communities, 6) to investigate the microbial groups and their methane and Fe(II) oxidation

metabolism n at active MVs in iron mats through the 16S rRNA gene, biomarker analysis, and metagenome sequencing, 7) to characterize the spatial differences of microbial diversity and relation to environmental factors shaping the benthic bacterial and archaeal microbial community composition along a long(~136 km) transect, 8) to analyze biomarkers and understand geochemical features associated with methane flux, and 9) to better understand the MV gas hydrate properties.

5.2. Methods

5.2.1. Sediment coring by multi-corer and gravity corer

Surface sediment coring for sedimentological, geochemical and biological analyses as well as sampling the water-sediment interface was carried out at 20 stations during the ARA13C cruise by means of a multicorer, the best suited device for undisturbed surface sediment sampling (Figure 5.1). The multicorer developed by Oktopus GmbH was equipped with an array of eight 10.5 cm diameter polycarbonate coring tubes of 80 cm length. MCs from each site were distributed among the participants for 1) sedimentology, organic geochemistry, pore water geochemistry, and mineralogy (1 core), 2) mercury chemistry (2 cores), and 3) water chemistry (1 core). All coring sites were selected using multibeam bathymetric maps and sub-bottom acoustic profile images. The multicore (MC) site metadata is represented in Table 5.1.

During the ARA13C cruise, gravity coring (GC) was also performed at 15 stations in the Beaufort Sea (Figure 5.1). The gravity corer consists of a steel coring barrel of 6 m length with a headstand weighing 1.0 metric tons and a steel head with core catcher. The core liner is 11 cm diameter plastic tube. The cores were inspected upon recovery for the presence of ice and gas hydrate and when either ice or hydrate was observed it was subsampled on deck.

The GC station data are listed in Table 5.2. They help identify sedimentary units, reconstruct the sedimentary history, recover ice, extract pore waters, and to collect samples for post-cruise research.

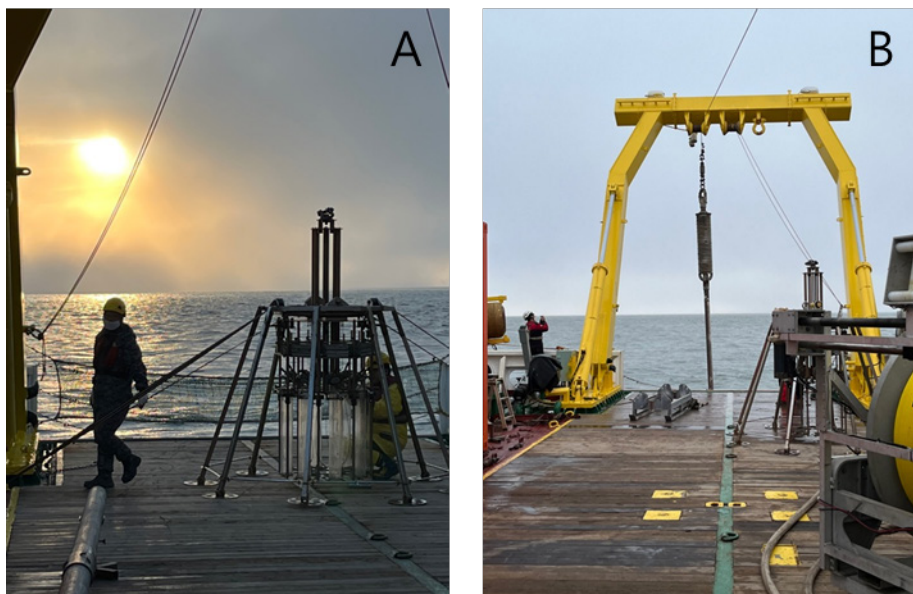


Figure 5.1. Sediment coring activities with A) a multicorer (MC) and B) a gravity corer (GC) during the ARA13C cruise in 2022. Photos courtesy of Korea Polar Research Institute.

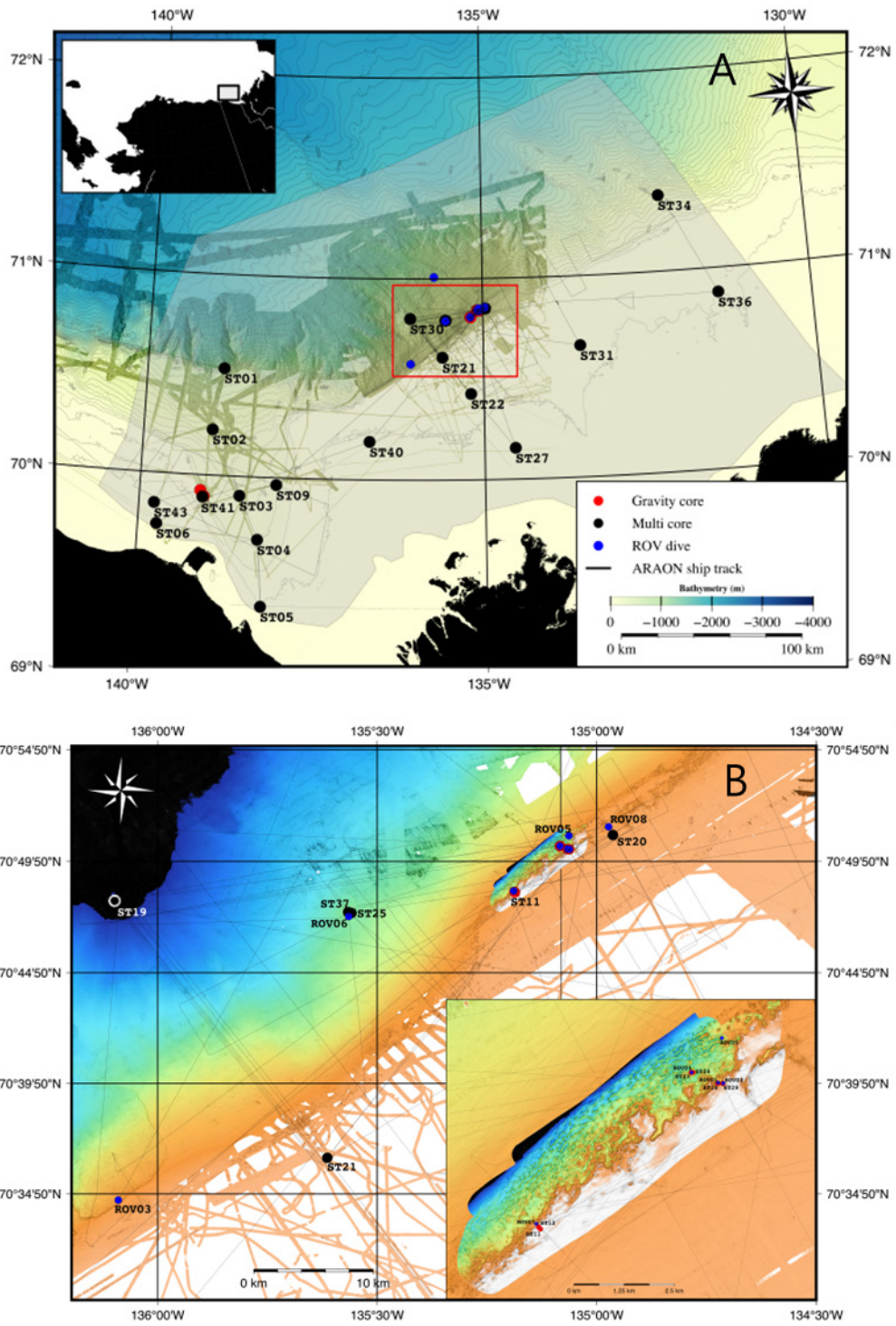


Figure 5.2. (A) Location map of coring stations during the ARA13C cruise. (B) Expanded location map of area outlined in red from (A) panel.

Table 5.1. Summarized information on MC stations during the ARA13C cruise in 2022

Station	Location		Water Depth (m)	Length (cm)	Remarks
	Latitude	Longitude			
ARA13C-ST01	70° 31.9494' N	138° 51.7226' W	1113	60	
ARA13C-ST02	70° 13.5913' N	138° 59.4380' W	423	51	
ARA13C-ST03	69° 54.2508' N	138° 33.4700' W	223	54	
ARA13C-ST04	69° 41.3565' N	138° 16.7076' W	142	51	
ARA13C-ST05	69° 21.5195' N	138° 11.9462' W	49	58	
ARA13C-ST06	69° 44.8004' N	139° 43.7802' W	32	< 5	Low recovery
	69° 44.8006' N	139° 43.7806' W			
ARA13C-ST06-1	69° 53.4639' N	139° 5.4437' W	92	16	
ARA13C-ST09	69° 57.8309' N	138° 1.9074' W	167	53	
ARA13C-ST19	70° 48.0622' N	136° 5.8661' W	746	55	MV
ARA13C-ST20	70° 51.0156' N	134° 57.7962' W	109	42	
ARA13C-ST21	70° 36.4654' N	135° 36.8100' W	76	47	
ARA13C-ST22	70° 25.5955' N	135° 11.5361' W	63	29	
ARA13C-ST25	70° 47.55432' N	135° 33.9595' W	422	65	MV/Gas Hydrate found
ARA13C-ST27	70° 9.3073' N	134° 33.0552' W	35	44	
ARA13C-ST31	70° 39.2564' N	133° 32.7428' W	67	52	
ARA13C-ST34	71° 22.6606' N	132° 14.3334' W	446	-	For water chemistry
ARA13C-ST36	70° 52.6969' N	131° 25.0323' W	56	-	
ARA13C-ST37	70° 47.5159' N	135° 33.4973' W	430	-	
ARA13C-ST40	70° 11.3547' N	136° 41.2906' W	47	-	
ARA13C-ST43	69° 51.0073' N	139° 46.8960' W	37	-	

*- : not split

Table 5.2. Summarized information on GC stations carried out during the ARA13C cruise in 2022

Station	Location		Water Depth (m)	Length (cm)	Remarks
	Latitude	Longitude			
ARA13C-ST02	70° 13.5928' N	138° 59.4370' W	424	449	
ARA13C-ST05	69° 21.5195' N	138° 11.9462' W	49	375	
ARA13C-ST07	69° 53.6211' N	139° 4.3652' W	106.5	382	
ARA13C-ST08	69° 53.6127' N	139° 4.3241' W	114	334	
ARA13C-ST11	70° 48.4648' N	135° 11.2428' W	130	67	Ice found
ARA13C- ST12	70° 48.4364' N	135° 11.1667' W	120	181	
ARA13C- ST20	70° 51.0134' N	134° 57.7690' W	109	349	
ARA13C- ST23	70° 50.5215' N	135° 5.0408' W	156	198	Ice found
ARA13C- ST24	70° 50.5242' N	135° 4.9864' W	158	277	
ARA13C- ST25	70° 47.5564' N	135° 33.9675' W	422	139	MV
ARA13C- ST28	70° 50.3793' N	135° 3.9647' W	153	154	
ARA13C- ST29	70° 50.3761' N	135° 3.7598' W	130	206	Ice found
ARA13C- ST30	70° 48.0240' N	136° 5.7694' W	739	532	MV/Gas Hydrate found
ARA13C- ST41	69° 53.4600' N	139° 5.2762' W	87	256	
ARA13C- ST42	69° 55.3638' N	139° 7.5375' W	141	219	

5.2.2. ROV push coring

The MiniROV push corer takes up to seven < 20 cm long push cores designed to retrieve precisely located samples of deposits or fauna from the seafloor. The samples included orange chemical precipitates that formed at the locations of underwater springs, clam shells, tubeworms, and rock clasts from diamictons. In addition, precisely stratigraphically located samples along outcrops were taken for radiocarbon and/or ²¹⁰Pb dating, to determine sedimentation rates for Holocene sediments (Table 5.3; Figure 5.2). Pore water and mud samples collected with push cores are also utilized to understand the microbial communities found in the different seafloor environments. Sampled environments included shelf edge sediments both inside and outside newly formed depressions, slide scar surfaces, varied seafloor textures atop MV 420, and sites of deep-water springs (Table 5.3; Figure 5.3).

Table 5.3. Summarized information on push core stations for microbial and pore water analysis during the ARA13C cruise in 2022

DIVE No.	Station characteristics	Water depth (m)	Push core no.	Latitude (°N)	Longitude (°W)	No. of sediment samples	No. of pore water	No. of samples for CH ₄ analysis	
DIVE182	Giant Hole	156.2	10	70.839725	135.066052	14	5		
DIVE183	Old Hole	129	10	70.840257	135.06095	15	5		
		152.2	17	70.839734	135.062606	12	5	5	
DIVE184	Shelf Edge Slump East Hole	152.8	11	70.573532	136.085325	11	5	4	
		169	17	70.574638	136.086095	15	4		
DIVE185	Ice Hole	160	5	70.842002	135.084135	2	4		
DIVE186	Collapsed Ridge Hole	157.5	11	70.849512	135.060916	11	4		
		162	13	70.849551	135.062051	19	6	7	
DIVE187	MV 420 m	421.2	1	70.789727	135.566271	13	4	7	
		420.8	11	70.789593	135.565826	16	5	5	
DIVE188	ST11	128.6	12	70.807957	135.186774	1	1		
		129	19	70.807962	135.186966	1	1		
		125.4	11	70.855887	134.972356	10	4		
DIVE189	ARA05C Line 1 mound	124.6	12	70.856152	134.972714	9	5		
		131.1	18	70.856052	134.974137	10	4		
		131.1	13	70.856048	134.974122	0	5		
		888.7	14	71.006164	135.739538	4	3		
		888.9	3	71.006164	135.739512	12	4		
DIVE190	890 m Orange Mounds	887.2	4	71.006079	135.739591	7	4		
		889.8	5	71.006505	135.741418	12	4		
		888.7	6	71.006161	135.739512	6	5		
							3		

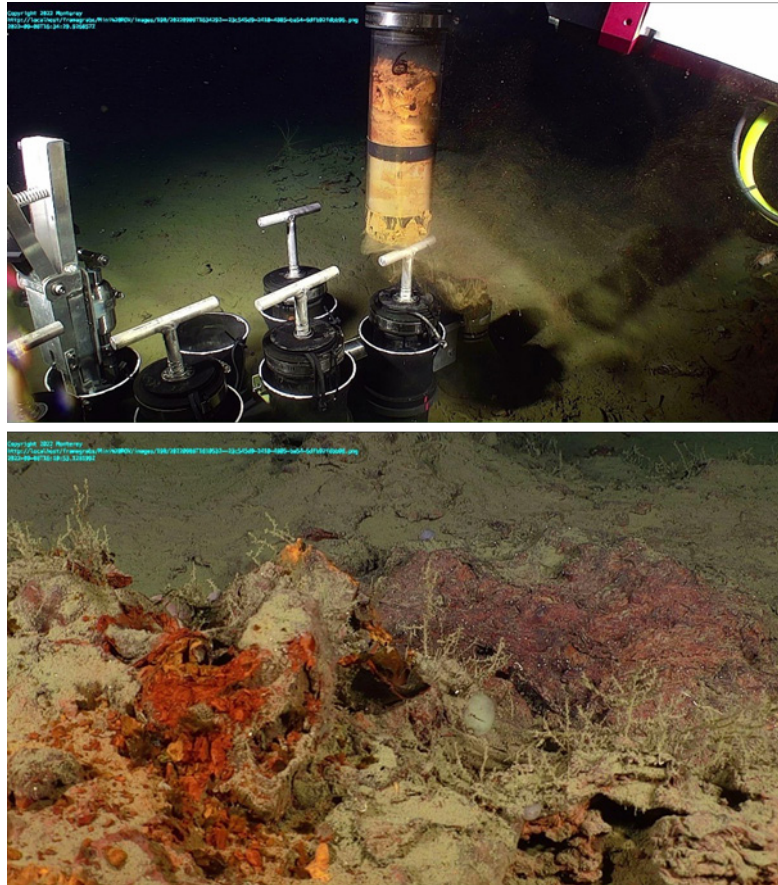


Figure 5.3. Collection of iron-mat using ROV. Photos courtesy of Monterey Bay Aquarium Research Institute.

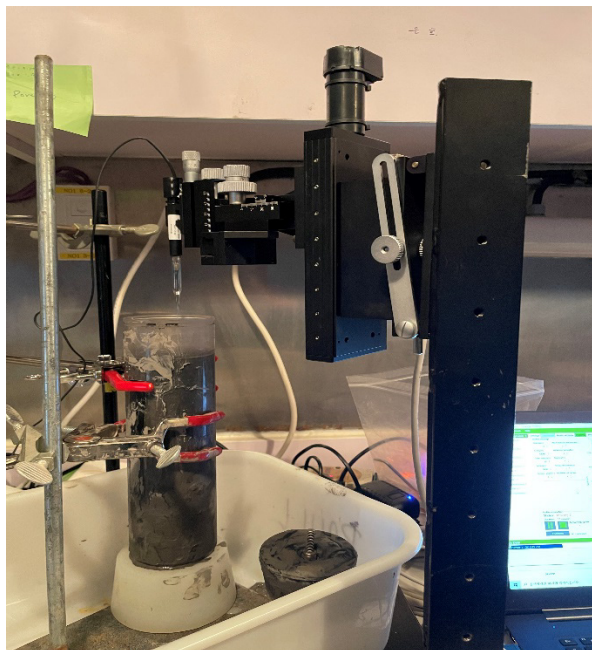


Figure 5.4. Oxygen measurement using microsensor. Photos courtesy of Korea Polar Research Institute.

After recovery, oxygen measurement was performed immediately upon the retrieval using O2-100 Microsensor (Unisense, Denmark) according to manufacturer's instructions (Figure5.4). Pore water was extracted by Rhizon. The detailed procedure of extracted pore

water was described in Section 5.2.3. Pore water analysis (e.g, cations and anions) will be performed at Hanyang University. Sediment samples at 1 cm interval were collected for the post-cruise research. Aliquots of sediment samples and samples suspended in 20% glycerol (v/v) were stored at -80°C, respectively for DNA/RNA extraction and cultivation or single cell sorting. Samples for fluorescence in situ hybridization (FISH) were fixed with 4% formaldehyde, washed with PBS, and stored in PBS/EtOH (1:1) at -20°C. In cases where two push cores were obtained at the same site, sediments at 3 cm interval were subsampled and sealed immediately with butyl rubber stoppers and stored at -20°C for methane concentration analysis.

5.2.3. Pore water

Pore water was extracted by Rhizon in whole round cores (Figure 5.5). The sampling interval of pore water is every 12 cm in MCs and 20-50 cm at GCs, respectively. Additional pore water was extracted from MCs and seawater was sampled as close as possible to the water-sediment interface for high resolution DOC analyses. Since pore water was slowly extracted by Rhizon, its maximum extraction time was performed about < 1.5 day at room temperature.

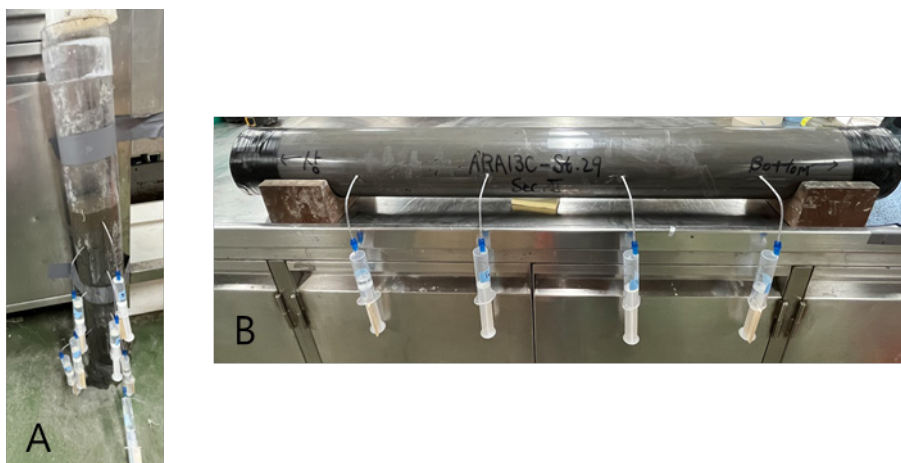


Figure 5.5. Pore water extraction by Rhizon in A) a multicore (MC) and B) a gravity core (GC). Photos courtesy of Korea Polar Research Institute.

Extracted pore water was collected in 24 ml HCl -prewashed syringes and filtered by in-line 0.2- μ m disposable polytetrafluoroethylene filter. Pore water aliquots were transferred into HCl-prewashed high density polyethylene bottles (~2-4 ml) for shipboard and anion analyses, and for major/minor cations and unconventional isotopes analyses (~2-4 ml). Three ml water samples were collected into glass vial for anions and stable isotope analyses at MBARI and ~1-5 ml was sampled into acid-prewashed plastic bottles for DOM analyses at Sejong University. Subsamples were collected in 2 ml septum screw-lid glass vials for characterization of the δ D and δ^{18} O, and of δ^{13} C. Samples for major and minor cations were acidified with 20 μ l ultrapure grade HNO₃ and samples for dissolved inorganic carbon (DIC) were treated with 20 μ l HgCl₂ at room temperature. For the ¹⁴C age dating analysis in DIC, 1-5 ml pore water stored at syringe with capping was frozen immediately. For DOM molecular analysis using Fourier-transform ion cyclotron resonance mass spectrometry approach, five pore water samples from the MCs at Sites ARA13C-ST01, ARA13C-ST02, ARA13C-ST03, ARA13C-ST04, and ARA13C-ST05 (a mixture of 10 ml collected from four different depths of each MC) were acidified and performed solid phase extractions on board; then, the cartridges were

completely dried by nitrogen gas and immediately frozen at -20°C for later extraction using methanol in laboratory at Sejong University.

Pore water samples were routinely analyzed for refractive index with automatic portable refractometer immediately after pore water extraction. The refractive index was converted to salinity based on repeated analyses of International Association of Physical Sciences of the Oceans (IAPSO) standard seawater (reference value: 34.99‰). Chlorinity (Cl^-) and alkalinity have been analyzed by titration using 0.1N AgNO_3 and 0.02N HCl , respectively, on board. The reproducibility of alkalinity and Cl^- titrations was monitored by repeated analysis of IAPSO standard seawater and 0.02N Na_2CO_3 in-house standard solution, yielding $< 1.3\%$ ($n=25$) and $< 2.0\%$ ($n=15$), respectively.

Pore water samples for shipboard analyses, major and minor ions, and isotope compositions were stored $\sim 4^{\circ}\text{C}$ in the refrigerator while DOM samples have been stored in the freezer (-20°C) until analysis (within 1 month from sampling).

5.2.4. Gas sampling

Bulk sediments (3 ml) for headspace (HS) gas analysis were sampled from bottom of MCs and from each section of GCs with a 5 ml cut-off plastic syringe. The sediments were extruded into 20 ml headspace glass vials filled with 2 ml of saturated NaCl solution, and then the vials were immediately capped with rubber septa and sealed with aluminum caps. Additionally, bulk sediments (15 ml) for the ^{14}C age dating of CH_4 in HS gas were sampled from each section of gravity core with a 5 ml cut-off plastic syringe. The sediments were extruded into 60 ml headspace glass vials filled with 10 ml of saturated NaCl solution, and then the vials were immediately capped with rubber septa and sealed with aluminum caps. Approximately 2 ml of sediments for measurement of water content were sampled at the same depths as the headspace gas sampling, which were collected in pre-weighed plastic vials (3 ml). They were stored $\sim 4^{\circ}\text{C}$ in refrigerators.

Void gases (VG) were collected by a gas-tight 60 ml syringe through hole punched on core liner. The void gases were injected into 60 ml glass vial filled with saturated NaCl solution.

A total of 48 HS samples and 5 void gas samples were collected during the cruise to analyze compositional and isotopic properties of gas during the post-cruise research. 30 samples for ^{14}C age dating and 31 sediments (~ 2 ml) were also samples for the analyses of age and water contents, respectively. The summarized list for HS, void gas, ^{14}C age dating, and sediments in each site is represented at Table 5.4.

Table 5.4. Summarized total samples number of HS, void gas, ¹⁴C age dating and sediment

Station	Core type	HS	Void Gas	¹⁴ C age dating	Sediment
ARA13C-ST01		1			
ARA13C-ST02		1			
ARA13C-ST03		1			
ARA13C-ST04		1			
ARA13C-ST05		1			
ARA13C-ST19	MC	1	1		
ARA13C-ST20		1			
ARA13C-ST21		1			
ARA13C-ST22		1			
ARA13C-ST25		1	1		
ARA13C-ST27		1			
ARA13C-ST02		4		3	3
ARA13C-ST05		4		3	3
ARA13C-ST07		4		3	4
ARA13C-ST08		3	1	3	3
ARA13C-ST11		1			
ARA13C-ST12		2		1	1
ARA13C-ST20		3		3	3
ARA13C-ST23	GC	2		2	2
ARA13C-ST24		2		2	2
ARA13C-ST25		2	1	1	1
ARA13C-ST28		1		1	1
ARA13C-ST29		2		2	2
ARA13C-ST30		3	1	2	2
ARA13C-ST41		2		2	2
ARA13C-ST42		2		2	2

5.2.5. Dissociated ice water sampling

Ice was found in GCs at three stations (ARA13C-ST11, ARA13C-ST23, and ARA13C-ST29) during the ARA13C cruise. Dissociated ice water sampling was conducted onboard the IBRV ARAON immediately after retrieving ice samples (without freezing them). Ice was removed from sediment and inserted into 60 ml plastic syringes. It was dissociated under room temperature. The water was filtered by 0.2 μm disposable polytetrafluoroethylene filter and was placed in a polypropylene (PP) bottle for the analyses of anions, cations, and in glass vial for the δD and $\delta^{18}\text{O}$ analysis during the post cruise. Dissociated ice water samples were analyzed for salinity, Cl⁻, and alkalinity onboard with the same method as the pore water. These samples were kept $\sim 4^{\circ}\text{C}$ in the refrigerator of the IBRV ARAON until analysis.

5.2.6. Sampling for microbial diversity and metagenome analysis

Sediment samples from MCs, GCs, and push cores were collected at 1 cm to 40 cm intervals (Tables 5.3 and 5.5). Aliquots of sediment samples and samples suspended in 20% glycerol (v/v) were stored at -80°C , respectively for DNA/RNA extraction and cultivation or single cell sorting. For the bacterial and archaeal community analysis, total genomic DNA will be extracted and 16S rRNA gene sequences will be amplified and sequenced. In addition, cultivation, single cell sorting, or metagenome analysis will be performed to understand the physiological and metabolic potential of core taxa.

5.2.7. Biomarker

Microbial lipids, such as crocetane, archaeol and glycerol dialkyl glycerol tetraethers (GDGTs) could be used as proxy for identifying and quantifying the archaea related with methane cycle in sediment environment. Also, stable isotope ratios of those biomarkers, total organic carbon, and sulfur indicate the fate of carbon and offer the evidence of anaerobic oxidation of methane environment signatures. To analyze biomarkers and geochemical features associated with microbial-methane flux, sediment samples were collected from 14 GCs and 13 MCs in Mackenzie Trough, permafrost area and mud volcano sites. Each core sediment sample was subsampled at 1 cm interval. Core samples were stored at -20°C until lipid analysis (Table 5.6).

Table 5.5. List of samples collected for microbial analysis from the Beaufort Sea

Station	Core Type	No. of samples
ARA13C-ST01		9
ARA13C-ST02		8
ARA13C-ST03		6
ARA13C-ST04		6
ARA13C-ST05		8
ARA13C-ST06_1		3
ARA13C-ST19	MC	7
ARA13C-ST20		6
ARA13C-ST21		5
ARA13C-ST22		5
ARA13C-ST25		6
ARA13C-ST27		5
ARA13C-ST31		7
ARA13C-ST02		12
ARA13C-ST05		12
ARA13C-ST07		19
ARA13C-ST08		17
ARA13C-ST11		9
ARA13C-ST12		8
ARA13C-ST20		21
ARA13C-ST23	GC	12
ARA13C-ST24		14
ARA13C-ST25		3
ARA13C-ST28		10
ARA13C-ST29		10
ARA13C-ST30		4
ARA13C-ST41		12
ARA13C-ST42		10

Table 5.6. Information of core sample list for microbial lipid biomarker analysis

Station	Core type	No. of Samples	Remark
ARA13C-ST01		8	Mackenzie Trough
ARA13C-ST02		8	Mackenzie Trough
ARA13C-ST03		6	Mackenzie Trough
ARA13C-ST04		6	Mackenzie Trough
ARA13C-ST05		8	Mackenzie Trough
ARA13C-ST06_1		3	
ARA13C-ST19	MC	7	
ARA13C-ST20		6	Shell in surface
ARA13C-ST21		5	
ARA13C-ST22		5	
ARA13C-ST25		6	
ARA13C-ST27		5	
ARA13C-ST31		7	
ARA13C-ST02		12	Mackenzie Trough
ARA13C-ST05		12	Mackenzie Trough
ARA13C-ST07		19	Black layers, Gas seeping in 2017
ARA13C-ST08		17	
ARA13C-ST11		9	Ice (35 ~ 51 cm)
ARA13C-ST12		8	
ARA13C-ST20	GC	21	
ARA13C-ST23		12	Ice (198~239 cm)
ARA13C-ST24		14	Shell in 157 cm
ARA13C-ST25		3	
ARA13C-ST28		10	
ARA13C-ST29		10	
ARA13C-ST41		12	
ARA13C-ST42		10	

5.2.8. Mineralogy

Marine sediment from the ARA13C cruise (depth 35 m to 1,113 m) were collected by GCs and MCs to analyze X-ray diffraction (XRD) focused on clay minerals (e.g., smectite, illite, chlorite, kaolinite) (Table 5.7). Samples of 1 cm thickness were collected at intervals of 5 to 10 cm using chemical spoons. These samples are used to gain the basic data for the submarine mineral process in the Arctic Ocean.

Table 5.7. Summarize sample number in each station for X-ray diffraction analysis

Station	Core Type	No. of Sample	
ARA13C-ST01		17	
ARA13C-ST02		13	
ARA13C-ST03		15	
ARA13C-ST04		13	
ARA13C-ST05		11	
ARA13C-ST06_1		6	
ARA13C-ST09	MC	10	
ARA13C-ST19		14	
ARA13C-ST20		11	
ARA13C-ST21		10	
ARA13C-ST22		6	
ARA13C-ST25		13	
ARA13C-ST27		6	
ARA13C-ST31		9	
ARA13C-ST02			89
ARA13C-ST05			74
ARA13C-ST07		120	
ARA13C-ST08		92	
ARA13C-ST11		7	
ARA13C-ST12		17	
ARA13C-ST20		46	
ARA13C-ST23	GC	21	
ARA13C-ST24		30	
ARA13C-ST25		10	
ARA13C-ST28		16	
ARA13C-ST29		18	
ARA13C-ST30		32	
ARA13C-ST41		24	
ARA13C-ST42		41	

5.2.9. Biological samples

The annelid clade Siboglinidae consists of tube dwelling worms that obtain nutrients from endosymbiotic bacteria. Frenulate lineage within Siboglinidae are abundant and widely distributed. In the high Arctic, frenulates are the sole confirmed chemosynthetic megafauna at cold seeps, implying that they alone are likely to perform ecosystem engineering (Sen et al., 2018). Thus, identification of the frenulate species and investigating their endosymbiotic bacteria is important for understanding the poorly studied ecosystems of Arctic cold seeps. The presence of Frenulate tubeworm *Oligobrachia* sp. in the mud volcano of the Beaufort Sea and endosymbiont and its potential metabolism have been reported (Paull et al., 2015; Lee et al., 2019). However, the interaction between host and its endosymbionts which will give critical clues on how these species are abundant in high Arctic cold seeps has not been investigated. Thus, to investigate the interactions between host worm and endosymbionts, we collected tubeworms from MV420 using ROV and multi-corer (Figure 5.6). Samples were washed with seawater and stored at -80°C in ethanol and without fixative. In addition, biological samples including starfish and sea lily (Figure 5.7) were collected and stored at -80°C .

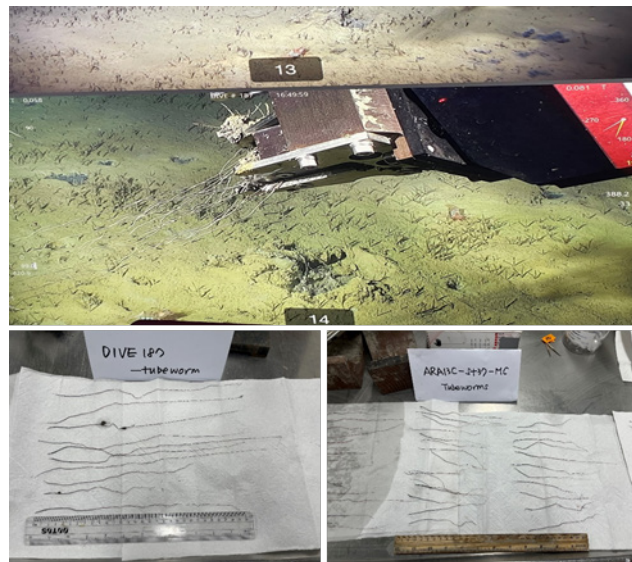


Figure 5.6. Tubeworms collected using ROV and MC. Photos courtesy of Korea Polar Research Institute.



Figure 5.7. Biological samples obtained by push or MCs. Photos courtesy of Korea Polar Research Institute.

5.3. Results

5.3.1. Sedimentology

14 MCs and 15 GCs were split longitudinally onboard. One half of the core, as the working half, was subsampled for mineralogy, microbiology, organic geochemistry, and sedimentology investigations and the other half served as an archive. After opening, photographs were taken of the archive half and then described in detail. The archive halves were all stored at $\sim 4^{\circ}\text{C}$ for later analysis.

The gas hydrate samples collected at Station ARA13C-ST30 (MV 420) were stored in liquid nitrogen for the post-cruise analysis (e.g., crystallography, structure, etc) at Ulsan National Institute of Science and Technology (UNIST).

5.3.2. Pore water chemistry

A total of 172 pore water samples (50 samples from 11 MCs and 122 samples for 15 GCs) were collected. The salinity and Cl^{-} concentration of pore waters extracted from MCs have a relatively constant value in each station (Table 5. 8; Figure 5.8). However, the Cl^{-} concentration shows some spatial variation apparently related to water depth of the coring station; 1) Cl^{-} increases downcore profile at stations shallower than 150 m, 2) has a constant value (548 mM) at stations deeper than 200 m (Table 5.8; Figures 5.2 and 5.8). The salinity profile does not change distinctly downcore with the water depth shown as the Cl^{-} concentration; 1) it has a constant value ($\sim 32.1\text{‰}$) at stations where water depth ranges from 35 m to 109 m, 2) it has a range from 33.1‰ to 35.0‰ at stations where water depth is deeper than 140 m (Table 5.8; Figure 5.8). The salinity and Cl^{-} concentrations in pore water from the two MVs (ARA13C-ST 19: 740 m, ARA13C-ST 25: 420 m), in contrast, show a marked downcore decrease (freshening), ranging from 13.6‰ to 35.0‰ and 203 mM to 547 mM (Table 5.8; Figure 5.8),

respectively. In situ gas hydrates were found at the bottom of Station ARA13C-ST 25 collected at MV 420 m.

Table 5.8. Summarize sample number, salinity, Cl⁻, and alkalinity of pore waters in each station.

Station	Coring Type	Sample Number	Salinity (%)		Cl ⁻ (mM)		Alkalinity (mM)	
			Minimum	Maximum	Minimum	Maximum	Minimum	Maximum
ARA13C-ST01	MC	5	35.0	35.0	547.9	558.0	3.0	3.4
ARA13C-ST02		5	35.0	35.0	547.9	547.9	2.5	3.0
ARA13C-ST03		5	34.1	34.1	547.9	547.9	3.0	5.1
ARA13C-ST04		5	33.1	33.1	537.7	537.7	3.0	6.3
ARA13C-ST05		5	32.1	32.1	507.3	507.3	3.0	10.1
ARA13C-ST19		5	15.6	35.0	243.5	547.9	3.0	34.2
ARA13C-ST20		4	32.1	32.1	522.5	522.5	3.0	3.8
ARA13C-ST21		4	32.1	32.1	517.4	517.4	3.0	3.8
ARA13C-ST22		3	32.1	32.1	512.4	517.4	3.0	3.8
ARA13C-ST25		5	13.6	34.1	202.9	537.7	4.9	55.5
ARA13C-ST27		4	31.1	32.1	507.3	512.4	3.4	10.5
ARA13C-ST02	GC	9	27.2	35.0	436.3	558.0	3.0	11.0
ARA13C-ST05		9	31.1	32.1	507.3	517.4	7.2	25.7
ARA13C-ST07		9	30.2	32.1	517.4	527.6	6.7	17.8
ARA13C-ST08		8	30.2	33.1	527.6	527.6	7.2	19.0
ARA13C-ST11		3	24.3	32.1	390.6	517.4	3.0	4.2
ARA13C-ST12		6	32.1	33.1	507.3	527.6	3.0	3.4
ARA13C-ST20		8	30.2	33.1	497.2	527.6	3.4	6.3
ARA13C-ST23		8	23.4	34.1	385.6	537.7	3.4	4.6
ARA13C-ST24		7	29.2	33.1	476.9	537.7	3.4	4.6
ARA13C-ST25		5	13.6	19.5	192.8	294.2	45.7	59.8
ARA13C-ST28		7	30.2	33.6	497.2	537.7	4.6	6.7
ARA13C-ST29		10	8.8	30.2	121.8	502.2	3.0	6.7
ARA13C-ST30		10	11.7	35.0	172.5	568.2	3.5	45.7
ARA13C-ST41		12	28.2	32.1	487.0	527.6	3.4	10.5
ARA13C-ST42		11	31.1	32.1	517.4	527.6	5.1	19.8

The salinity and Cl⁻ concentration of pore water from the GCs can be divided into four groups in combination with their concentration and geological setting. The first group observed at Stations ARA13C-ST05 and ARA13C-ST42 shows relatively constant salinity and Cl⁻ concentration with depth, ranging from 31.1‰ to 32.1‰ and from 507.3 to 527.6 mM, respectively (Table 5.8; Figure 5.9). The second group characteristic manifests at Stations ARA13C-ST07 and ARA13C-ST08 with near-constant downcore Cl⁻ concentration (517-527 mM) while salinity decreases with depth, ranging from 30.2‰ to 33.1‰ (Table 5.8; Figure 5.9). Further research may identify the reason for a decoupling between the salinity and Cl⁻ concentration. The third group includes Stations ARA13C-ST02, ARA13C-ST11, ARA13C-ST12, ARA13C-ST20, ARA13C-ST23, ARA13C-ST24, ARA13C-ST28, ARA13C-ST29, and ARA13C-ST41. All have a decreasing downcore profile of both salinity and Cl⁻ concentration (Table 5.8; Figure 5.9). The minimum salinity and Cl⁻ concentration are 8.8‰ and 121.8 mM from 1.4 mbsf to 1.6 mbsf of Station ARA13C-ST29. The pore water chemistry from these stations clearly illustrates downward fluid freshening. The measured salinity and Cl⁻ concentration in the bottom seawater at Stations ARA13C-ST 02, ARA13C-ST20, and ARA13C-ST23 are ~35.0‰ and ~548 mM, 32.1‰ and ~517 mM, ~33.1‰ and ~538 mM, respectively (data are not shown here). Since Station ARA13C-ST24 is located close to Stations ARA13C-ST23 and the water depth of ARA13C-ST11, ARA13C-ST12, ARA13C-ST28, and ARA13C-ST29 is similar to that of Station ARA13C-ST23, we assumed that the Cl⁻ concentration in the bottom seawater at Stations ARA13C-ST11, ARA13C-ST12, and ARA13C-ST24 is ~33.1‰ and ~538 mM. The maximum degrees of freshening at each station within the retrieved core length relative to the measured and assumed bottom seawater at each station are estimated by the equation, $[Cl_{\text{seawater}} - Cl_{\text{pore water}}]/Cl_{\text{seawater}} \times 100$, which yields ~20%, ~27%, ~6%, ~5%, ~28%, ~11%, ~8%, and ~76% at Stations ARA13C-ST02, ARA13C-ST11, ARA13C-ST12, ARA13C-ST20, ARA13C-ST23, ARA13C-ST24, ARA13C-ST28, and ARA13C-ST29, respectively. However, we cannot estimate the maximum freshening ratio at Station ARA13C-ST41 without Cl⁻ concentration of bottom water. Since abundant ice has been observed at Stations ARA13C-ST11, ARA13C-ST21, and ARA13C-ST29, salinity and Cl⁻ concentration of melting ice from Stations ARA13C-ST11, and ARA13C-ST29 are ~0‰ and <~5.1 mM, respectively; the fluid freshening is associated with the ice melting in the sediment column.

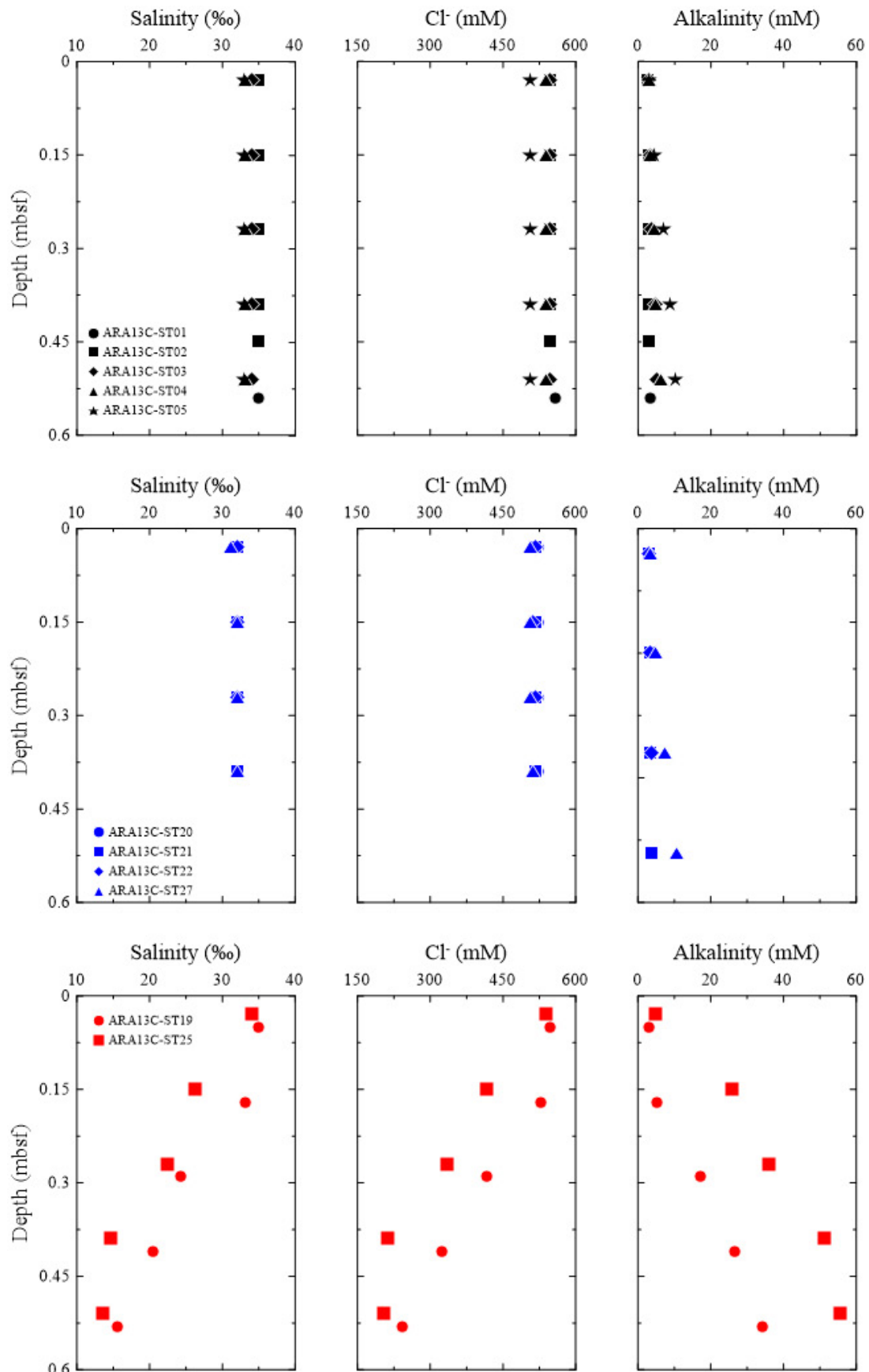


Figure 5.8. Downcore profiles of salinity, Cl⁻, and alkalinity in pore water from MCs.

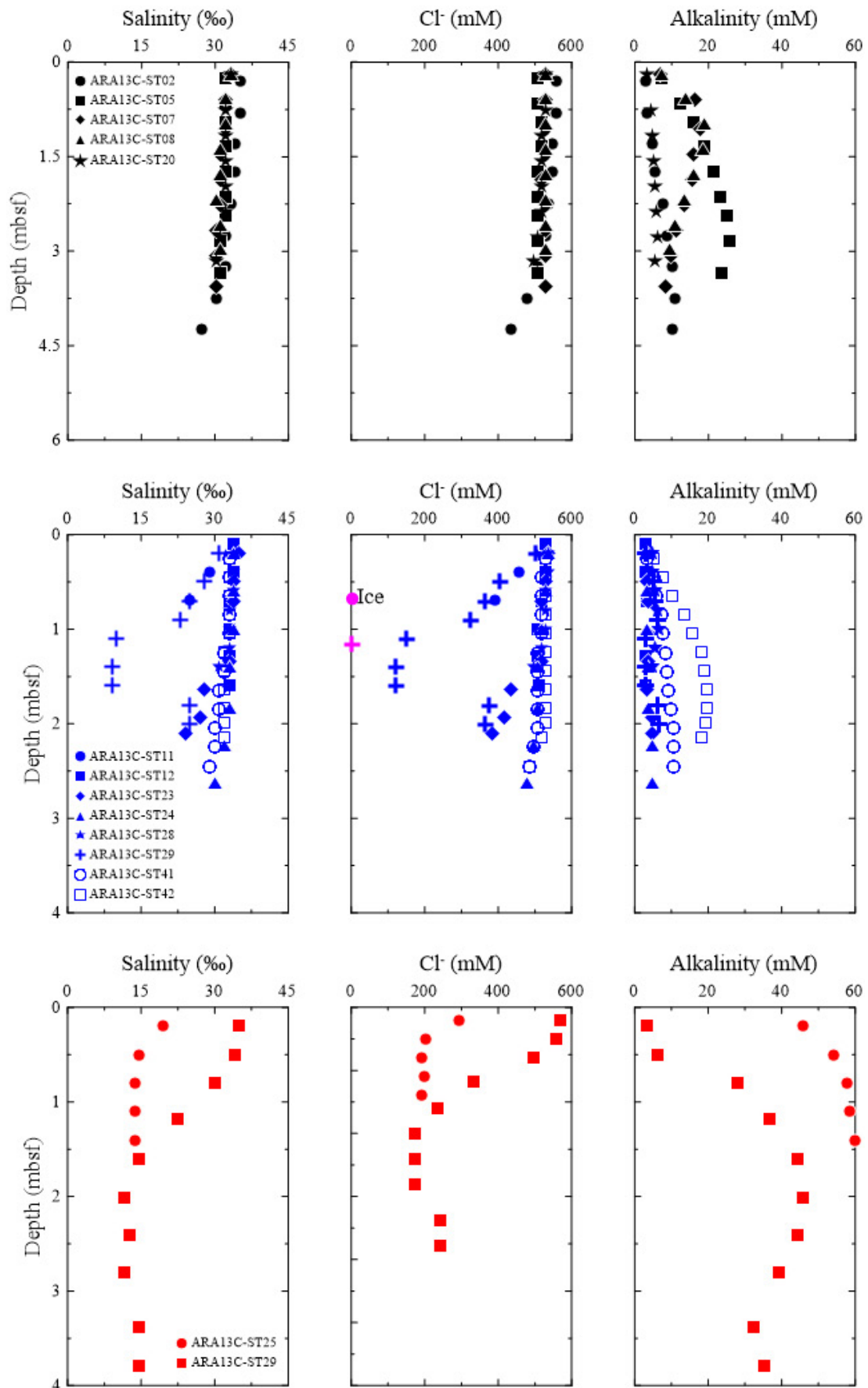


Figure 5.9. Downcore profiles of salinity, Cl⁻, and alkalinity in pore water from GCs.

The last group is observed at mud volcanos, Stations ARA13C-ST25 and ARA13C-ST30. It shows decreasing salinity and Cl⁻ concentration from the seafloor to 0.8 mbsf at Station ARA13C-ST25 and to 2.0 mbsf at ARA13C-ST30 and, ranges from ~19.5‰ to ~13.6 ‰ and from ~294 mM to ~193 mM, and from ~35.0‰ to ~11.7 ‰ and from ~568 mM to ~173 mM, respectively, and then it has a relatively constant or slightly increased salinity and Cl⁻ concentration (~13.6 ‰ and ~294 mM at Station ARA13C-ST25, and ~14.6 ‰ and ~246 mM at Station ARA13C-ST30) below it (Table 5.8; Figure 5.9). In situ gas hydrates were found at Station ARA13C-ST30 collected at MV740 m in both the MC and GC. The source of freshening fluid at these stations is probably originated from the deep-seated fluid, given the obvious fluid efflux setting of the mud volcano.

Alkalinity of pore water from at Stations ARA13C-ST02, ARA13C-ST03, ARA13C-ST04, ARA13C-ST05, ARA13C-ST20, ARA13C-ST21, and ARA13C-ST27 collected in MCs show a relatively constant or slightly increasing value with depth. The maximum alkalinity at these stations is less than 11 mM (Table 5.8; Figure 5.8). In contrast, alkalinity of pore water at MC Stations ARA13C-ST19 and ARA13C-ST25 increases with depth and has a ~34 mM and ~56 mM maximum value at the core base (Figure 5.8).

Alkalinity of pore water from Stations ARA13C-ST02, ARA13C-ST11, ARA13C-ST12, ARA13C-ST20, ARA13C-ST23, ARA13C-ST24, ARA13C-ST28, ARA13C-ST29, and ARA13C-ST41 sampled from GCs has a relatively constant value or displays slightly increasing trend with depth (Table 5.8; Figure 5.9). Station ARA13C-ST29, with known ice thawing, has particularly low values from 1.1 mbsf to 1.6 mbsf. The maximum alkalinity at these stations is less than 11 mM. In contrast, alkalinity of pore water from at GC Stations ARA13C-ST05, ARA13C-ST 07, ARA13C-ST 08, and ARA13C-ST42 shows a mid-core maximum, and then decrease with depth in core (Table 5.8; Figure 5.9). The maximum value is about ~26 mM at ~2.9 mbsf Station ARA13C-ST 05, ~18 mM at ~1.1 mbsf of Station ARA13C-ST07, ~19 mM at ~1.0 mbsf of Station ARA13C-ST 08, ~19 mM at ~1.8 mbsf of Stations ARA13C-ST42, respectively (Table 5.8; Figure 5.9). The alkalinity profile of pore water from Station ARA13C-ST25 sampled by GC shows a similar trend to that of pore water collected by MC (Table 5.8; Figures 5.8 and 5.9). It increases from the seafloor to ~0.8 mbsf and has a relatively constant value (~60 mM) (Figure 5.9). The downcore profile of Station ARA13C-ST30 is similar to that of Station ARA13C-ST25, however, the maximum alkalinity at this station is ~46 mM (Table 5.8; Figure 5.9). Unfortunately, SO₄²⁻ concentration of pore water had not been analyzed onboard during this cruise, thus the depth of sulfate-methane transition zone (SMTZ) cannot be estimated.

5.3.3. Oxygen measurement

The outermost MacKenzie Trough station shows a more gradual downcore oxygen depletion than those further in landward Trough (5.64 cm at ARA13C-ST01, 2.71 ± 0.15 cm at ARA13C-ST02, 2.39 ± 0.39 cm at ARA13C-ST03, and 1.53 ± 0.30 cm at ARA13C-ST04) (Figure 5.10). The correlation between oxygen concentration and terrestrial input and microbial communities will be investigated.

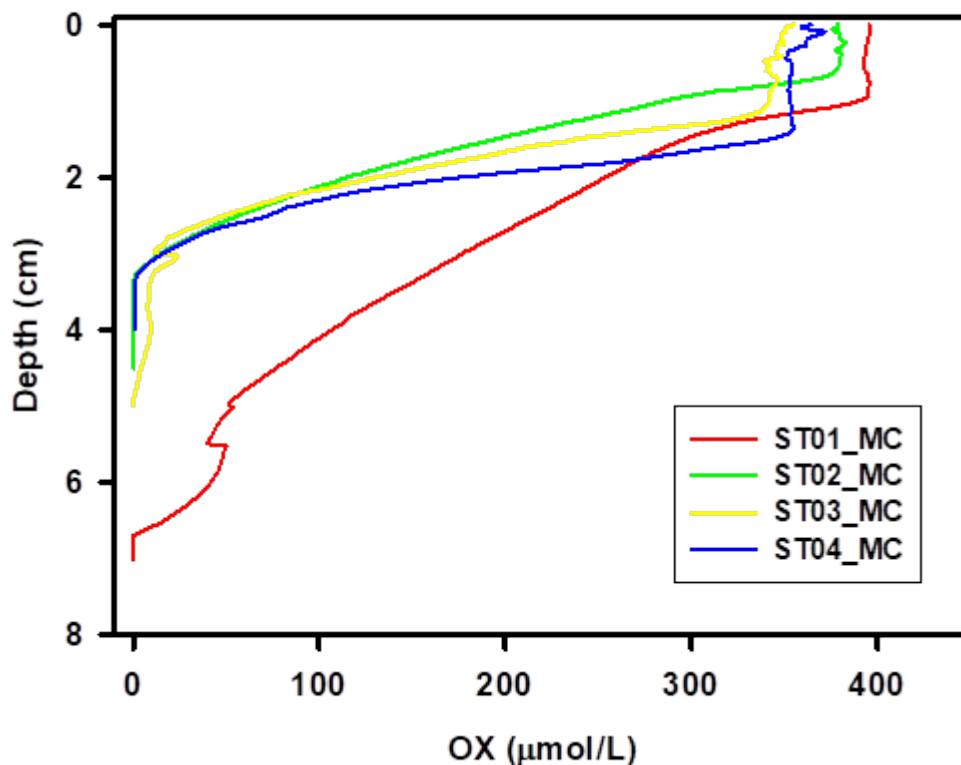


Figure 5.10. Profiles of oxygen concentration with depth in multi-cores.

5.4. Summary

A total of 21 MCs, 15 GCs, and 9 MiniROV push cores were collected from a variety of environments within the Canadian Beaufort Sea during the ARA13C cruise. In situ ice and gas hydrate were also found. In addition, we observed the freshening in several stations and oxygen depletion depth of the sediments from the outermost MacKenzie Trough station was deeper than that from landward Trough. The sample analyses permit some groupings and trends, both geographically and downcore. The initial results and planned post cruise research are suitable to address the goals of this cruise.

References

- Delpech, L.-M., Vonnahme, T.R., McGovern, M., Gradinger, R., Præbel, K. and Poste, A.E. 2021. Terrestrial inputs shape coastal bacterial and archaeal communities in a high Arctic Fjord (Isfjorden, Svalbard). *Frontiers in Microbiology*, 12: 614634.
- Garneau, M.-È., Vincent, W.F., Terrado, R. and Lovejoy, C. 2009. Importance of particle-associated bacterial heterotrophy in a coastal Arctic ecosystem. *Journal of Marine Systems*, 75 (1-2), 185-197.
- Glöckner, F.O., Gasol, J.M., McDonough, N. and Calewaert, J.-B. 2012. Marine microbial diversity and its role in ecosystem functioning and environmental change. *European Science Foundation* 2012.
- Gwiazda, R., Paull, C. K., Dallimore, S. R., Melling, H., Jin, Y. K., Hong, J. K., Riedel, M., E. Lundsten, E., Anderson, K., and K. Conway, K., 2018, Freshwater seepage into sediments of the shelf, shelf edge, and continental slope of the Canadian Beaufort Sea.

- Geochemistry, Geophysics, Geosystems, 19, <https://doi.org/10.1029/2018GC007623>
- Hauptmann, A.L., Markussen, T.N., Stibal, M., Olsen, N.S., Elberling, B., Bælum, J., Sicheritz-Pontén, T. and Jacobsen, S.J. 2016. Upstream freshwater and terrestrial sources are differentially reflected in the bacterial community structure along a small Arctic River and its estuary. *Frontiers in Microbiology*, 7: 1474.
- Kallmeyer, J., Pockalny, R., Adhikari, R., Smith, D.C. and D'Hondt, S. 2012. Global distribution of microbial abundance and biomass in subseafloor sediment. *Proceedings of the National Academy of Sciences*, 109 (40), 16213-16216.
- Lee, D.-H., Kim, J.-H., Lee, Y.M., Kim, J.-H., Jin, Y.K., Paull, C., Ryu, J.-S. and Shin, K.-H. 2019. Geochemical and Microbial Signatures of Siboglinid Tubeworm Habitats at an Active Mud Volcano in the Canadian Beaufort Sea. *Frontiers in Marine Science*, 8: 656171.
- Lee, Y.M., Noh, H.-J., Lee, D.-H., Kim, J.-H., Jin, Y. K. and Paull, C. 2019. Bacterial endosymbiont of *Oligobrachia* sp.(Frenulata) from an active mud volcano in the Canadian Beaufort Sea. *Polar Biology*, 42: 2305-2312.
- Li, Y., Hong, Y., Wu, J., Wang, Y. and Ye, F. 2021. Spatial variability pattern of the anaerobic ammonia-oxidizing bacterial community across a salinity gradient from river to ocean. *Ecotoxicology*, 30: 1743-1753.
- McClelland, J.W., Holmes, R. Dunton, K. and Macdonald, R. 2011. The Arctic Ocean estuary. *Estuaries and Coasts*, 35: 353-368.
- Paull, C.K., Dallimore, S., Caress, D., Gwiazda, R., Melling, H., Riedel, M., Jin, Y.K., Hong, J.K., Kim, Y.-G., Graves, D., Sherman, A., Lundsten, E., Andersen, K., Lundsten, L., Villinger, H., Kopf, A., Johnson, S.B., Clarke, J.H., Blasco, S., Conway, K., Neelands, P., Thomas, H., Côté, M. 2015. Active mud volcanoes on the continental slope of the Canadian Beaufort Sea. *Geochemistry, Geophysics, Geosystems*, 16(9), 3160-3181.
- Paull, C.K., Dallimore, S., Jin, Y.K., Caress, D.W., Lundsten, E., Gwiazda, R., Anderson, K., Hughes Clarke, J., Youngblut, S. and Melling H., 2022. Rapid seafloor changes associated with the degradation of Arctic submarine permafrost. *Proceeding of the National Academy of Sciences*, 119 (12) e2119105119.
- Sen, A., Duperron, S., Hourdez, S., Piquet, B., Léger, N., Gebruk, A., Le Port, A.S., Svenning, M.M., Andersen, A.C. 2018. Cryptic frenulates are the dominant chemosymbiotrophic fauna at Arctic and high latitude Atlantic cold seeps. *Plos One*, 13(12), e0209273.
- Sipler, R.E., Kellogg, C.T., Connelly, T.L., Roberts, Q.N., Yager, P.L. and Bronk, D.A. 2017. Microbial community response to terrestrially derived dissolved organic matter in the coastal Arctic. *Frontiers in Microbiology*, 8: 1018.
- Walker, A.M., Leigh, M.B. and Mincks, S.L. 2021. Patterns in benthic microbial community structure across environmental gradients in the Beaufort Sea shelf and slope. *Frontiers in Microbiology*, 37.
- Whitman, W.B., Coleman, D.C. and Wiebe, W.J. 1998. Prokaryotes: the unseen majority. *Proceedings of the National Academy of Sciences*, 95(12), 6578-6583.
- Yang, J., Ma, L.A., Jiang, H., Wu, G. and Dong, H. 2016. Salinity shapes microbial diversity and community structure in surface sediments of the Qinghai-Tibetan Lakes. *Scientific Reports*, 6(1), 1-6.
- Zhang, G., Bai, J., Tebbe, C.C., Zhao, Q., Jia, J., Wang, W., Wang, X. and Yu, Lu. 2021. Salinity controls soil microbial community structure and function in coastal estuarine wetlands. *Environmental Microbiology*, 23(2), 1020-1037.

ARA13C Cruise report

Chapter 6. Heat flow measurements

Y.-G. Kim, H. Kim and Y. Baek

6.1. Introduction

Mud volcanoes are surface expressions generically formed by a surface discharge of focused fluid flow (Niemann and Boetius, 2010; Mazzini and Etiope, 2017), triggered mainly by mudflow discharge (including fluid and gas) caused by high pressure at great depth or instability of sediments (Kopf, 2002; Niemann and Boetius, 2010; Mazzini and Etiope, 2017). While a study of onshore mud volcanoes in terms of tectonic settings, mechanism, and activity began in the early 1900s, a comprehensive study of offshore mud volcanoes was promoted in the late 1900s with help from the enhanced capability of subaqueous geophysical survey instruments and accuracy of the positioning of bottom samplers (Milkov, 2000). Offshore mud volcanoes can be identified based on seafloor structure implying subsurface expulsion (subcircular elevated bathymetry), and fluid and gas expulsion above the seafloor (Milkov, 2000). Offshore mud volcanoes often occur on continental margins and rarely in the abyssal plains, and their total number in the oceans varies with studies from at least 300 (Etiope and Milkov, 2004) to the order of 10^3 - 10^5 (Milkov, 2000).

Recent studies have shown that mud volcanoes may be offshore sources of methane, with potential greenhouse gas implications (Dimitrov, 2003; Sauter et al., 2006; Wallmann et al., 2006; Menapace et al., 2017). Although the annual amount of methane emitted to the atmosphere through mud volcanoes was estimated to be ~ 5 Tg CH₄ (Dimitrov, 2003), the estimated value does not take into account the consumption of methane by anoxic methane oxidation (AOM) in surface sediments in the offshore mud volcanoes. For example, methane flux estimates from the offshore mud volcanoes in the Black Sea may be an order of magnitude lower when considering the AOM process (Wallmann et al., 2006). Mudflow discharge rate, a source of energy for chemosynthetic communities to carry out the AOM process, is one of the controlling factors regulating the AOM processes inside mud volcanoes (de Beer et al., 2006; Niemann and Boetius, 2010). Mudflow and associated porewater discharge are observed from the surface sediment (Paull et al., 2015, Gwiazda et al., 2019) and variability of discharge rates occurs both between and within sites, rendering net discharge estimates challenging.

To better understand the discharge, in a vertical section of the mud volcano it could be helpful to know thermodynamic properties of the deeper mudflow migration path as flow paths can branch or change off toward the seafloor according to our current knowledge (Burhannudinnur and Noeradi, 2021; Menapace et al., 2017; Loher et al., 2018). Since the driving force of the discharge is the difference in pressure and temperature of the migration path with respect to outside of the path, such information is essential for quantifying the magnitude of discharge but remains poorly understood owing to a lack of observation. Temperature/pressure gradient measurements are generally restricted to the length of corer penetration, however in very soft sediments, overpenetration of the gravity corer below the seafloor has been experienced. For instance, a low thermal gradient at the depth interval of ~ 25 - 40 meters below seafloor (mbsf) was reported from the Håkon Mosby mud volcano in the

Barents Sea (Feseker et al., 2008) and ~63-67 mbsf from the Dvurechenskii mud volcano in Black Sea (Feseker et al., 2009). The over-penetrating depth was determined only by mud smear on the winch cable.

In 2017, a joint Korea-USA-Canada research team operated the icebreaker RV Araon at the 420 m mud volcano (MV420) area on the continental slope of the Canadian Beaufort Sea (Jin et al., 2018). A multibeam sonar backscatter image obtained in 2017 delineates newly-formed mound morphology at the top of the volcano (Figure 6.1c) (Jin et al., 2018). A heavy-weighted marine heat probe, consisting of a gravity corer as a frame and pressure, temperature, and tilt sensors, was lowered into these newly-formed mound morphologies. Based on pressure reading, we determined that the probe reached a depth of several dekameters beneath the MV420 top (i. e. overpenetration). Furthermore, the probe was descended several times in controlled increments. All three sensors were time-synchronized so that the data illustrate temperature and pressure changes correlated with changes in the inclination of the probe. Pressure changes with depth below the seafloor account for sediment loading, such that this overpenetration experiment allows some assessment of the sediment bulk density in the mudflow migration path

Again in 2022 the joint research team visited in MV420 and operated MiniROV survey, AUV survey for observation of bathymetry, and coring for both collection of gas hydrate and tubeworms as well as heat flow measurements. For the three sites C, D and E observed in 2017, heat flow measurements were conducted with the new Small Deep Sea (NSDS) winch which provides time series in tension, length, and speed of winch cable payout. These parameters provide additional evidence for the overpenetration performance. Such winch information was not recorded in 2017 because integration of the NSDS to Araon's DADIS was not completed at that time. Additional investigation in the 2022 expedition involved post-heat-probe deployment with MiniROV cameras by re-occupying three exact probe sites and visual inspection to further observe what probe behavior phenomena occurred as a consequence of its overpenetration. This can be integrated with any measured change in bathymetry and backscatter intensity obtained by the AUV toward establishing eruption dynamics at the three sites.

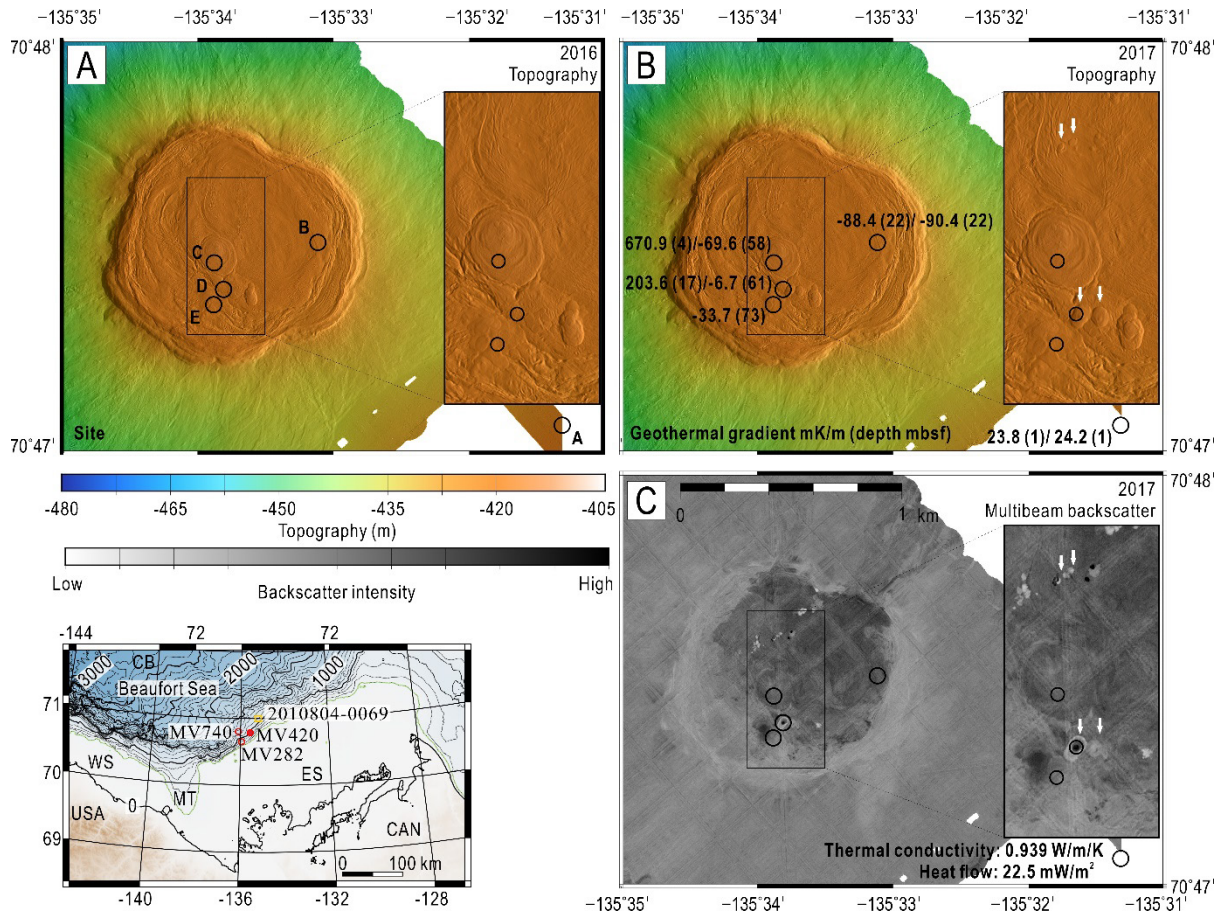


Figure 6.1. Acoustic survey results with the autonomous underwater vehicle (AUV) at MV420. Multibeam echosounder bathymetry obtained in 2016 (A) and 2017 (B), and backscatter intensity images from multibeam echosounder in 2017 (C) are shown. New mound morphologies (white arrows in Figure subset B) formed in one year. Five sites (A to E in Figure subset A) and observed geothermal gradient (numbers in Figure subset B) with penetrating depth (numbers with parentheses in Figure subset B) for each site are depicted in Table 6.1. Thermal conductivity and heat flow for Site A (reference site) values are shown in C. Inset exhibits regional bathymetry of the Canadian Beaufort Sea and the location of three mud volcanoes (red circles): MV282, MV420 (closed), and MV740 (Paull et al., 2015). The subsea permafrost limit is considered to follow an isobath of water depth ~100 meters below sea level (dashed green line) (Taylor et al., 2013). WS: Western Shelf, MT: Mackenzie Trough, ES: Eastern Shelf, CB: Canadian Basin.

6.2. Methods

6.2.1. Temperature, pressure, and tilt

Temperature (Type 1854 Miniaturized Temperature Data Logger; ANTARES Datensysteme GmbH, Stuhr, Germany) and depth loggers (DST Tilt; Star-Oddi, Garðabær, Iceland) were attached to the 6 m-long barrels of the gravity corer to increase survey efficiency by simultaneously collecting a sediment core along with the heat flow measurement (Figure 6.2a) (Kim et al., 2020; Kim et al., 2022). All sensors record data every second, so observation results of temperature, pressure, and tilt can be synchronized via time stamps. Six temperature loggers were attached, separated by 70–120 cm (Figure 6.2a and 6.2b). The temperature resolution is 0.001 °C with a range of -5–50 °C. A tilt sensor was located on the head (Figure 6.2a and 6.2c), and the tilt resolution is 1° along three axes. The depth resolution is 0.9 m. Data from the loggers were downloaded after recovering the heat probe (all sensors attached to the gravity corer). Measurement of heat flow consisted of 4 steps:

- Deployment from ship.
- 5–10 min wait over the seafloor to secure the vertical alignments of the probe and the relative corrections between temperature sensors.
- 20–25 min wait while in the sediments after penetration with a falling speed of 30–50 m/min to allow thermal equilibrium.
- Retrieval.

During the measurements, the dynamic positioning capability of the ship and tension control of the winch are crucial to avoid secondary thermal effects due to friction between the sediments and falling corer for such long in situ time.

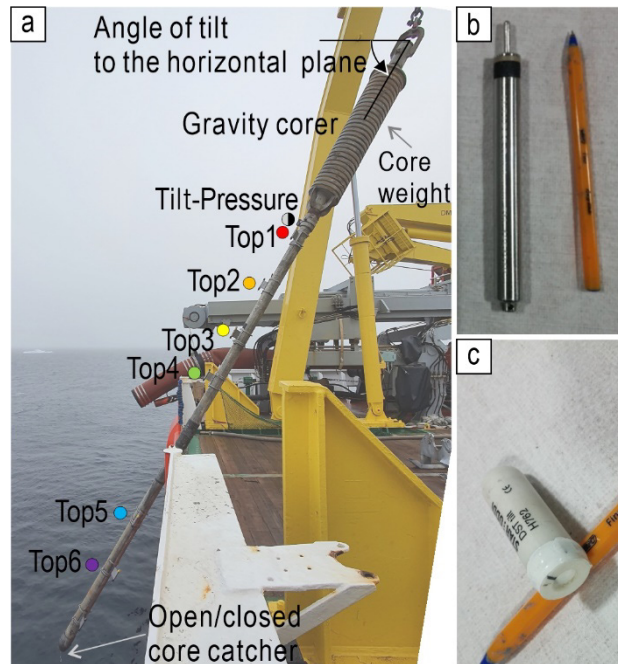


Figure 6.2. The heat probe consists of the gravity corer as a frame, temperature sensors (Antares Miniaturized Temperature Data Logger (MTL); Top1 to 6 in A), and tilt-pressure sensor (Star-Oddi DST Tilt; Tilt-Pressure in A), which was operated in the main back deck of IBRV Araon. Winch cable with the heat probe is connected to the top of the corer. The length of the corer is 7.5 m. The tilt sensor records an angle of the corer with respect to a horizontal plane such that a tilt reading of 90° implies that the corer stands perpendicular to the horizontal plane. The MTL and DST Tilt are shown in B and C, respectively, together with a ball-point pen for scale. Modified from Kim et al. (2022a). Photos courtesy of Korea Polar Research Institute.

6.2.2. Experiment with descending the probe by a controlled distance during overpenetration

Penetration depth of the gravity corer depends on various parameters such as lithology, frictional coefficient with sediments, weight of core, speed of penetration and so on (Wu et al., 2020). Given conditions where all parameters are the same, penetration depth of the corer increases with decreased frictional coefficient. Under laboratory experiments, frictional coefficient of pure clay composition is decreased to 0.1 at minimum, leading to two times deeper penetration compared to 1:1 clay-silicic grain composition, corresponding to a frictional coefficient of 0.3 (Kopf and Brown, 2003; Wu et al., 2020). The friction coefficient, in general, decreases with an increase in water content (Kuo et al., 2011).

Since data recording by the temperature, pressure, and tilt sensors is at one second intervals, the position of the heat probe is deciphered by analysis of sensor readings after retrieval of the heat probe. Both the impact of the heat probe on the seafloor and the initiation of pulling-out

are represented by an abrupt increase in temperature readings together with a change in tilt readings (Figure 6.3). When the heat probe penetrated the sea floor, there were little changes in readings of tilt and pressure from sensors attached to the probe because the probe is fixed in position and angle within the sediments. In addition, the pressure during penetration into the sediments falls into estimates considering water depth and atmospheric pressure (Figure 6.3a). Recognition of overpenetration might register by a pressure reading higher than the water depth at the site and possibly a coincident anomalous temperature reading. Small changes in tilt reading is generally identical regardless of seabed penetration (Figure 6.3b). Cable length and tension data obtained on this expedition add confidence in recognizing overpenetration of the probe and amount of controlled penetration depth increments.

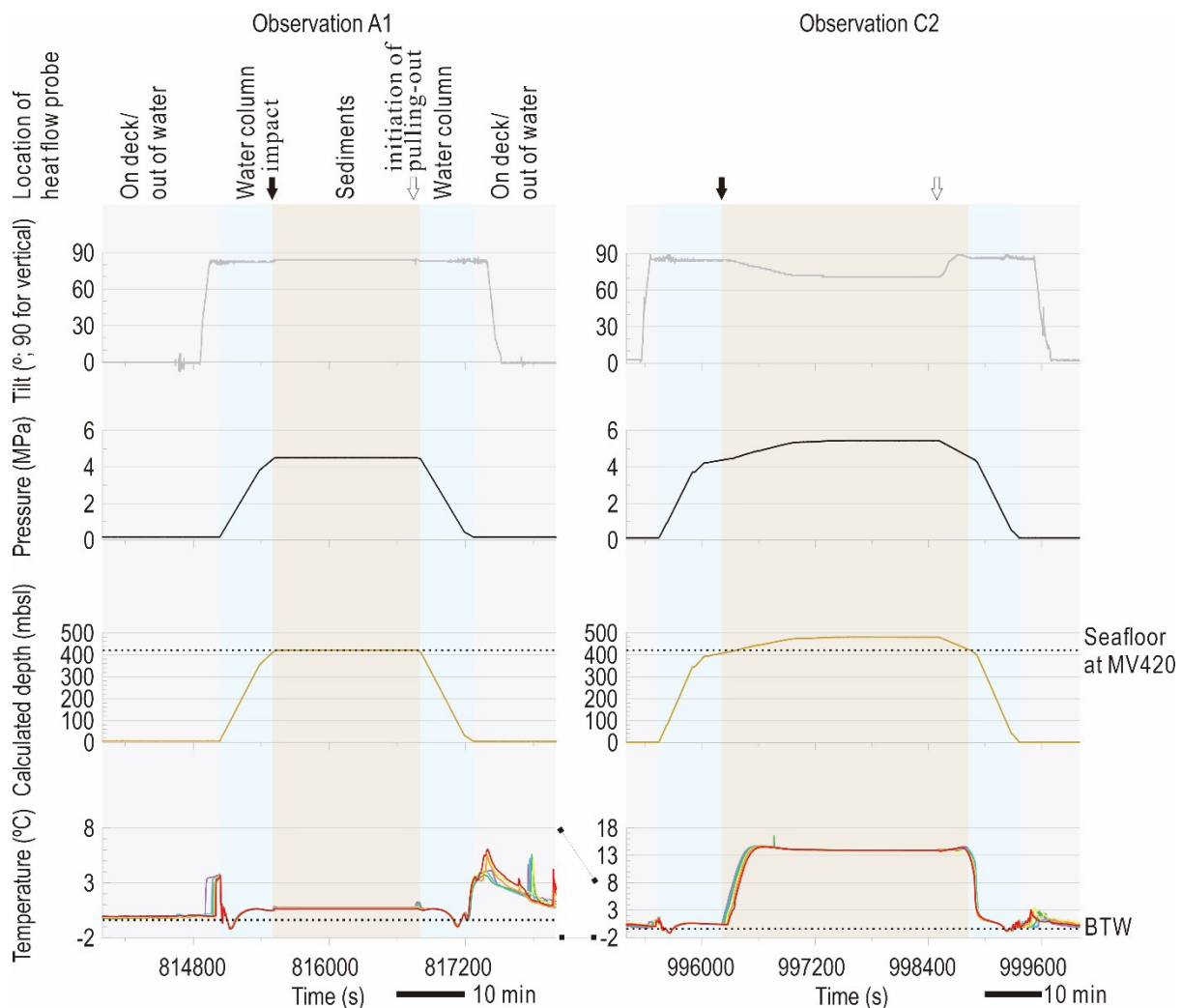


Figure 6.3. Comparison of heat flow measurements in normal penetration and overpenetration obtained during the ARA08C expedition in 2017. Analysis of time series of tilt (first row), pressure (second row), and temperature (fourth row) recordings allow for discriminating the location of the heat flow probe. The timing of impact (black arrow) and initiation of pulling-out (white arrows) of the heat probe can be identified from the abrupt changes in temperature and tilt readings. In the case of overpenetration, it takes more time for the heat probe to escape sediments after the initiation of pulling-out. Depth (third row) is converted from pressure data (see text). Water depth 420 and bottom water temperature are marked in the third and fourth rows. The heat probe remained in the sediment for at least 20 min after penetration/impact. Horizontal scale bar is 10 min.

During overpenetration, we experimented with releasing the winch cable in controlled increments (Figure 6.4). For instance, we paid out a winch cable by controlled amount more at

Step #N. During this time, the motion and position of the probe within sediment may or may not change. Such changes in motion and position are reflected in readings of pressure and tilt sensors. Three different theoretical cases can be inferred;

- In the case the probe sank by the same amount as the cable increment, it is expected that the tilt reading remains unchanged, but the pressure reading increases.
- If the probe inclined, the tilt reading would reflect this, and the pressure reading would increase slightly.
- If the probe was fixed, the tilt and pressure readings would remain unchanged.

Thus, deciphering the readings of sensors will help us interpret the position and motion of the probe at Step #N+1. This experiment was done during Observation C2 at Site C.

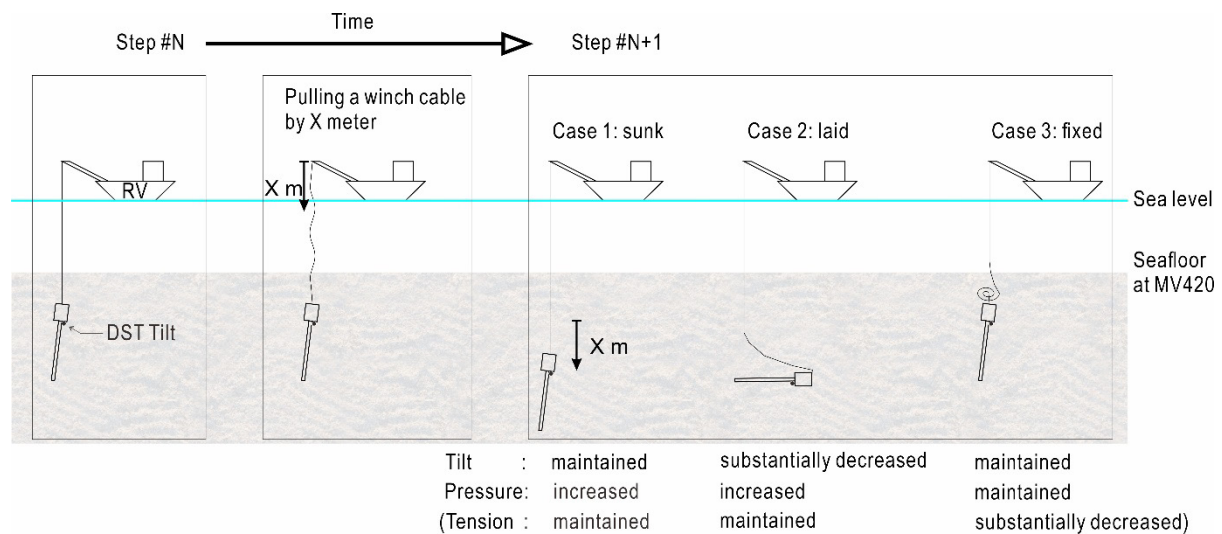


Figure 6.4. Schematic diagram of the experiment during overpenetration of the heat probe. A cable from the winch was released by controlled amount after Step #N then the heat probe responded to the cable increment at Step #N+1. Response can be categorized into three situations: sunk, inclined, and fixed (stable). Sensor readings can differentiate the three situations. Cable tension was not recorded digitally due to a malfunction of the winch but manually (handwriting) in 2017 while it was successfully done in 2022 (ARA13C).

6.2.3. Bottom water temperature and pressure calibration

The Conductivity-Temperature-Depth (CTD) tool is standard and essential equipment that provides physical, chemical, and biological information through the water column. It was cast to several meters above the seafloor to observe bottom water temperature. CTD casting was carried out at Station 14 and the bottom water temperature was observed with lowering of the CTD by 417 meters (Table 6.1).

6.3. Results

6.3.1. Locations



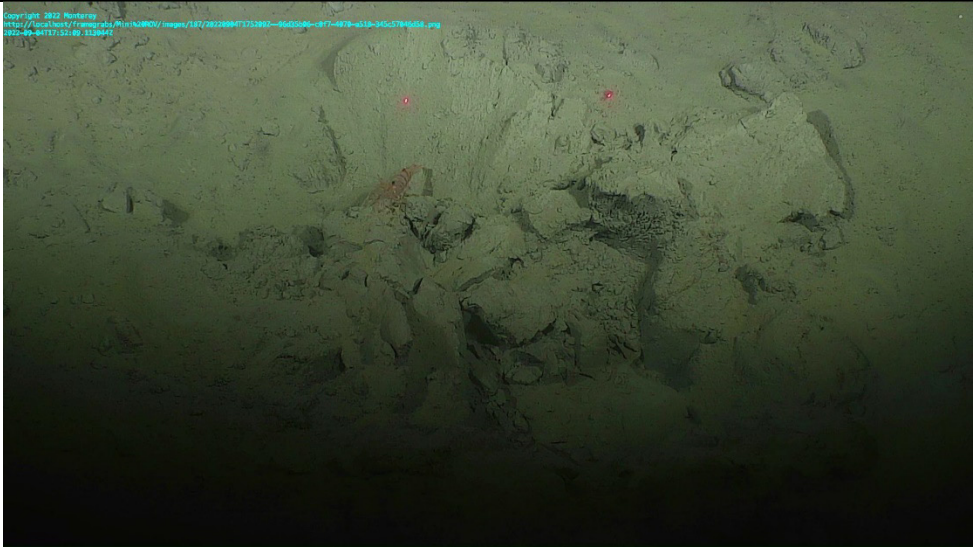
Heat flow measurements were conducted to determine the thermal structure of MV420 at three stations (ARA13C Stns. 15-17) and to estimate the gas hydrate stability zone at one station north of MV420 (ARA13C Stn. 18) (Table 6.1). The MiniROV performed Dive #187 on MV420 3 days after the heat flow measurements. Visual inspection of the seafloor by MiniROV enable us to identify the actual impact holes at each station (Table 6.2). In the case of Stn. 17 it was not easy to identify the hole because it was rather small and collapsed. However, a cable trail cast leading to the hole helped us to find and confirm the hole location. Recorded GPS locations between targeted and actual sites are slightly different (Figure 6.5). We deployed the heat probe at the targeted position, but the heat probe touched the seafloor of the MV420 at the actual position. Difference ranges from 5 to 13 meters.

Vigorous expulsion of fluid was expected at the impact holes but it was not observed. A slight increase in temperature from 0.54°C as background to 0.66°C in the middle of the hole at Stn. 16 and a gathering of shrimp around the hole are observed. The shrimp dispersed when the arm of MiniROV entered the hole, only to gathered again with its removal. These may indicate the occurrence of flow expulsion from depth, otherwise invisible through optical inspection. Diameter of the hole varies across stations but is the largest at Stn. 15 where there were two times of overpenetration (work orders 1 and 2 in Table 6.1).

Table 6.1. Summary of heat flow stations during the ARA13C expedition

St n.	WO	Gear	Ship's sampling location		miniROV's location		WD (m)	Remark
			Lat (D:M)	Lon (D:M)	Lat (D:M)	Lon (D:M)		
14	1	CTD	70:47.3867	-135:33.6047	NA	NA	425	Lowered by 417 mbsl
15	1	HF	70:47.4602	-135:33.8775	70:4575	-135:33.8974	423	13.1 m difference; Previously ARA08C Stns. 30 and 33
15	2	HF	70:47.4602	-135:33.8775	70:4575	-135:33.8974	423	13.1 m difference; Previously ARA08C Stns. 30 and 33
16	1	HF	70:47.3958	-135:33.8036	70:47.3966	-135:33.8137	423	6.4 m difference; Previously ARA08C Stns. 29 and 34
17	1	HF	70:47.3589	-135:33.8813	70:47.3566	-135:33.8858	425	5.0 m difference; Previously ARA08C Stn. 35
18	1	HF	70:49.8978	-135:39.543	NA	NA	562	Outside of MV420; gas hydrate stability zone

Table 6.2. Photos of holes at the seafloor formed by impact of the heat flow probe obtained during MiniROV's dive #187. Distance between two red laser points is about 13 cm. Photos courtesy of MBARI

Station	Hole
Stn. 15	 <p>Copyright 2022 Monterey https://commons.wikimedia.org/wiki/File:MiniROV/images/187/20220904T1853163--0602040--077--078--053--045-5794658.png 2022-09-04T18:53:16.806952Z</p>
Stn. 16	 <p>Copyright 2022 Monterey https://commons.wikimedia.org/wiki/File:MiniROV/images/187/20220904T1852292--0602040--077--078--053--045-5794658.png 2022-09-04T18:52:29.739956Z</p>
Stn. 17	 <p>Copyright 2022 Monterey https://commons.wikimedia.org/wiki/File:MiniROV/images/187/20220904T1752002--0602040--077--078--053--045-5794658.png 2022-09-04T17:52:00.313946Z</p>

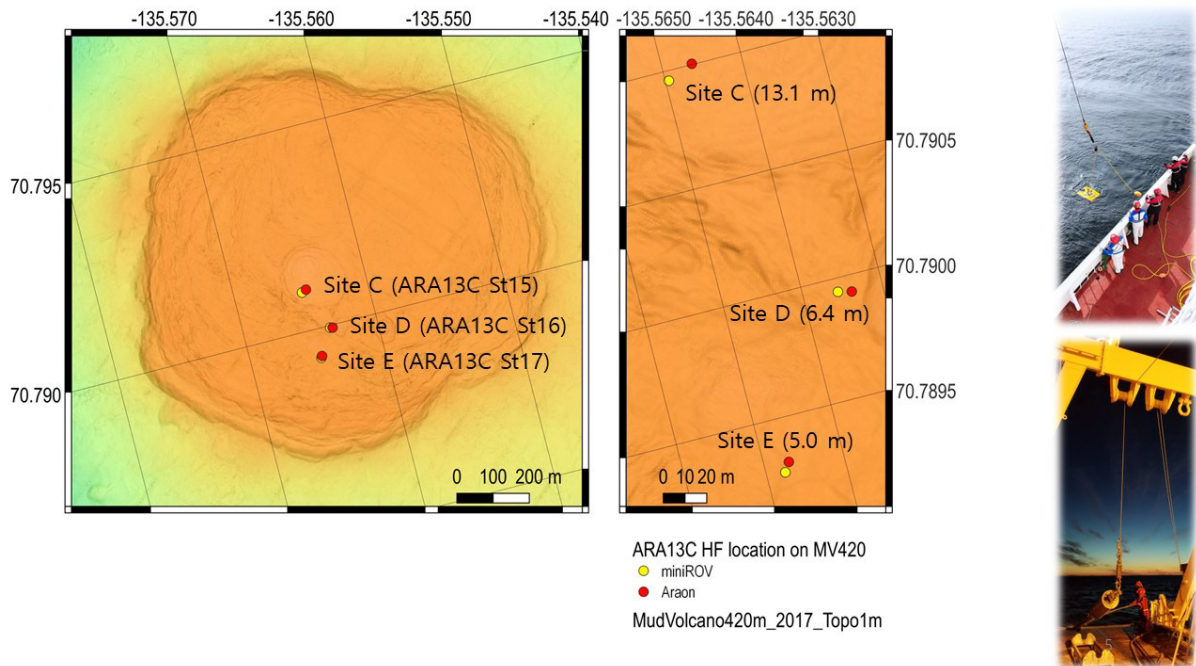


Figure 6.5. Location of heat flow measurements during the ARA13C expedition, which coincides with heat flow stations on MV420 during the ARA08C expedition (Table 6.1). Locations between targeted (red) and actual sites (yellow) are rather different. Actual ARA13C impact holes were found during MiniROV's Dive #187.

6.3.2. Time series of probe sensors and winch readings

At all four sites of heat flow measurements, winch cable information was successfully recorded as a time series, together with sensor information of tilt, temperature, and pressure (Figures 6.6, 6.7, and 6.8). It consists of three kinds of readings of cable length, speed and tension of the NSDS winch. In 2017, the cable information was not recorded because the data integration of the NSDS winch into the DADIS was not completed.

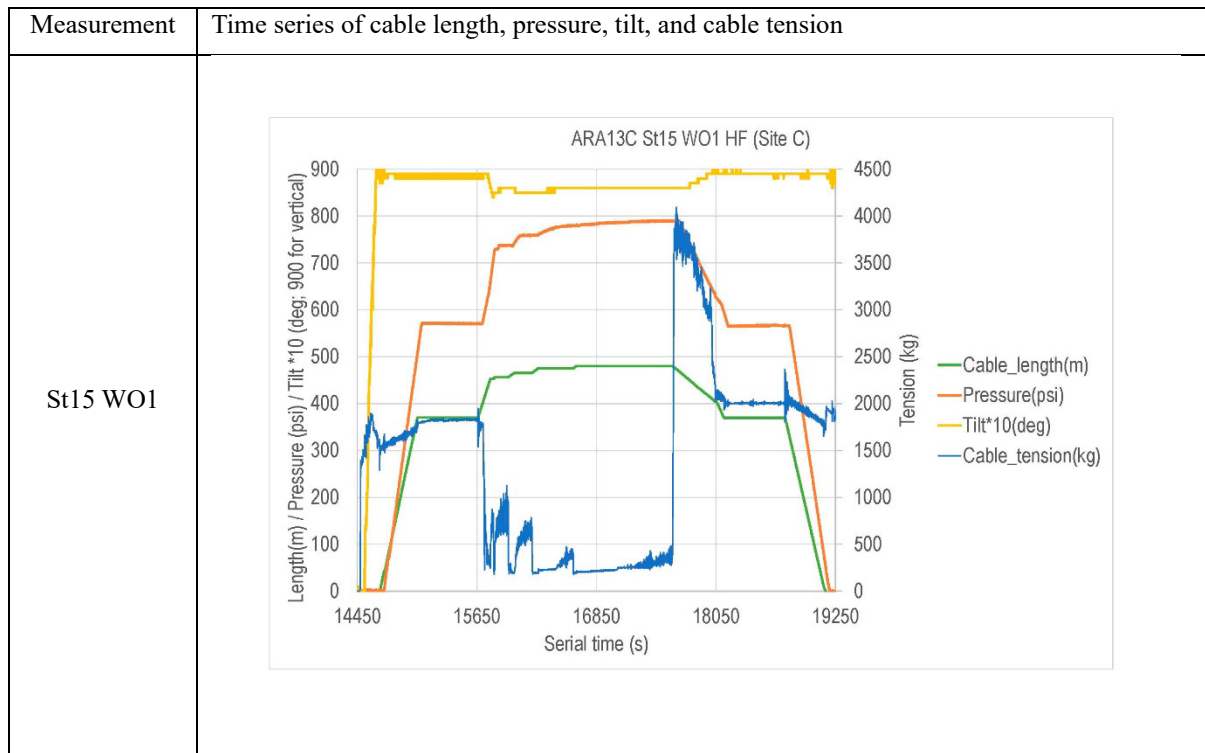
At cable length of 370 m, the heat flow probe was hung for 10 mins to calibrate the readings of 6 temperature sensors attached to the barrel. The cable was released by an additional 5-20 meters after the impact of the probe with the seafloor. The cable was then paid out by controlled increments of 5-15 m every ~2 minutes. Cable tension is recovered during the 2 min-pause with abrupt decrease at the onset of paying-out. If the cable tension has not recovered, or stabilized, the heat probe is left for an additional 20 min to determine the geothermal gradient. Then, the probe is retrieved with the ascend speed of 10 m/min until it reaches the water column. During the period of ascending through the sediments, cable tension abruptly increases but decreases with time in general except for a peak at subsurface near the seafloor. Exceptionally, a 10 min-waiting in water column during retrieval of the probe was done only at Stn. 15. Inclination of the probe remains almost vertical (more than 80 deg) during the whole procedure from water-in to water-out, indicating that the probe was not laid within sediments after impact to the seafloor. Peak of pressure reading occurs just before the onset of retrieval, that is, the end of 20 min-waiting within the sediments.

Figure 6.6 shows readings of cable length, cable tension, tilt and pressure at each station. The heat probe was operated twice at Stn. 15 and noted as Work Order 1 and 2. At Stns. 16 and 17, the operation was performed only once. Four types of data for four measurements at the three stations shows similar trends with respect to the operation of cable length.

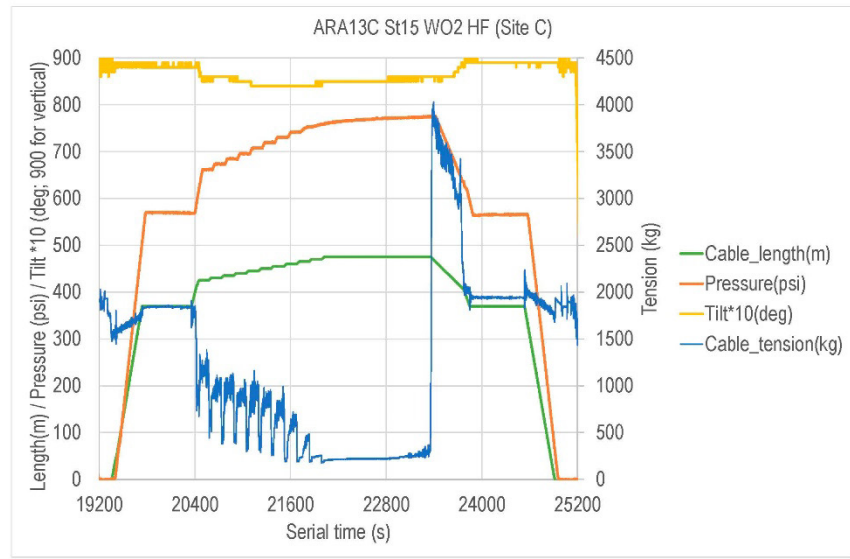
Averaged temperatures of the six temperature sensors are plotted with pressure as shown in Figure 6.7. Initiation of pressure axis is determined from pressure reading corresponding to water depth of 420 m. Pressure increase rate is similar to descending speed of the probe after impact with the seafloor. The pressure reading can be further converted into penetrating depth of the probe when estimating bulk density of the sediments. For all four measurements, averaged temperature substantially increases with pressure to some extent, then slightly decrease with pressure. Highest temperature point, termed the local thermal maximum point, lies far below the seafloor. Maximum temperature and pressure of the local thermal maximum point vary with stations, possibly reflecting eruption activity level (Kim et al., 2022b).

During the period of retrieval, cable tension and tension were recorded, plotted in (Figure 6.8). Despite rather constant ascending winch speed, cable tension changes with time (or penetrating depth), characteristic all deployments.

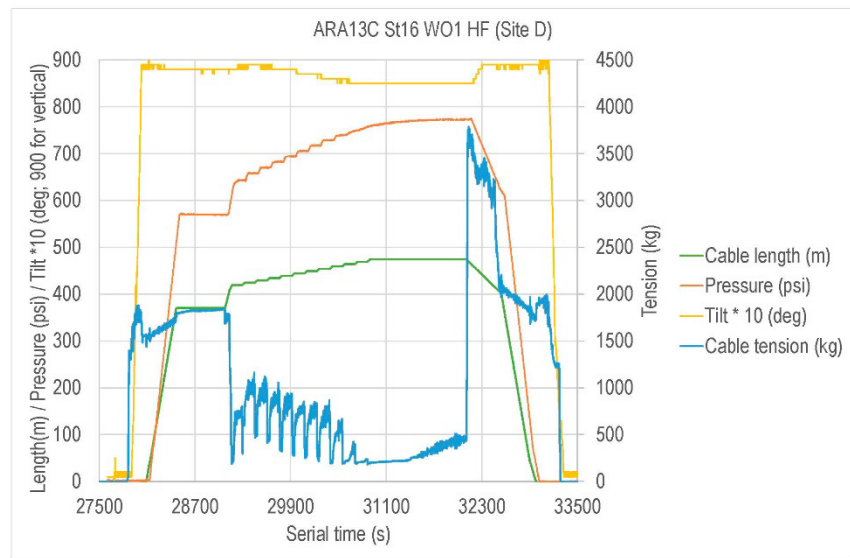
Based on preliminary results, it looks that the goal to reproduce overpenetration experiment of a heat probe on the MV420 was successfully achieved at all sites, following in 2017. As stated above, winch information during overpenetration was also successfully collected for the first time. Further analysis will be carried out onshore.



St15 WO2



St16 WO1



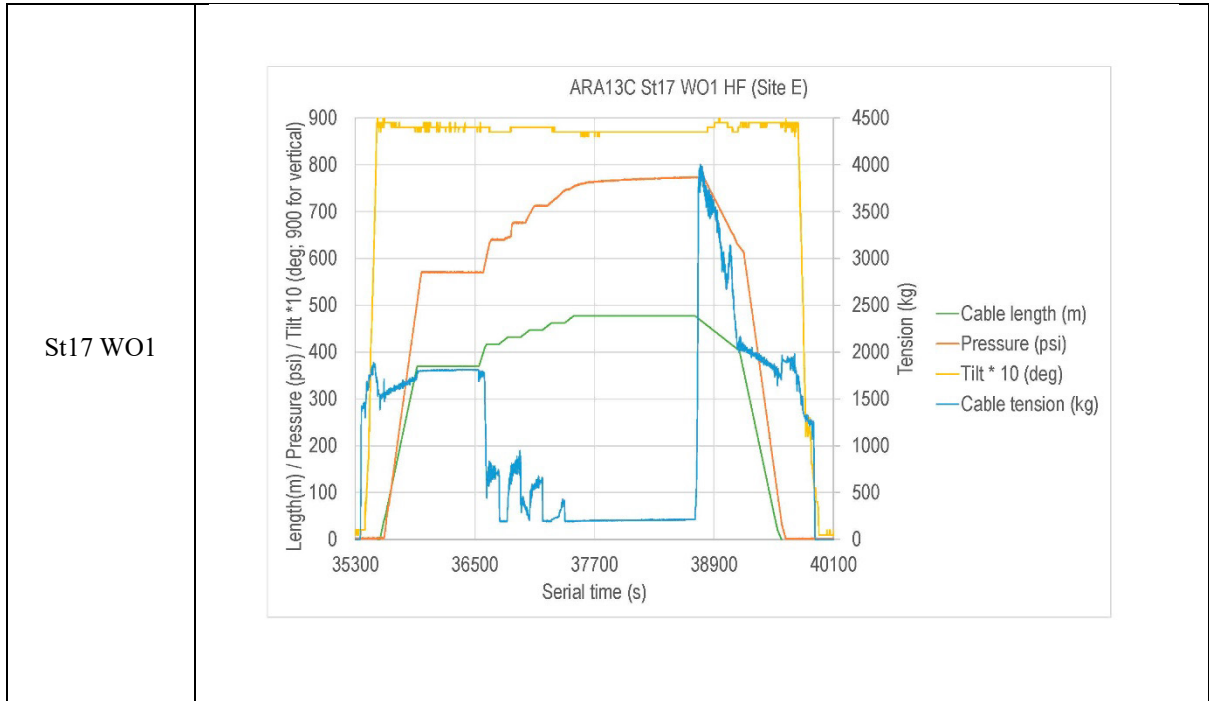
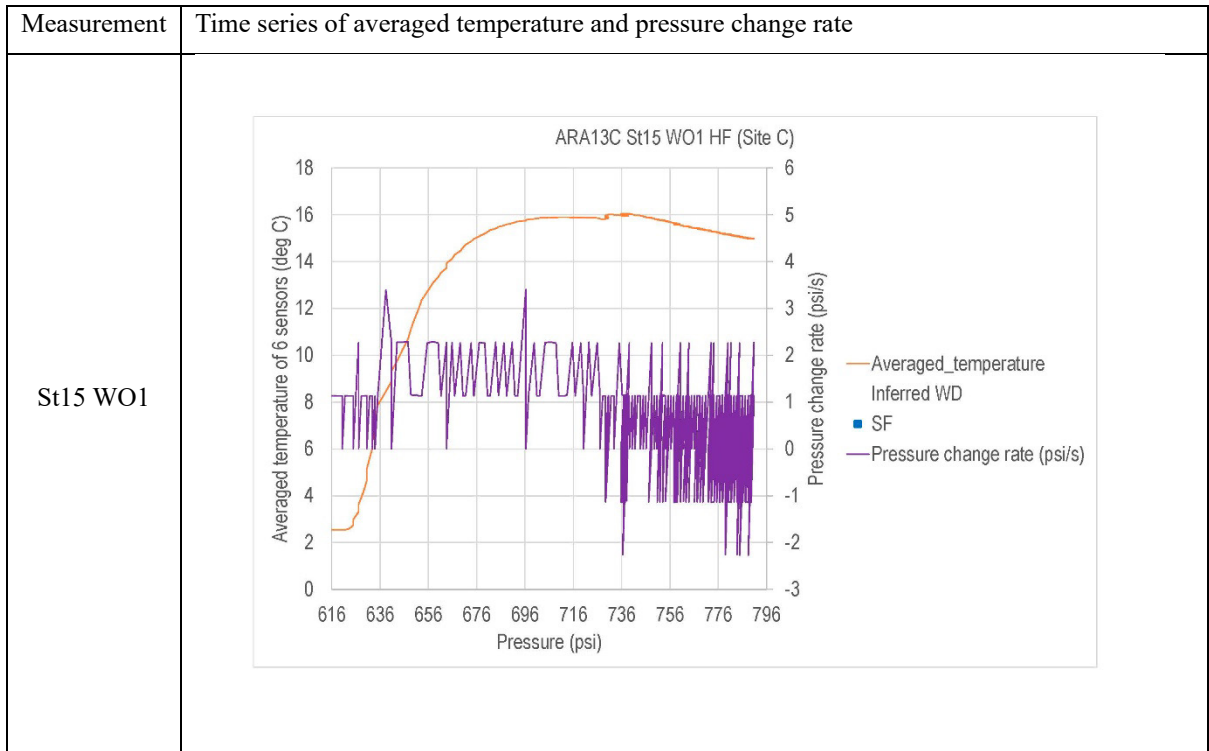
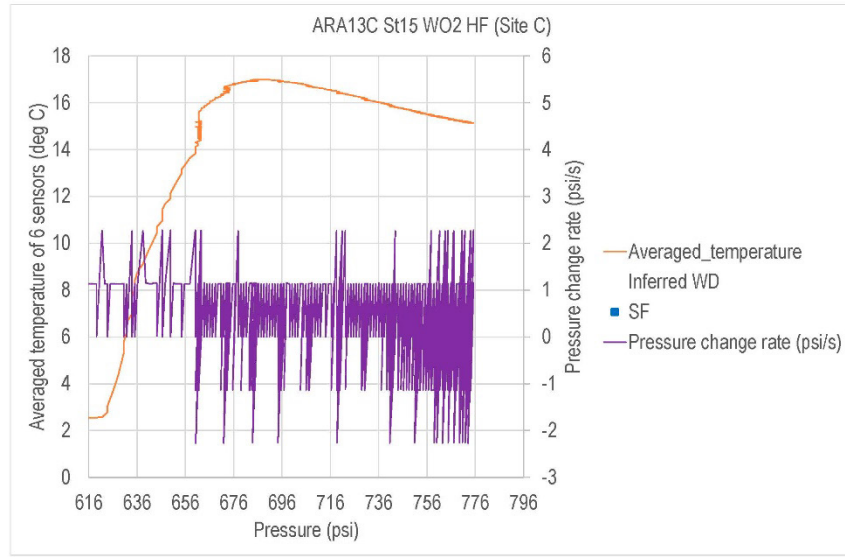


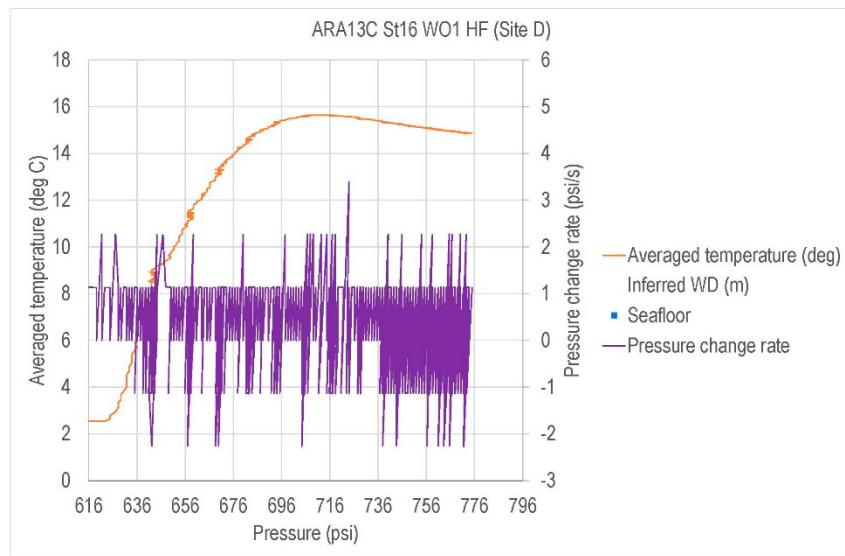
Figure 6.6. Results of cable length, cable tension, pressure, and tilt through the whole measurement at each station.



St15 WO2



St16 WO1



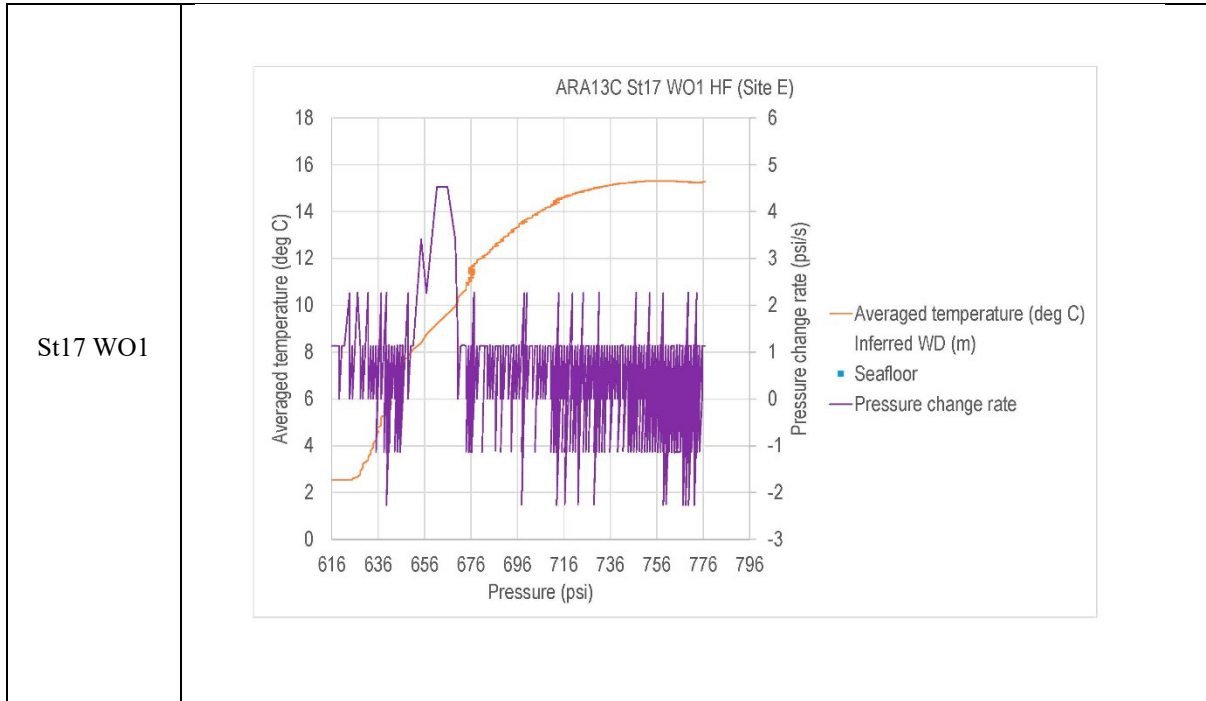
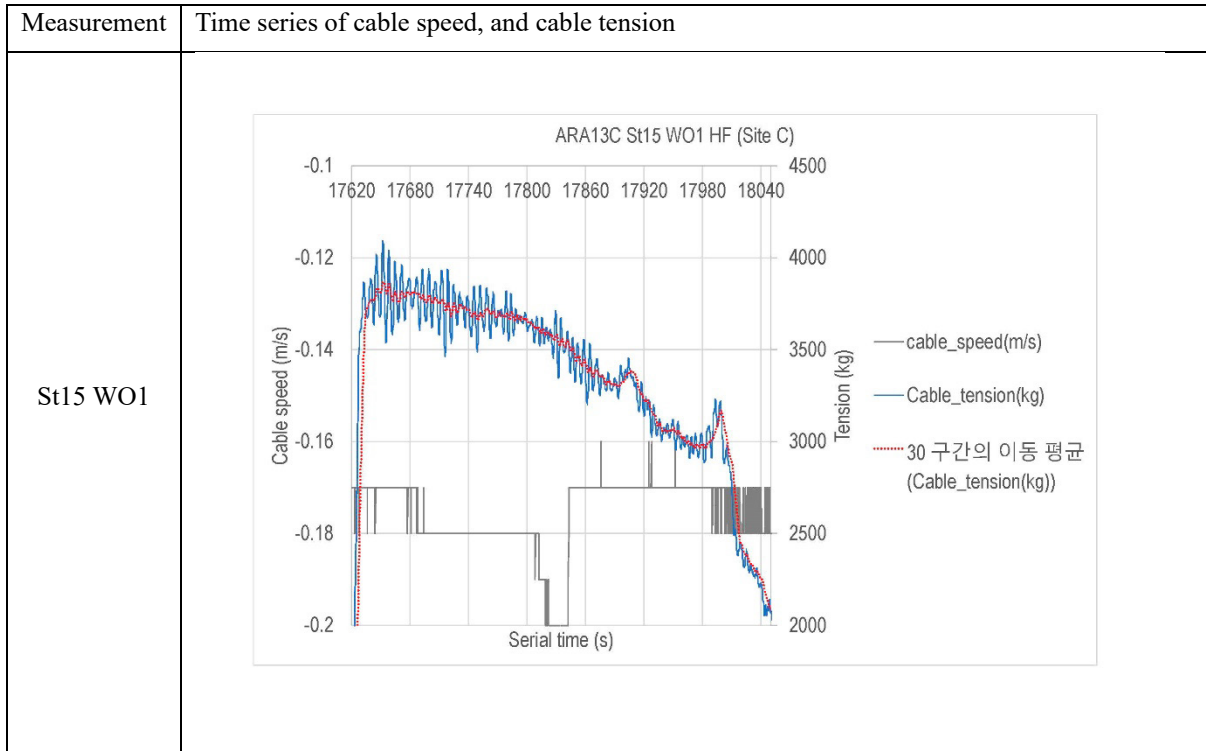
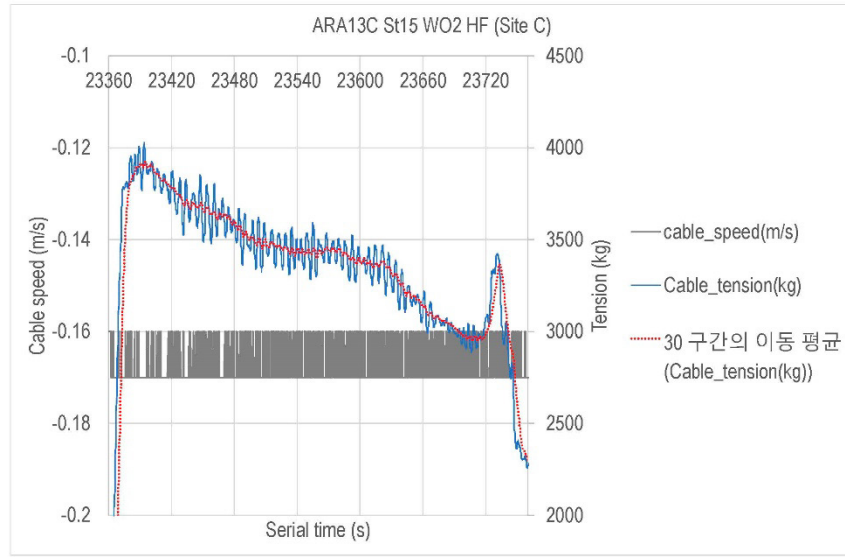


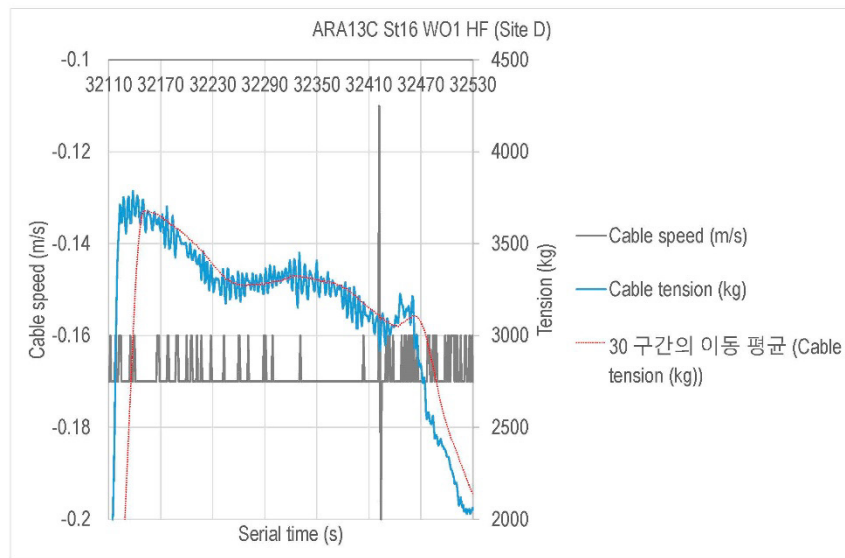
Figure 6.7. Results of cable length, averaged temperature and pressure change rate between timings for the probe to reach to pressure corresponding to 420 m water depth to highest pressure. Pressure reading is not converted to penetrating depth yet. At Stn. 15, the temperature curve varies with pressure change rate (similar to descending speed behavior). Rapid descending speed of Stn.15 WO1 may effectively deepen the depth and highest temperature of thermal maximum point because response time of a temperature sensor may be somewhat delayed.



St15 WO2



St16 WO1



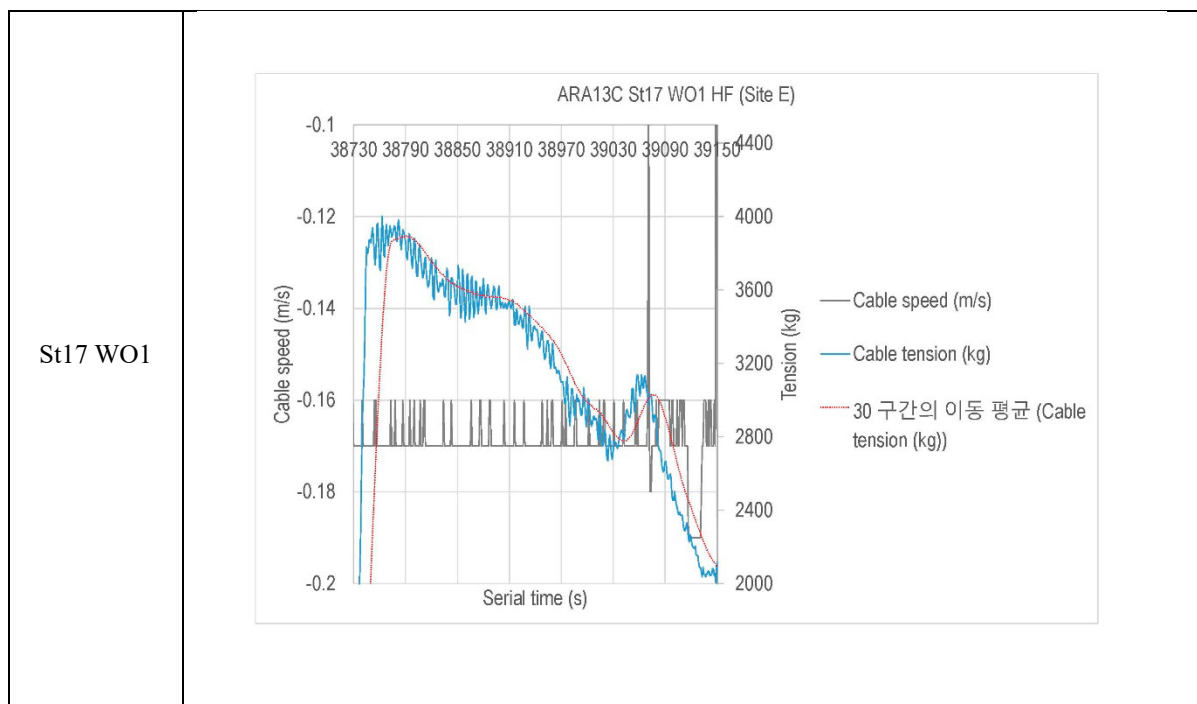


Figure 6.8. Results of cable speed and cable tension for the retrieval period of the probe through the sediments. Similar trends are seen. Slightly higher cable tension in WO1 compared to WO2 occurs for the time span with a higher ascending speed.

6.4. Future Work

6.4.1. Estimation of bulk density and thermal structure and their change with time

The overpenetration experiment with incremental cable paying-out during overpenetration of the probe allows an estimate of bulk density and penetration depth below the seafloor. Despite of a lack of winch information, ARA08C results allowed us to estimate bulk density and penetrating depth although the experiment was done only at Site C and only once (Kim et al., 2022b). At that site, a sinking reaction of the heat probe in response to incremental paying-out during overpenetration is assumed despite a lack of such winch information. The probe's sinking (overpenetration) behavior is confirmed based on the new ARA13C results. More data, four measurements at three stations (Sites C, D, and E), were collected during this expedition. We expect that overall trends of bulk density and thermal structure estimated from the ARA08C expedition may be reproducible from results of this expedition. Furthermore, change, if any, between estimates from the ARA08C results and from the ARA13C may reflect either temporal variation or eruption activity over the timespan of 5 years.

6.4.2. Estimation of other geotechnical properties

The winch information obtained in this ARA13C expedition, offers an opportunity to derive another important geotechnical property of sediments in MV420. During the retrieval of the probe through the sediments, the probe rose with the same speed as the winch cable speed. The winch was operated to keep a constant speed of 10 m/min for that retrieval period. Because ascending speed of the probe is fixed and its motion is vertical upward against gravity, any change in cable tension with pressure (depth) shown in Figure 6.8 is related to change in drag force together with weight of cable as the probe rose. This relationship can be written by

$$\text{Cable tension} = \text{drag force} * \text{gravity acceleration} + \text{weight of cable and the probe}$$

In addition, weight of cable and the probe can be eliminated by comparison between tension at the seafloor and one at certain depth.

Drag force is exerted on the object moving relatively with respect to the surrounding medium against the direction of relative motion. Under assumptions of spherical-shaped heat probe and neglecting cable weight below the seafloor, the drag force, F_d , is given by

$$F_d = 6 * \pi * r * v * \mu$$

where μ for viscosity of sediments, v for ascending speed for the case of retrieval of the heat probe, and r is radius of the heat probe, 0.2 m.

Results of the first-order estimation of sediment viscosity shows a general increasing trend with depth as well as an abrupt peak at subsurface (Figure 6.9). The abrupt peak at the immediate subsurface (1 to 3 m bsf) underlain by a deep trough in the estimated viscosity profile seems to reflect the reality because viscosity, sensitive to pressure, does not resemble the pressure profile. Estimated viscosities range between $2 * 10^3$ and $1 * 10^4$ Pa·s. This is about one tenth of results from natural samples drilled at serpentine mud volcanoes in the Mariana forearc (Menapace et al., 2019). It is encouraging that the two results do not show large differences considering the first-order estimation for the ARA13C observation with an assumption that the shape of the heat probe resembles a sphere. Further analysis helps to determine sediment viscosity along with mudflow migration path of MV420, which is an important parameter to infer the eruption system of mud volcanoes (Zoporowski and Miller, 2009).

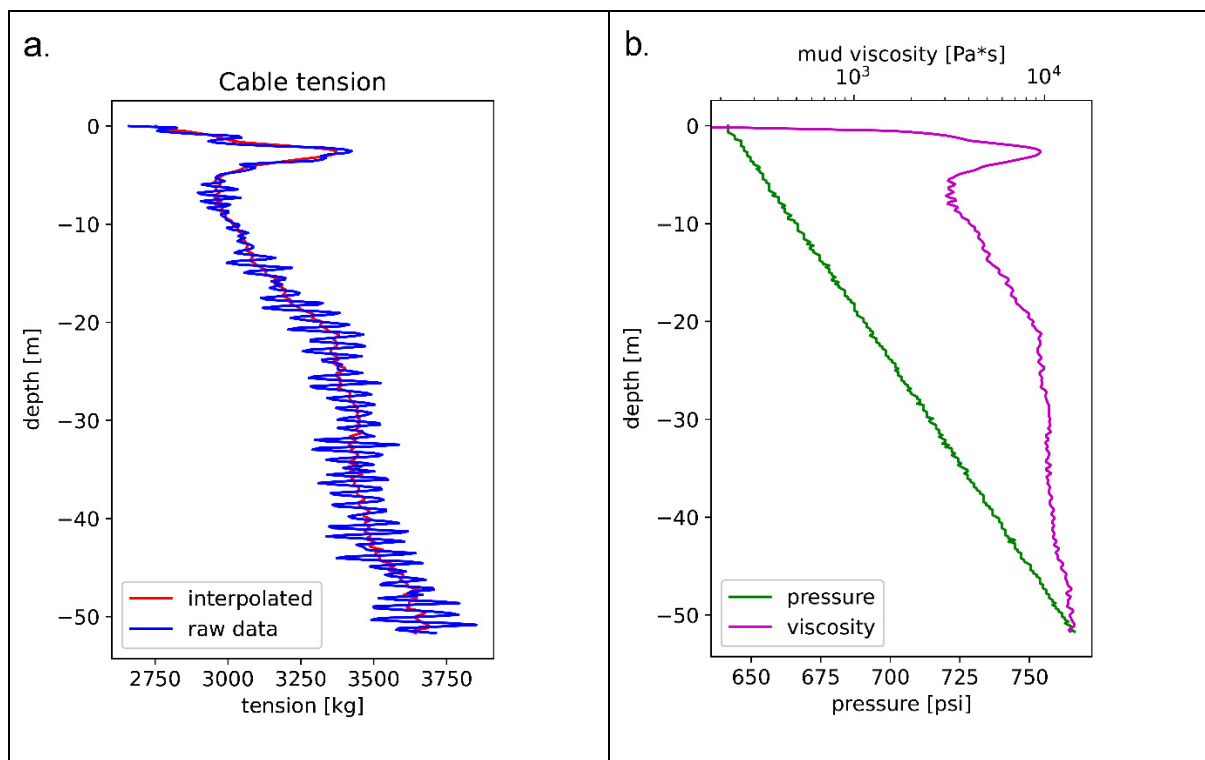


Figure 6.9. Sediment viscosity profile (b) obtained from cable tension profile (a). Depth is considered to increase linearly with pressure.

6.4.3. Geotechnical properties in relation to eruption activity

Temporal changes in geotechnical properties of bulk density and temperature profiles in MV420 over 5 years can be identified from comparison between results of ARA08C and ARA13C expeditions. Even though changes between the two expeditions are either substantial

or neglectable, the comparison can increase our understanding of eruption activity of MV420 as well as bathymetry change over 5 years because the latter two were confirmed already by AUV mapping in this expedition.

References

- Burhannuddinur, M., and Noeradi, D., 2021, Understanding Mud Volcano System Using Hele-Shaw (H-S) Experiment: Seismic Confirmation at East Java Mud Volcano: *Journal of Geoscience, Engineering, Environment, and Technology*, v. 6, no. 4, p. 206-216.
- De Beer, D., Sauter, E., Niemann, H., Kaul, N., Foucher, J.-P., Witte, U., Schlüter, M., and Boetius, A. 2006. In situ fluxes and zonation of microbial activity in surface sediments of the Håkon Mosby Mud Volcano. *Limnology and Oceanography*, 51, 1315-1331.
- Dimitrov, L.I. 2003. Mud volcanoes—a significant source of atmospheric methane. *Geo-Marine Letters*, 23, 155-161.
- Etiopo, G., and Milkov, A.V. 2004. A new estimate of global methane flux from onshore and shallow submarine mud volcanoes to the atmosphere. *Environmental Geology*, 46, 997-1002.
- Feseker, T., Foucher, J.P., and Harmegnies, F. 2008. Fluid flow or mud eruptions? Sediment temperature distributions on Håkon Mosby mud volcano, SW Barents Sea slope. *Marine Geology*, 247, 194-207.
- Feseker, T., Pape, T., Wallmann, K., Klapp, S.A., Schmidt-Schierhorn, F., and Bohrmann, G. 2009. The thermal structure of the Dvurechenskii mud volcano and its implications for gas hydrate stability and eruption dynamics. *Marine and Petroleum Geology*, 26, 1812-1823.
- Gwiawza, R., Paull, C. K., Dallimore, S. R., Melling, H., Jin, Y. K., Hong, J. K., Riedel, M., Lundsten, E., Anderson, K., and Conway, K., 2018, Freshwater Seepage Into Sediments of the Shelf, Shelf Edge, and Continental Slope of the Canadian Beaufort Sea: *Geochemistry, Geophysics, Geosystems*, v. 19, no. 9, p. 3039-3055.
- Jin, Y.K., Côté, M.M., Paull, C.K., and King, E.L. 2018. 2017 Korea-Canada-U.S.A. Beaufort Sea (offshore Yukon and Northwest Territories) research program: 2017 Araon expedition (ARA08C) cruise report. in: Geological Survey of Canada, Open File. Geological Survey of Canada).
- Kim, Y.-G., Hong, J.K., Jin, Y.K., Jang, M., and So, B.D. 2022a. Preliminary Results of Marine Heat Flow Measurements in the Chukchi Abyssal Plain, Arctic Ocean, and Constraints on Crustal Origin. *The Journal of Engineering Geology*, 32, 113-126.
- Kim, Y.-G. Jin, Y.K., Hong, J.K., Paull, C., Caress, D., Jang, C., So, B.-D., 2022b. Thermal structure and sediment bulk density of the MV420 mud volcano on the continental slope of the Canadian Beaufort Sea and its implications for the plumbing system. *Frontiers in Earth Science*, 10: 963580.
- Kim, Y.-G., Kim, S.K., Lee, D.-H., Lee, Y.M., Kim, H.J., Kang, S.-G., and Jin, Y.K. 2020. Occurrence of active gas hydrate mounds in the southwestern slope of the Chukchi Plateau, Arctic Ocean. *Episodes* 43, 811-823.
- Kopf, A., and Brown, K.M. 2003. Friction experiments on saturated sediments and their implications for the stress state of the Nankai and Barbados subduction thrusts. *Marine Geology*, 202, 193-210.
- Kopf, A.J. 2002. SIGNIFICANCE OF MUD VOLCANISM. *Reviews of Geophysics*, 40, 2-1-2-52.
- Kuo, C.Y., Tai, Y.C., Chen, C.C., Chang, K.J., Siau, A.Y., Dong, J.J., Han, R.H., Shimamoto, T., and Lee, C.T. 2011. The landslide stage of the Hsiaolin catastrophe: Simulation and validation. *Journal of Geophysical Research: Earth Surface*, 116.

- Loher, M., Pape, T., Marcon, Y., Römer, M., Wintersteller, P., Praeg, D., Torres, M., Sahling, H., and Bohrmann, G., 2018, Mud extrusion and ring-fault gas seepage – upward branching fluid discharge at a deep-sea mud volcano: *Scientific Reports*, v. 8, no. 1, p. 6275.
- Mazzini, A., and Etiope, G. 2017. Mud volcanism: An updated review. *Earth-Science Reviews*, 168, 81-112.
- Menapace, W., Kopf, A., Zabel, M., and Beer, D.D. 2017. 3. Mud volcanoes as dynamic sedimentary phenomena that host marine ecosystems. in *Life at Vents and Seeps*, ed. K. Jens. De Gruyter, 53-84.
- Menapace, W., Tanguan, D., Maas, M., Wililams, T., and Kopf, A. 2019. Rheology and biostratigraphy of the Mariana serpentine muds unravel mud volcano evolution.
- Milkov, A.V. 2000. Worldwide distribution of submarine mud volcanoes and associated gas hydrates. *Marine Geology*, 167, 29-42.
- Niemann, H., and Boetius, A. 2010. Mud Volcanoes, in *Handbook of Hydrocarbon and Lipid Microbiology*, ed. K.N. Timmis. (Berlin, Heidelberg: Springer Berlin Heidelberg), 205-214.
- Paull, C.K., Dallimore, S.R., Caress, D.W., Gwiazda, R., Melling, H., Riedel, M., Jin, Y.K., Hong, J.K., Kim, Y.-G., Graves, D., Sherman, A., Lundsten, E., Anderson, K., Lundsten, L., Villinger, H., Kopf, A., Johnson, S.B., Hughes Clarke, J., Blasco, S., Conway, K., Neelands, P., Thomas, H., and Côté, M. 2015. Active mud volcanoes on the continental slope of the Canadian Beaufort Sea. *Geochemistry, Geophysics, Geosystems* 16, 3160-3181.
- Sauter, E.J., Muyakshin, S.I., Charlou, J.-L., Schlüter, M., Boetius, A., Jerosch, K., Damm, E., Foucher, J.-P., and Klages, M. 2006. Methane discharge from a deep-sea submarine mud volcano into the upper water column by gas hydrate-coated methane bubbles. *Earth and Planetary Science Letters*, 243, 354-365.
- Taylor, A.E., Dallimore, S.R., Hill, P.R., Issler, D.R., Blasco, S., and Wright, F. 2013. Numerical model of the geothermal regime on the Beaufort Shelf, arctic Canada since the Last Interglacial. *Journal of Geophysical Research: Earth Surface* 118, 2013JF002859.
- Wallmann, K., Drews, M., Aloisi, G., and Bohrmann, G. 2006. Methane discharge into the Black Sea and the global ocean via fluid flow through submarine mud volcanoes. *Earth and Planetary Science Letters*, 248, 545-560.
- Wu, H., Liu, N., Peng, J., Ge, Y., and Kong, B. 2020. Analysis and modelling on coring process of deep-sea gravity piston corer. *The Journal of Engineering*, 2020, 900-905.
- Zoporowski, A., and Miller, S.A. 2009. Modelling eruption cycles and decay of mud volcanoes. *Marine and Petroleum Geology*, 26, 1879-1887.

ARA13C Cruise report

Chapter 7. Water Column Characterization

T.S. Rhee, M.-S. Kim, M. Kim and H. Park

7.1. Introduction

This is the fourth expedition campaigned in the Beaufort Sea onboard R/V Araon. The first campaign was carried out in 2013 and the Arctic environment has since changed. One such change is the dramatic decrease of the sea ice extent in summer and the rapid increase of the atmospheric temperature in the Arctic.

The Beaufort Sea is one of the six marginal seas composing the Arctic Ocean, located in the continental shelf area north to the eastern part of Alaska and Canada. Recent rapid warming in the Arctic (Comiso et al., 2008) affects the Beaufort Sea as the sea ice extent falls significantly (Jackson et al., 2010; Perovich et al., 2007). This decrease in sea ice extent has led to an increase of solar energy absorbed by the ocean surface which enhances temperature increase in the water column, which will further propagate the heat flux down to the seafloor and leads to warming permafrost underneath (Biastoch et al., 2011; Mestdagh et al., 2017).

The Mackenzie Delta region on the coast of the Beaufort Sea is known for gas and oil deposits and gas hydrates underneath the permafrost. To investigate the potential release of methane from the sediment associated with the current Arctic warming, we surveyed CH₄ and other trace gases, N₂O and CO₂, which are important to the global climate, in the Mackenzie Delta and offshore. We have carried out three scientific surveys of dissolved CH₄ in the Beaufort Sea under the Canada-Korea collaboration program in 2013, 2014, and 2017. During these expeditions, the surface water was slightly supersaturated with respect to the atmospheric CH₄ which was surprising. As the survey area for this expedition is located partly in the Mackenzie Delta region, we expected high CH₄ concentration dissolved in seawater.

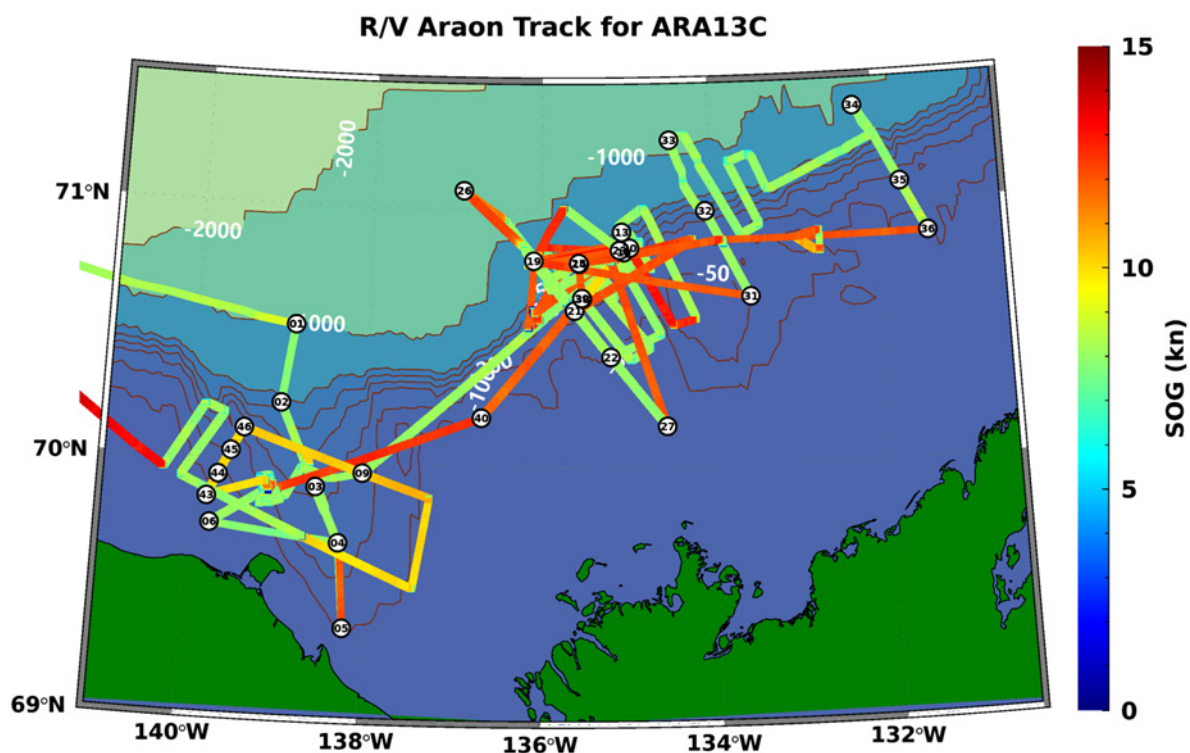


Figure 7.1. Hydrographic stations visited in the Beaufort Sea during ARA13C.

Our objectives for this expedition are threefold; one is to quantify the air-sea CH_4 flux from the survey area, another is the estimation of the amount of the CH_4 released from the sediment floor, and finally, to evaluate temporal and spatial variability of the dissolved CH_4 content by incorporating the previous observations.

The expedition was carried out during 24 days from August 22 to September 13, 2022 onboard the Korean ice breaker R/V Araon on the Yukon and Mackenzie continental shelves, the Mackenzie Trough between, and the Mackenzie continental shelf break (Figure 7.1). We conducted hydrographic castings at 31 stations to gain physical and chemical properties in situ and to collect water samples (Table 7.1).

Table 7.1. CTD/Rosette system

STN	Cast	Date	Time	DO	CH_4	DOC	DIC	Isotope	Isotope - CH_4	Nutrients	POC
1	1	8/26/2022	15:55	6	9	0	9	9	0	9	0
1	2	8/26/2022	19:15	0	0	5	0	0	0	0	2
2	1	8/27/2022	0:06	5	7	5	6	7	0	7	0
3	1	8/27/2022	14:04	5	6	4	6	6	0	6	1
3	2	8/27/2022	15:50	0	0	0	0	0	0	0	1
4	1	8/27/2022	18:12	3	7	0	7	7	0	7	0
5	1	8/28/2022	3:30	2	4	4	4	4	0	4	2
6	1	8/28/2022	15:57	2	4	0	4	4	0	4	0
9	1	8/29/2022	3:58	4	7	0	7	7	0	7	0

10	1	8/30/2022	0:20	4	6	0	6	6	0	6	0
13	1	8/31/2022	7:28	6	9	0	9	9	0	8	0
14	1	9/1/2022	3:00	6	9	0	9	9	4	9	0
19	1	9/2/2022	3:30	7	10	0	10	10	0	10	0
20	1	9/2/2022	7:35	4	7	0	7	7	1	7	0
21	1	9/3/2022	4:50	4	6	6	6	6	1	7	2
22	1	9/3/2022	8:04	4	5	0	5	5	1	5	0
23	1	9/4/2022	5:58	5	6	0	6	6	0	6	0
25	1	9/4/2022	22:30	7	9	3	9	9	2	9	3
26	1	9/5/2022	22:13	6	8	0	8	8	0	0	0
26	2	9/6/2022	0:22	9	5	0	0	0	0	5	0
27	1	9/7/2022	4:30	5	5	5	4	5	0	5	0
31	1	9/9/2022	4:10	4	5	0	5	5	0	5	0
32	1	9/9/2022	8:18	5	7	0	7	7	1	7	0
33	1	9/9/2022	11:02	5	7	0	7	7	1	7	0
34	1	9/10/2022	2:35	4	8	4	8	8	1	8	2
35	1	9/10/2022	7:00	4	5	3	5	5	1	5	2
36	1	9/10/2022	15:57	2	5	3	5	5	1	5	2
38	1	9/11/2022	04:45	0	0	0	0	0	0	0	0
39	1	9/11/2022	05:18	0	0	0	0	0	0	0	0
40	1	9/11/2022	9:04	2	4	0	4	4	2	4	0
43	1	9/12/2022	5:50	2	4	0	4	4	1	4	0
44	1	9/12/2022	7:40	2	4	0	4	4	1	4	0
45	1	9/12/2022	8:55	2	4	0	4	4	1	4	0
46	1	9/12/2022	10:00	2	5	0	5	5	1	5	0

7.2. Methods

7.2.1. *In situ hydrographic measurements*

A SBE 911plus CTD (Sea-Bird Scientific Co., although CTD stands for conductivity, temperature, and depth, the instrument includes versatile sensors shown in Table 7.2) and Rosette system was used to measure vertical profiles of temperature, salinity, dissolved oxygen, fluorescence, turbidity, and photosynthetically active radiation (PAR) in situ (Table 7.2). Their signals were transmitted to the deck unit in the lab and presented on the monitor by which the seawater sampling depths are determined (Figure 7.2). The Rosette system is composed of 24 10-L Niskin bottles in which seawater was collected at the given depths while ascending. The water samples were further analyzed for biogeochemical parameters including methane. The CTD/Rosette system was cast 34 times at 31 hydrographic stations (Table 7.1).

Table 7.2. CTD/Rosette system

Instrument	Model	Serial Number
Main housing	SBE9P	61315-1008
Thermometer	SBE3P	4995, 5111
Conductometer	SBE4C	3586, 3587
DO meter	SBE43	1614
Fluorometer	Wet Lab	FLRTD-2020
Transmissometer	Wet Lab C-Star	CST-1227DR
PAR	PAR-Log ICSW	1023
Altimeter	Teledyne Benthos	PSA-916
LADCP	Teledyne RD Instruments	

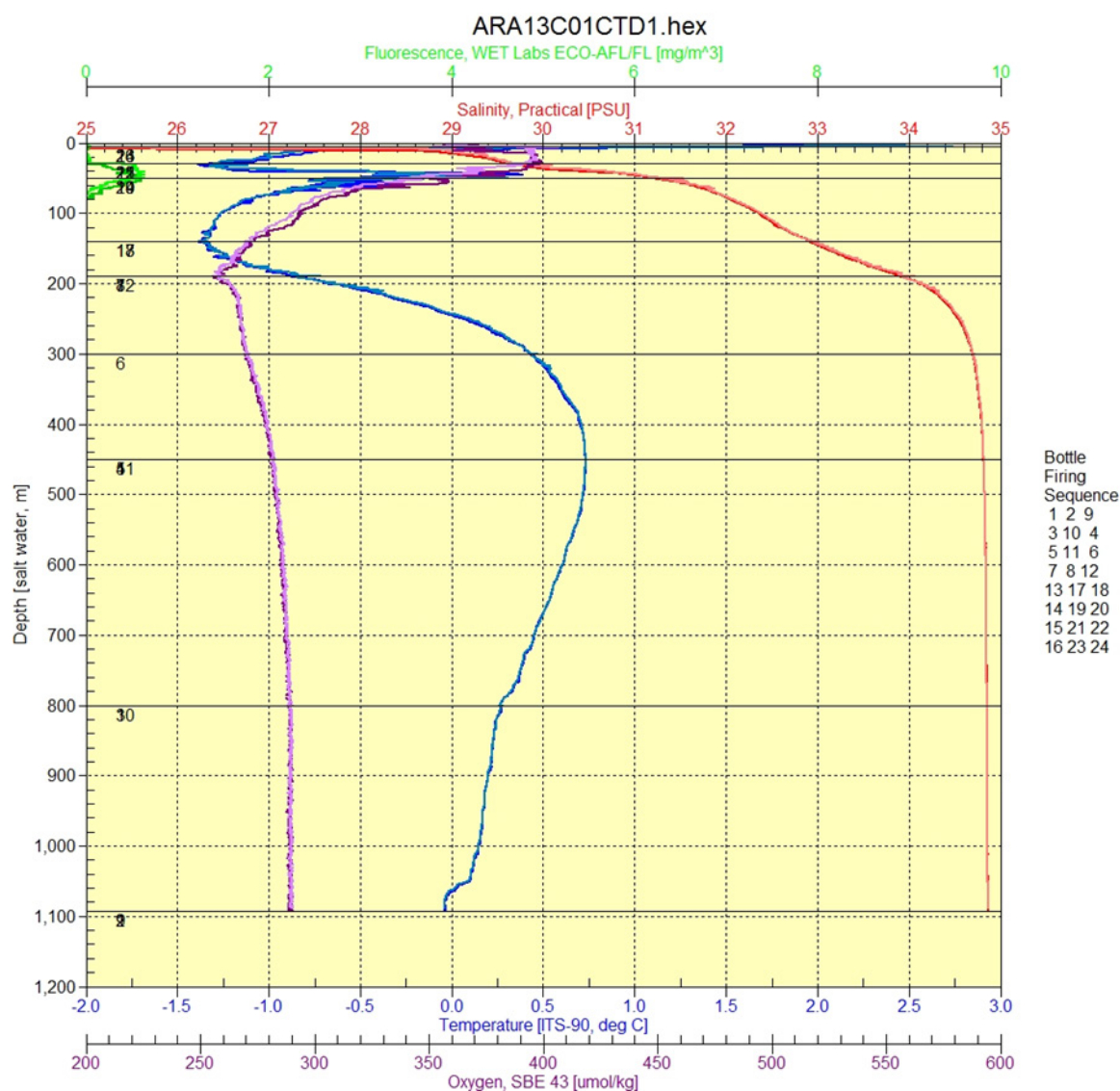


Figure 7.2. Depth profiles of temperature (blue), salinity (red), fluorescence (green), and dissolved oxygen (violet) recorded from the SBE911+ mounted on the CTD/Rosette instrument. Horizontal lines indicate where Niskin bottles were fired.

7.2.2. Ocean current measurements

A lowered acoustic Doppler current profiler (LADCP; 300 kHz RDI) was mounted on the CTD/Rosette frame to measure a full-depth profile of current velocities. Using the conventional “shear method” for processing (e.g., Fischer and Visbeck, 1993), overlapping profiles of

vertical shear of horizontal velocity were averaged and gridded to form a full-depth shear profile. The bin size was chosen at 5 meters.

7.2.3. Supplementary measurements

In addition to the routine measurements of hydrographic parameters using CTD/Rosette system, conductivity, temperature, dissolved oxygen sensors installed in vehicles and attached temporarily on the frame were used to log the data in situ. AUV and ROV contain their own CTD system. An oxygen sensor (ARO-USB05, Rinko, Ltd) was mounted on the AUV and sometimes on the frame of the CTD/Rosette. Another oxygen sensor (ARO-USB, Rinko, Ltd) and a thermometer (Solo-T, RBR) were mounted on the Multi-corer frame to log dissolved oxygen and temperature in situ while casting it to the sea floor. These data will be used to support the routine measurements.

7.2.4. Seawater sampling

Seawater was collected at 31 stations in the Yukon and Mackenzie continental shelves and slopes and Mackenzie Trough (Table 7.1 and Figure 7.1). As soon as the CTD/Rosette was on the deck, an aliquot of seawater for dissolved gas analyses was first subsampled to avoid the potential leaks or outgassing through the vent. Then, subsampling for other analyses were carried out.

7.2.5. Surface sediment sampling

Surface sediments were collected at 17 stations using a multi-corer; two stations in the Yukon shelf, 6 stations in the Mackenzie Trough, and 9 stations on the Beaufort Shelf. The bottom water above the sediment in the core was collected for further analyses immediately after the recovery of the multi-corer. In addition, water samples at four depths above the sea floor were collected using syringes to investigate if gradients in the CH₄ concentrations exist. A sediment core was dedicated for both CH₄ flux experiment and the CH₄ measurement in the surface sediment.

7.2.6. Methane analysis

An aliquot of seawater from each Niskin bottle attached in the CTD/Rosette was subsampled into a glass jar. The glass jar was specially designed for analyses of dissolved gases in order to avoid any contamination from the lab air during sampling. In the laboratory, 50 mL of pure N₂ gas (99.9999%) was injected into the glass jar bottles using a gastight glass syringe (SEB). The glass jar was then immersed in a water bath at 20°C for longer than an hour. To minimize underway data loss, measurements of CH₄ concentrations in water column were carried out when R/V Araon stopped at hydrographic stations for other operations (e.g., coring). About 40 mL of the headspace gas was drawn from the glass jar using another gastight glass syringe, and injected into a gas chromatographic system (Agilent Technologies 7890A) equipped with a flame ionization detector (FID) to quantify CH₄ concentrations in water column [Rhee et al., 2009] (Figure 7.3).



Figure 7.3. CH₄ analysis systems. Gas chromatographic system (left) and cavity ring-down spectroscopic system (CRDS) (right) were operated to measure the methane dissolved in the seawater and the air. Photo courtesy of Korea Polar Research Institute.

During the expedition, underway measurements of CH₄ were carried out along the cruise track. Surface seawater at ca. 6 m deep was pumped into a Weiss-type equilibrator to obtain dissolved gases in seawater. The headspace air in the equilibrator, which was dynamically in equilibrium with dissolved gas concentration in seawater, was supplied to the gas chromatographic (GC) system. For one cycle, it takes about an hour to analyze the gases from the ambient air and seawater, including calibration gases. In addition to the GC system, a cavity ring-down spectroscopic analytical system (CRDS) (Picarro G2301-f) was employed to measure methane every second. This was dedicated to the continuous observation as the optic cell in the detector is in a closed-loop with a dynamic equilibration system, which enables to measure methane at high temporal resolution (~1Hz).

7.2.7. Dissolved inorganic carbon and total alkalinity

Seawater for dissolved inorganic carbon (DIC) and total alkalinity (TA) analyses was subsampled in pre-cleaned 500 mL borosilicate bottles. The seawater samples were poisoned with 100 µl of 50% HgCl₂ to halt biological activity. Then the bottles were sealed with vacuum grease on the surface of the lid to prevent any CO₂ gas leaks until analysis in the laboratory at Korea Polar Research Institute. The seawater samples will be analyzed using a VINDTA (Versatile INstrument for the Determination of Total Alkalinity) system at the institute.

7.2.8. Nutrients

Seawater samples for nutrient (NH₄⁺, NO₃⁻, PO₄³⁻, SiO₄²⁻) analyses were collected in 50mL conical tubes and stored in a deep-freezer at -80°C prior to chemical analyses. The samples will be analyzed with standard colorimetric methods using a Quatro Auto Analyzer at Korea Polar Research Institute.

7.2.9. Underway pCO₂ measurement

The flux of CO₂ across the sea surface is directly proportional to the difference in the fugacity of CO₂ between the atmosphere and the seawater. The fugacity is obtained by correcting the partial pressure of CO₂ (pCO₂) for non-ideality of the gas with respect to molecular interactions between CO₂ and other gases in air, thus making pCO₂ an important parameter to measure [Pierrot et al., 2009]. To investigate air-sea exchange rate of CO₂, pCO₂ were monitored in real time using an automated flowing pCO₂ measuring system (Model 8050, General Oceanics Inc., USA). The system is compact and operates by directing seawater flow

through a chamber (the equilibrator) where the CO₂ contained in the water equilibrates with the gas present in the chamber (the headspace gas). To determine the CO₂ in the headspace gas, it was pumped through a non-dispersive infrared analyzer (LICOR), which measured its CO₂ mole fraction instantaneously, and then returned to the equilibrator thus forming a closed loop. Periodically, atmospheric air was also pumped through the analyzer and its CO₂ mole fraction was measured. The analyzer was calibrated with four CO₂ standard gases at regular intervals.

7.2.10. Dissolved oxygen

As forementioned, a dissolved oxygen sensor was equipped in the CTD/Rosette and needs to be calibrated. Thus, we collected seawater samples in various depths and they were analyzed by amperometric technique. Seawater was subsampled in a ~120 mL glass jar after flushing with sufficient amount of seawater to avoid a potential influence of trapping the laboratory air. The dissolved O₂ was fixed by adding MnCl₂ and Alkaline iodide immediately after collection of seawater. The blanks in the chemicals were measured and the amperometer were calibrated with the known concentration of KIO₃.

The dissolved O₂ concentration in the surface water delivered into the laboratory were monitored using a commercially available optic sensor, Optode (Aanderra). This sensor was also calibrated by immersing in saturated distilled water at the given temperature (5°C).

7.2.11. Dissolved organic carbon

Seawater for dissolved organic carbon (DOC) analysis was collected at 10 stations in the Mackenzie Trough and adjacent continental shelf using a Niskin bottle attached in CTD/Rosette sampling system (Table 7.1). A pre-cleaned DOC-free silicon tube was used to connect between spigot and pre-cleaned 47 mm filtration holder made of polypropylene. About 40 ml of seawater was collected from in-line filtration through a pre-combusted 0.7 µm Whatman GF/F filter under gravity. The filtered samples were collected directly into pre-cleaned EPA glass bottles. Each vial was quick-frozen, and preserved at approximately -80°C until the analysis inshore.

A 10 L of seawater was filtered by gravity for the analysis of particulate organic carbon (POC). The GF/F filter papers used were pre-combusted at 550°C for 6 hours. The POC samples were stored at -80°C.

7.2.12. Microbial oxidation experiments

About 2 L of seawater were filled in a glass flask after filtering the seawater from Niskin bottles. Immediately after collection, 100 mL of N₂ gas or a known concentrations of CH₄ in N₂ gas was injected. At set intervals, the water was displaced with 100 mL of CH₄-free N₂ gas. Approximately 40 mL of the seawater displaced was used to flush the tube and syringe and the rest was sampled in a syringe to equilibrate dissolved CH₄ in headspace.

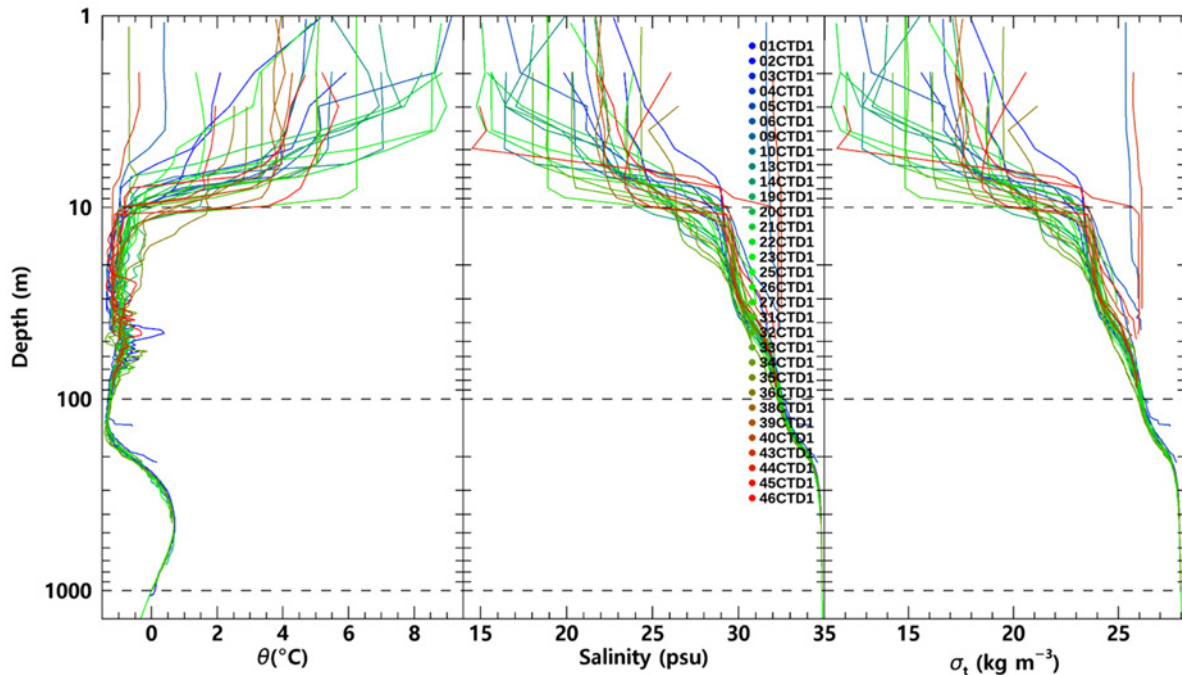


Figure 7.4. Depth profiles of potential temperature, salinity, and density (σ_t) at the hydrographic stations.

7.3. Results

7.3.1. Physical properties of water masses

During the expedition 31 hydrographic stations were occupied (Figure 7.1). Among them 5 stations were located in the Yukon Shelf, 6 stations in the Mackenzie Trough, and 20 stations are on the Mackenzie continental shelf, break, and slope. Figure 7.4 shows the vertical profiles of potential temperature, salinity, and density (σ_t) collected at all hydrographic stations. At most stations the bottom of the mixed layer locates at 10 m deep at which temperature and salinity changed abruptly due likely to the impact of fresh water discharge from the Mackenzie River with the exception of the Yukon shelf where salinity and density are vertically well mixed at some stations.

Surface temperature varied from -0.7°C at station 34 to 9°C at station 5 near the Mackenzie River mouth. The lowest salinity of 15 was observed at station 22 in the middle of the Beaufort Shelf and highest salinity of 32 at station 43 inshore of the Yukon shelf.

Below the mixed layer, temperature of the water mass approached the freezing point, in particular in the Yukon Shelf. In case of the Beaufort Shelf the temperature is a few tenths degree Celsius greater. This water mass might originate from the melting of sea ice as the salinity is lesser than the Pacific Summer Water (PSW) underneath whose characteristic high temperature was detected at the depths between 30 – 80 m. Below PSW temperature decreased by a few tenths degree Celsius and salinity increased by ca. 1 psu indicating the Pacific Winter Water (PWW) centering at the depth of ~ 150 m. Potential temperature increased with depth below PWW reaching $\sim 1^\circ\text{C}$ at ~ 500 m deep warmest water mass below the mixed layer with the salinity approaching 35. This water mass originates from the Atlantic Ocean and is named the Atlantic Deep Water (ADW). The water temperature below ADW decreased with depth but the salinity continues to increase, which is the Arctic Bottom Water (ABW) formed during the sea ice formation.

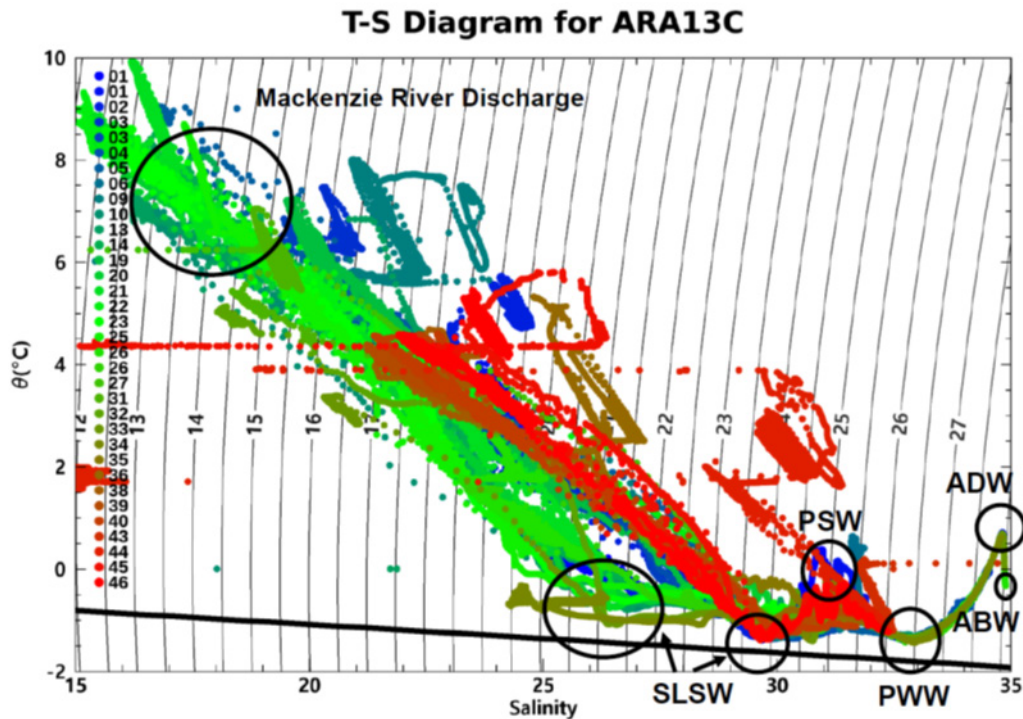


Figure 7.5. Scatter plot for the potential temperature vs. salinity measured using SBE911+ CTD.

The interaction between various water masses can be identified in the T-S diagram (Figure 7.5). This clearly shows that the water masses are vertically separated while the surface waters varied in temperature and salinity influenced by Mackenzie River discharge. On the other hand, the water masses of PWW, ADW, and ABW are well homogenized in the survey area of the Beaufort Sea implying that the sea ice melts and river discharge impact the surface mixed layer or PSW beneath.

7.3.2. Methane in the surface waters and overlying air

As forementioned, two instruments were run to measure the methane in the surface waters along the cruise track. The gas chromatographic system, however, needs multiple steps of calibration and correction processes which needs time. Thus, in the cruise report we used the data from the cavity ring-down spectroscopic system which generated concentration values that were converted from the electric signal by a provisional calibration scale embedded in the internal computer.

Figure 7.6 shows the atmospheric methane in the marine boundary layer at ~29 m above sea level. During the campaign, the atmospheric concentration concentrated on ~2.05 ppm as expected from the figure. High CH_4 concentrations were sporadically logged which may come from the ship's exhaust while staying at stations operating vehicles and equipment onboard.

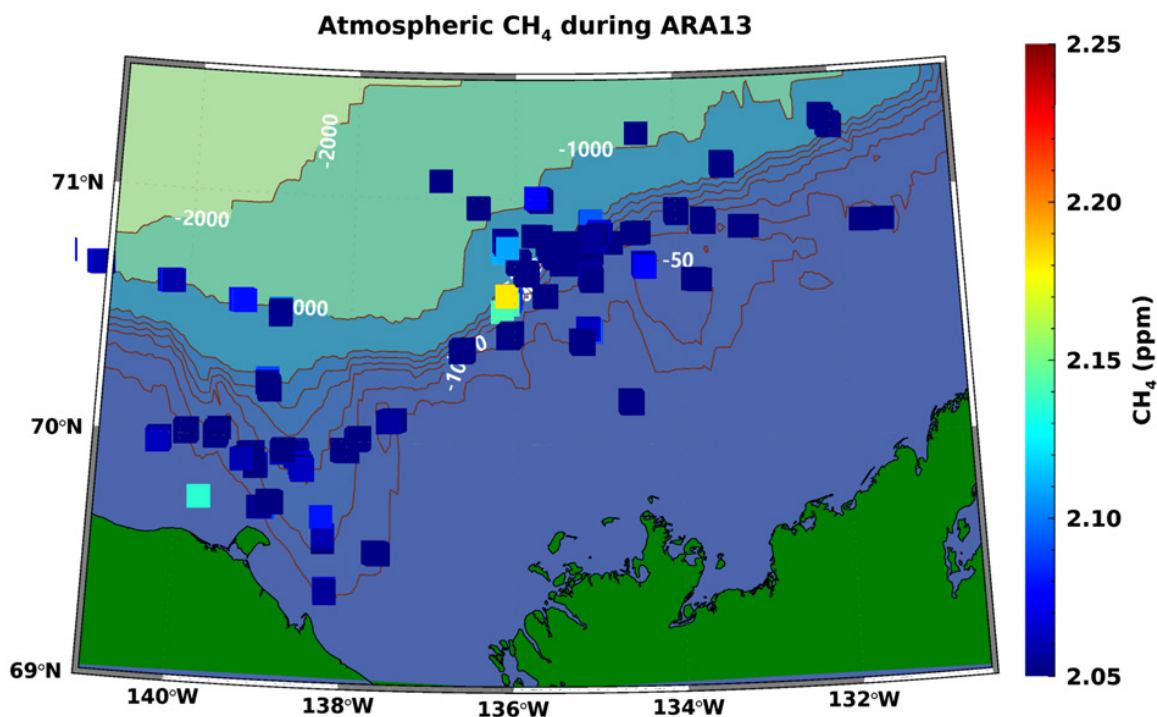


Figure 7.6. Atmospheric methane mole fractions over the Beaufort Sea.

While atmospheric CH₄ were fed into CRDS every 6 hours the dissolved CH₄ in the surface waters measure almost continuously every second except for the period of calibration and atmospheric air analyses. Figure 7.7 shows the CH₄ concentrations in the surface waters. The surface waters were super-saturated with respect to the atmospheric CH₄ along most of the cruise track although its magnitude did not stand out except on the Yukon continental shelf. Sailing into the Canada Basin and then into the Mackenzie Trough during the early stage of the campaign, the dissolved CH₄ concentrations were merely slightly supersaturated. This was suddenly changed in the Yukon Shelf where the dissolved CH₄ increased up to ~6 ppm. Such a high CH₄ seawater was never previously measured in the Beaufort Sea survey area. Even in the region of mud volcanos the surface CH₄ concentrations were slightly supersaturated and the CH₄ in the surface waters of the inner shelf at the depth of < 50 m the CH₄ concentration did not increase as did in the Yukon shelf; most regions of the surface water in the Beaufort Shelf were only above the atmospheric concentration.

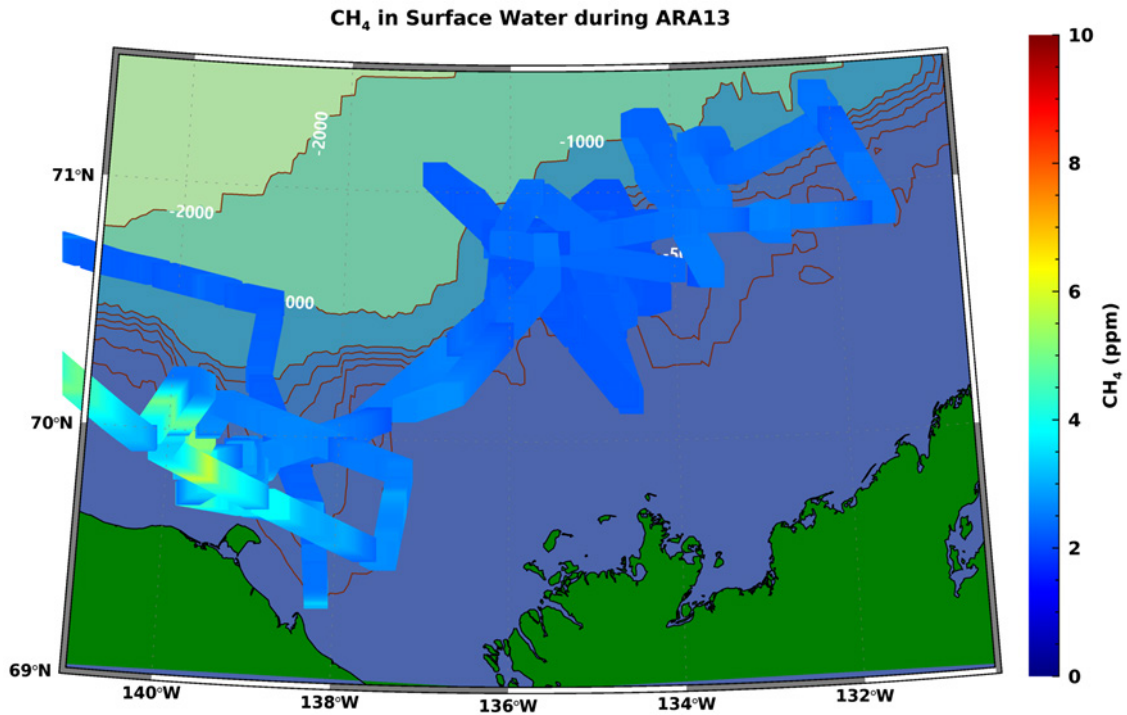


Figure 7.7. Dissolved methane in surface waters.

7.3.3. Dissolved oxygen

We collected 137 seawater samples at 31 hydrographic stations to calibrate the dissolved oxygen sensors of SBE43 and Optode (Table 7.1). The amperometric analyzer was calibrated with standard solution of KIO₃ onboard. Analytical results need to be corrected for temperature and salinity as we assumed the temperature and salinity at 0°C and 35, respectively, when analyzing. We made a comparison test of oxygen sensors at station 26 (Figure 7.8). ARO5-USB had been mounted on AUV during the AUV deployment. To validate the sensor detection and calibration, it was mounted on the frame of CTR/Rosette to compare the dissolved oxygen concentration logged by SBE43 attached on SBE911+. As shown in Figure 7.8, they are very comparable showing the ARO5-USB sensor is reliable.

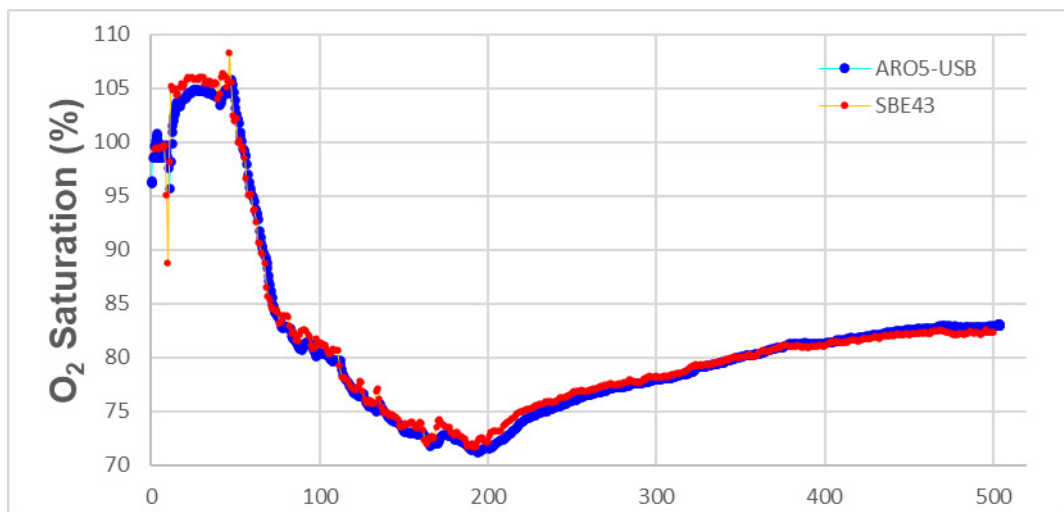


Figure 7.8. Comparison of dissolved oxygen saturation along the water depth at station 26.

7.3.4. Other parameters

In addition to the in situ observations, the seawater samples collected will be analyzed in the laboratory. These include nutrients, dissolved inorganic carbon, total alkalinity, dissolved organic carbon, particulate organic carbon, stable isotope ratio of methane, etc. (see Table 7.1). It will take several months to complete all the sample analyses.

7.4. Summary

The expedition ARA13C was conducted in the Canadian Beaufort Sea as an international collaborative work with scientists from MBARI and NRL in U.S.A. and the GSC in Canada. Oceanographic investigation in the water column was mainly carried out by KOPRI focusing on the methane budget and cycle in the Beaufort Sea. We surveyed on the Yukon Shelf, Mackenzie Trough from inner shore to the outer shore, and Beaufort Shelf, break, and slope. Surface distribution of methane indicates mild super-saturation except on the inner shelf of the Yukon Shelf suggesting the strong stratification prohibits the upward advective diffusion of methane from the sea floor.

Methane concentrations within the water column may give us clue on why the methane in the surface water of the Beaufort Sea is slightly super-saturated. Other parameters such as inorganic and organic carbon distributions and stable isotope ratios of methane could also hint at the processes occurring in the water column by which methane may be oxidized to the final products. To answer these questions, we have to dig further into the data obtained during the expedition.

References

- Biaostoch, A., Treude, T., Rüpke, L. H., Riebesell, U., Roth, C., Burwicz, E. B., Park, W., Latif, M., Böning, C. W. and Madec, G. 2011. Rising Arctic Ocean temperatures cause gas hydrate destabilization and ocean acidification, *Geophysical Research Letters*, 38(8).
- Comiso, J. C., Parkinson, C. L., Gersten, R. and Stock, L. 2008. Accelerated decline in the Arctic sea ice cover, *Geophysical Research Letters*, 35(1).
- Fischer, J. and Visbeck, M. 1993. Deep velocity profiling with self-contained ADCPs, *Journal of Atmospheric and Oceanic Technology*, 10, 764-773.
- Jackson, J. M., Carmack, E., McLaughlin, F., Allen, S. E. and Ingram, R. 2010. Identification, characterization, and change of the near-surface temperature maximum in the Canada Basin, 1993–2008, *Journal of Geophysical Research: Oceans*, 115(C5).
- Mestdagh, T., Poort, J. and De Batist, M. 2017. The sensitivity of gas hydrate reservoirs to climate change: Perspectives from a new combined model for permafrost-related and marine settings, *Earth-Science Reviews*, (169), 104-131.
- Perovich, D. K., Light, B., Eicken, H., Jones, K. F., Runciman, K. and Nghiem, S. V. 2007. Increasing solar heating of the Arctic Ocean and adjacent seas, 1979–2005: Attribution and role in the ice-albedo feedback, *Geophysical Research Letters*, 34(19).
- Pierrot, D., Neill, C., Sullivan, K., Castle, R., Wanninkhof, R., Luger, H., Johannessen, T., Olsen, A., Feely, R. A. and Cosca, C. E. 2009. Recommendations for autonomous underway pCO₂ measuring systems and data-reduction routines, *Deep-Sea Research Part II-Topical Studies in Oceanography*, 56(8-10), 512-522.
- Rhee, T. S., Kettle, A. J. and Andreae, M. O. 2009. Methane and nitrous oxide emissions from the ocean: A reassessment using basin-wide observations in the Atlantic. *Journal of Geophysical Research-Atmospheres*, 114.

ARA13C Cruise report

Chapter 8. Mercury Study

S.W. Eom, J.H. Chae, H.K. Jeong, S.H. Lim, and Y.G. Kim

8.1. Introduction

The study of the fate and cycling of mercury (Hg) in the Arctic Ocean is important due to its impact on human health and reactivity to climate change (Chételat et al., 2022). Northern Peoples are at risk of elevated exposure to Hg because of their high consumption of fish or marine mammals. Their blood Hg levels are well above the U.S. EPA's blood Hg guideline ($5.8 \mu\text{g L}^{-1}$; AMAP, 2011), which has been linked to adverse effects on recognition memory and cardiovascular health (Valera et al., 2009). In the same context, high concentrations of Hg as a form of methylmercury (MeHg), which have been detected in fish and mammals in the Arctic Ocean, are emerging as a serious problem (Masbou et al., 2018). Despite the importance of the bioaccumulation of Hg in marine fish and mammals, the seasonal and spatial variations of Hg speciation and flux in the Arctic Ocean have not been fully understood due to insufficient observation data.

Sources of MeHg in Arctic seawater have been identified as *in situ* methylation occurring in the halocline layer intensified by freshwater discharge from sea ice and rivers (Lehnherr, 2014). In marine sediment, MeHg is commonly produced by *in situ* Hg(II) methylation by microbes that utilize Fe(III) and sulfate as electron acceptors and carry *hgcA* and *hgcB* genes (Lehnherr, 2014). The submarine permafrost in the shelf of the Beaufort Sea has been thawing in response to increased seawater temperature from climate warming, leading to active methane release from surface sediment and overlying seawater (Sparrow et al., 2018). The thawing of permafrost is further stimulated by heat flux through Mackenzie River discharge during the melting season (Paull et al., 2022). Seasonal warming in sediment related to these factors could alter heterotrophic microbial activities and, thus, change MeHg synthesis rates. Nonetheless, the consequences of sediment warming on MeHg production in the Beaufort Sea have not been reported.

It is important to understand the formation mechanisms of Hg(0) in the polar mixed layer of the Beaufort Sea as Hg(0) evasion is a major sink of bioavailable Hg(II) that can be transformed into MeHg in the halocline layer. Using the nitrogen purging and trapping method, Hg(0) can be measured as dissolved gaseous Hg (DGM), which mainly includes dimethylmercury and Hg(0) produced through photochemical and biological reactions (Deng et al., 2008; Kuss et al., 2015). The photochemical reduction rate of Hg(II) is dependent on the Hg(II) speciation and radiation wavelength. It has been reported that short wavelength radiation (e.g., UV-A or UV-B) mostly contributes to Hg(II) reduction in seawater (Qureshi et al., 2010; Si and Ariya, 2011). Regarding Hg speciation, the direct photolysis of Hg(II) complexed by dissolved organic matter containing thiol groups has been suggested as a potential reduction process for Hg(II) in oceanic water; however, the field evidence of this process remains limited (Jeremiason et al., 2015). The reduction of inorganic Hg(II) species by reactive oxygen species (e.g., superoxide) should also be tested, as reported in the Fe(III) case. Furthermore, DGM in surface seawater can be produced through biotic reactions (Kuss et al., 2015; Zhang et al., 2021). Given that the contribution of cyanobacteria to Hg(II) reduction has been reported in

the Baltic Sea and that cyanobacterial *nifH* sequences have been commonly found in the Chukchi and Beaufort Sea (Harding et al., 2015; Kuss et al., 2015), the potential of Hg(II) reduction by means of cyanobacteria needs to be investigated.

An increase in atmospheric temperature due to climate warming could enhance the input of Hg from snow, rivers, and permafrost connected to the Beaufort Sea and lead to increased Hg accumulation in pelagic zooplanktons. The main sources of Hg (e.g., atmospheric deposition, snow, rivers, coastal erosion, and permafrost) in pelagic zooplankton have been the subject of debate, and it is largely unknown how it accumulates in the Arctic marine food web. A novel tool—stable isotopes of Hg—has recently been applied to trace sources of Hg in different environmental media. The Hg isotope data collected through this survey will be used to identify the main source of Hg introduced to the zooplankton found in the Beaufort Sea by the joint research team of Pohang University of Science and Technology (POSTECH).

An expedition objective was to collect seawater, sediment, atmospheric, and plankton samples to measure diverse Hg species and stable isotopes in order to identify 1) whether seasonal warming of sediment produces variations in Hg(II) methylation rates and MeHg concentrations in sediment overlying discontinuous permafrost; 2) how air–sea exchange of Hg responds to Mackenzie River discharge and Pacific water inflow; and 3) the major sources of Hg in pelagic zooplankton and whether the size of this source is affected by Mackenzie River discharge in the Southern Beaufort Sea. Along with diverse samplings, DGM concentration in the polar mixed layer was continuously measured on board at a 5-min resolution. The depth profile of the DGM at each station was also measured on board using cold vapor atomic fluorescence spectroscopy (CVAFS). Total Hg (THg), MeHg, stable isotopes of Hg, dissolved organic carbon (DOC), excitation/emission matrices (EEMs) fluorescence, suspended particulate matter (SPM), dissolved inorganic nutrients, and cyanobacteria abundance in seawater will be measured in the Gwangju Institute of Science and Technology (GIST) and POSTECH laboratories in South Korea. From the sediment samples, THg, MeHg, the Hg(II) methylation rate, stable isotopes of Hg, and other conventional parameters (total carbon, nitrogen and sulfur) will be measured, and from the atmospheric and plankton samples, concentrations and stable isotopes of Hg will be determined in the same laboratories in South Korea.

8.2. Methods

8.2.1. Seawater sampling

Seawater samples were collected using a rosette sampling system equipped with acid-cleaned 10-L Niskin bottles at 15 stations in the Beaufort Sea (Table 8.1 and Figure 8.1). For THg, 1 L of seawater was obtained at each station in acid-cleaned Teflon bottles, using the clean-hands-dirty-hands protocol to prevent contamination. The seawater samples of THg were spiked with 0.4% HCl (v/v) and kept at 4°C under dark conditions to prevent a redox reaction from the Hg. Seawater samples for the DGM measurement were poured gently into a 1-L borosilicate bubbler. The DGM was measured within a few hours due to its rapid loss ($t_{1/2} \sim 10\text{--}20$ h) (Parker and Bloom, 2005). Prior to the measurement, the borosilicate bubbler was acid-cleaned and purged for 60 min with Milli-Q water to remove residual Hg on the glassware.

To measure the DOC concentration and EEMs fluorescence spectra, a 20-mL seawater sample was filtered through 0.2- μm PTFE syringe filters, collected in pre-combusted (at 450°C for 4 h) 30-mL glass bottles, and immediately frozen at -20°C . To measure the SPM, about 2–4 L of seawater was filtered through a pre-weighed 0.7- μm Whatman GF/F membrane under low vacuum conditions (< 100 mmHg). The particle-collected membranes were kept in petri

dishes and then frozen at -20°C for future analysis. The remaining seawater samples were filtered with a 0.2- μm PES syringe filter and frozen at -80°C to analyze the dissolved inorganic nutrients ($\text{NO}_3^- + \text{NO}_2^-$ and PO_4^{3-}). For cyanobacteria abundance, 2 L of seawater was filtered through a 0.2- μm polycarbonate membrane under low vacuum conditions (< 100 mmHg) and frozen at -80°C until analysis.

Table 8.1. Station number, water depth, GPS, sampling depth, and analytical parameters of seawater samples

Station	Depth (m)	GPS (latitude, longitude)	Sampling Depth (m)	Parameter
ST01	1113	138° 51.6127' W 70° 31.9439' N	5	THg, DGM, DOC/EEM, POC/PN, SPM
			30	
			50	
			140	
			190	
			450	
			800	
			1092	
ST02	423	138° 59.3458' W 70° 13.5725' N	5	THg, DGM, DOC/EEM, POC/PN, SPM
			20	
			40	
			120	
			180	
			300	
			413	
ST03	225	138° 33.3733 'W 69° 54.2668' N	5	THg, DGM, DOC/EEM, POC/PN, SPM
			20	
			40	
			125	
			175	
			214	
ST04	145	138° 16.6127' W 69° 41.3709' N	5	THg, DGM, DOC/EEM, POC/PN, SPM, cyanobacteria
			15	
			30	
			40	
			70	
			140	
ST05	43.5	138° 11.8499' W 69° 21.5193' N	2	THg, DGM, DOC/EEM, POC/PN, SPM, cyanobacteria
			12	
			25	
			43	
ST06	32	139° 43.7793' W 69° 44.8376' N	2	THg, DGM, DOC/EEM, POC/PN, SPM, cyanobacteria, Gross kr
ST09	166	138° 1.8008' W 69° 57.8358' N	2	THg, DGM, DOC/EEM, POC/PN, SPM, cyanobacteria, Gross kr
			30	

			45	
			120	
			158	
ST10	111	135° 1.9276' W 70° 50.0056' N	2	THg, DGM, DOC/EEM, POC/PN, SPM, cyanobacteria, Gross kr
			10	
			30	
			60	
			90	
			104	
ST13	367	135° 3.3195' W 70° 54.7309' N	2	THg, DGM, DOC/EEM, POC/PN, SPM, cyanobacteria, Gross kr
			15	
			30	
			50	
			80	
			170	
			300	
			360	
ST14	425	135° 33.6047' W 70° 47.3867' N	2	THg, DGM, DOC/EEM, POC/PN, SPM, cyanobacteria, Gross kr
			15	
			30	
			50	
			130	
			180	
			300	
			417	
ST19	748	136° 5.7806' W 70° 48.0513' N	2	THg, DGM, DOC/EEM, POC/PN, SPM, cyanobacteria, Gross kr
			10	
			30	
			50	
			145	
			190	
			500	
			737	
ST21	75	135° 36.9050' W 70° 36.4654' N	2	THg, DGM, DOC/EEM, POC/PN, SPM, cyanobacteria, Gross kr
			15	
			40	
			70	
ST22	63	135° 11.6298' W 70° 25.5955' N	2	THg, DGM, DOC/EEM, POC/PN, SPM, cyanobacteria, Gross kr
			15	
			30	
			46	
			55	
ST26	1401	136° 56.0013' W 71° 04.3001' N	2	THg, DGM, DOC/EEM, POC/PN, SPM, cyanobacteria, Gross kr
			30	

			55	
			150	
			200	
			450	
			1000	
			1390	
ST27	35	134° 33.0928' W 70° 9.3456' N	2	THg, DGM, DOC/EEM, POC/PN, SPM, cyanobacteria, Gross kr
			15	
			25	
			32	

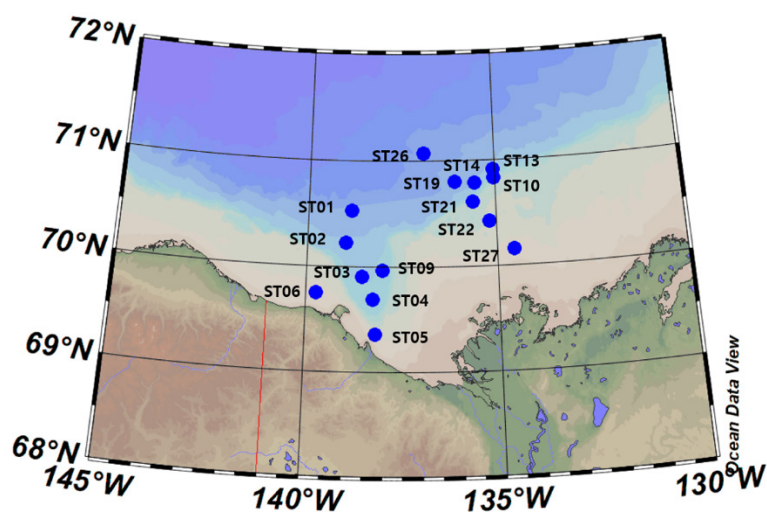


Figure 8.1. Seawater sampling locations

8.2.2. Sediment sampling

Sediment samples were obtained using the MUC 8 multicorer (Oktopus GmbH) equipped with 80 cm polycarbonate core liners. We removed overlying water from the core, and pore water was extracted at sediment depths of 2.5, 7.5, 12.5, 22.5, 32.5, 42.5, and 52.5 cm using a Rhizon sampler connected to a 25 mL syringe through a 0.2- μ m syringe filter at ST01, 02, 03, 04, 05, 09, 19, 20, 21, 22, 25, 27, and 31. The pore water samples were frozen for the later analysis of the dissolved inorganic nutrients and THg. The sediment samples, sliced from 0–5, 5–10, 10–15, 20–25, 30–35, 40–45, and 50–55 cm, were transferred into polyethylene tubes and kept in a freezer until analysis. Details of the sampling procedures are available in Table 8.2.

Table 8.2. Station number, water depth, GPS, sampling depth, and analytical parameters of sediment samples

Station	Depth (m)	GPS (latitude, longitude)	Sampling Depth (cm)	Parameter
ST01	1113	138° 51.6127' W 70° 31.9439' N	0-5	THg, MeHg, CHONS, 16S rRNA sequencing, km, kd
			5-10	
			10-15	
			20-25	

			30-35	
			40-45	
			50-55	
ST02	423	138° 59.3458' W 70° 13.5725' N	0-5	THg, MeHg, CHONS, 16S rRNA sequencing, km, kd
			5-10	
			10-15	
			20-25	
			30-35	
			40-45	
ST03	225	138° 33.3733 'W 69° 54.2668' N	0-5	THg, MeHg, CHONS, 16S rRNA sequencing, km, kd
			5-10	
			10-15	
			20-25	
			30-35	
			40-45	
ST04	145	138° 16.6127' W 69° 41.3709' N	0-5	THg, MeHg, CHONS, 16S rRNA sequencing, km, kd
			5-10	
			10-15	
			20-25	
			30-35	
			40-45	
ST05	43.5	138° 11.8499' W 69° 21.5193' N	0-5	THg, MeHg, CHONS, 16S rRNA sequencing, km, kd
			5-10	
			10-15	
			20-25	
			30-35	
			40-45	
ST09	166	138° 1.8008' W 69° 57.8358' N	0-5	THg, MeHg, CHONS, 16S rRNA sequencing, km, kd
			5-10	
			10-15	
			20-25	
			30-35	
			40-45	
ST19	748	136° 5.7806' W 70° 48.0513' N	0-5	THg, MeHg, CHONS, 16S rRNA sequencing, km, kd
			5-10	
			10-15	
			20-25	
			30-35	
			40-45	
			50-55	
ST20	105	134° 57.7545' W 70° 51.0101' N	0-5	THg, MeHg, CHONS, 16S rRNA sequencing, km, kd
			5-10	
			10-15	

			20-25	
			30-35	
			40-45	
ST21	75	135° 36.9050' W 70° 36.4654' N	0-5	THg, MeHg, CHONS, 16S rRNA sequencing, km, kd
			5-10	
			10-15	
			20-25	
			30-35	
			40-45	
ST22	63	135° 11.6298' W 70° 25.5955' N	0-5	THg, MeHg, CHONS, 16S rRNA sequencing, km, kd
			5-10	
			10-15	
			15-20	
			20-25	
			25-30	
ST25	415	135° 33.8672' W 70° 47.5405' N	0-5	THg, MeHg, CHONS, 16S rRNA sequencing, km, kd
			5-10	
			10-15	
			20-25	
			30-35	
			40-45	
			50-55	
ST27	35	134° 33.0928' W 70° 9.3456' N	0-5	THg, MeHg, CHONS, 16S rRNA sequencing, km, kd
			5-10	
			10-15	
			20-25	
			30-35	
			40-45	
			50-55	
ST31	64	133° 32.6353' W 70° 39.2484' N	0-5	THg, MeHg, CHONS, 16S rRNA sequencing, km, kd
			5-10	
			10-15	
			20-25	
			30-35	
			40-45	
			50-55	

8.2.3. DGM analysis

The DGM was simultaneously measured using a discrete method and the continuous equilibrium method (Figure 8.2). Approximately 400–900 mL of seawater was poured gently into a 1-L borosilicate bubbler to prevent the DGM from degassing. DGM was then collected with gold-coated glass traps by purging seawater with Hg-free N₂ gas at 450 mL min⁻¹ for 20–

60 min. The gold traps were heated to cause thermal desorption of Hg, and emitted gaseous Hg(0) was quantified using CVAFS (Brooks Rand Model III). The relative percentage difference (RPD) of the duplicate DGM measurements was 13.2 ± 12.5 (n = 83), and the mean recovery of the certified reference material (BCR-579, coastal seawater) was 114.2% (n = 2, RPD = 0.9%).

The continuous DGM measurement technique, which applies equilibrium between air and water, has been reported in multiple studies (Dimento et al., 2019; Mastromonaco et al., 2017; Sorensen et al., 2014) and is based on the opposite flow principle so that the contact time between the air and water is maximized, thereby easily generating equilibrium. In the opposite direction of the seawater flow, Hg-free air was consistently injected through the mass flow controller at a rate of $\sim 1.1 \text{ L min}^{-1}$. Seawater was continuously pumped from 6 m below the sea surface at a rate of 12 L min^{-1} . The purged air was continuously transported to the Tekran 2537X and measured at a resolution of every 5-minutes. The DGM concentration was calibrated with the internal calibration source equipped in the Tekran 2537X. The DGM concentration in the seawater was calculated using the following equations (Andersson et al., 2008), where k_H is Henry's law constant (dimensionless).

$$\text{DGM} = C_{\text{eq}} / k_H \quad (1)$$

$$k_H = \exp(-2404.3/T + 6.92) \quad (2)$$

8.2.4. Photoreduction rate constant (k_r) of Hg(II)

The photoreduction rate constant (k_r) is divided into the gross reduction rate constant (gross k_r) and the net reduction rate constant (net k_r). Only the gross k_r was measured in the present study. The zero DGM concentration of seawater in the quartz bubbler was obtained by purging it with Hg-free air ($\sim 1 \text{ h}$) in the UV photolysis box (Figure 8.2). The concentration of DGM produced by photoreduction was measured by the Tekran 2537X using eight UV-A lamps (F8T5BLB, Sankyo Denki) for $\sim 4 \text{ h}$ without additional Hg(II). Using the pseudo first-order model, the amount of photo-reducible Hg (Hg_{Red}) and gross k_r were calculated. The gross k_r of the surface seawater was calculated using the following equations:

$$\frac{d[Hg_{\text{Red}}]}{dt} = -k_r[Hg_{\text{Red}}] \quad (3)$$

$$\ln \frac{Hg_{\text{Red},t}}{Hg_{\text{Red},0}} = -k_r t \quad (4)$$

$$Hg_{\text{Red},t} = Hg_{\text{Red},0} \times e^{-k_r t} \quad (5)$$

$$Hg_{\text{Red},t} = Hg_{\text{Red},0} - \text{DGM} \quad (6)$$

$$\text{DGM} = Hg_{\text{Red}} \times (1 - e^{-k_r t}) \quad (7)$$

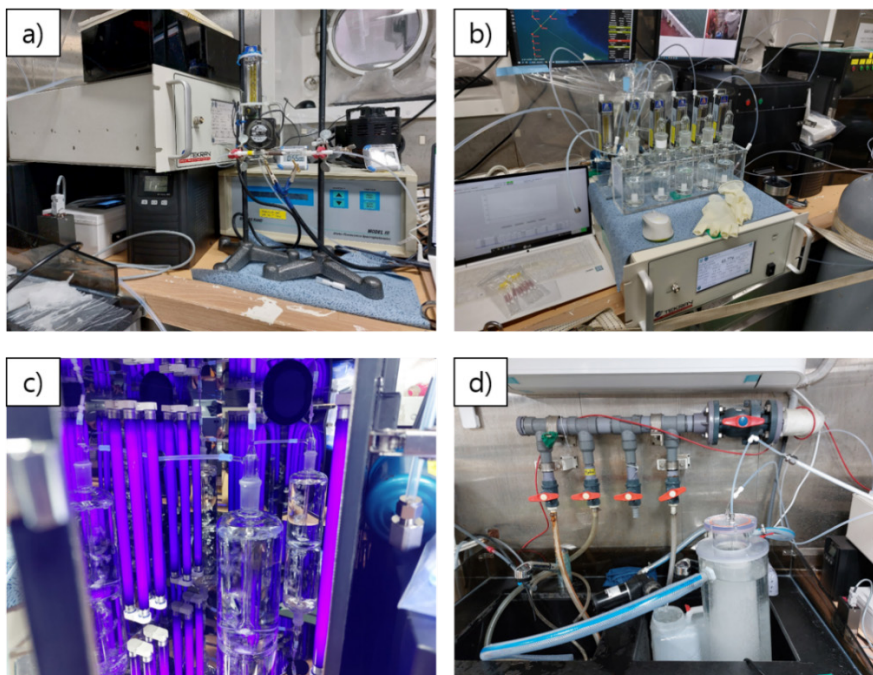


Figure 8.2. Experimental setups: a) CVAFS for Hg measurement (Tekran 2537X and Brooks Rand Model III), b) borosilicate bubblers for DGM measurement, c) UV photolysis box for the analysis of gross k_r , and d) continuous DGM measurement equipment. Photos courtesy of Korea Polar Research Institute.

8.2.5. Sampling procedure for stable Hg isotopes

A. Seawater

Seawater from six sites near the Mackenzie Trough was sampled. The targeted station numbers were from ST01 to ST05 and ST09. At each site, 40 L of seawater was sampled per depth, at two predetermined depths. The targeted depths were surface and subsurface chlorophyll maxima (SCM). The sampling depth was surface and bottom at locations that did not have SCM (i.e., ST04, ST05). Each seawater interval was sampled using a rosette sampling system and preserved in a 10-L glass carboy or a 20-L polycarbonate carboy. The sampled seawater was immediately treated with bromine chloride solution for Hg preservation. The carboys were tightly capped, blocked with parafilm, and preserved in amber condition to reduce the possibility of Hg loss. The seawater will be measured for Hg concentrations and stable isotopes at the POSTECH laboratory after the cruise.

B. Sediment

Sediments were sampled from the predetermined locations during cruise planning (ST01, 02, 03, 04, 05, 06, 09, 19, 21, 22, 25, 27, and 31). Surface sediment was sampled from the top 0- to 5-cm layer of each core and collected using multicorers. The samples were filled into two 40-mL conical tubes and preserved in the fridge at -80°C . The sediment will be used for to measure the concentrations and stable isotopes of Hg at the POSTECH laboratory after the cruise.

C. Plankton

Plankton were sampled at ST02 and ST04 in the Mackenzie Trough (Figure 8.3). Each sample was collected using a 150- μm mesh size net for 4~5 h per site. The targeted depths were 40 m and 190 m for ST02 and 35 m and 125 m for ST04. The depths were determined based on CTD data targeting the SCM and oxygen minimum zone where possible. At ST04 and ST05, where the oxygen minimum zone was not identified, the deepest depth of the seawater measured by CTD was targeted. The depth was confirmed at ST02 using only a pressure sensor from Dr. Y.G. Kim. The measured pressure data were converted into depth, as shown below (Figure 8.5). The sampled plankton were divided into three fractions of 0.2–1 mm, 1–5 mm, and > 5 mm using acid-washed Nitex mesh. Then, each sample was filtered onto a nylon net filter (30 μm , 47 mm) using a vacuum pump (Figure 8.4). The samples were preserved in a fridge at -80°C to analyze concentrations and stable isotopes of Hg at the POSTECH laboratory. If possible, MeHg concentration will also be measured.



Figure 8.3. Bongo nets (150- μm) used for plankton sampling. Photo courtesy of Korea Polar Research Institute.



Figure 8.4. Plankton-filtering equipment. Photo courtesy of Korea Polar Research Institute.

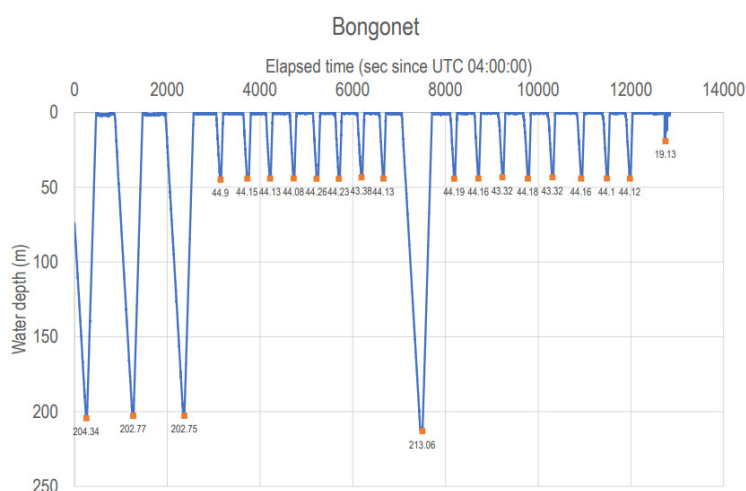


Figure 8.5. Plankton mesh depth profiles at ST02

D. Atmosphere

1) Total gaseous mercury (TGM)

TGM was sampled using a specialized gold trap for Hg (Brooks Rand Instruments) connected to a portable air pump on the compass deck of the Araon, with a volume of 1.68 L/min or 1.94 L/min per trap (Figure 8.6). The stable Hg isotope values of TGM are known to show different values with the presence of light. Fog and high wind speed also affect the TGM value. Therefore, sampling was conducted four times during the cruise during daylight without fog for 11–13 h. Each gold trap was capped tightly in amber condition for preservation (Table 8.3). The concentrations and stable isotopes of Hg will be measured at the POSTECH laboratory after the cruise.

Table 8.3. TGM sampling sites and sample volumes

TGM no.	Site number	Volume sampled
1	ST01-ST02	8260 L
2	ST03-ST04	12743 L
3	ST09-ST10	10372 L
4	ROV1-ROV2	9208

2) Reactive gaseous mercury (RGM)

RGM was captured using a polyethersulfone filter trapped in a filter holder for the duration of the cruise. Because RGM requires at least 2 weeks for one analysis of stable Hg isotopes, the RGM sampling was conducted over 20 days (Figure 8.7). Due to battery limitations and weather conditions, the quantity of RGM may have been inadequate. Regardless, the filter was collected and preserved in a fridge at -80°C . The analysis of the stable isotopes and concentrations of Hg will be performed at the POSTECH laboratory after the cruise.

3) Precipitation

Strong wet precipitation occurred only once in the early stage of the cruise on August 25, and the period of precipitation was too short to collect an adequate sample volume for stable Hg isotope analysis. Nevertheless, the sample was collected, and the isotopes will be measured to determine whether an adequate amount was sampled.



Figure 8.6. TGM sampling tools. Photo courtesy of Korea Polar Research Institute.



Figure 8.7. RGM sampling tools. Photo courtesy of Korea Polar Research Institute.

8.3. Results

The DGM was measured discretely at 15 stations (Table 8.1) during this expedition (Figure 8.8). Duplicate DGM samples were analyzed, and the RPD ($13.2 \pm 12.5\%$) was similar to that in a previous study ($14 \pm 11\%$) of the Arctic Ocean (Agather et al., 2019). The range of the DGM in the surface seawater was 0.10–0.63 pM, which is similar to previous findings (Andersson et al., 2008; Dimento et al., 2019). Among the two latitudinal transects, the DGM in the polar mixed layer was higher in the western than eastern transects (t-test, $p = 0.013$), which might be the effect of Pacific water input through the Bering Strait. Low DGM concentrations were observed in the top layer due to the evasion to the atmosphere, similar to the result of a previous study of the Western Arctic Ocean (Agather et al., 2019). The DGM increased toward 130–200 m and then decreased toward ~1,000 m. This vertical distribution of DGM should be further investigated using ancillary parameters and water mass properties.

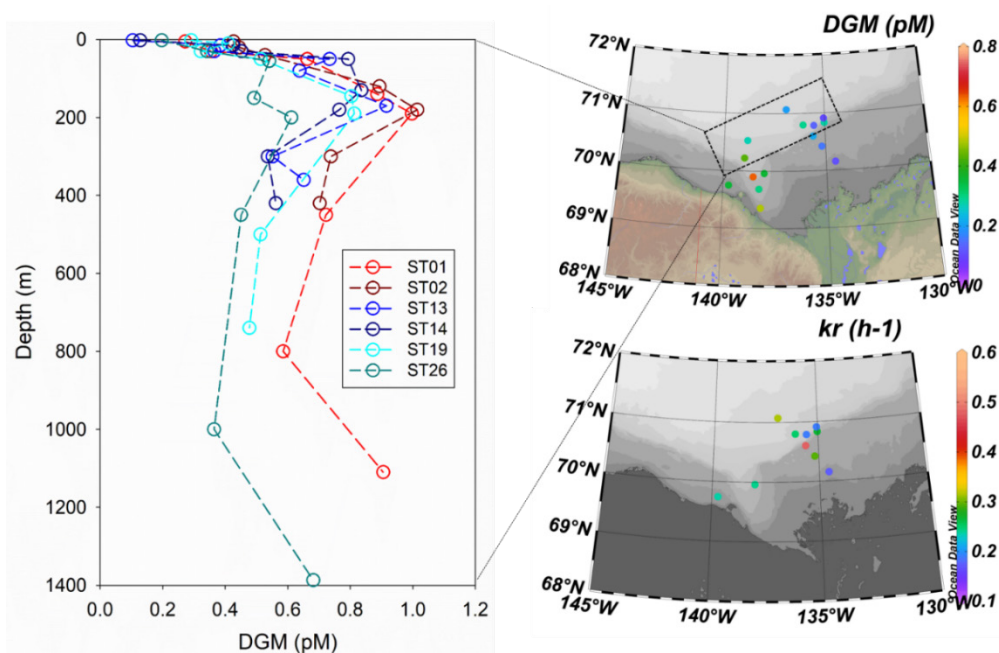


Figure 8.8. The depth distributions of DGM and DGM and gross k_r distributions in the polar mixed layer

The gross k_r of surface seawater was measured at 10 stations outside the Mackenzie Trough (Figure 8.9). The curves of the cumulative DGM as a function of time were well satisfied with the pseudo first-order kinetic model ($r^2 > 0.999$, $p < 0.001$). The gross k_r ranged from 0.17 to 0.48 h^{-1} , and higher values were found at the edge of the shelf where water of lower salinity was found. The maximum value of k_r (0.48 h^{-1}) was observed at ST21.

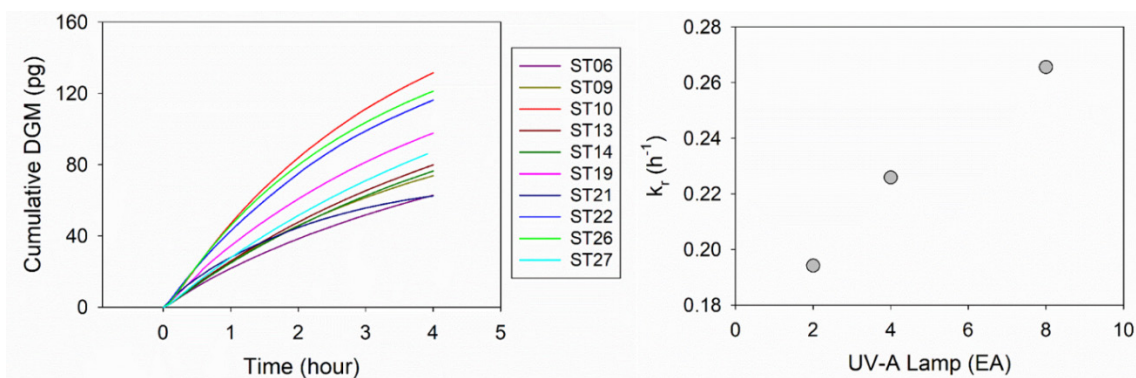


Figure 8.9. The cumulative DGM curves to calculate gross k_r and gross k_r versus the number of UV-A lamps tested with seawater from ST10

8.4. Summary

During the ARA13C expedition, diverse environmental samples, including air, seawater, sediment, and zooplankton, were collected along the longitudinal and latitudinal transects of the Beaufort Sea for the measurement of diverse species (DGM, THg, and MeHg) and stable isotopes of Hg. The measurements of DGM and k_r in the surface seawater were carried out on board in order to understand how the air–sea exchange of Hg would respond to the Mackenzie River discharge. Further analysis results of Hg species and isotopes in the GIST and Postech laboratories in South Korea will be used to identify whether seasonal warming of sediment overlying discontinuous permafrost produces variations in Hg(II) methylation rates and MeHg

concentrations and investigate potential sources of Hg in pelagic zooplankton in the Beaufort Sea.

The DGM in the surface layer, which ranged from 0.064 to 0.63 pM, was generally higher in the western than eastern transect, which might be related to the Hg input from Pacific water following the eastward coastal current as the salinity was also higher in the western than eastern transect. The DGM concentration increased toward a water depth of 130–200 m, and below that, it decreased toward a water depth of 800–1,000 m. The gross k_r in the surface seawater ranged from 0.19 to 0.48 h⁻¹, and the value was higher at the lower salinity sites influenced by Mackenzie River discharge. The distribution of DGM and k_r in the surface seawater will be further explained using DOC, EEMs fluorescence, SPM, and the other water parameters measured in the GIST laboratory. The air–sea exchange flux of Hg will then be estimated using the field concentrations of DGM and atmospheric Hg(0).

References

- Agather, A.M., Bowman, K.L., Lamborg, C.H. and Hammerschmidt, C.R. 2019. Distribution of mercury species in the Western Arctic Ocean (U.S. GEOTRACES GN01). *Marine chemistry*, 216: 103686.
- Andersson, M.E., Sommar, J., Gårdfeldt, K. and Lindqvist, O. 2008. Enhanced concentrations of dissolved gaseous mercury in the surface waters of the Arctic Ocean. *Marine Chemistry* 110: 190 – 194.
- AMAP, 2021. AMAP. AMAP Assessment 2021: Mercury in the Arctic. Arctic Monitoring and Assessment Programme (AMAP), Tromsø, Norway.
- Chételat, J., McKinney, M.A., Amyot, M., Dastoor, A., Douglas, T.A., Heimbürger-Boavida, L., Kirk, J., Kahilainen, K.K., Outridge, P.M., Pelletier, N., Skov, H., Pierre, K.S., Vuorenmaa, J. and Wang, F. 2022. Climate change and mercury in the Arctic: Abiotic interactions. *Science of the Total Environment*, 824: 153715.
- Deng, L., Wu, F., Deng, N. and Zuo, Y. 2008. Photoreduction of mercury(II) in the presence of algae, *Anabaena cylindrical*. *Journal of Photochemistry and Photobiology B: Biology*, 91: 117–124.
- DiMento, B.P., Mason, R.P., Brooks, S. and Moore, C. 2019. The impact of sea ice on the air-sea exchange of mercury in the Arctic Ocean. *Deep-Sea Research Part I* 144: 28-38.
- Harding, K., Turk-Kubo, K.A., Sipler, R.E. and Zehr J.P. 2015. Symbiotic unicellular cyanobacteria fix nitrogen in the Arctic Ocean. *PNAS* 52: 13371-13375.
- Jeremiason, J.D., Portner, J.C., Aiken, G.R., Hiranaka, A.J., Dvorak, M.T., Tran, K.T. and Latch, D.E. 2015. Photoreduction of Hg(II) and photodemethylation of methylmercury: the key role of thiol sites on dissolved organic matter. *Environmental Science Processes & Impacts*, 17: 1892-1903.
- Kuss, J., Wasmund, N., Nausch, G. and Labrenz, M. 2015. Mercury Emission by the Baltic Sea: A Consequence of Cyanobacterial Activity, Photochemistry, And Low-Light Mercury Transformation. *Environmental Science and Technology*, 49: 11449 – 11457.
- Lehnerr, I. 2014. Methylmercury biogeochemistry: a review with special reference to Arctic aquatic ecosystems. *Environmental Review*, 22: 229-243.
- Masbou, J., Sonke, J., Amouroux, D., Guillou, G., Becker, P.R. and Point, D. 2018. Hg-stable isotope variations in marine top predators of the Western Arctic Ocean. *ACS Earth and Space Chemistry*, 2.5: 479-490.
- Mastromonaco, M.G.N., Gårdfeldt, K. and Wängberg, I. 2017. Seasonal and spatial evasion of mercury from the western Mediterranean Sea. *Marine Chemistry*, 193: 34-43.

- Parker, J.L. and Bloom, N.S. 2005. Preservation and storage techniques for low-level aqueous mercury speciation. *Science of the Total Environment*, 337: 253-263.
- Paull, C. K., Dallimore, S. R., Jin, Y. K., Caress, D. W., Lundsten, E., Gwiazda, R., Anderson, K., Clarke, J.H., Youngblut, Scott, Melling, H. 2022. Rapid seafloor changes associated with the degradation of Arctic submarine permafrost. *Proceedings of the National Academy of Sciences*, 119(12), e2119105119.
- Qureshi, A., O'Driscoll, N., MacLeod, M., Neuhold, Y. and Hungerbühler, K. 2010. Photoreactions of Mercury in Surface Ocean Water: Gross Reaction Kinetics and Possible Pathways. *Environmental Science and Technology*, 44: 644-649.
- Si, L. and Ariya, P.A. 2011. Aqueous photoreduction of oxidized mercury species in presence of selected alkanethiols. *Chemosphere*, 84: 1079-1084.
- Sorensen, A.L., Mason, R.P., Balcom, P.H., Jacob, D.J., Zhang, Y., Kuss, J. and Sunderland E.M. 2014. Elemental Mercury Concentrations and Fluxes in the Tropical Atmosphere and Ocean. *Environmental Science and Technology*, 48: 11312-11319.
- Sparrow, K.J. Kessler, J.D., Southon, J.R., Garcia-Tigueros, F., Schreiner, K.M., Ruppel, C.D., Miller, J.B., Lehman, S.J., Xu, X. 2018. Limited contribution of ancient methane to surface waters of the U.S. Beaufort Sea shelf. *Science Advances*, 4: eaao4842
- Valera, B., Dewailly, E. and Poirier, P. 2009. Environmental mercury exposure and blood pressure among Nunavik Inuit adults. *Hypertension*, 54: 981–986.
- Zhang, X., Guo, Y., Liu, G., Liu Y., Song M., Shi, J., Hu, L., Li, Y., Yin, Y., Cai, Y. and Jiang, G. 2021. Dark Reduction of Mercury by Microalgae-Associated Aerobic Bacteria in Marine Environments. *Environmental Science and Technology*, 55: 14258-14268.

ARA13C Cruise report

Appendix 1. Participants

No	Organization	Name	Contact	Works in the expedition
1	KOPRI	Jong Kuk Hong	jkhong@kopri.re.kr	Chief Scientist
2	KOPRI	Seung Goo Kang	ksg9322@kopri.re.kr	Geophysics
3	KOPRI	Yeonjin Choi	yjchoi@kopri.re.kr	Geophysics
4	KOPRI	Youngil Choi	yichoi@kopri.re.kr	Geophysics
5	KOPRI	Hyoung Jun Kim	jun7100@kopri.re.kr	Multi-beam & SBP
6	KOPRI	Yung Mi Lee	ymlee@kopri.re.kr	Microbiology
7	KOPRI	Woohyun Kim	wooppe@kopri.re.kr	Microbiology
8	KOPRI	Tae Siek Rhee	rhee@kopri.re.kr	Oceanography
9	KOPRI	Minjee Kim	minjee913@hanyang.ac.kr	Oceanography
10	KOPRI	Hyebin Park	agnespl@naver.com	Oceanography
11	KOPRI	Mi Seon Kim	mskim@kopri.re.kr	Chemical Oceanography
12	KOPRI	Heungsoo Moon	jepy@kopri.re.kr	Coring Operator
13	KOPRI/Inha Univ.	Youngkyu Ahn	youngq@inha.edu	Sedimentology
14	KIGAM	Ji Hoon Kim	save@kigam.re.kr	Geochemistry
15	Kangwon University	Young-Gyun Kim	younggyun.kim@gmail.com	Marine Geology
16	Kangwon University	Hyeonseob Kim	7890hyunmin@kangwon.ac.kr	Numerical Geodynamic
17	Kangwon University	Yijeong Baek	yijung0320@kangwon.ac.kr	Numerical Geodynamic
18	Hanyang University	See Ryang Seong	sserex@hanyang.ac.kr	Organic Geochemistry
19	Gyeongsang National University	Sangmi Lee	cnqtm21@gnu.ac.kr	Mineralogy
20	Sejong University	Thi Hien Nguyen	hien08nguyenthi@gmail.com	Environmental Engineering
21	UNIST	Jungwhoun Mok	daiana1147@unist.ac.kr	Chemical Engineering
22	GIST	Sangwoe Eom	sangwooe@gm.gist.ac.kr	Biochemistry
23	GIST	Juhyeong Chae	cjh081111@gist.ac.kr	Biochemistry
24	GIST	Hakwon Jeong	hk.jeong@gm.gist.ac.kr	Biochemistry

25	POSTECH	Younggwang Kim	glorykim@postech.ac.kr	Environmental Engineering
26	POSTECH	Seunghyeon Lim	llsh0331@postech.ac.kr	Environmental Engineering
27	Arts Council Korea	Kiwon Hong	kiwon.hong1@gmail.com	Photographer
28	Republic of Korea Navy	Eunsang Yun	lpeng2@alaska.edu	Navy
29	GSC	Virginia Brake	virginiairene.brake@nrcan-nrcan.gc.ca	Marine Geology
30	Edgewise Environmental	Ashley Noseworthy	ashley@edgewiseenvironmental.com	Marine Mammal Observer
31	NRL	Maureen Walton	maureen.walton@nrlssc.navy.mil	Marine Geophysics
32	NRL	Jeffrey Blake	jeffrey.obelcz@nrlssc.navy.mil	Marine Geology
33	MBARI	Charles Paull	paull@mbari.org	Marine Geology
34	MBARI	Eve Lundsten	eve@mbari.org	Marine Geology
35	MBARI	Roberto Gwiazda	rgwiazda@mbari.org	Geochemistry
36	MBARI	Frank Flores	frank@mbari.org	ROV Chief
37	MBARI	Dale Graves	graves.dale@gmail.com	ROV Pilot
38	MBARI	Eric Martin	emartin@mbari.org	ROV Pilot/AUV Operator
39	MBARI	Randall Prickett	rprickett@mbari.org	AUV Chief
40	MBARI	Jordan Caress	jordan@mbari.org	AUV Operator
41	MBARI	Tanner Poling	tanner@mbari.org	AUV Operator
42	MBARI	David Caress	caress@mbari.org	Seafloor Mapping
43	MBARI	Jennifer Paduan	paje@mbari.org	Seafloor Mapping

ARA13C Cruise report

Appendix 2. List of Stations and Line Survey

Station / Waypoint	Work order	*Gear	Time (UTC)				Longitude	Latitude	Depth (m)	Gyro (°)	Remark
			start		end						
			Date	Time	Date	Time					
Depart			2022-08-25	10:00			159° 49.5711' W	71° 24.4299' N		34.6	
Station 01	1	CTD	2022-08-26	16:09	2022-08-26	17:16	138° 51.6127' W	70° 31.9439' N	1113	107.5	
	2	MC	2022-08-26	17:31	2022-08-26	18:19	138° 51.6125' W	70° 31.9453' N	1113	96.4	
	3	CTD	2022-08-26	19:16	2022-08-26	20:07	138° 51.6184' W	70° 31.9406' N	1105	148.2	
Station 01 to 02	1	MB/SBP	2022-08-26	20:27			138° 51.6951' W	70° 31.7768' N	1077	187.9	
	2	MB/SBP			2022-08-26	22:53	138° 59.4195' W	70° 13.5892' N	422	100.9	
Station 02	1	CTD	2022-08-27	0:12	2022-08-27	0:42	138° 59.3458' W	70° 13.5725' N	423	134	
	2	MC	2022-08-27	0:57	2022-08-27	01:18	138° 59.3412' W	70° 13.5743' N	423	117.4	Bottom touch 01:08 UTC
	3	GC	2022-08-27	2:07	2022-08-27	2:39	138° 59.3424' W	70° 13.5745' N	424	119.8	Bottom touch 02:27 UTC
	4	BongoNet	2022-08-27	3:39	2022-08-27	07:25	138° 59.3429' W	70° 13.5752' N	422	120	
Station 02 to 03	1	MB/SBP	2022-08-27	7:32			138° 59.3434' W	70° 13.5731' N	423	131.9	
	2	MB/SBP			2022-08-27	14:02	138° 33.4000 'W	69° 54.2688' N	223	62.9	
Station 03	1	CTD	2022-08-27	14:10	2022-08-27	14:31	138° 33.3733 'W	69° 54.2668' N	225	62.4	
	2	MC	2022-08-27	14:53	2022-08-27	15:08	138° 33.3728' W	69° 54.2664' N	223	65	Bottom touch 15:00 UTC
	3	CTD	2022-08-27	15:53	2022-08-27	16:05	138° 33.3761' W	69° 54.2681' N	223	48.8	
Station 03 to 04	1	MB/SBP	2022-08-27	16:15			138° 33.3724' W	69° 54.2657' N	222	157	

	2	MB/SBP			2022-08-27	18:04	138° 16.6414' W	69° 41.3644' N	145	108.4	
Station 04	1	CTD	2022-08-27	18:10	2022-08-27	18:35	138° 16.6127' W	69° 41.3709' N	145	104.7	
	2	MC	2022-08-27	18:45	2022-08-27	18:57	138° 16.6157' W	69° 41.3749' N	142	60	Bottom touch 18:51 UTC
	3	ROV.	2022-08-27	21:20	2022-08-27	23:19	138° 16.6134' W	69° 41.3740' N	145	79.7	test
	4	AUV.	2022-08-28	00:01	2022-08-28	00:39	138° 16.6447' W	69° 41.3716' N	145	80.1	test
Station 04 to 05	1	MB/SBP	2022-08-28	00:56			138° 16.5145' W	69° 41.3491' N	146	139.3	
	2	MB/SBP			2022-08-28	03:30	138° 11.8383' W	69° 21.5160' N	49	96.3	
Station 05	1	CTD	2022-08-28	03:37	2022-08-28	03:55	138° 11.8499' W	69° 21.5193' N	46	43.5	
	2	MC	2022-08-28	04:04	2022-08-28	04:16	138° 11.8435' W	69° 21.5131' N	49	100	Bottom touch 04:10 UTC
	3	GC	2022-08-28	05:10	2022-08-28	05:18	138° 11.8435' W	69° 21.5131' N	49	100	Bottom touch 05:13 UTC
Station 05 to 04	1	MB/SBP	2022-08-28	06:10			138° 11.8435' W	69° 21.5131' N	49	100	
	2	MB/SBP			2022-08-28	07:55	138° 16.6663' W	69° 41.3529' N	146	352.3	
Station 04	1	BongoNet	2022-08-28	08:00	2022-08-28	10:55	138° 16.6258' W	69° 41.3694' N	145	66.7	
Station 04 to 06	1	MB/SBP	2022-08-28	11:02			138° 16.7630' W	69° 41.3696' N	145	275.8	
	2	MB/SBP			2022-08-28	15:00	139° 43.7988' W	69° 44.8476' N	33	248.2	
Station 06	1	CTD	2022-08-28	16:05	2022-08-28	16:19	139° 43.7793' W	69° 44.8376' N	32	0.3	
	2	MC	2022-08-28	16:33	2022-08-28	16:43	139° 43.7789' W	69° 44.8372' N	32	0.72	Bottom touch 16:37 UTC
	3	MC	2022-08-28	16:55	2022-08-28	17:02	139° 43.7802' W	69° 44.8375' N	32	0.2	Bottom touch 16:59 UTC
Station 06 to 06_1	1	MB/SBP	2022-08-28	17:32			139° 43.7769' W	69° 44.8432' N	33	16.3	
	2	MB/SBP			2022-08-28	19:35	139° 5.4130' W	69° 53.4471' N	95	88.6	
Station 06_1	1	MC	2022-08-28	19:48	2022-08-28	19:58	139° 5.3757' W	69° 53.4354' N	92	140.6	Bottom touch 19:53 UTC
Station 07	1	GC	2022-08-28	20:44	2022-08-28	20:54	139° 4.3169' W	69° 53.5882' N	106.5	153.2	Bottom touch 20:49 UTC
Station 08	1	GC	2022-08-28	21:56	2022-08-28	22:09	139° 4.2686' W	69° 53.5812' N	114	148.8	Bottom touch 22:03 UTC
Station 08 to 09	1	MB/SBP	2022-08-28	22:50			139° 4.2661' W	69° 53.5708' N	114	169.7	
	2	MB/SBP			2022-08-28	23:30	139° 11.6921' W	69° 49.6226' N	50	15.7	Deck work

	3	MB/SBP	2022-08-28	00:12			139° 11.6930' W	69° 49.6476' N	50	32.7	line survey start
	4	MB/SBP			2022-08-28	3:54	138° 1.8026' W	69° 57.8359' N	166	82.7	line survey end
Station 09	1	CTD	2022-08-29	04:00	2022-08-29	4:24	138° 1.8008' W	69° 57.8358' N	166	82.4	
	2	MC	2022-08-29	4:40	2022-08-29	4:55	138° 1.8008' W	69° 57.8358' N	167	82.3	Bottom touch 04:45 UTC
Station 09 to ROV01	1	MB/SBP	2022-08-29	05:25			138° 1.8005' W	69° 57.8352' N	166	79.1	
	2	MB/SBP			2022-08-29	15:31	135° 3.9952' W	70° 50.3769' N	157	42.3	
ROV01 to Station 10	1	MB/SBP	2022-08-29	16:59			135° 3.9425' W	70° 50.3819' N	161	79.3	multibeam/SBP survey
	2	MB/SBP			2022-08-30	00:13	135° 1.9276' W	70° 50.0056' N	111	53.7	
Station 10	1	CTD	2022-08-30	0:30	2022-08-30	00:42	135° 1.8966' W	70° 50.0096' N	111	114.3	
Station 10 to ROV01	1	MB/SBP	2022-08-30	00:49			135° 1.8966' W	70° 50.0096' N	112	193	multibeam/SBP survey
	2	MB/SBP			2022-08-30	16:24	135° 3.9421' W	70° 50.3771' N	159	96.5	
ROV01	1	ROV	2022-08-30	16:52	2022-08-30	20:22	135° 3.9498' W	70° 50.3856' N	159	97.1	
AUV01	1	AUV	2022-08-30	21:53	2022-08-30	22:26	135° 1.8701' W	70° 49.9856' N		223.1	AUV Deploy
AUV02	1	AUV.	2022-08-31	0:29	2022-08-31	0:40	134° 55.7837' W	70° 51.4724' N		205.3	AUV Deploy, fail
	2	AUV.	2022-08-31	2:05	2022-08-31	2:32	134° 55.7977' W	70° 51.5071' N		269.6	AUV Recovery
Station 11	1	GC	2022-08-31	4:42	2022-08-31	4:56	135° 11.3138' W	70° 48.4934' N	130	320.8	Bottom touch 04:49 UTC
Station 12	1	GC	2022-08-31	5:58	2022-08-31	6:06	135° 11.2374' W	70° 48.4651' N	120	321	Bottom touch 06:02 UTC
Station 12 to Station 13	1	MB/SBP	2022-08-31	6:56			135° 7.7110' W	70° 51.2351' N	260	21.8	Resume log after passing the AUV site
	2	MB/SBP			2022-08-31	7:28	135° 3.3195' W	70° 54.7309' N	367	356.8	
Station 13	1	CTD	2022-08-31	7:30	2022-08-31	08:05	135° 3.3195' W	70° 54.7309' N	367	356.8	
Station 13 to AUV01	1	MB/SBP	2022-08-31	8:09			135° 3.3112' W	70° 54.7309' N	367	321.9	
	2	MB/SBP			2022-08-31	12:49	134° 11.4525' W	70° 34.4118' N	62	204.7	ship speed 8 knot -> 12 knot
	3	MB/SBP			2022-08-31	15:05	135° 1.8333' W	70° 50.0096' N	111	256.6	
AUV01	1	AUV.	2022-08-31	17:24	2022-08-31	17:49	135° 3.0451' W	70° 51.0140' N	150	209.7	AUV Recovery
AUV_TEST	1	AUV.	2022-08-31	18:50	2022-08-31	20:20	135° 1.7909' W	70° 49.3490' N	101	209.2	AUV test

ROV02	1	ROV	2022-08-31	21:10	2022-09-01	0:47	135° 3.7398' W	70° 50.3802' N		202.7	
ROV02 to Station 14	1	MB/SBP	2022-09-01	1:25			135° 13.9293' W	70° 50.3363' N	130	216	
	2	MB/SBP			2022-09-01	03:01	135° 33.6037' W	70° 47.3876' N	425	110.2	
Station 14	1	CTD	2022-09-01	03:03	2022-09-01	03:38	135° 33.6047' W	70° 47.3867' N	425	110.5	MV420m
Station 15	1	HF	2022-09-01	3:57	2022-09-01	5:20	135° 33.7792' W	70° 47.4506' N	423	110.7	Bottom touch 04:23 UTC, MV420m
	2	HF	2022-09-01	05:22	2022-09-01	6:58	135° 33.7800' W	70° 47.4497' N	423	111	Bottom touch 05:41 UTC, MV420m
Station 16	1	HF	2022-09-01	07:44	2022-09-01	09:10	135° 33.7049' W	70° 47.3880' N	423	110.8	Bottom touch 08:06 UTC, MV420m
Station 17	1	HF	2022-09-01	9:53	2022-09-01	11:01	135° 33.7896' W	70° 47.3496' N	425	111.1	Bottom touch 10:12 UTC, MV420m
Station 17 to Station 18	1	MB/SBP	2022-09-01	11:14			135° 33.7521' W	70° 47.3580' N	423	345	
	2	MB/SBP			2022-09-01	11:36	135° 39.4721' W	70° 49.8754' N	562	138.9	
Station 18	1	HF	2022-09-01	11:41	2022-09-01	13:30	135° 39.4721' W	70° 49.8754' N	562	138.9	Bottom touch 12:09 UTC
Station 18 to ROV03	1	MB/SBP	2022-09-01	13:50			135° 39.5637' W	70° 49.9051' N	562	154.9	
	2	MB/SBP			2022-09-01	15:26	136° 5.4246' W	70° 34.5522' N	179	117.2	
ROV03	1	ROV	2022-09-01	16:24	2022-09-01	20:00	136° 5.3626' W	70° 34.5489' N	149	214.8	
AUV02	1	AUV	2022-09-01	22:02	2022-09-01	22:18	136° 1.1292' W	70° 34.1227' N		200.2	AUV Deploy
AUV03	1	AUV.	2022-09-01	23:32	2022-09-01	23:48	136° 8.7760' W	70° 32.4426' N		215.5	AUV Deploy, fail
	2	AUV.	2022-09-02	0:50	2022-09-02	1:27	136° 9.5323' W	70° 32.6279' N		180.1	AUV Recovery
AUV02 to Station 19	1	MB/SBP	2022-09-02	1:47			136° 9.6563' W	70° 32.6073' N	117	315.3	
	2	MB/SBP			2022-09-02	3:10	136° 5.2234' W	70° 48.2831' N	783	8.4	
Station 19	1	CTD	2022-09-02	3:40	2022-09-02	4:22	136° 5.7806' W	70° 48.0513' N	748	218.1	MV780m
	2	MC	2022-09-02	4:31	2022-09-02	5:02	136° 5.7554' W	70° 48.0560' N	746	99.7	Bottom touch 04:46 UTC
Station 19 to Station 20	1	MB/SBP	2022-09-02	5:30			136° 5.7547' W	70° 48.0564' N	746	99.7	
	2	MB/SBP			2022-09-02	07:35	134° 57.7545' W	70° 51.0101' N	109	136.4	
Station 20	1	CTD	2022-09-02	07:03	2022-09-02	07:50	134° 57.7545' W	70° 51.0101' N	109	136.4	
	2	MC	2022-09-02	08:11	2022-09-02	08:23	134° 57.6843' W	70° 51.0113' N	109	96.7	Bottom touch 08:17 UTC

	3	GC	2022-09-02	09:15	2022-09-02	09:29	134° 57.6568' W	70° 51.0104' N	109	94.7	Bottom touch 09:21 UTC
Station 20 to AUV02	1	MB/SBP	2022-09-02	10:30			134° 57.6567' W	70° 51.0107' N	109	95	
	2	MB/SBP	2022-09-02	11:21			135° 13.7083' W	70° 49.2961' N	235	134.2	Line survey start, ship speed 5kn
	3	MB/SBP	2022-09-02	11:36			135° 11.3138' W	70° 48.4934' N	125	133.5	Station 11
	4	MB/SBP	2022-09-02	11:36			135° 11.2374' W	70° 48.4651' N	125	133.5	Station 12
	5	MB/SBP			2022-09-02	11:49	135° 8.8380' W	70° 47.6381' N	103	134.1	Line survey end
	6	MB/SBP			2022-09-02	14:40	136° 1.1269' W	70° 34.1269' N	99	226	
AUV02	1	AUV.	2022-09-02	17:15	2022-09-02	17:37	136° 5.3098' W	70° 35.7808' N		152.1	AUV Recovery
	2	AUV.	2022-09-02	17:47	2022-09-02	18:16	136° 5.3030' W	70° 35.7836' N		125.3	AUV test
AUV02 to ROV04	1	MB/SBP	2022-09-02				136° 5.3332' W	70° 35.7740' N			
	2	MB/SBP			2022-09-02	20:32	135° 5.0418' W	70° 50.5093' N	162	323.6	
ROV04	1	ROV	2022-09-02	21:03	2022-09-02	1:24	135° 5.0225' W	70° 50.5229' N	161	180	
ROV04 to AUV03	1	MB/SBP	2022-09-03	1:31			135° 5.0297' W	70° 50.4547' N	168	217.6	
	2	MB/SBP			2022-09-03	02:28	135° 17.4516' W	70° 44.4099' N	108	317.3	
AUV03	1	AUV	2022-09-03	2:58	2022-09-03	03:20	135° 17.3561' W	70° 44.3713' N	108	230.8	AUV Deploy, Low vision
AUV03 to Station 21	1	MB/SBP	2022-09-03	03:40			135° 17.5942' W	70° 44.3927' N	101	232.4	
	2	MB/SBP			2022-09-03	04:48	135° 36.9039' W	70° 36.4638' N	75	270.1	
Station 21	1	CTD	2022-09-03	04:53	2022-09-03	05:10	135° 36.9050' W	70° 36.4654' N	75	269.5	
	2	MC	2022-09-03	05:20	2022-09-03	05:34	135° 36.9212' W	70° 36.4655' N	76	270.2	Bottom touch 05:28 UTC
Station 21 to Station 22	1	MB/SBP	2022-09-03	6:08			135° 36.9211' W	70° 36.4657' N	74	265.9	
	2	MB/SBP			2022-09-03	07:59	135° 11.6413' W	70° 25.5979' N	61	230.5	
Station 22	1	CTD	2022-09-03	08:06	2022-09-03	08:26	135° 11.6298' W	70° 25.5955' N	63	243.9	
	2	MC	2022-09-03	08:35	2022-09-03	08:47	135° 11.6462' W	70° 25.5960' N	63	270.7	Bottom touch 08:41 UTC
Station 22 to ROV05	1	MB/SBP	2022-09-03	09:25			135° 11.7466' W	70° 25.5966' N	63	62.6	
	2	MB/SBP			2022-09-03	14:27	135° 3.8437' W	70° 50.9984' N	157	130.6	

ROV05	1	ROV	2022-09-03	16:03	2022-09-03	19:52	135° 3.7967' W	70° 50.9810' N	162	135.4	ROV Dive
ROV05 to AUV04	1	MB/SBP	2022-09-03	20:03			135° 3.6741' W	70° 50.9003' N	160	212.3	
	2	MB/SBP			2022-09-03	20:55	135° 32.3903' W	70° 47.8671' N	450		ARAON DADIS gyro error
AUV03	1	AUV.	2022-09-03	21:01	2022-09-03	22:36	135° 34.8188' W	70° 47.3312' N	453		AUV Recovery
AUV03 to Station 23	1	MB/SBP	2022-09-03	22:54			135° 34.9125' W	70° 47.3122' N	446		
	2	MB/SBP			2022-09-03	23:47	136° 7.2780' W	70° 47.0872' N	750	119.4	AUV Deploy try
	1	AUV.	2022-09-04	0:21	2022-09-04	00:30	136° 7.2769' W	70° 47.1337' N	750	114.6	AUV Deploy, fail
	2	MB/SBP	2022-09-04	3:40			136° 10.6437' W	70° 47.0205' N	726	115.2	
	3	MB/SBP			2022-09-04	05:51	135° 5.0537' W	70° 50.5296' N	164	76	
Station 23	1	CTD	2022-09-04	6:02	2022-09-04	6:21	135° 5.0251' W	70° 50.5332' N	156	72.6	St 23, St24, Ship speed 5kn
	2	GC	2022-09-04	6:45	2022-09-04	6:57	135° 4.9321' W	70° 50.5119' N	156	105.1	Bottom touch 06:51 UTC
Station 24	1	GC	2022-09-04	08:05	2022-09-04	08:19	135° 4.8781' W	70° 50.5141' N	158	105.8	Bottom touch 08:12 UTC
Station 24 to ROV6	1	MB/SBP	2022-09-04	09:22			135° 4.8671' W	70° 50.5114' N	167	88.3	
	2	MB/SBP			2022-09-04	14:35	135° 33.8755' W	70° 47.3542' N	424	136.2	
ROV06	1	ROV	2022-09-04	16:01	2022-09-04	21:55	135° 33.8793' W	70° 47.3604' N	423	124.1	Station 17 (HF)
Station 25	1	CTD	2022-09-04	22:51	2022-09-04	23:27	135° 33.8672' W	70° 47.5405' N	434	115.4	
	2	GC	2022-09-04	23:33	2022-09-04	23:54	135° 33.8662' W	70° 47.5404' N	422	115.6	Bottom touch 23:45 UTC
	3	MC	2022-09-05	00:29	2022-09-05	00:51	135° 34.0717' W	70° 47.5557' N	422	272.4	Bottom touch 16:41 UTC
Line Survey	1	MB/SBP	2022-09-05	02:01			135° 34.0716' W	70° 47.5559' N	422	282	
	2	MB/SBP			2022-09-05	09:24	136° 27.8024' W	70° 57.9112' N	1063	351.3	Away from the current position due to weather condition
Station 26	1	CTD	2022-09-05	22:14	2022-09-05	23:17	136° 56.0013' W	71° 04.3001' N	1401	344.6	
	2	CTD	2022-09-06	00:18	2022-09-06	00:56	136° 56.0055' W	71° 4.3000' N	1408	335.7	
Station 26 to ROV07	1	MB/SBP	2022-09-06	01:04			136° 55.8821' W	71° 4.3181' N	1405	140.8	

	2	MB/SBP			2022-09-06	14:15	135° 11.3398' W	70° 48.5052' N	146	241.6	
ROV07	1	ROV	2022-09-06	16:07	2022-09-06	20:49	135° 11.3330' W	70° 48.5063' N	146	30.1	
ROV07 to AUV04	1	MB/SBP	2022-09-06	21:06			135° 11.1467' W	70° 48.5082' N	126	62.4	
	2	MB/SBP			2022-09-06	21:38	134° 54.9234' W	70° 51.3401' N	113	39	
AUV04	1	AUV	2022-09-06	21:54	2022-09-06	21:30	134° 55.0098' W	70° 51.3586' N	113	40.7	AUV Deploy
AUV04 to AUV05	1	MB/SBP	2022-09-06	22:57			135° 01.9061' W	70° 49.7853' N			
	2	MB/SBP			2022-09-06	23:15	135° 10.8646' W	70° 47.7985' N			
AUV05	1	AUV	2022-09-06	23:42	2022-09-07	00:05	135° 11.0501' W	70° 47.7738' N	114	41.2	AUV Deploy
AUV05 to Station 27	1	MB/SBP	2022-09-07	0:55			135° 11.4293' W	70° 47.7621' N	120	70.7	
	2	MB/SBP			2022-09-07	04:23	134° 33.0863' W	70° 9.3360' N	35	278.7	
Station 27	1	CTD	2022-09-07	04:32	2022-09-07	04:46	134° 33.0928' W	70° 9.3456' N	35	340.3	
	2	MC	2022-09-07	04:56	2022-09-07	5:08	134° 33.0920' W	70° 09.3420' N	35	340.2	Bottom touch 05:00 UTC
Station 27 to AUV04	1	MB/SBP	2022-09-07	05:05			134° 33.2350' W	70° 9.3731' N	35	340	
	2	MB/SBP			2022-09-07	15:09	134° 57.2435' W	70° 52.3246' N	134	63.1	
AUV04	1	AUV.	2022-09-07	16:45	2022-09-07	16:59	134° 57.1384' W	70° 52.1670' N	134	126.5	AUV Recovery
AUV05	1	AUV.	2022-09-07	18:44	2022-09-07	19:16	135° 14.9954' W	70° 48.2448' N		126.6	AUV Recovery
ROV08	1	ROV	2022-09-07	20:21	2022-09-08	0:04	134° 58.3753' W	70° 51.3820' N	121	90	
ROV08 to AUV06	1	MB/SBP	2022-09-08	00:10			134° 58.0826' W	70° 51.3646' N	127	11.3	
	2	MB/SBP			2022-09-08	02:05	136° 6.7471' W	70° 47.0907' N	741.6	137.1	
AUV06	1	AUV	2022-09-08	02:25	2022-09-08	04:45	136° 6.6283' W	70° 47.1128' N	741.6	136.9	AUV Deploy
AUV06 to Station 28	1	MB/SBP	2022-09-08	04:18			136° 6.6280' W	70° 47.0809' N	740	139.1	
	2	MB/SBP			2022-09-08	06:16	135° 3.9002' W	70° 50.3725' N	143	96.8	

Station 28	1	GC	2022-09-08	06:29	2022-09-08	06:41	135° 3.8691' W	70° 50.3988' N	153	58.1	Bottom touch 06:35 UTC
Station 29	1	GC	2022-09-08	07:23	2022-09-08	07:37	135° 3.6649' W	70° 50.3960' N	130	57.5	Bottom touch 07:30 UTC
Station 29 to ROV09	1	MB/SBP	2022-09-08	08:40			135° 3.6657' W	70° 50.3959' N	130	306	
	2	MB/SBP			2022-09-08	10:49	135° 44.1938' W	71° 0.4315' N	865.4	305.2	
ROV09	1	ROV	2022-09-08	13:05	2022-09-08	19:46	135° 44.1988' W	71° 0.4343' N	866	71.3	
ROV09 to AUV06	1	MB/SBP	2022-09-08	20:00			135° 44.8249' W	71° 0.1183' N	825	210.1	
	2	MB/SBP			2022-09-08	21:09	136° 4.0197' W	70° 48.8107' N	767	205.8	
AUV06	1	AUV.	2022-09-08	21:17	2022-09-08	21:34	136° 4.1484' W	70° 48.8409' N	767	201.5	AUV Recovery
Station 30	1	GC	2022-09-08	22:18	2022-09-08	23:01	136° 5.6600' W	70° 48.0323' N	739	77	Bottom touch 10:39 UTC
Station 30 to Station 31	1	MB/SBP	2022-09-08	23:43			136° 5.6521' W	70° 48.0283' N	740	86.4	
	2	MB/SBP			2022-09-09	4:06	133° 32.6347' W	70° 39.2477' N	67	101.5	
Station 31	1	CTD	2022-09-09	4:09	2022-09-09	04:24	133° 32.6353' W	70° 39.2484' N	67	102	
	2	MC	2022-09-09	4:33	2022-09-09	4:45	133° 32.6339' W	70° 39.2485' N	67	102.3	Bottom touch 04:38 UTC
Station 31 to Station 32	1	MB/SBP	2022-09-09	5:20			133° 32.6345' W	70° 39.2487' N	67	102	
	2	MB/SBP			2022-09-09	08:15	134° 3.4972' W	70° 59.4053' N	221	81.5	
Station 32	1	CTD	2022-09-09	08:22	2022-09-09	08:45	134° 3.4624' W	70° 59.3951' N	221.2	149.6	
Station 32 to Station 33	1	MB/SBP	2022-09-09	08:54			134° 3.4627' W	70° 59.3910' N	221.5	130	
	2	MB/SBP			2022-09-09	11:23	134° 28.4023' W	71° 16.0145' N	1004	36	
Station 33	1	CTD	2022-09-09	11:30	2022-09-09	12:19	134° 28.4071' W	71° 16.0268' N	1012	112.1	
Station 33 to Station 34	1	MB/SBP	2022-09-09	12:25			134° 28.4021' W	71° 16.0292' N	1007	114.6	
	2	MB/SBP			2022-09-10	02:00	132° 12.5419' W	71° 22.5941' N	435	143	
Station 34	1	CTD	2022-09-10	02:35	2022-09-10	03:04	132° 14.2240' W	71° 22.6489' N	451	126.4	

	2	MC	2022-09-10	03:11	2022-09-10	03:35	132° 14.2215' W	71° 22.6510' N	446	105	Bottom touch 03:27 UTC
Station 34 to Station 35	1	MB/SBP	2022-09-10	04:09			132° 14.2272' W	71° 22.6480' N	446	145.9	
	2	MB/SBP			2022-09-10	6:54	131° 42.9837' W	71° 4.5115' N	66.3	133.5	
Station 35	1	CTD	2022-09-10	07:03	2022-09-10	07:20	131° 42.9719' W	71° 4.5159' N	66	129.1	
Station 35 to Station 36	1	MB/SBP	2022-09-10	7:25			131° 42.9728' W	71° 4.5169' N	66	117	
	2	MB/SBP			2022-09-10	09:07	131° 25.0511' W	70° 52.6905' N	56	93.4	
Station 36	1	CTD	2022-09-10	16:02	2022-09-10	16:18	131° 25.0300' W	70° 52.6977' N	56	93	
	2	MC	2022-09-10	16:28	2022-09-10	16:40	131° 24.9263' W	70° 52.7095' N	56	70	Bottom touch 16:33 UTC
Station 36 to 60mPLFs to Station 37	1	MB/SBP	2022-09-10	17:13			131° 24.9156' W	70° 52.7055' N	55	353	
	2	MB/SBP			2022-09-11	2:40	135° 33.3786' W	70° 47.5232' N	423	46.5	
Station 37	1	MC	2022-09-11	2:48	2022-09-11	3:00	135° 33.3915' W	70° 47.5282' N	430	70.5	Bottom touch 03:02 UTC
Station 37 to Station 38	1	MB/SBP	2022-09-11	3:32			135° 33.5751' W	70° 47.5082' N	420	69.4	
	2	MB/SBP			2022-09-11	4:35	135° 31.4785' W	70° 39.2442' N	82	823	
Station 38	1	CTD	2022-09-11	4:43	2022-09-11	4:58	135° 31.4563' W	70° 39.2403' N	82	90.3	
Station 39	2	CTD	2022-09-11	5:12	2022-09-11	5:41	135° 31.7332' W	70° 39.3659' N	90	91.3	
Station 39 to Station 40	1	MB/SBP	2022-09-11	5:50			135° 31.7525' W	70° 39.3718' N	90	100.2	
	2	MB/SBP			2022-09-11	8:59	136° 41.2608' W	70° 11.3575' N	47	245.6	
Station 40	1	CTD	2022-09-11	9:06	2022-09-11	9:19	136° 41.2597' W	70° 11.3592' N	47	242.3	
	2	MC	2022-09-11	9:27	2022-09-11	9:37	136° 41.2090' W	70° 11.3791' N	47	48.6	Bottom touch 09:32 UTC
Station40 to ROV10	1	MB/SBP	2022-09-11	10:18			136° 41.2058' W	70° 11.3776' N	47	48.4	
	2	MB/SBP			2022-09-11	14:36	139° 4.3954' W	69° 52.9691' N	110	195.5	
ROV10	1	ROV.	2022-09-11	16:07	2022-09-11	16:40	139° 4.3183' W	69° 52.9412' N	107	120.6	

Multibeam survey	1	MB/SBP	2022-09-11	17:10			139° 4.5602' W	69° 52.9888' N	98	127.4	
	2	MB/SBP			2022-09-11	21:50	139° 5.3308' W	69° 52.9186' N	74	196.3	
Deck work	1	Deck work	2022-09-11	23:00	2022-09-12	1:31	139° 5.3308' W	69° 52.9186' N	74	196.3	
Station 41	1	GC	2022-09-12	1:48	2022-09-12	2:06	139° 5.1801' W	69° 53.4437' N	87	116.3	Bottom touch 01:59 UTC
Station 42	1	GC	2022-09-12	2:56	2022-09-12	3:14	139° 7.4395' W	69° 55.3487' N	121	114.1	Bottom touch 03:08 UTC
Station 42 to Station 43	1	MB/SBP	2022-09-12	04:11			139° 7.4523' W	69° 55.3435' N	125	186.6	
	2	MB/SBP			2022-09-12	5:42	139° 46.8071' W	69° 50.9881' N	37	96.6	
Station 43	1	CTD	2022-09-12	5:48	2022-09-12	6:00	139° 46.8097' W	69° 50.9860' N	37	98.6	
	2	MC	2022-09-12	6:10	2022-09-12	6:19	139° 46.8095' W	69° 50.9856' N	37	126	Bottom touch 06:14 UTC
Station 43 to Station 44	1	MB/SBP	2022-09-12	6:58			139° 46.8097' W	69° 50.9854' N	37	126	
	2	MB/SBP			2022-09-12	7:34	139° 39.8594' W	69° 56.2224' N	49	81.5	
Station 44	1	CTD	2022-09-12	7:44	2022-09-12	8:00	139° 39.8448' W	69° 56.2237' N	50	120	
Station 44 to Station 45	1	MB/SBP	2022-09-12	8:06			139° 39.8448' W	69° 56.2237' N	50	120	
	2	MB/SBP			2022-09-12	8:48	139° 32.0754' W	70° 1.8624' N	54	177	
Station 45	1	CTD	2022-09-12	8:57	2022-09-12	9:12	139° 31.9928' W	70° 1.8634' N	53	104.8	
Station 45 to Station 46	1	MB/SBP	2022-09-12	9:17			139° 31.9928' W	70° 1.8634' N	53	120	
	2	MB/SBP			2022-09-12	9:57	139° 23.8591' W	70° 7.3081' N	92	101	
Station 46	1	CTD	2022-09-12	10:04	2022-09-12	10:19	139° 23.8172' W	70° 7.3328' N	97	109.9	
Methane survey	1	Methane	2022-09-12	10:24			139° 23.8172' W	70° 7.3328' N	97	96	

*MB : Multi-Beam Echosounder / SBP : Sub-bottom profiler / MC : Multi core / GC : Gravity core / HF : Heat flow measurement / CTD : Conductivity-temperature-density /

ROV : Remotely operated vehicle / AUV : Autonomous underwater vehicle

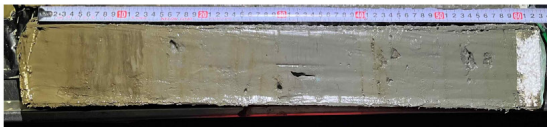
ARA13C Cruise report

Appendix 3. Photos and Descriptions of Sediment Cores

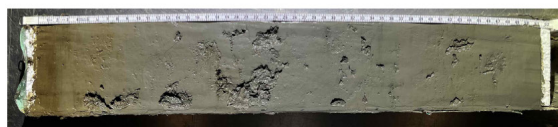
Photos courtesy of Korea Polar Research Institute.

3.1. Multi Cores

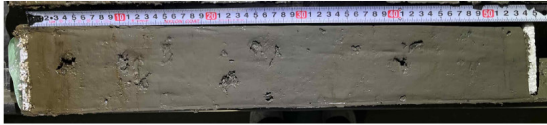
ARA13C-ST01 (60cm)



ARA13C-ST02 (51cm)



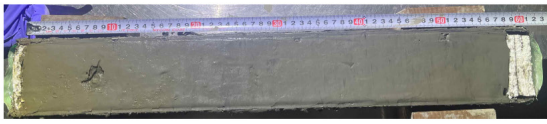
ARA13C-ST03 (54cm)



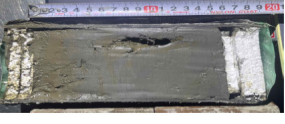
ARA13C-ST04 (51cm)



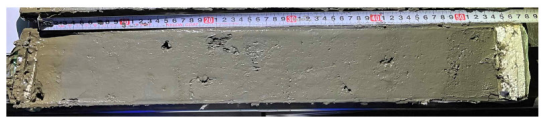
ARA13C-ST05 (58cm)



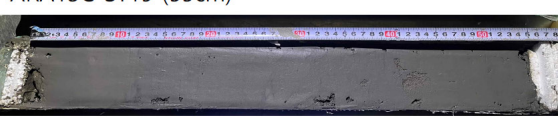
ARA13C-ST06 (16cm)



ARA13C-ST09 (53cm)



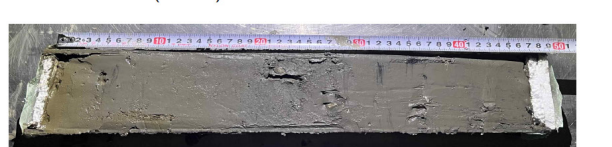
ARA13C-ST19 (55cm)



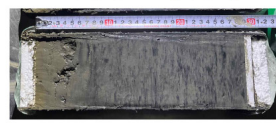
ARA13C-ST20 (42cm)



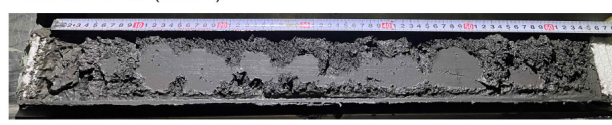
ARA13C-ST21 (47cm)



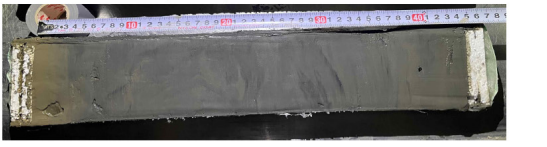
ARA13C-ST22 (29cm)



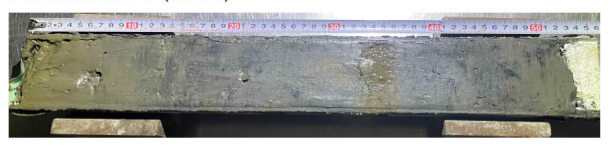
ARA13C-ST25 (65cm)



ARA13C-ST27 (44cm)




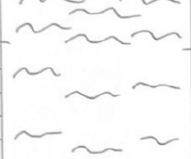

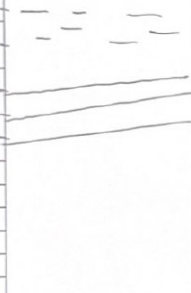
ARA13C-ST31 (52cm)



Core description

Date: 22/08/26

Core: ARA 13C - 5T01 - MUC (0-60 cm)

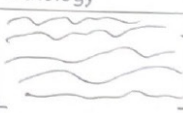


	Lithology	Description
0		0-4 cm
10		Brown (10YR 5/3); very soft, silty mud; homogeneous; lower boundary relatively distinct by color change.
20		4-14 cm Grayish brown to gray (10YR 5/3 to 10YR 5/1); relatively stiff, silty mud with fine coarse grains; heavily mottled with very dark grayish brown (10YR 3/2); gradual transition.
30		14-31 cm Gray (10YR 5/1); soft, silty mud; mottled with yellowish brown (10YR 5/6); lower contact not distinct.
40		31-60 cm Gray (10YR 5/1); soft, silty mud; ^{mostly} homogeneous, very dark gray (10YR 3/1), even laminations with poor lateral continuity occurred at 33-36 cm, declined, sandy mud laminations at 40, 42, 44 cm.
60		Bottom core end.

Ahn

Core description

Date: 22/08/27

Core: ARA13C-ST02-MVC (0-51 cm)

Lithology	Description
	<p>0-2 cm Dark brown (10YR 3/3); soft, silty mud; mottled; gradual transition to next unit</p>
	<p>2-8 cm Gray (10YR 5/1); moderately soft, silty mud; slightly mottled with yellowish brown (10YR 5/6); lower contact not distinct</p>
	<p>8-51 cm Gray (10YR 5/1); moderately soft to relatively stiff, clayey mud; mostly homogeneous, coarse grains with dark yellowish brown mottling at 17-19 cm and 40-46 cm.</p> <p>core end.</p>
<p>50</p>	<p>core end</p>

bioturbation? burrow?

Ahn

Core description

Date:


Core: ARA13C - ST03 - MC (54 cm)

Lithology	Description
0	0 - 4 cm
10	Brown (10YR 5/3) ; soft, silty mud ; homogeneous ; distinct lower boundary with color change
4	4 - 10 cm
20	Gray (10YR 5/1) ; slightly stiff, clayey mud ; yellowish brown mottles ; gradual transition to next unit
10	10 - 54 cm
30	Gray (10YR 5/1) ; stiff, clayey mud ; homogeneous
40	
50	
54	Core end
60	

Core description

Date:

Core: ARA 13C - ST04-MC (51 cm)

	Lithology	Description
0		0-2 cm Brown (10YR 5/3) ; soft, silty mud ; homogeneous
10		2-51 cm Gray (10YR 5/1) ; slightly stiff, clayey mud ; massive, black mottles at 8 - 35 cm (28-33 cm: dark layer)
20		
30		
40		
50		Core end .
60		
		Ahn

Core description

Date:

Core: ARA13C-ST04-MC (58 cm)

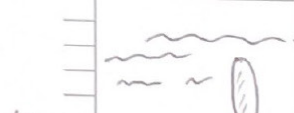
Lithology	Description
0-6 cm	0-6 cm
6-58 cm	Gray (10XR 5/1); slightly soft, clayey mud; slightly mottled with yellowish brown (10XR 5/6); gradual transition to next unit
6-58 cm	6-58 cm Gray (10XR 5/1); stiff, clayey mud; homogeneous, shell fragments (23, 30-31 cm)
60	Core end

Ahn

Core description

Date:

Core: ARA 13C - 5T06⁰⁶⁻¹-MC (16 cm)

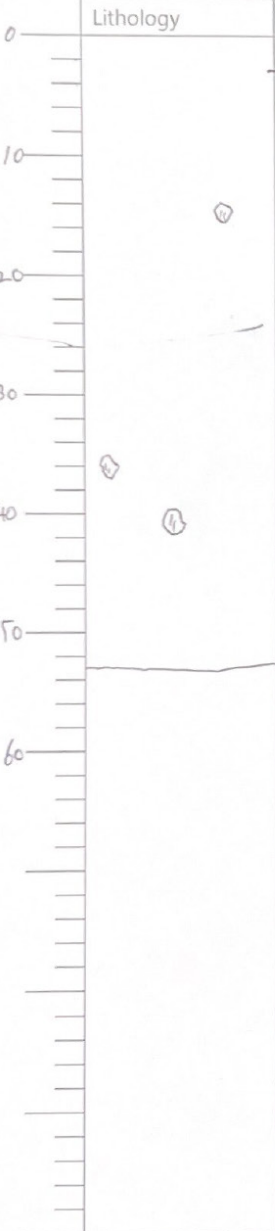
Lithology	Description
	<p>0-3 cm Brown (10YR 5/3); relatively soft, silty mud; homogeneous; contact distinct by color change</p>
<p>3-16 cm</p>	<p>Gray (10YR 5/1); slightly stiff, clayey mud; brown mottles at 3-7 and 12-13 cm, brown colored burrow at 5-11 cm.</p>

Ahn

Core description

Date:

Core: ARA13C-5T09-MC (53 cm)

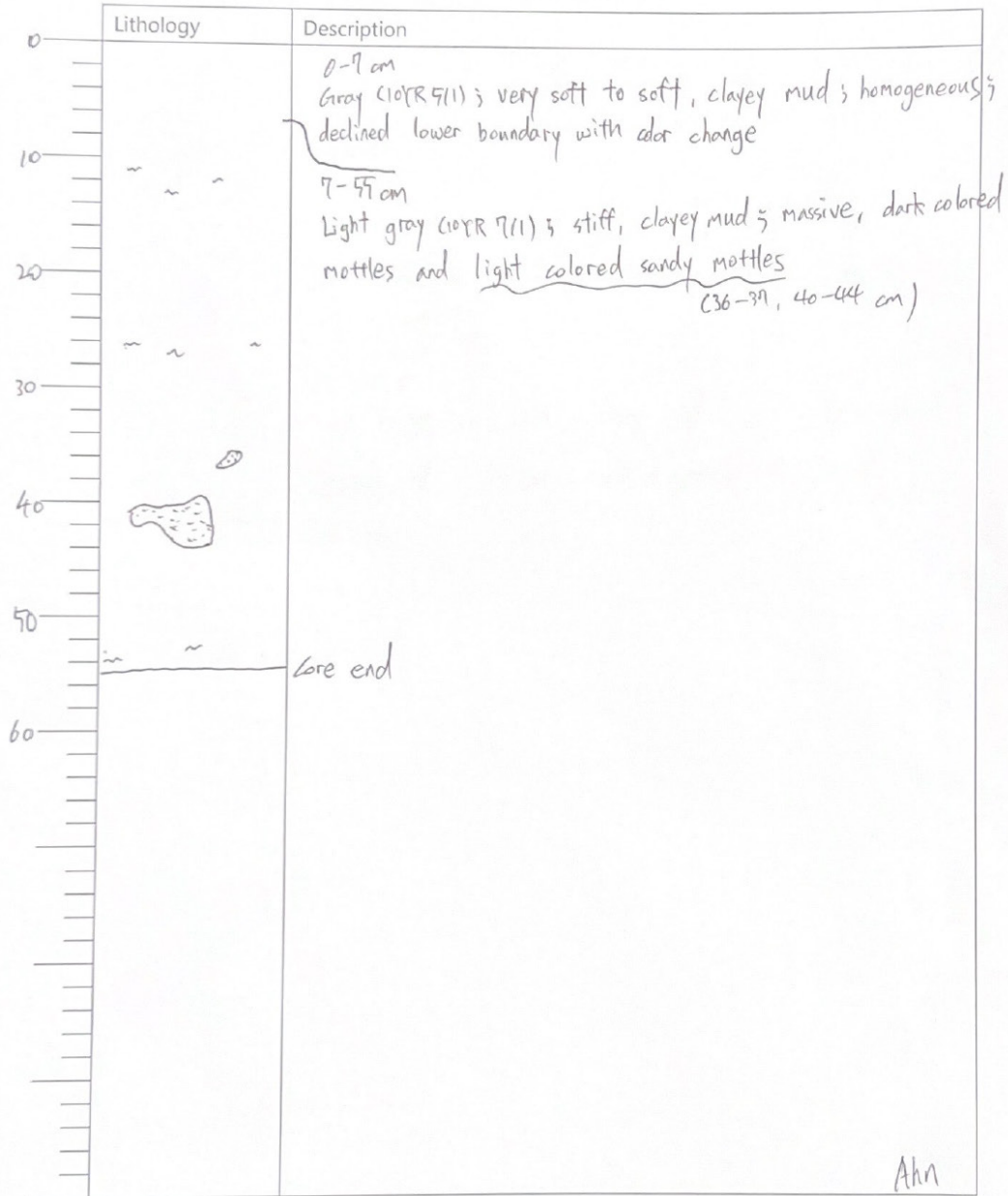
0	Lithology	Description
0-3 cm		Brown (10YR 5/3); very soft, silty mud; homogeneous; contact distinct by color change
3-53 cm		Gray (10YR 5/1); soft, clayey mud; burrows (?) surrounded by brown color at 14-16, 35-39, and 40-42 cm
10		
20		
30		
40		
50		Core end
60		

Ahn

Core description

Date:

Core: ARA13C-ST19-MC (55 cm)







Ahn

Core description

Date:

Core: ARA13C - 5T20 - MC (42 cm)




Lithology	Description
	<p>0-2 cm Brown (10YR 5/3); soft, silty mud with coarse grains & homogeneous; gradual transition to next unit</p>
	<p>2-10 cm Gray (10YR 5/1); slightly stiff, clayey mud; massive, massive brown mottles (especially 8-10 cm); gradual transition to next unit</p>
	<p>10-42 cm Gray (10YR 5/1); stiff, clayey mud; mostly homogeneous; burrow at 12-14 cm, shell fragments (15, 32 cm)</p>
	<p>Core end</p>

Ahn

Core description

Date:

Core: ARA13C-ST21-MC (49 cm)

Lithology	Description
	<p>0-2 cm Brown (10YR 5/3); very soft, silty mud; homogeneous; distinct contact with color change</p>
	<p>2-49 cm Gray (10YR 5/1); soft, clayey mud; mostly homogeneous (6-12 cm: burrow? (dark yellowish brown). (32-49 cm: mottled (black) shell: fragments (21-29, 35-39 cm) intact (29 cm)</p>
	<p>Core end</p>

Ahn

Core description

Date:



Core: ARA13C-ST22-MC (29 cm)

	Lithology	Description
0	~ ~ ~	0-2 cm
	~ ~ ~	Brown (10YR 5/3); very soft, silty mud; homogeneous;
	~ ~ ~	gradual transition to next unit
10	~ ~ ~	2-8 cm (10YR 9/1)
	~ ~ ~	light gray; soft, clayey mud; slightly mottled (black);
	~ ~ ~	blurred even lower boundary
20	~ ~ ~	8-29 cm
	~ ~ ~	Gray (10YR 5/1); slightly soft, clayey mud;
	~ ~ ~	lots of black mottles.
30	Core end	

Core description

Date:

Core: ARA13C -ST25- MC (65 cm)

Lithology	Description
	<p data-bbox="582 560 1117 616">whole core affected by methane gas</p> 

Core description

Date:

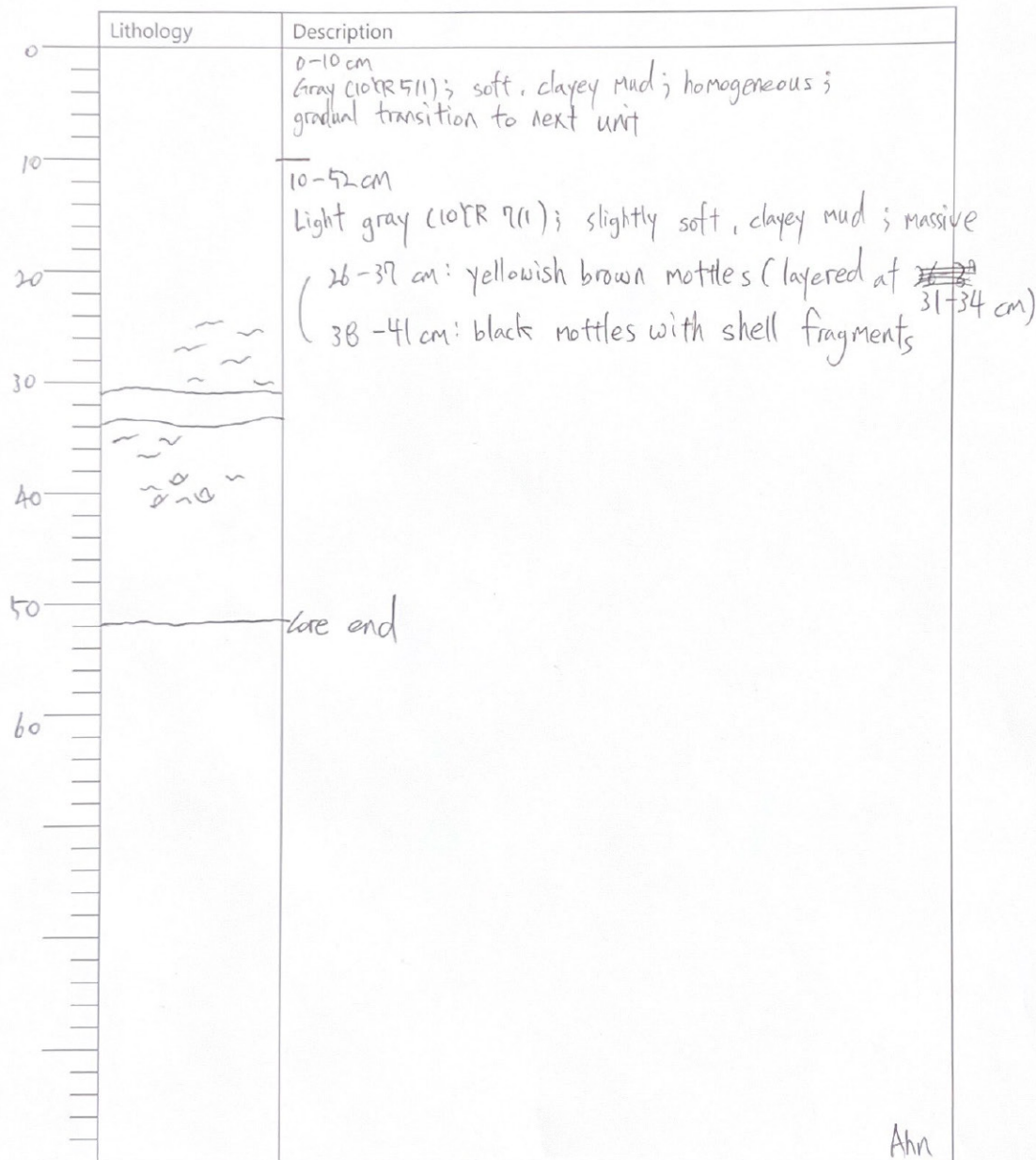
Core: ARA13C-ST29-MC (44 cm)

Lithology	Description
0-4 cm	Brown (10YR 5/3); soft, clayey mud; homogeneous; gradual transition to next unit
4-44 cm	light gray to gray (10YR 7/1 to 5/1); slightly soft, clayey mud; blurred mottles at 28-32 cm (dark color)
~ - ~ - ~	
core end	
50	Ahn

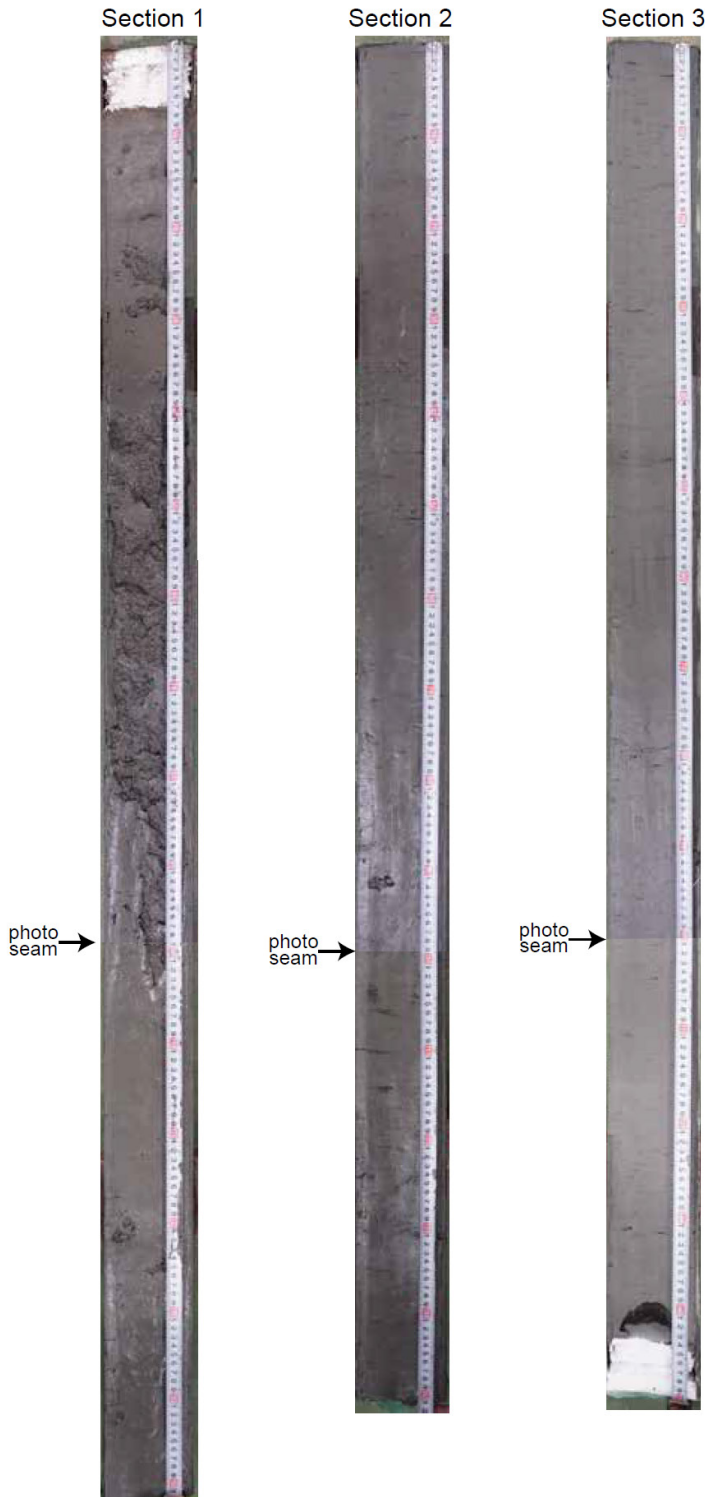
Core description

Date:

Core: ARA 13C - ST31 - MC (52 cm)



3.2. Gravity Cores



ARA13C-ST02-GC

Location: -138.9906167 W
70.22654667 N

Geographic description:
Seaward of Mackenzie
Trough

Date (local): 8/26/2022
Time (local): 1839

Depth (bottom touch): 424 m

Total length: 462 cm
Section 1 length: 162 cm
Section 2 length: 150 cm
Section 3 length: 150 cm

Physical description:

Section 1
0 – 162 cm: Massive dark
gray/olive clay.

Section 2
0 – 150 cm: Massive dark
gray/olive clay, small black
inclusions, at 40-50 cm
invertebrate worm.

Section 3
0 – 150 cm: Massive dark
gray/olive clay, small black
organic inclusions.

Section 1



Section 2



Section 3



photo seam →

photo seam →

ARA13C-ST05-GC

Location: -138.1991033 W
69.35865833 N

Geographic description:
South of Mackenzie Trough

Date (local): 8/27/2022
Time (local): 2118

Depth (bottom touch): 49 m

Total length: 385 cm
Section 1 length: 85 cm
Section 2 length: 150 cm
Section 3 length: 150 cm

Physical description:

Section 1
0 – 85 cm: Dark gray/olive clay with intermittent bands (40-45, 60-70 cm) of black spots/smears.

Section 2
0 – 10 cm: Dark gray/olive clay with few black spots.
10 – 150 cm: Dark gray/olive clay with abundant black spots/smears.

Section 3
0 – 150 cm: Dark gray/olive clay with abundant black spots/smears/blobs.

Section 1



Section 2



Section 3



ARA13C-ST07-GC

Location: -139.0727533 W
69.893685 N

Geographic description:
Herschel Knolls

Date (local): 8/28/2022

Time (local): 1254

Depth (bottom touch): 106.5 m

Total length: 386 cm

Section 1 length: 86 cm

Section 2 length: 150 cm

Section 3 length: 150 cm

Physical description:

Section 1

0 – 86 cm: Dark gray/olive clay with 1-5 cm wide bands of black sed. Very dark prominent black band at 12-15 cm. 2 cm wide void from core face directly through to liner at 15-18 cm.

Section 2

0 – 150 cm: Same lithology as section 01. Small (< 1 cm) crack at 148 cm.

Section 3

0 – 150 cm: Same lithology as sections 01 and 02. Very thick dark black bands at 16-19, 38-43 cm.

photo seam →

photo seam →

shadow

Section 1



Section 2



Section 3



ARA13C-ST08-GC

Location: -139.0720683 W
69.893545 N

Geographic description: West
Mackenzie Trough near
Herschel Knolls

Date (local): 8/28/2022

Time (local): 1409

Depth (bottom touch): 114 m

Total length: 339 cm

Section 1 length: 39 cm

Section 2 length: 150 cm

Section 3 length: 150 cm

Physical description:

Section 1

0 – 38 cm: Dark gray/olive
clay with black bands, 1-4 cm
thickness. Bands darken ~20
cm downcore.

Section 2

0 – 150 cm: Same lithology
as section 01. No systematic
thickening/darkening of
bands apparent.

Section 3

0 – 150 cm: Same lithology
as sections 01 and 02.
Thickest dark bands ~3 cm at
85 cm depth.

Physical samples:

Mud from core catcher (~5
cc)

Section 1



Section 2



ARA13C-ST11-GC

Location: -135.18738 W
70.80774667 N

Geographic description:
Shelf edge

Date (local): 8/30/2022
Time (local): 2056
Depth (bottom touch): 130 m

Total length: 79 cm
Section 1 length: 61 cm
Section 2 length: 18 cm

Deck description:
Short core, sediments dark gray, ice in small ~ 1 cm chunks close to core catcher, 2-3 cm thick lens of ice taken and frozen for analysis.

Physical description:

Section 1
0 – 10 cm: Void space.
10 – 32 cm: Dark gray, soft plastic clay with angular clasts (~5 cm) making matrix.
32 – 39 cm: Dark gray, soft plastic clay with no clasts. Rugose texture, small (1-2 cm) pebbles of very hard clay/chert embedded.
39 – 46 cm: Dark gray, soft plastic clay with 1-2 cm embedded chert and shell fragments (chert is rounded).

Section 2
0 – 18 cm: Dark gray soft plastic clay, ~2 cm pebble embedded in face.

Subsamples:
Section 1 32 – 34 cm: clay
Section 1 35 cm: shell
Section 1: 36 – 38 cm: clay
Ice between sections 1 and 2
Pebble (broken)



↑
cut ice sample

←
ice sample



←
ice visible through core liner on deck

Section 1



ARA13C-ST12-GC

Location: -135.1861117 W
70.80727333 N

Geographic description:
Shelf edge background

Date (local): 8/30/2022
Time (local): 2206

Depth (bottom touch): 120 m

Total length: 182 cm
Section 1 length: 182 cm

Physical description:

Section 1

0 – 150 cm: Dark gray, soft, plastic clay.
3 cm: Dark black smear
18, 34, 38, 46, 48, 61, 67, 75, 81, 88, 102, 134, 142, 157, 163, 177 cm: Irregularly shaped (laminar to lenticular) ~0.5 cm rugose textured areas, same sediment appearance as matrix.
182 cm: Small red (rust colored) spot.

Subsamples:

3 – 5 cm: clay
90 – 92 cm: clay
178 – 180 cm: clay

Section 1



Section 2



Section 3



ARA13C-ST20-GC

Location: -134.9628167 W
70.85022333 N

Geographic description: ESE of
Big Hole

Date (local): 9/2/2022

Time (local): 0129

Depth (bottom touch): 109 m

Total length: 356 cm

Section 1 length: 56 cm

Section 2 length: 150 cm

Section 3 length: 150 cm

Physical description:

Section 1

0 – 56 cm: Dark gray/olive clay with oxidation (8 cm depth), small (1 cm) holes, small black flecks, ~1 cm thick black band at 54 cm. Small shell fragment at 45 cm depth.

Section 2: Same color/texture matrix as above.

0 – 38 cm: Small black flecks.

38 cm: Mousse textured band < 1 cm thick.

44 cm: 1 cm void within mousse band.

48 – 50 cm: Organic black band.

50 – 93 cm: Black flecks.

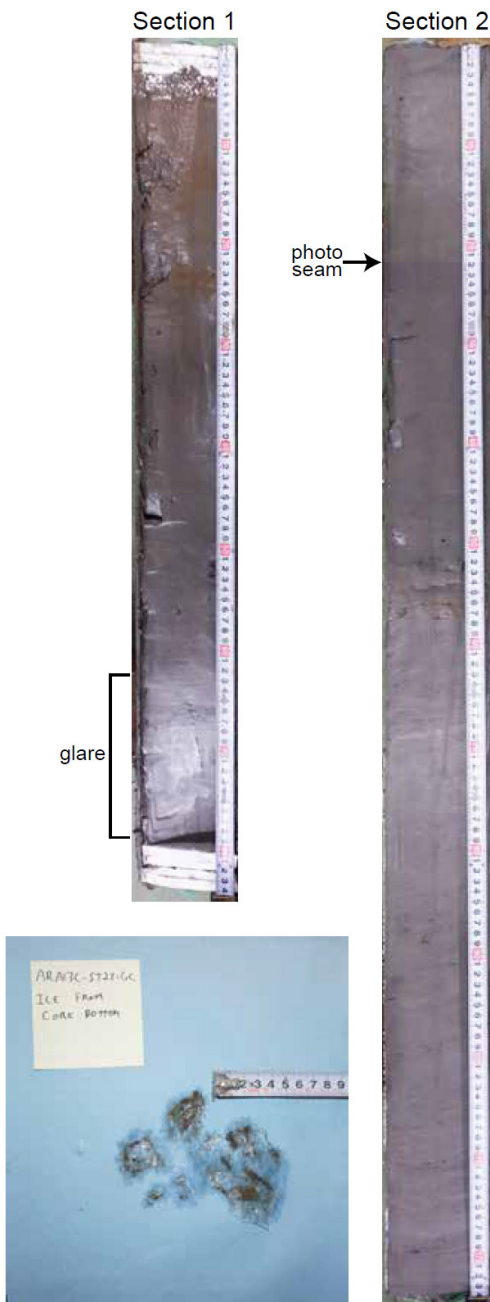
93 cm: Mousse band.

94 – 150 cm: Less frequent black flecks.

126: Small crack, 1 cm long, Not all the way across.

Section 3: Same color/texture matrix as above, thick black

chunks/bands of moussey black fine material at 28, 30, 63, 65, 67, 82, 92, 127, 134 cm. At 88 cm depth, darker gray, less textured than moussey band, 1 cm.



ARA13C-ST23-GC

Location: -135.0840133 W 70.842025 N

Geographic description: Ice hole

Date (local): 9/3/2022

Time (local): 2257

Depth (bottom touch): 156 m

Total length: 207 cm

Section 1 length: 84 cm

Section 2 length: 123 cm

26 cm gap between core catcher and section 3

Section 3 length: 15 (0 – 5 cm void where core was extruded)

Physical description:

Section 1

0 – 25 cm: Massive dark gray clay, wet/shiny appearance.

12 – 29 cm: Red rust-colored bands.

10 – 47 cm: Several cm-scale void spaces.

51 – 72 cm: Possible voids, maybe from splitting core.

Section 2

0 – 54 cm: Dark gray clay with black flecks.

44 – 53 cm: Very small holes (burrows?).

29 – 33 cm, 37 – 40 cm: Shallow ~3 cm voids.

54 – 58 cm: Rust-colored bands.

58 – 110 cm: Uniform dark clay with black flecks.

110 – 123 cm: Darker black bands.

Section 3: Dark gray/olive clay.

Physical sample:

Mud from core catcher.



ARA13C-ST24-GC

Location: -135.0831067 W
70.84207 N

Geographic description: Outside ice hole

Date (local): 9/4/2022

Time (local): 0019

Depth (bottom touch): 158 m

Total length: 286 cm
Section 1 length: 153 cm
Section 2 length: 133 cm

Physical description

Section 1: Matrix of dark gray/olive clay.
0 – 11 cm: Rust-colored bands.
11 – 58 cm: Infrequent black flecks.
58 – 63 cm: Black banding.
63 – 88 cm: Dark gray/olive clay.
85 – 101 cm: Prominent black bands/flecks.
101 – 153 cm: Organic/black flecks.

Section 2: Dark gray/olive clay matrix.
5 – 7 cm: Tilted black band 2 cm thick.
24 – 30 cm: Tilted 2 cm thick black band.
0 – 43 cm: Black flecks.
43 – 108 cm: Tilted to straight moussey dark bands.
108 – 111 cm: Fine sand burrow.
111 – 115 cm: Mousse lens.
115 – 133 cm: Dark gray clay.

Section 1



ARA13C-ST25-GC

Location: -135.566125 W
70.79260667 N

Geographic description: Mud
volcano 420 m

Date (local): 9/4/2022

Time (local): 1554

Depth (bottom touch): 422 m

Total length: 157 cm
Section 1 length: 157 cm

Physical description:

Section 1
0 – 153 cm: Dark gray clay,
sediments very fluffy and
mousse-like.

Section 1



ARA13C-ST28-GC

Location: -135.0660783 W
70.839655 N

Geographic description: Big oval
hole PNAS

Date (local): 9/7/2022
Time (local): 2241

Depth (bottom touch): 153 m

Total length: 164 cm
Section 1 length: 164 cm

Physical description:

Section 1: Dark gray/olive clay
matrix.
10 – 18 cm: Void space on one
side of core.
18 – 100: Uniform clay.
100: Black splats.
128: Black splats.

Section 1



Section 2



ARA13C-ST29-GC

Location: -135.0626633 W 70.83960167 N

Geographic description: Old hole

Date (local): 9/7/2022

Time (local): 2337

Depth (bottom touch): 130 m

Total length: 228 cm

Section 1 length: 128 cm

Section 2 length: 100 cm

Physical description:

Section 1: Dark gray/olive clay matrix

0 – 44 cm: Uniform other than 1 thin black band at 30 cm.

44 – 61 cm: Less shiny, denser clay layer.

61 – 104 cm: Uniform, black band 79-82 cm, 1-2 cm voids: 62, 84, 92, 101 cm.

104 – 128 cm: Disturbed, liquid water, oxidized clay.

Section 2: Dark gray/olive clay matrix.

0 – 20 cm: Few (6) visible cm-scale voids.

20 – 44 cm: Lots of voids, melted ice, wet.

46, 48 cm: Small voids.

57 – 60 cm: Black smears.

80 – 81 cm: Bivalve shell, intact.

Melted ice extraction (from rhizon in section 2, 40 cm depth):

-60 ml sample preserved

-50 ml discarded

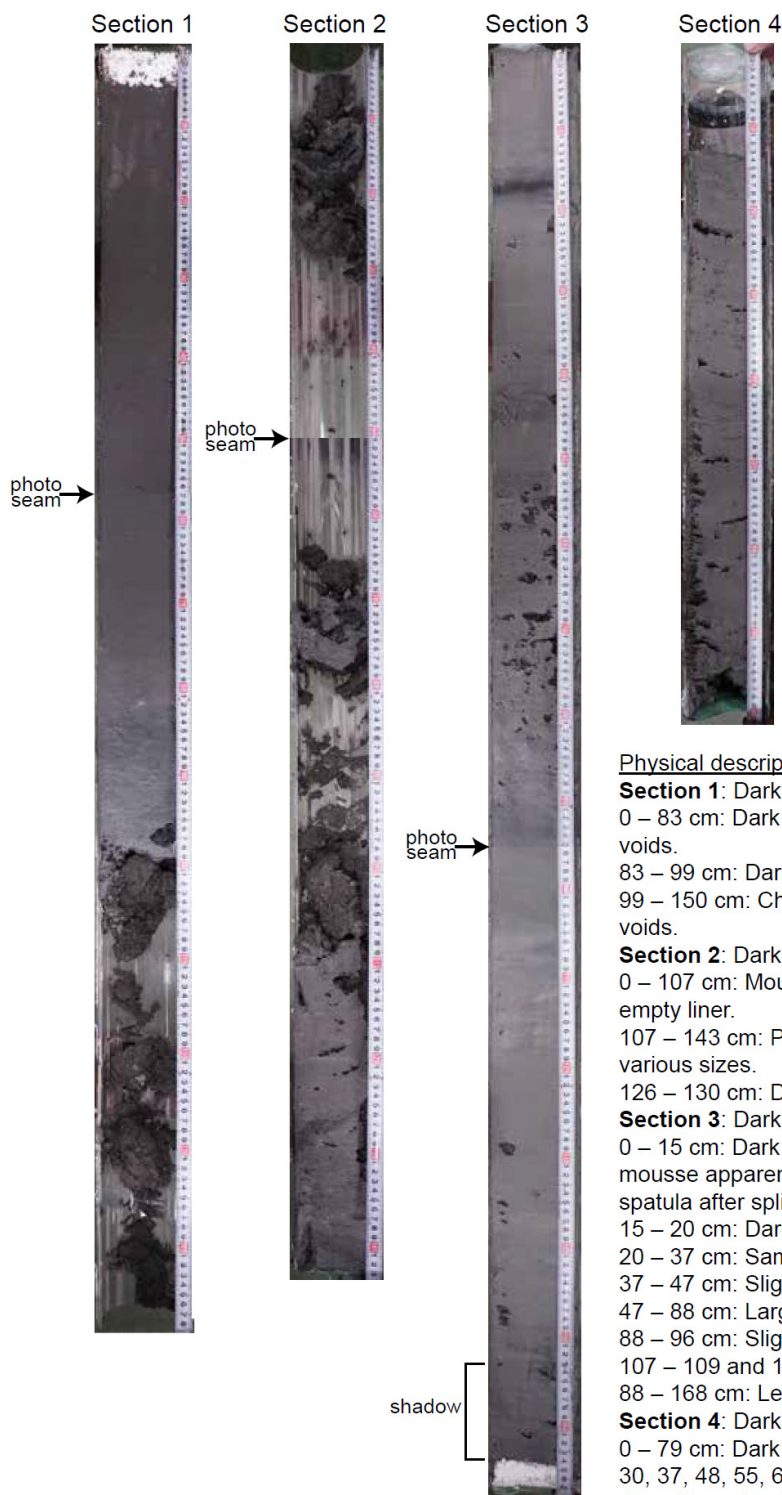
-40 ml subsampled for Jihoon

-50 ml discarded

-50 ml discarded

collapsed sediment from melted ice; visible through liner
→





ARA13C-ST30-GC

Location: -136.0961567 W
70.8004 N

Geographic description: Mud volcano 740 m

Date (local): 9/8/2022
Time (local): 1501

Depth (bottom touch): 739 m

Total length: 541 cm

Section 1 length: 150 cm
(split at void between section 1 and 2)
Section 2 length: 143 cm
(split at void between section 1 and 2)
Section 3 length: 169 cm
Section 4 length: 79 cm

Physical description:

Section 1: Dark gray/olive clay matrix.
0 – 83 cm: Dark gray/olive clay, small sub-cm scale voids.

83 – 99 cm: Darker gray/olive, distinct color change.
99 – 150 cm: Chunks of moussey clay and large voids.

Section 2: Dark gray/olive clay matrix.
0 – 107 cm: Moussey, very disturbed, but mostly empty liner.
107 – 143 cm: Pockets of moussey texture, voids of various sizes.

126 – 130 cm: Duller, less shiny wedge of clay.

Section 3: Dark gray/olive clay matrix.
0 – 15 cm: Dark gray/olive clay with pinprick voids with mousse apparent below core face (flattened with spatula after splitting).

15 – 20 cm: Dark/black mousse banding.

20 – 37 cm: Same as 0 -15 cm.

37 – 47 cm: Slightly darker gray banding.

47 – 88 cm: Large 4-5 cm voids.

88 – 96 cm: Slightly darker organics.

107 – 109 and 150-153 cm: More bands.

88 – 168 cm: Less voids than upper, but still some.

Section 4: Dark gray/olive clay matrix.

0 – 79 cm: Dark gray/olive moussey clay, voids at 21, 30, 37, 48, 55, 60, cm-scale, irregular shapes.

12 – 17 cm: Dark bands.

Section 1



Section 2



ARA13C-ST41-GC

Location: -139.0879367 W 69.891 N

Geographic description: West Mackenzie Trough ridge depression

Date (local): 9/11/2022

Time (local): 1806

Depth (bottom touch): 87 m

Total length: 262 cm

Section 1 length: 155 cm

Section 2 length: 107 cm

Physical description:

Section 1: Dark gray/olive clay matrix with small black specks throughout.

0 - 7 cm: Rust-colored band.

16 - 21 cm: Angled (40-45 deg) bands of dark/black fine fluffy material; same at 53 - 61, 66 - 72, 86 - 93, 95 - 104, 112 - 116, 133 - 137 cm.

Section 2: Dark gray/olive clay, black specks.

27 cm: Black specks increase downcore.

19 - 21 cm: Flat-lying black fluffy band.

35 - 39 cm: Tilted (20 - 30 deg) black band.

87 cm: Small shell fragment.

photo seam →

shadow [

Section 1



Section 2



photo
seam →

ARA13C-ST42-GC

Location: -139.125625 W 69.92273 N

Geographic description: West
Mackenzie Trough ridge

Date (local): 9/11/2022

Time (local): 1914

Depth (bottom touch): 121 m

Total length: 230 cm

Section 1 length: 94 cm

Section 2 length: 136 cm

Physical description:

Section 1: Dark gray/olive clay matrix with small black specks throughout. Several cm-thick dark gray bands every several cm.

4 – 7 cm: Rust-colored fine band.

58 – 59, 65 – 67, 88 – 89 cm: Fibrous wood in black bands.

Section 2: Dark gray/olive clay, black specks. Layers of fluffy dark organics every few cm.

35 – 37 86 – 90 cm: Very dark thick fibrous layer.

105 – 107 cm: Slightly less fibrous.

ARA13C Cruise report

Appendix 4. Marine mammal observations report

The following report, provided by Edgewise Environmental Consultancy Ltd. was not edited as part of the ARA13C cruise report. All photos included in the report were taken during mission ARA13C, courtesy of Edgewise Environmental Consultancy Ltd.

ARA13C MMO REPORT

VERSION 1.3



PREPARED FOR
NATURAL RESOURCES CANADA
GEOLOGICAL SURVEY OF CANADA - PACIFIC

4 JANUARY 2023

Document Information

	INFORMATION
Prepared By	Ashley Noseworthy: Edgewise Environmental Consultancy Ltd
Issue Date	25 Nov 2022
Last Saved Date	05 Dec 2022
File Name	ARA13C : MMO REPORT

Document History

VERSION	ISSUE DATE	CHANGES
1.0	25 Nov 2022	
1.1	05 Dec 2022	<i>Approved track changes from Project Manager, reformatted document</i>
1.2	20 Dec 2022	<i>Added information on marine mammal sightings. Reformatted document.</i>
1.3	4 Jan 2023	<i>Final edits requested from Project Manager.</i>

Table of Contents

DOCUMENT INFORMATION	1
DOCUMENT HISTORY	1
1.0 EXECUTIVE SUMMARY	3
2.0 PROJECT DESCRIPTION.....	3
2.1 PERMITTING.....	5
3.0 OPERATIONS.....	5
3.1 MMO EQUIPMENT	6
3.2 VISUAL OBSERVATION EFFORT.....	6
3.3 WEATHER CONDITIONS.....	6
4.0 MARINE MAMMAL OBSERVATIONS.....	10
4.1 MARINE MAMMAL MITIGATION MEASURES	13
5.0 OTHER INFORMATION	13
APPENDIX A.....	14
APPENDIX B.....	16
APPENDIX C.....	18

1.0 Executive Summary

The ARA13C program, located in the Canadian Beaufort Sea was completed over 18 days from August 26th, 2022 to September 12th, 2022. The program is part of a collaboration between the Korea Polar Research Institute (KOPRI), the Monterey Bay Aquarium Research Institute (MBARI), Natural Resources Canada's (NRCan) - Geological Survey of Canada (GSC) and the U.S Navy Research Laboratory (NRL). Surveying was completed by the ice breaker research vessel Araon, owned and operated by KOPRI and focused along the outer shelf and slope of the Canadian Beaufort Sea. Scientific data collection included geological surveys and sampling, oceanographic and atmospheric sampling, and measurements. The purpose of this program is to address knowledge gaps related to thawing of subsea permafrost and seabed stability. This program was part of the fourth multidisciplinary research program in the Canadian Beaufort and builds upon research programs conducted in 2013, 2014 and 2017 under the same collaboration.

Weather was favourable during the majority of surveying however, after completing the program the vessel encountered remnants of Typhoon Merbok forcing the vessel to take shelter North of Nome for three days.

A Marine Mammal Observer was contracted to collect visual marine mammal observation data during the entirety of the research program. A total of 170.5 hours of visual observation were completed consisting of 7 marine mammal sightings, 3 confirmed species and 8 individuals.

2.0 Project Description

The Beaufort Sea Geoscience Research Program is a collaboration between the Korea Polar Research Institute (KOPRI), the Monterey Bay Aquarium and Research Institute (MBARI), Natural Resources Canada's (NRC) - Geological Survey of Canada (GSC) and the U.S Navy Research Laboratory (NRL). This program utilizes ship-based surveys, geological surveys and sampling, oceanographic and atmospheric sampling, and measurements for the purposes of collecting data on the outer shelf and slope of the Beaufort Sea. The data collected are intended to inform knowledge gaps related to thawing of subsea permafrost and seabed stability. The program took place within the Canadian Beaufort Sea predominantly along the edge of the slope. The overall project area is highlighted in yellow in Figure 1. The dotted lines show the vessels' track during the project.

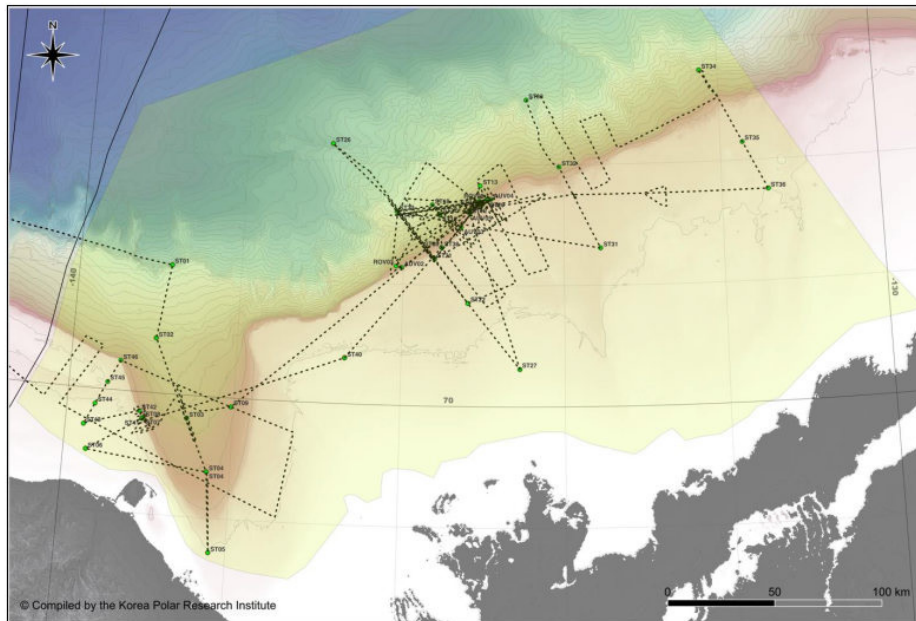


Figure 1. Survey area of ARA13C program (26-Aug-2022 – 12-Sept 2022). The yellow area shows the overall survey areas. The dotted lines show the vessel's track for the entirety of the project.

The program began August 24th, 2022 and ended September 19th, 2022 with data collection occurring between August 26th, 2022 and September 12th, 2022 onboard the Icebreaker Research Vessel (IBRV) Araon (Figure 2). The IBRV Araon was mobilized in Utqiagvik (Barrow), Alaska and demobilized in Nome, Alaska.

During the engagement and program review process, the Inuvialuit Game Council requested that marine mammal observations be recorded during the research program. A Marine Mammal Observer, who met the strict health and safety requirements of KOPRI, was contracted to collect visual marine mammal observation data during the entirety of the research program. There was one dedicated Marine Mammal Observer (MMO) onboard for the entirety of the ARA13C program. No marine mammal mitigation was required as part of any permit or licence granted to the program due to the nature of the research activities. A total of 170.5 hours of visual observation were completed consisting of 7 marine mammal sightings, 3 confirmed species and 8 individuals.

The MMO used a custom spreadsheet based on the Joint Nature Conservation Commission (JNCC) MMO spreadsheet to record and report. All raw effort data have been supplied to the client.

The Marine Mammal Observer was stationed on the bridge, approximately 16.3m above the water line, during all watches with a 360-degree view around the vessel.

2.1 Permitting

The project abided by the following permits:

- Marine Science Research Permit IGR-1283
- Inuvialuit Environmental Impact Screening Committee (EISC) – EISC Registry File [01-22-08]
- Northwest Territories Scientific Research Licence – Licence No. 16995
- Yukon – Canada Scientists and Explorers Act Licence – Licence No. 22-11S&E

3.0 Operations

There was one dedicated Marine Mammal Observer (MMO) onboard for the entirety of the ARA13C program. The MMO kept watch for 8 hours per day during active science survey days and maintained periods of watch during periods of transit and when not collecting data. No marine mammal mitigation was required for this project.

The MMO used a custom spreadsheet based on the Joint Nature Conservation Commission (JNCC) MMO spreadsheet to record and report. All raw effort data have been supplied to the client.

Throughout the duration of surveying the MMO completed a total of 170 hours and 31 minutes of observation hours between 25 August – 12 Sept 2022.

3.1 MMO Equipment

The Marine Mammal Observer used Nikon Prostaff 7 binoculars with a magnification of 10 x 42. A pair of reticle binoculars with a magnification of 10 x 50 were also used to determine distance. A radar, range stick and by-eye were also used depending on the circumstances of the sighting. A Canon 1000D camera with Tamron 70-300 Telescoping lens and were used to obtain photographs of sightings when possible.

3.2 Visual Observation Effort

There was one dedicated Marine Mammal Observer (MMO) onboard for the entirety of the ARA13C program. The MMO kept watch for 8 hours per day during active survey days and maintained periods of watch during periods of transit and when not collecting data.

The MMO used a custom spreadsheet based on the Joint Nature Conservation Commission (JNCC) MMO spreadsheet to record and report.

Throughout the duration of surveying the MMO completed a total of 170 hours and 31 minutes of observation hours between 25 August – 13 Sept 2022.

3.3 Weather Conditions

The weather conditions during the survey period between August 26th, 2022 and September 12th, 2022 were favourable for marine mammal observation. The wind was predominantly from the East (Figure 3) with a speed of 11-16 knots for 38% of the trip (Figure 4). There was no significant swell (over 4m) for the duration of the project except for the transit to Nome when the vessel encountered a weather system. This data is not included in weather conditions as this was outside active surveying. The program saw a Beaufort between 2-5 for 77% of surveying (Figure 5). Visibility was greater than 5km for 64% of the project (Figure 6) and there was no glare for the majority of the project (Figure 7). There was fog present for almost half of the project (Figure 8).

When sailing from the survey site to the planned disembarkation port of Nome the project encountered remnants of Typhoon Merbok. This delayed transit as the vessel had to shelter in-

place north of Nome for approximately 3 days. This weather was not recorded by the MMO and thus not reported as it would skew the average weather reported during the survey when operations took place. The MMO did take note of the average daily weather conditions during the weather event reporting an average Beaufort of 8-9 with wind gusts up to 45 knots.

All numerical weather data and position coordinates were sourced from the ship’s navigation platform accessible on a private network. A screenshot of the interface can be found in Appendix B.

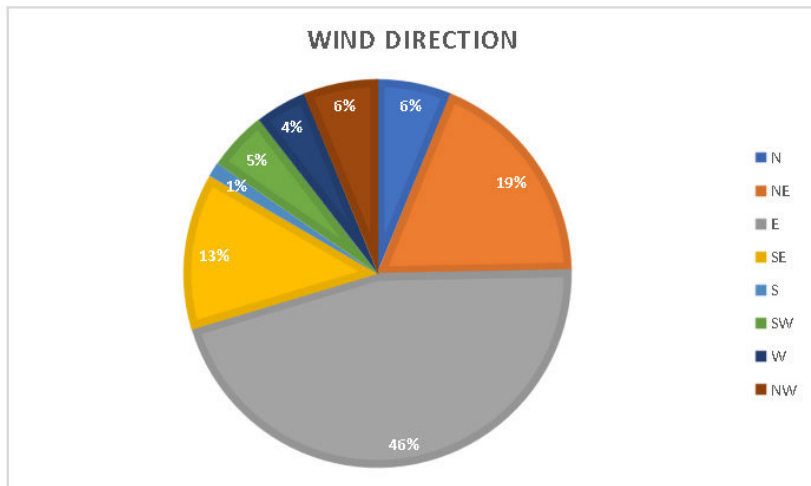


Figure 3. Wind direction observations for the ARA13C 2022 Survey (25 August 2022 – 13 Sept 2022). Numbers represent the percentage of time a corresponding condition was observed.

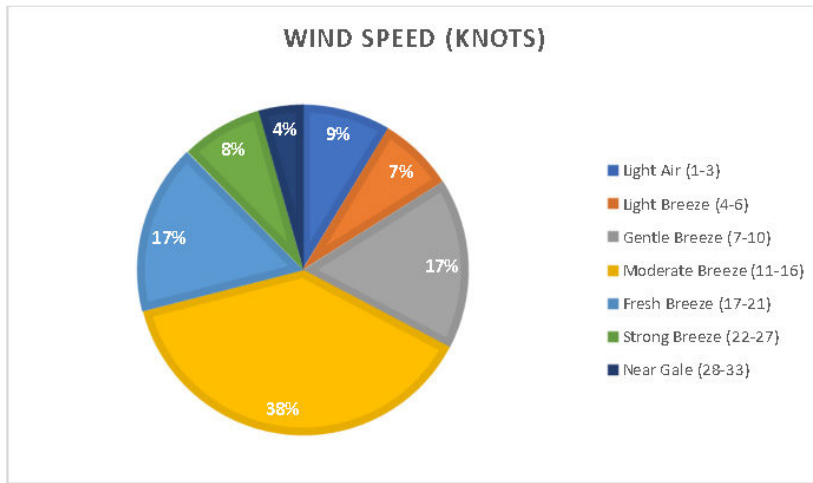


Figure 4. Wind speed observations for the ARA13C 2022 Survey (25 August 2022 – 13 Sept 2022). Numbers represent the percentage of time a corresponding condition was observed.

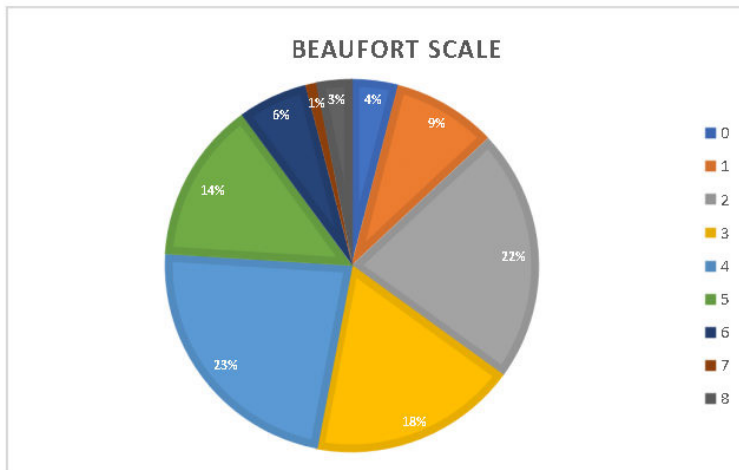


Figure 5. Beaufort (sea state / wind force) observations for the ARA13C 2022 Survey (25 August 2022 – 13 Sept 2022). Numbers represent the percentage of time a corresponding condition was observed.

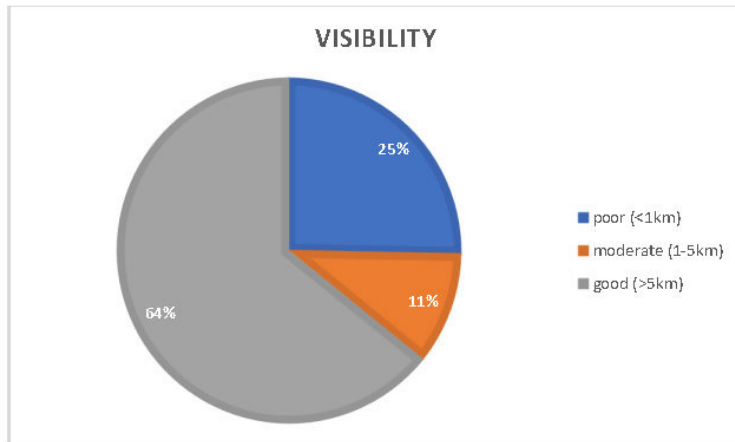


Figure 6. Visibility observations for the ARA13C 2022 Survey (25 August 2022 – 13 Sept 2022). Numbers represent the percentage of time a corresponding condition was observed.

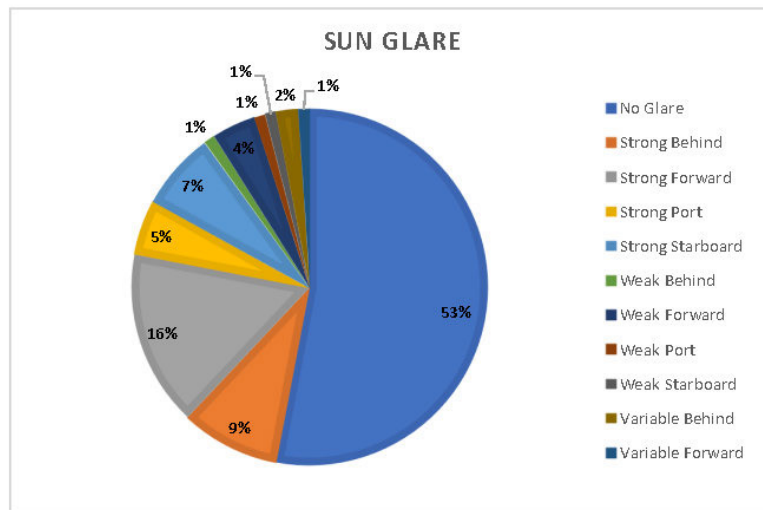


Figure 7. Sun glare observations for the for the ARA13C 2022 Survey (25 August 2022 – 13 Sept 2022). Numbers represent the percentage of time a corresponding condition was observed.

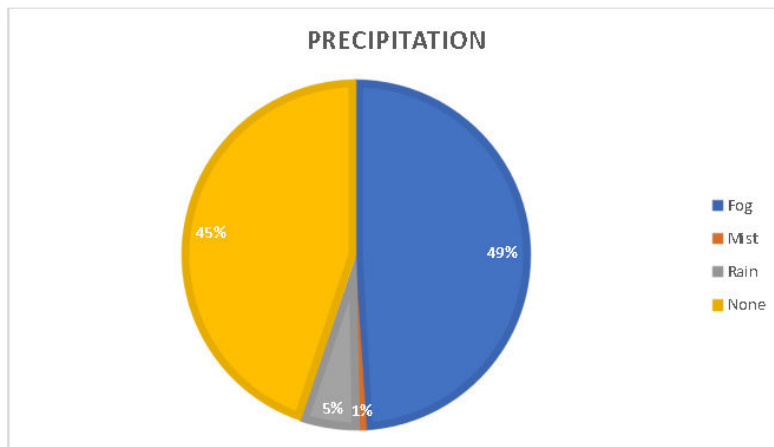


Figure 8. Precipitation observations for the ARA13C 2022 Survey (25 August 2022 – 13 Sept 2022). Numbers represent the percentage of time a corresponding condition was observed.

4.0 Marine Mammal Observations

A total of 7 sightings of 8 individuals and 3 confirmed species were observed during program. (Table 3). Five of the sightings were observed by the MMO and 2 were spotted incidentally by a member of the scientific crew with one subsequently confirmed and observed by the MMO shortly after. All incidental sightings were relayed to the MMO and recorded.

All except for one sighting were phocids (Table 3). One polar bear was observed on pack ice as the vessel approached a station to complete a CDT cast.

The marine mammal sightings occurred sporadically within the survey area with one sighting made when the vessel was just outside of Barrow, prior to departure. This sighting does not show up on the map (Appendix A). Three of the 7 sightings were made in close location of one another near the southern boundary of the survey area near Herschel Island (Appendix A).

Photos from select sightings can be found in Appendix C. A summary of the marine mammal observations are presented in Table 1 on the next page. Full data, which includes the following information can be accessed in the accompanying Excel Spreadsheet;

- Sighting #
- Date
- Start and end time and duration of observation
- How animals were first detected
- Observer name
- Position of sighting (latitude and longitude)
- Vessel heading
- Water depth
- Species / species group
- Description of species / species group
- Bearing and range to animal
- Total number of animals (indicating number of adults, juveniles and calves)
- Description of behaviour
- Direction of travel
- Vessel operations when first and last detected
- Closest distance of animal
- Closest time of approach

Table 1. Marine Mammal Sightings for the ARA13C program (25 August 2022 – 14 September 2022)

SIGHTING #	DATE	SPECIES	DURATION OF OBSERVATION (HH:MM)	LATITUDE	LONGITUDE	VESSEL HEADING (DEGREES)	CLOSEST DISTANCE OF ANIMAL(s) (M)	DIRECTION OF TRAVEL (from True North)
1	24-08-2022	Harbour Seal (<i>Phoca vitulina</i>)	0:03	71 22.298 N	156 54.246 W	323	50	Southwest
2	27-08-2022	Harbour Seal (<i>Phoca vitulina</i>)	0:02	69 41.371 N	138 16.644 W	080	40	Unknown
3	28-08-2022	Unidentified Seal (<i>Phocid sp.</i>)	0:01	69 50.288 N	139 10.187 W	214	750	Unknown
4	28-08-2022	Bearded Seal (<i>Erignathus barbatus</i>)	0:25	69 49.645 N	139 11.700 W	018	20	Unknown
5	28-08-2022	Unidentified Seal (<i>Phocid sp.</i>)	0:01	69 49.645 N	139 11.700 W	018	500	Unknown
6	02-09-2022	Unidentified Seal (<i>Phocid sp.</i>)	0:01	70 47.445 N	135 17.587 W	055	750	Unknown
7	10-09-2022	Polar Bear (<i>Ursus maritimus</i>)	1:10	71 22.604 N	132 12.477 W	141	550	Various

4.1 Marine Mammal Mitigation Measures

There was no mitigation required for the ARA13C program. It is worth noting that 4 of the observations were observed within 500m of the vessel and all marine mammal observations came within less of 1 kilometre at their closest approach.

5.0 Other Information

The crew of the Araon took great interest in the marine mammal species that could be observed in the Arctic. It was requested of the MMO to provide posters, that were printed and laminated onboard and posted on the bridge. This provided to be an informative visual reference when any crew had questions about general marine mammal species of the Western Arctic. The MMO also had field ID guides for marine mammals and seabirds available during the program.

APPENDIX A

Map of Marine Mammal Observations

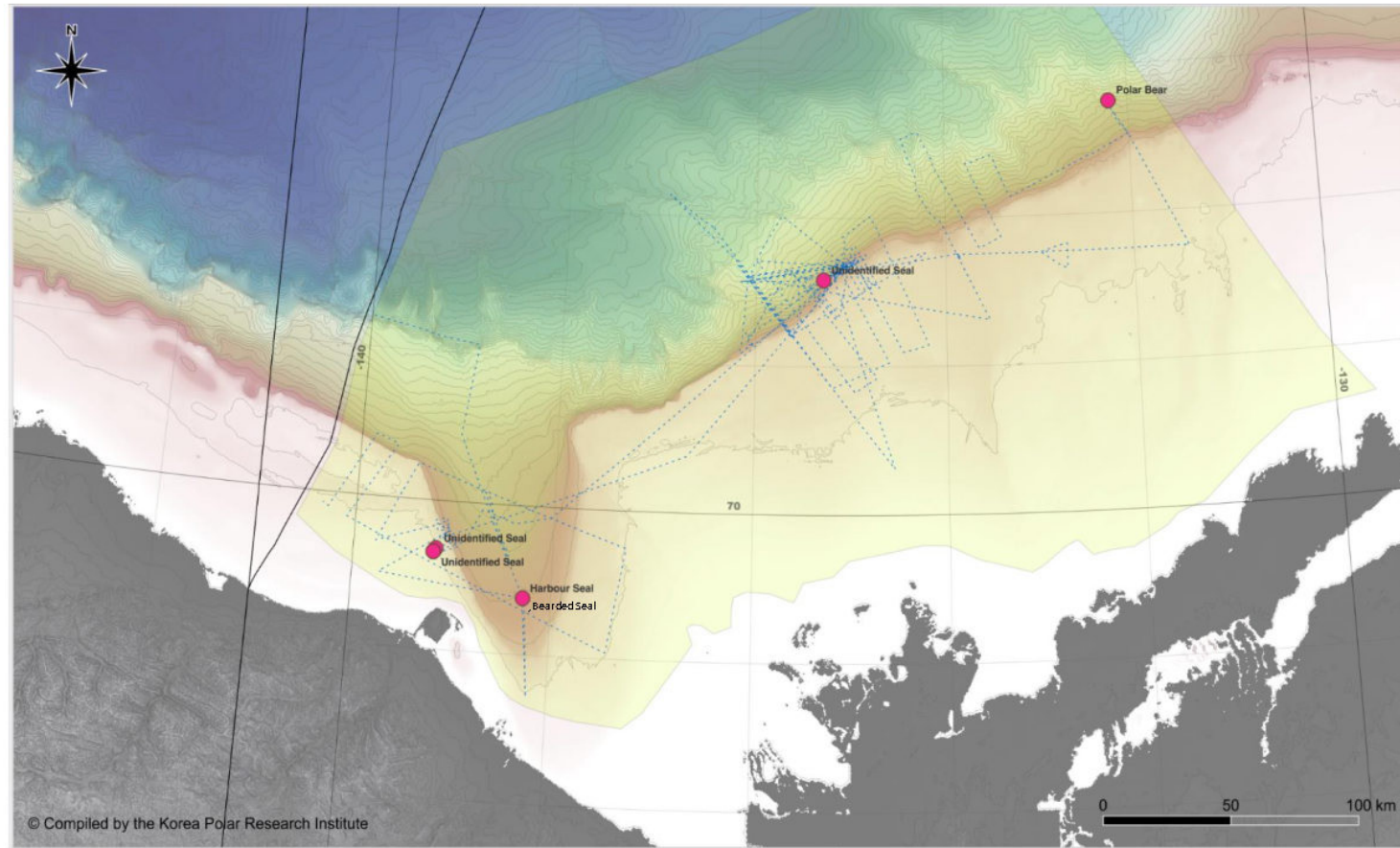


Figure 9. ARA13C 2022 marine mammal sightings onboard the IBRV (25 August 2022 – 13 Sept 2022). One observation of a Harbour Seal is not depicted on the map due to this observation being made before departure from Barrow, Alaska and outside the survey area.

APPENDIX B

Screenshot of Vessel Map Interface



Figure 10. Screenshot of IBRV Araon vessel navigation interface.

APPENDIX C

Select Marine Mammal Observation Photographs



Observation #4. Bearded Seal



Observation #7. Polar Bear

ARA13C Cruise report

Appendix 5. Group Photo

2022 ARAON BEAUFORT SEA CRUISE ARA13C expedition <23. Aug. ~ 18. Sep.>



 Jong Kuk Hong 홍중국, KOPRI Chief scientist	 Tae Sleek Rhee 이태석, KOPRI Oceanography	 Seung-Goo Kang 강승구, KOPRI Geophysics	 Yung Mi Lee 이영미, KOPRI Microbiology	 Heungsoo Moon 문홍수, KOPRI Coring operator	 Hyoungjun Kim 김형준, KOPRI Multibeam	 Youngil Choi 최영일, KOPRI Geophysics
 Yeonjin Choi 최연진, KOPRI Geophysics	 Mi Seon Kim 김미선, KOPRI Chemical oceanography	 Youngkyu Ahn 안영규, KOPRI/Inha Univ. Sedimentology	 Woohyun Kim 김우현, KOPRI Microbiology	 Minjee Kim 김민지, KOPRI Oceanography	 Hyebin Park 박혜빈, KOPRI Oceanography	 Ji Hoon Kim 김지훈, KIGAM Geochemistry
 Young-Gyun Kim 김영균, Kangwon Univ. Marine geology	 Thi Hien Nguyen 김미선, KOPRI Environmental engineering	 See Ryang Seong 성시량, Hanyang Univ. Organic geochemistry	 Jungwhoun Mok 목정훈, UNIST Chemical engineering	 Hyeon Seob Kim 김현섭, Kangwon Univ. Numerical geodynamic	 Yijeong Baek 백이정, Kangwon Univ. Numerical geodynamic	 Sangmi Lee 이상미, Syeongsang Univ. Mineralogy
 Sangwoo Eom 임상우, GIST Biogeochemistry	 Juhyeong Chae 채주형, GIST Biogeochemistry	 Hakwon Jeong 정하권, GIST Biogeochemistry	 Younggwang Kim 김영광, POSTECH Environmental engineering	 Seunghyeon Lim 임승현, POSTECH Environmental engineering	 Kiwon Hong 홍기원 Artist	 Eunsang Yun 윤은상 Navy
 Charles Paull MBARI Marine geology	 David Caress MBARI Seafloor mapping	 Jennifer Paduan MBARI Seafloor mapping	 Roberto Gwiazda MBARI Geochemistry	 Frank Flores MBARI ROV	 Dale Graves MBARI ROV	 Eve Lundsten MBARI Marine geology
 Jordan Caress MBARI AUV	 Tanner Poling MBARI AUV	 Randall Prickett MBARI AUV				
 Eric Martin MBARI AUV/ROV	 Maureen Walton NRL Marine geophysics	 Jeffrey Blake NRL Marine geology				
 Virginia Brake GSC Marine geology	 Ashley Noseworthy Edgewise Environmental MMO	 Daeyoung Lee 이대영 Medical doctor				
						



Photo courtesy of Korea Polar Research Institute.